

On the Subject of Phase Transitions and Thermoelectric Properties

by

Duncan Hardie

A Thesis Submitted in Fulfilment of the Requirements for the Degree of Doctor
of Philosophy in Theoretical Chemistry at Cardiff University

29th June 2018



DECLARATION

This work has not been submitted in substance for any other degree or award at this or any other university or place of learning, nor is being submitted concurrently in candidature for any degree or other award.

Signed Date

STATEMENT 1

This thesis is being submitted in partial fulfilment of the requirements for the degree of Ph.D.

Signed Date

STATEMENT 2

This thesis is the result of my own independent work/investigation, except where otherwise stated, and the thesis has not been edited by a third party beyond what is permitted by Cardiff University's Policy on the Use of Third Party Editors by Research Degree Students. Other sources are acknowledged by explicit references. The views expressed are my own.

Signed Date

STATEMENT 3

I hereby give consent for my thesis, if accepted, to be available online in the University's Open Access repository and for inter-library loan, and for the title and summary to be made available to outside organisations.

Signed Date

ACKNOWLEDGEMENTS

I would like to take the opportunity to thank my supervisor, Dr Stefano Leoni, for his insight, patience and sense of humour. He has a knack for coming up with interesting projects, and I hope to work with him again in the future. Let it be known that I am so very grateful for the opportunities you have given me. And I have learned a lot, though the topics need not strictly be in computation!

I give thanks also, to the gents in the office who have kept me entertained these past four years. Samuel Jobbins, Timothy Flack, Darren Wragg and Jordan Rundle, I cannot thank you enough for your company and collaboration, I will miss your eloquent conversation...

I must thank my parents, for their continued support and guidance. I am indebted to each of you for helping me to get this far. I am looking forward to spending a little more time with you!

To my extended family and friends, and to anyone who has checked in on me whilst I have spent my evenings alone with my laptop, I am so glad to have you behind me.

Thanks, must also go to Martin Boughtwood, Dr Benjamí Martorrel Masip, Dr Steven Hepplestone, Dr Georgios Tritsarlis and everyone else at Deregallera. Thank you for your sponsorship, your ideas and your time, I have enjoyed working with you all and am looking forward to continuing to do so.

CONTENTS

Declaration	i
Acknowledgements	ii
Contents	iii
List of Publications	vi
Summary	vii
1 – Introduction	1
1.1 – General Introduction	1
1.2 – Overview	2
2 – Computational Theory	4
2.1 – Introduction	4
2.2 – Origins of Density Functional Theory	5
2.2.1 – Hartree Method	5
2.2.2 – Early Density Functional Theory	7
2.2.3 – Modern Density Functional Theory	8
2.2.4 – Kohn-Sham Equations	9
2.2.5 – Local Density Approximation	10
2.2.6 – Generalised Gradient Approximation	11
2.2.7 – Hybrid Functionals	12
2.3 – Tight Binding Approach	12
2.3.1 – Density Functional Based Tight Binding	13
2.3.2 – Electronic Transport	14
2.4 – Codes Used	16
2.4.1 – Siesta	16
2.4.2 – Quantum ESPRESSO	17
2.4.3 – DFTB+	18
2.4.4 – gDFTB+	18
2.5 – Techniques	18
2.5.1 – Geometry Optimisations	19
2.5.2 – Molecular Dynamics	22
2.6 – References	28

CONTENTS

3 – Thermoelectric Materials Review	31
3.1 – Introduction to Thermoelectric Materials	31
3.2 – Modern Theory of Thermoelectricity	35
3.3 – Methods of Improving Thermoelectric Materials	37
3.3.1 – Defect Mechanisms	37
3.3.2 – Size Defects	40
3.3.3 – Critical Phenomena	41
3.3.4 – Anharmonicity	42
3.3.5 – Spin Effects	42
3.3.6 – Hierarchical Architectures in Thermoelectrics	43
3.4 – Materials of Interest	44
3.4.1 – Post Transition Metal Chalcogenides	44
3.4.2 – Oxyselenides	44
3.4.3 – Silicon Germanium Compounds	45
3.4.4 – Copper Chalcogenides	45
3.4.5 – Half Heuslers	46
3.4.6 – Filled Skutterudites	46
3.5 – Derivation of Thermoelectric Coefficients from Electronic Transmission	47
3.6 References	49
4 – Effect of Pressure-Induced Phase Transitions on the Thermoelectric Properties of Black Phosphorus	53
4.1 – Introduction	53
4.1.1 – Allotropy in Phosphorus	54
4.1.2 – Objectives	56
4.2 – Black Phosphorus	57
4.3 – Electronic Transport in Black Phosphorus Thin Films	58
4.4 – Electronic Transport in Bulk Black Phosphorus	65
4.5 – Effect of Pressure on the Band Structure of Black Phosphorus	70
4.6 – Pressure Phase Transitions – The Effect of Pressure on Thermoelectricity	74
4.6.1 – Phase Transitions in Black Phosphorus	74
4.6.2 – Phase Transitions and Thermoelectric Properties	82
4.7 – Summary	100
4.8 – References	101

CONTENTS

5 – Tin Sulfides as Thermoelectric Materials	103
5.1 – Introduction	103
5.2 – Literature	104
5.3 – Crystallographic Study of Ground State Crystal Structures	105
5.3.1 – DOS	109
5.3.2 – Bands	111
5.3.3 – Equations of State	113
5.4 – Transport in Tin Sulfides	117
5.4.1 – Transmission in Tin Sulfides	117
5.4.2 – Thermoelectric Properties of Herzenbergite	122
5.4.3 – Thermoelectric Properties of Berndtite	130
5.4.4 – Thermoelectric Properties of Ottemannite	136
5.4.5 – Discussion of Results of NSCC DFTB	141
5.4.6 – SCC Thermoelectric Properties of Herzenbergite	142
5.4.7 – SCC and Thermoelectric Properties of Berndtite	148
5.5 – Novel Materials	151
5.5.1 – Structures, Symmetry	151
5.5.2 – DOS	152
5.5.3 – Bands	154
5.5.4 – Transport and Thermoelectric Properties of β -SnS	156
5.5.5 – Transport and Thermoelectric Properties of π -SnS	158
5.5.6 – Discussion	160
5.6 – Conclusions	160
5.7 – References	162
6 – Final Notes	164
6.1 – Computational Methods	164
6.2 – Thermoelectric Materials	164
6.3 – On Phosphorus as a Model Thermoelectric Material	164
6.4 – On Tin Sulfides as Thermoelectric Materials	165
6.5 – Closing Remarks	166

LIST OF PUBLICATIONS

The Effect of the Pressure Induced Phase Transition on the Thermoelectric Properties of Black Phosphorus – *In Preparation*

Novel Phases of Tin Sulfides as Thermoelectrics – *In Preparation*

SUMMARY

In this work, Density Functional based Tight Binding methods are used according to the Non-Equilibrium Greens Function method, to calculate the thermoelectric properties of phosphorus materials and tin sulfide phases. The effects of several types of phase transitions, on the thermoelectric properties of these layered materials, are considered.

It is shown that, not only is consideration of structural and electronic rearrangements within the operating conditions of thermoelectric materials necessary, but that the presence of structural phase transitions, in the absence of an electronic phase transition, may in fact be a powerful means of enhancing the thermoelectric properties of a material.

1 – INTRODUCTION

1.1 – GENERAL INTRODUCTION

In this work, Density Functional based Tight Binding (DFTB) methods are applied to the modelling of large systems of thousands of atoms. The Non-Equilibrium Greens Functions approach to modelling electronic transport is used as a means to derive the electronic transmission. According to the Landauer-Büttiker formalism, the thermoelectric transport properties of several novel materials are modelled, with the aim of constructing a framework from which exciting new thermoelectric materials may be created.

Thermoelectric materials are a time-honoured means of generating electricity from waste heat, in a solid-state device. The search for new sustainable technologies needs no introduction, and it is due to the impact of climate change on society that there has been a substantial increase in funding for potential green technologies.

2D-layered materials are a key research topic in the electronics community, due to their novel phenomena. Layered materials have become especially of interest to the thermoelectric community, as several of the most recent advances in efficiencies have been realised in layered compounds.

Thermoelectric devices tend to operate at higher efficiencies at elevated temperatures, and it is this subjection to extreme conditions that makes the concept of phase transitions in thermoelectric materials so intriguing. The notion that a phase transition may occur within the operating conditions of a material, and have a beneficial impact upon its figure of merit is an exciting concept.

In this work, the effect of several distinct, unique phase transitions on the electronic thermoelectric transport properties are investigated. These include both pressure, and temperature induced structural phase transitions, pressure induced electronic phase transitions, and the seemingly size-dependent transition of a recently discovered phase of tin sulfide.

The concept of utilising the structural disorder observed during a phase transition to enhance these thermoelectric properties is developed, and some interesting results are presented.

1.2 – OVERVIEW

The thesis is structured in such a way that the aforementioned methodology of thermoelectric material enhancement is gradually developed from simple concepts. The general outline of the thesis is as follows.

The first chapter is a general introduction to the thesis.

The second chapter forms the basis for the theoretical work of this thesis. In this section, the derivation of computational methods such as Density Functional Theory and Density Functional based Tight Binding theory is presented. An introduction to the methods used within computational chemistry simulations follows, with a discussion of the merits of such methodologies for specific purposes. The codes used within this thesis are then explained, and the theoretical section is concluded.

The third chapter is an introduction to the field of thermoelectrics. The basic concepts upon which the theory of thermoelectricity is built are introduced, along with a derivation of the various figures of merit applied to the understanding of a thermoelectric materials waste-heat conversion efficiency. A basic review of the state-of-the-art methods of thermoelectric material optimisation is presented, followed by a review on the state-of-the-art in thermoelectric materials. Finally, an introduction to the methodologies used to derive the thermoelectric properties from electronic transport calculations concludes the chapter.

The fourth chapter begins with an investigation into electronic transport in thin-film nanowires of black phosphorus. The impact of film thickness on the transport properties is considered, and familiarity with the methodology of transmission calculations is established. An investigation into the effect of pressure on the electronic structure of black phosphorus is conducted, which suggests that an electronic phase transition may be induced in black phosphorus, under uniaxial pressure. The concept of high pressure phase transitions in phosphorus allotropes is introduced, along with a theory of how the influence of pressure may enhance the thermoelectric properties of black phosphorus. The electronic transport properties of several known phosphorus allotropes are calculated, with the intention of forming a grounding for the methodology. Once these calculations brought confidence to the method, an approach was developed from which metastable intermediate structures from along the transition pathway of black phosphorus under high pressures were obtained. The electronic transport properties were then calculated for these materials and an investigation into the impact on the thermoelectric properties of these materials was conducted. The results were discussed, along with the conclusion of the suitability of the meta-stable phase transition intermediate approach to layered materials.

In the fifth chapter, the various compounds and phases of tin sulfide are reviewed, with an overview of why these layered materials are of such interest to the thermoelectric community. A crystallographic study of the various phases, both naturally occurring and theoretical, is undertaken, and the electronic structures of these materials are explored. The thermoelectric transport properties of the ground-state, naturally occurring tin sulfides are calculated and presented in full. A discussion as to the applicability of the formalisms applied in this thesis to this chemical system follows. The methods and techniques devised during this work are then applied to the non-ambient phases of tin sulfide, and an appreciation of the effect of the temperature- and scale-induced phase transitions on the thermoelectric properties of tin sulfide is developed.

The thesis is then concluded.

2 – COMPUTATIONAL CHEMISTRY

This chapter concerns the computational theory and methods used in the work of this thesis. The first section details the derivation of Density Functional Theory, DFT, from first principles, followed by the derivation of Density Functional based Tight Binding theory, DFTB, along with the application of these methods and a summary of the codes used. Finally, the types of calculations performed in this work and across various codes are detailed and some background theory given.

“The Calculation of molecular orbitals” by John C. Slater, *“Basic Quantum Chemistry”* by Leon F. Phillips, *“The Basics of Theoretical and Computational chemistry”* by Rode, Hofer and Kugler, *“Quantum Chemistry”* by McQuarrie, and *“An Introduction to Molecular Dynamics and Chemical Kinetics”* were used extensively as the backbone of the theoretical concepts in this chapter.¹⁻⁵

2.1 – INTRODUCTION

As models of the atom grow more complex, so have the associated calculations. In the early 1900s, it was not uncommon for the calculation of individual orbital energies to be performed by hand, and later with the aid of a pocket calculator.¹ The advances in computing in the last several decades have allowed for these calculations to be performed at superior speed, and massively parallelised.⁶ This rise in computational power has seen calculations involving single atoms and diatomic molecules evolve into giant systems of thousands of atoms, multiple phases and yield a host of calculable properties.⁷⁻⁹

Whilst the calculation of atoms can, for certain circumstances, be reduced to problems of classical mechanics, the accurate description of electrons within a chemical system requires the application of quantum mechanics, which initially made these calculations impossible.

“From our point of view the most serious assumption of classical mechanics is that any dynamic system can be regarded as an assemblage of particles whose masses, positions, and velocities can be determined precisely at any instant.”

Leon F. Phillips

In 1926 Erwin Schrödinger published *Quantisierung als Eigenwertproblem*, presenting his now famous equation on the subject of wave mechanics.¹⁰

$$\hat{H} | \Psi \rangle = E | \Psi \rangle \quad (1)$$

Equation 1 is the time independent Schrödinger equation.¹¹ Much of computational chemistry is at some level dependent on solving the Schrödinger equation in some form to derive energies and subsequent forces within a system.

To fully describe a quantum system, a function Ψ , is specified. This *wave function* is required to be finite, single-valued and continuous. The wave function is noted to be complex, though the physical properties of a system depends on the *real* quantity $\Psi^*\Psi$, where Ψ^* is the complex conjugate of Ψ .¹

2.2 – ORIGINS OF DENSITY FUNCTIONAL THEORY

The roots of density functional theory, DFT, can be traced back to D. R. Hartree who, in 1928, introduced the term *self-consistent field* to the area of atomic modelling.¹² The concept was applied to the modelling of molecules by J. E. Lennard-Jones, F. Hund and R. S. Mulliken at the same time, which provided the foundations for the theories of electrons in crystals, as determined by F. Bloch, L. Brillouin, W. Heisenberg and A.H. Wilson.³

2.2.1 – HARTREE METHOD

The work of Hartree began with the relatively simple problem of solving the Schrödinger equation for an electrical system within the vicinity of a single nucleus or ion. For a system of N electrons about a stationary nucleus of atomic number Z , each electron is acted upon by the nucleus and $N - 1$ electrons. For Hartree, the logical step was to replace the electronic field with a single potential describing the averaged positions of the other electrons, such that the Schrödinger equation may be solved for the wave functions of singular electrons acted upon by singular nuclear and electronic potentials. This effectively reduced the many-body $3N$ -dimensional problem for each of N electrons, to N individual 3-dimensional problems – a massive simplification for any system with more than one electron.³ If we define ψ_i as a wave function, normalised such that the integral over all space of $\psi_i^*\psi_i$ is equal to 1 and

thus finite, the occupied orbitals can be denoted as $N\psi_i$. The term $\psi_i^*\psi_i$ thus represents the charge density of the i^{th} electron, such that we can define the total electronic charge density of our system as

$$\rho = - \sum_i (i)n_i\psi_i^*\psi_i \quad (2)$$

whereby the summation over all orbitals includes those that are empty.

With energy in Rydberg's and radii in Bohr, Hartree defines the potential of the nucleus at distance r as $2Z/r$. The potential of a charge at point 1 separated from point 2 by distance r_{12} in all volume elements $d\mathbf{v}_2$ is thus

$$\int_0^\infty \rho(2) \left(\frac{2}{r_{12}} \right) d\mathbf{v}_2 \quad (3)$$

where $\rho(2)$ is the charge density at point 2. Assuming that an electron could not act upon itself, Hartree decided that $\psi_i^*\psi_i$ should not be included in the charge density of the electron in the i^{th} orbital defined in equation 2. This allows for the definition of the potential acting on the i^{th} electron at position 1 as

$$V_i(1) = V_N(1) + V_e(1) + V_{Xi}(1) \quad (4)$$

where the nuclear potential

$$V_N(1) = \frac{2Z}{r_1} \quad (5)$$

and the averaged electronic potential

$$V_e(1) = \int \rho(2) \left(\frac{2}{r_{12}} \right) d\mathbf{v}_2 \quad (6)$$

whilst V_{Xi} is the correction term for the absence of an electron in one orbital acting upon itself. For an electron in the i^{th} orbital, Hartree assumed the Schrödinger equation to be

$$-\nabla^2\psi_i(1) - V_i\psi_i(1) = \epsilon_i\psi_i(1) \quad (7)$$

where $-\nabla^2$ is the kinetic energy in atomic units, $-V_i$ is the potential energy of the electron in the averaged potential in equation 4, and ϵ_i is the one electron energy.¹ Equation 7 is relatively straightforward to solve due to the spherical symmetry of the atom, yielding a solution in spherical polar coordinates which are the products of spherical harmonics of the angles and vectors of radius vector r . The differential of this radial function can be solved simply. For certain discrete energies, the eigenvalues, the eigenfunctions are found to be regular at the nucleus and infinity.

For self-consistency, these normalised functions should be identical with the functions Ψ_i of equation 1. This is not automatic however, and so Hartree stipulated that these should be iteratively adjusted, until this condition was met to a certain level of accuracy. More specifically, using the Ψ_i 's from equation 7 and substituting them into equation 1 to begin the next iteration. He then termed the resultant field, potential and wave functions *self-consistent*. The self-consistent charge density from equation 1 approximated the experimentally determined atomic charge density rather well. Better still, the differences between the energies of the occupied and unoccupied states approximated the experimentally determined excitation energies. For the ground state atom, it was found that in most cases, the lowest energy eigenfunctions should be occupied, satisfying the recently stipulated *Aufbau Principle* of N. Bohr and W. Pauli.

As previously mentioned, while Hartree was working on these principles, Lennard-Jones, Hund and Mulliken were trying to apply similar concepts to simple molecules.^{13,14} The distinction being that the nuclear potential, \mathcal{V}_N (equation 4) should be replaced by a term equating to the sum of such nuclear potentials within the molecule. The absence of spherical symmetry meant Schrödinger equations for such systems were, initially, deemed impractically complex to solve within realm of calculative capabilities at the time.

2.2.2 – EARLY DENSITY FUNCTIONAL THEORY

Initially conceptualised by L. Thomas and E. Fermi in 1927, almost immediately after the Schrödinger equation was published, the principle of Density Functional Theory, or DFT, is to use electron density instead of wave functions to derive the energies of chemical systems.^{15,16} The *Thomas-Fermi Model* precedes modern DFT but due to its limitations, was unsuccessful in becoming a standard model at the time.

The approach was adapted by J. C. Slater around 1950, who redefined the Hartree-Fock exchange, defining the exchange energy as

$$E_X = \frac{1}{2} \int \int \frac{\rho(r_1) \hat{h}_X(r_1; r_2)}{r_{12}} dr_1 dr_2 \quad (8)$$

where $\rho(r_1)$ is the electron density and $\hat{h}_x(r_1; r_2)$ is the local exchange operator. Previously, Fermi had shown that the hole created by the charge deficiency in the region of each electron amounts to the charge of 1 electron. This hole is spherical with a radius defined by E. Wigner and F. Seitz as

$$r_s = \left(\frac{3}{4\pi}\right)^{\frac{1}{3}} \rho(r_1)^{-\frac{1}{3}} \quad (9)$$

meaning it was possible to express the exchange energy as

$$E_X[\rho] \cong C_X \int \rho(r_1)^{\frac{4}{3}} dr_1 \quad (10)$$

where C_X is a numerical constant. Slater then introduced an adjustable parameter, α , to improve the approximation. This *Hartree-Fock-Slater X α Method* was now expressed as

$$E_{X\alpha}[\rho] = -\frac{9}{8} \left(\frac{3}{\pi}\right)^{\frac{1}{3}} \alpha \int \rho(r_1)^{\frac{4}{3}} dr_1. \quad (11)$$

This method showed promise in solid-state applications, but failed to accurately describe molecular systems.

2.2.3 – MODERN DENSITY FUNCTIONAL THEORY

In the 1960s, the conceptual use of electronic densities was further developed by P. Hohenberg and W. Kohn, who devised several theorems.¹⁷ The first theorem introduced in *inhomogeneous electron gas* relates the external potential of a system to its electron density:

“We shall now show that conversely $v(\mathbf{r})$ is a unique functional of $n(\mathbf{r})$, apart from a trivial additive constant.”

where $v(\mathbf{r})$ is the external potential, and $n(\mathbf{r})$ is the electron density otherwise denoted as ρ in this thesis. If the many-particle ground state is a unique functional of $\rho(\mathbf{r})$, then the external potential determining the Hamiltonian is $\rho(\mathbf{r})$. As such, all components of the ground state energy can also be determined by the electron density:

$$E_o[\rho_o] = T[\rho_o] + E_{ee}[\rho_o] + E_{Ne}[\rho_o] \quad (12)$$

The second theorem was established:¹⁷

“We shall now show that $E_v[n]$ assumes its minimum value for the correct $n(r)$, if the admissible functions are restricted by the condition

$$N[n] \equiv \int n(r)dr = N." \quad (13)$$

Here, $N[n]$ is the number of electronic densities considered and $n(r)$ is the ground state electronic density. Essentially, the functional F_{HK} yielding the true ground state energy must correspond to the correct ground state density, ρ_0 . Any other density would result in a higher energy, for the case of a trial density, $\tilde{\rho}$ we get

$$E_0 \leq E[\tilde{\rho}] = T[\tilde{\rho}] + E_{ee}[\tilde{\rho}] + E_{Ne}[\tilde{\rho}] \quad (14)$$

It is apparent therefore that we have a scheme with which to optimise the density functional, for the ground state.

2.2.4 – KOHN SHAM EQUATIONS

As we saw, Hohenberg had been working with Kohn to establish a method of using electronic density instead of wave functions to model chemical systems.¹⁸ The Hohenberg Kohn theorems laid the foundations for Kohn and L. J. Sham to produce a series of equations, the *Kohn-Sham Equations*, which consolidated the work of Thomas, Fermi and Slater with the orbital theory of the Hartree-Fock method.¹⁹ Using a Slater determinant modified for DFT and atomic orbitals, the Kohn-Sham equations can be expressed as a one-electron operator, as with the Hartree-Fock equations:

$$\hat{f}_{KS} = \varepsilon_i | \Psi_i \rangle = \left[-\frac{1}{2} \Delta + \hat{V}_S(r) \right] \Psi_i \rangle \quad (15)$$

The electron density is obtained from the $\Psi_i^* \Psi_i$ values. To calculate the kinetic energy, which is not determined by the functional as in the Hartree-Fock formula

$$T_S = -\frac{1}{2} \sum_i^N \langle \Psi_i | \Delta | \Psi_i \rangle \quad (16)$$

we must split the functional

$$F[\rho(r)] = T_S[\rho(r)] + J[\rho(r)] + E_{XC}[\rho(r)] \quad (17)$$

into its kinetic energy and Coulomb term, alongside an exchange correlation term. This exchange correlation incorporates a correction term for the kinetic energy, as well as the expected exchange and correlation effects:

$$E_{XC}[\rho] \equiv (T[\rho] - T_S[\rho]) + (E_{ee}[\rho] - J[\rho]) = T_C[\rho] + E_{ncl}[\rho] \quad (18)$$

T_C is the *true* kinetic energy and E_{ncl} incorporates all non-classic effects, such as self-interaction correction, exchange and correlation. Next we must formulate the potential operator \hat{V}_S in the Kohn-Sham operator \hat{f}_{KS} , by approximating it as an effective operator

$$\hat{V}_{eff} = \int \frac{\rho_{12}}{r_{12}} dr_2 - \sum_A \frac{Z_A}{r_{iA}} + V_{XC} \quad (19)$$

where V_{XC} describes the exchange-correlation energy effect, and is unknown, so must be defined as a derivative of the exchange-correlation energy:

$$V_{XC} \equiv \frac{\delta E_{XC}}{\delta \rho} \quad (20)$$

If E_{XC} and V_{XC} could be derived, the exact ground state energy could be calculated. Unfortunately, they cannot, leading to the first problems of density functional methods.

Although similar to Hartree-Fock, Kohn-Sham DFT differs in several key ways, the main being that Hartree-Fock works with discrete operators, refining results by optimising the probability function. In the Kohn-Sham method, the operator is altered by the ground state energy from the electron density, without obtaining a physical probability function.

2.2.5 – LOCAL DENSITY APPROXIMATION (LDA)

The Local Density Approximation stems from the older concept of a homogenous electron gas.^{20,21} In fact, the only systems that LDA provides a suitable approximation for are simple metals. Any system with a more specific electronic density distribution will not be accurately described by LDA. However, this flaw is also the main reason for its continued use, as the exchange and correlation terms can be calculated with high accuracy from the inhomogeneous electron cloud.

$$E_{XC}^{LDA}[\rho] = \int \rho(r) \epsilon_{XC}(\rho(r)) dr \quad (21)$$

Here $\varepsilon_{XC}(\rho(r))$ is the particle exchange-correlation energy within the electron gas.

$$\varepsilon_{XC}(\rho(r)) = \varepsilon_X(\rho(r)) + \varepsilon_C(\rho(r)) \quad (22)$$

The exchange-correlation energy is simply the sum of the exchange and correlation energies for each particle. The exchange term can also be expressed as

$$\varepsilon_X = -\frac{3}{4} \sqrt{\frac{3\rho(r)}{\pi}}. \quad (23)$$

There are a multitude of refined expressions for ε_C , each named after its author e.g. VWN5, PW92. For the unrestricted case, there is a further development termed Local Spin-Density Approximation (LSD), allowing for derivations of ε_{XC} for spin-polarised systems:

$$E_{XC}^{LSD}[\rho_\alpha, \rho_\beta] = \int \rho(r) \varepsilon_{XC}(\rho_\alpha(r), \rho_\beta(r)) dr \quad (24)$$

Both LDA and LSD are mainly used to model solid state materials; they describe molecular systems rather poorly.

2.2.6 – GENERALISED GRADIENT APPROXIMATION (GGA)

The electronic density, $\rho(r)$, is the basis for all prior methods within DFT, but the addition of the density gradient, $\Delta\rho(r)$, allows for the non-homogeneity of the electron density to be accounted for.²² The Gradient Expansion Approximation:

$$E_{XC}^{GEA}[\rho_\alpha, \rho_\beta] = \int \rho \varepsilon_{XC}(\rho_\alpha, \rho_\beta) dr + \sum_{\sigma, \sigma'} \int C_{XC}^{\sigma, \sigma'}(\rho_\alpha, \rho_\beta) \frac{\Delta\rho_\sigma}{\rho_\sigma^{\frac{2}{3}}} \frac{\Delta\rho_{\sigma'}}{\rho_{\sigma'}^{\frac{2}{3}}} dr + \dots \quad (25)$$

is the next stage in the development of the LDA, in the sense that it includes the second term of a Taylor expansion as well as the first which describes the LDA. In this form, the functional yields little improvement due to an inability to describe the exchange term, but by further approximating the restrictions of the ‘real’ exchange behaviour, we arrive at the Generalised Gradient Approximation, GGA:

$$E_{XC}^{GGA}[\rho_\alpha, \rho_\beta] = \int F(\rho_\alpha(r), \rho_\beta(r), \Delta\rho_\alpha(r), \Delta\rho_\beta(r)) dr \quad (26)$$

Once again, E_{XC}^{GGA} can be split into E_X^{GGA} and E_C^{GGA} to work on the solutions to each of these terms separately. Function F has been obtained by many individual methods, usually by iterative fitting procedures, and the derived functionals are again named after their authors, for example: PBE, BLYP, etc..

2.2.7 – HYBRID FUNCTIONALS

So far for DFT methods, we have seen that the exchange terms of the exchange-correlation functionals have been approximations which are prone to errors, such as issues with unphysical self-interaction. It was later determined that this term should be obtained from the ‘exact’ Hartree-Fock formalism, whilst deriving a functional for the correlation term from the Kohn-Sham method:

$$E_{XC} = E_X^{exact} + E_C^{KS} . \quad (27)$$

The nomenclature *hybrid functional methods* stems from the combination of DFT methods and a HF step in calculations, occasionally referred to as HDFT. Additionally, both the LSD and GGA functionals are incorporated into adaptations of the correlation functionals, further supporting the term *hybrid*. There are many functionals in use in the current literature, but for an example, the most popular B3LYP (Becke-3, Lee, Yang, Parr) can be expressed:²³⁻²⁵

$$E_{XC}^{B3LYP} = (1 - a)E_X^{LSD} + aE_X^{\lambda=0} + bE_X + cE_C^{LYP} + (1 - c)E_C^{LSD} \quad (28)$$

with $\lambda = 0$ indicating the values for non-interacting particles, and a, b, c, are coefficients obtained by fitting the functional to total energies, ionisation energies and proton affinities. Hybrid functionals usually the best suited to molecular problems of all DFT methods, making them rather popular in today’s literature.

2.3 – TIGHT-BINDING APPROACH

Also known as the LCAO or Bloch approximations, the tight binding approximation was originally proposed by Bloch.²⁶ It consists of a Linear Combination of Atomic Orbitals (LCAO) representing the various atoms within a crystal, with coefficients determining the values of the planes waves where the atoms are located.²⁷ The method was originally limited in application due to the large number of complex integrals that must be solved, though modern computing capabilities have allowed for the method to become commonplace. The strength of the method lies in its ability to provide symmetry properties of the energy bands, and allows for trivial calculation of band energies at arbitrary points within the Brillouin zone.

2.3.1 – DENSITY FUNCTIONAL BASED TIGHT BINDING

In the DFTB approach, each one-electron wavefunction, $\Psi(\mathbf{r})$, can be expressed as a linear combination, LCAO, of atomic orbitals $\phi_\mu(\mathbf{r})$ such that

$$\Psi(\mathbf{r}) = \sum_{\mu} C_{\mu} \phi_{\mu}(\mathbf{r}) \quad (29)$$

leaving the solution to the eigenproblem

$$\sum_{\nu} H_{\mu\nu}^{\sigma} C_{\nu}^{\sigma} = E_{\mu}^{\sigma} \sum_{\nu} S_{\mu\nu} C_{\nu}^{\sigma} \quad (30)$$

where

$$H_{\mu\nu}^{\sigma} = \langle \phi_{\mu} | \hat{H}^{\sigma} | \phi_{\nu} \rangle \quad (31)$$

and

$$S_{\mu\nu} = \langle \phi_{\mu} | \phi_{\nu} \rangle \quad (32)$$

are the Hamiltonian and overlap matrices, and σ is the spin state, 1 or \downarrow .^{28,29} If ϕ_{μ} and ϕ_{ν} are located on separate atoms, a and b , the Hamiltonian matrix element $H_{\mu\nu}^{\sigma}$ for spin-polarised self-consistent charge (scc) case is evaluated as

$$\begin{aligned} H_{\mu\nu}^{\sigma} = & \langle \phi_{\mu} | \hat{H}^{\sigma} | \phi_{\nu} \rangle \\ & + \frac{1}{2} S_{\mu\nu} \sum_c \sum_{l'' \in c} (\gamma_{al,cl''} + \gamma_{bl',cl''}) \Delta q_{cl''} \pm \frac{1}{2} S_{\mu\nu} \sum_{l'' \in a} W_{all''} m_{all''} \\ & + \sum_{l'' \in a} W_{bl'l''} m_{bl'l''} \left(\sum_{l'' \in a} W_{all''} m_{all''} + \sum_{l'' \in b} W_{bl'l''} m_{bl'l''} \right) \end{aligned} \quad (33)$$

where the first term is the non-scc DFTB Hamiltonian matrix element. The second term is the scc contribution, summed over all shells, l'' , of all atoms, cl'' , in the system. $(\gamma_{al,cl''} + \gamma_{bl',cl''}) \Delta q_{cl''}$ is the scc potential of sites al and bl .

$$\gamma_{al,cl''} = \frac{1}{R_{ac}} - S(U_{a,l}, U_{c,l''}, R_{ac}) \quad (34)$$

Here the first term is a long range pure coulombic term and the second is a short-range term. R_{ac} is the distance between atoms a and c , and each U_l is the Hubbard parameter for the relevant atom and shell. $\Delta q_{cl''}$ is the charge difference in Mulliken charges between shell l of atom c and the charge of

the equivalent shell for an isolated atom. The last term in equation 33 denotes the spin contribution. $W_{all'}$ are the spin coupling constants with l and l' as shells of the same atom.

$$m_{al} = q_{al\uparrow} - q_{al\downarrow} \quad (35)$$

m_{al} is the spin polarisation of shell l on atom a and equates to the difference of the sum of the Mulliken charges on the spin up and spin down orbitals of the shell.

2.3.2 – ELECTRONIC TRANSPORT

Quantum transport may be calculated for large systems utilising the DFTB method, but in order to realise accurate values of electrical conductivity for complex systems with charge transfer and applied bias, an approach must take into consideration charge density and transport in open systems. One such approach is the use of Non-Equilibrium Green's Function theory, NEGF.^{9,30,31} This method allows for the calculation of tunnelling current between two contacts, under both open and periodic boundary conditions. NEGF theory also allows for computation of charge density in systems under applied bias, which is necessary for a self-consistent solution to the Kohn-Sham equations.³²

The NEGF method has become popular, despite its inherent mathematical complexity, owed in part to its versatility and in part to its numerical stability. Open boundary conditions may be applied by mapping contact leads to small, finite parts of the system. The NEGF approach may also be adapted to include many-body quantum theory, allowing for the inclusion of electron-phonon and electron-electron interactions.

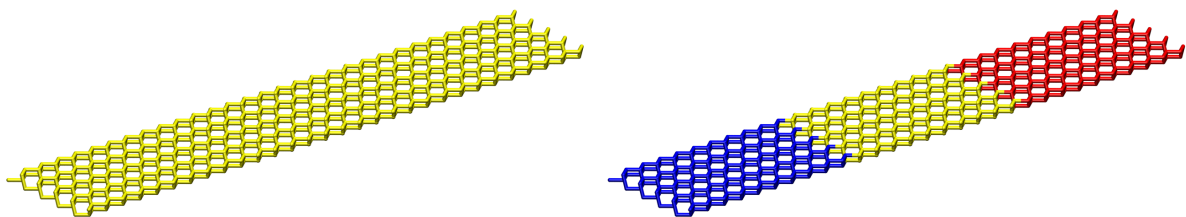


Figure 1 – Left: a representation of a phosphorus nanowire in vacuum. Right: The red and blue regions are contacts, the source and drain regions respectively.

The systems of interest may be represented as in figure 1, divided into contact and device regions. The contacts are assumed to be semi-infinite, exhibiting the same properties as the bulk, and multiple contacts may be defined. The device portion of the system consists of the atoms linking the contacts, forming a molecular bridge, along with the segments of the contacts representing the surfaces in contact with the molecular region, ensuring the contacts are defined as bulk-like. This assumption is validated by examining the charge density in the region of the contact-surface boundary, to check for smooth transition between the regions. By maintaining different potentials at each contact, current fluxes are driven across the device.

It is not possible to make the assumption of thermodynamic equilibrium in solving the transport problem; no global fermi energy can be defined. As such, it can only be assumed that the contacts are reservoirs of defined potential, with the electrons in these regions under maintained equilibrium. The molecular bridge must offer the majority of the resistance for this assumption to be valid, such that the potential drops across the device region. The density matrix is computed

$$\rho = \frac{1}{2\pi i} \int_{-\infty}^{+\infty} dE G^<(E) \quad (36)$$

with $G^<$ as the electron-electron correlation matrix, represented on the local basis and proportional to the spectral density of occupied states. $G^>$ represents the density of empty states, as we shall see. An altered Green's function can express the spectral density of states as

$$A(E) = i[G^r(E) - G^{r\dagger}(E)] \quad (37)$$

where

$$G^r(E) = [ES - H + \Sigma^r(E)]^{-1} \quad (38)$$

and $\Sigma^r(E)$ is the retarded self-energy, which accounts for the contacts and other perturbing influences, such as phonons, impurities and other electrons. The derived results are only valid in steady-state conditions such that the two-time Green's functions, $G(t, t')$, depend only on the time difference, $t - t'$, and the energy may be derived from Fourier transform.³¹ An advantage of the approximation is that the contacts may be mapped exactly into the extended molecule using appropriate self-energies. This contact self-energy can be easily calculated considering that the Hamiltonian describing the interactions between the contact and devices consists of a finite region of atoms close to the junctions. Thus, the required Green's function may be solved for the matrix block corresponding to the atoms nearest the extended molecule region, then used to calculate Mulliken charges:

$$\Delta q_i = \sum_{\mu E i} \sum_v \text{Re}[\rho_{\mu\nu} S_{\nu\mu}] - q_i^0 \quad (39)$$

Where q_i^0 are the reference atomic charges. Inelastic-scattering processes affecting occupation dynamics are given by the Keldysh-Kadanoff-Baym (KKB) equation. Within the Tight-Binding approximation, the steady-state solution of the KKB equation is expressed as matrices terms

$$G^{<>}(E) = G^r(E) \Sigma^{<>}(E) G^a(E) \quad (40)$$

where $G^a = G^{r\dagger}$ is the advanced Green's function, $\Sigma^{<}$ and $\Sigma^{>}$ are the non-equilibrium self-energies. $G^{<}$ can be practically divided into three terms to obtain the density matrix:

$$\begin{aligned} \rho = & \int_{-\infty}^{+\infty} dE f_c(E) G^r(E) \\ & - \int_{-\infty}^{+\infty} dE f_c(E) G^a(E) \\ & + \sum_{\alpha \neq c} \int_{-\infty}^{+\infty} dE [f_\alpha(E) - f_c(E)] G^r(E) \Gamma_\alpha(E) G^a(E) \end{aligned} \quad (41)$$

where f_c is related to the contact at the lowest potential. The first term is calculated on a contour, the second by the adjoint of the first. The integration of the third term must be performed along the real axis defining

$$\Gamma_\alpha(E) = i[\Sigma_\alpha^r(E) - \Sigma_\alpha^{r\dagger}(E)]. \quad (42)$$

2.4 – CODES USED

The following section details the codes used in this work, along with some details as to their construction.

2.4.1 – SIESTA

Siesta is both a method and its implementation.⁷ It is a self-consistent density functional method, that uses norm-conserving pseudopotentials and a linear combination of atomic orbitals basis set, which allows for polarised and multiple-zeta orbitals. Spin density or generalised gradient approximations are used to account for exchange and correlation. To calculate Hartree and exchange-correlation potentials, basis functions and electron density are projected on a real space grid with a number of

operations that scales linearly with the size of a system. The use of localised, Wannier-like, electron wave functions allows for computational time and memory to also scale linearly with system size. Forces and stresses are accurately calculated, for structural relaxation and molecular dynamics simulations.

Pseudopotentials are not strictly necessary for atomic orbital basis sets, however, the benefit of their use in the siesta method is twofold: They remove the need to calculate properties for core electrons, and ensure that the expansion of charge density is smooth on a uniform spatial grid.

2.4.2 – QUANTUM ESPRESSO

Quantum ESPRESSO is a suite of codes for electronic structure calculations and materials modelling.^{8,33} Based on Density Functional Theory, it utilises plane waves and pseudopotentials and aims to provide an efficient platform for parallel architectures. The main difference between quantum QE and other codes is that QE is not a single code, but rather a package of complementary codes whose inputs and outputs are cross compatible. This modular distribution is intended to encourage innovation and flexibility in the field of electronic structure calculations and materials modelling, by being open source and freely alterable. This has led to an array of complementary codes simultaneously developed by specialists in various fields to utilise several core packages developed by a small, dedicated quantum espresso group, with an extensive online repository and community.

These features make QE a powerful tool in the field of solid-state modelling, with the ability to calculate a variety of properties and coefficients. The two major codes within QE are PWscf, plane wave code, and PHonon. PWscf is a self-consistent DFT based plane-wave code. It allows for accurate electronic calculations and atomistic simulations, including structural optimisation and molecular dynamics. PHonon implements Density Functional Perturbation Theory (DFPT) to calculate second and third order energy derivatives with respect to atomic displacements and electronic fields. Symmetry is fully exploited in both codes for the reduction of calculation times due to energetic redundancies.

2.4.3 – DFTB+

DFTB+ is an implementation of the DFTB method, which exploits the *sparsity* of the corresponding equations, for an efficient application.^{9,34} In section 2.3.1 we derived the equations for the matrices of the non-scc Hamiltonian, equation 33. The matrix elements for non-scc and overlap matrices vanish with increasing interatomic distance, resulting in matrices containing mostly zeros. The patterning of the non-zero elements is defined by the geometry (and ordering) of the atoms in the system we are calculating.

The scc shift contribution contains both long and short range terms as shown in equation 33, but the total scc contribution is screened by the overlap matrix, such that the pattern of non-zero contributions to each matrix is identical. Because the scc and non-scc Hamiltonians are tabulated on identical grids to the same cut-offs, the patterns of matrix elements are the same, as is the spin contribution matrix. By determining these patterns at the start of the calculation, and for each successive alteration to the geometry, it is possible to store and calculate only for the non-zero elements, significantly reducing the complexity and time of the calculation.

This is the heart of the DFTB+ code, and its efficient implementation allows for calculations of large systems involving tens of thousands of orbitals and thus thousands of atoms.

2.4.4 – DFTB+ NEGF (OR GDFTB+)

The Non-Equilibrium Green's Function method is established and here applied to the DFTB+ code.³⁰ It allows for the self-consistent solution of charge density in biased systems to derive the electronic tunnelling and subsequent conductivity as described in 2.3.2. This code utilises DFTB+'s implementation of the sparse matrix approach to efficiently tackle the problem, in periodic and open systems

2.5 – TECHNIQUES

This section details the theory behind some of the capabilities of the above codes. In some cases, the methods are applicable to several codes, the use of which will be specified.

2.5.1 – GEOMETRY OPTIMISATIONS

The most stable atomic configuration is known as the ground state of a system, and corresponds to the lowest energy configuration.³⁵⁻³⁷ By testing various configurations, one may determine which is the lowest energy and thus most likely to be the ground state. To express this task, one may create a *Potential Energy Surface*, PES, a 3D representation of energy (usually z-axis) versus two collective variables, such as bond angles, bond lengths or coordination numbers. By populating this PES, a map of the energy vs coordinates may be created, which consists of 5 distinct types of points:

- i) Global Maximum – The highest energy configuration across the whole PES.
- ii) Global Minimum – The lowest energy configuration across the whole PES.
- iii) Local Maxima – The highest energy point within a region of the PES.
- iv) Local Minima – The lowest energy point within a region of the PES.
- v) Saddle points – A point from which one direction leads to a maximum, and another direction leads to a minimum.

Many methods exist with which to iteratively search the PES, by recalculation of the systems energy along a coordination path. What follows is an introduction to each of the methods of geometry optimisation used within the work of this thesis, across various codes

2.5.1.1 – STEEPEST DESCENT (DFTB)

The Steepest Descent (SD) method follows a force vector from the initial configuration to one wherein the resultant forces are zero.³⁷ With an initial configuration R , an iteration j and a force F , each step of the SD method proceeds in the direction:

$$R_{j+1} = R_j + \alpha F_j \quad (43)$$

α is an adjustable parameter, often chosen to be the inverse of the curvature along the F_j direction. This allows the SD method to proceed to the minimum energy value in this direction. Consecutive steps will further move the system towards its *Local Minimum*. This makes the SD method the simplest with which to optimise geometries, though it is prone to converge slowly within shallow regions of a systems PES.

2.5.1.2 – CONJUGATE GRADIENT (S) (DFTB)

An improvement upon the SD method, Conjugate Gradient (CG) methods proceed along the PES in conjugate directions, rather than in the direction of force.³⁵⁻³⁷ Employing the Polak-Ribière algorithm, the method proceeds as follows:

- 1) Determine initial search direction using force method

$$d_0 = F_0 \quad (44)$$

- 2) Calculate step size, λ , via line minimisation

$$R_{j+1} = R_j + \lambda d_j \quad (45)$$

- 3) Under the assumption that

$$\gamma = F_{j+1} \cdot \frac{(F_{j+1} - F_j)}{|F_j|^2} \quad (46)$$

Asses the new search direction

$$d_{j+1} = F_{j+1} + \gamma d_j \quad (47)$$

For each iteration, a single Newton's method step is required to minimise forces along d_j , though the force must be evaluated twice for each iteration, such that the derivative of the force along the search direction may be calculated. The CG method is often the geometry optimiser of choice for both the siesta and dftb+ methods.

2.5.1.3 – BROYDEN (QE)

The Broyden method, or BFGS method, is one of the most efficient quasi-Newton methods widely available in atomistic simulation packages. The method was in fact suggested by 4 authors independently: Broyden, Fletcher, Goldfarb, Shanno; hence the terms Broyden and BFGS are used almost interchangeably in the field.

The methods gathers information of the second derivatives of forces during optimisation, so as to step towards the predicted minimum. Construction of the inverse Hessian matrix, H^{-1} , is performed iteratively in two steps:

- 1) As in the CG method, a search direction is defined

$$d_j = F_j H_j^{-1} \quad (48)$$

- 2) Then a line minimiser is used to proceed to the energetic minimum along this direction

$$R_{j+1} = R_j + \lambda d_j \quad (49)$$

The similarities between methods can be appreciated by noting that equations 45 and 49 are identical, the difference lies in the fact that the BFGS method utilises the reconstructed Hessian matrix to determine the search direction, rather than simply searching conjugate gradients. The Broyden method is the default for the quantum espresso codes.

2.5.1.4 – DAMP – QUICK MINIMUM VELOCITY VERLET (QE)

This method seeks to improve upon the SD method, by implementing a more aggressive search, accelerating the system in the direction of greatest force (akin to SD).³⁷ This method is a damping routine, wherein the damping parameter is replaced by a projection of the velocity along the force. It proceeds as follows:

- 1) The velocity is projected along the direction of the force

$$V_j = (V_j \hat{F}_j) \hat{F}_j \quad (50)$$

- 2) Make velocity zero if it is antiparallel to the force

$$\text{if } V_j \hat{F}_j < 0, \quad \text{then } V_j = 0$$

- 3) The *Velocity Verlet* algorithm is used to differentiate Newton's equations of motion and determine the both the position and velocity simultaneously

$$R_{j+1} = R_j + \Delta t V_j \quad (51)$$

$$V_{j+1} = V_j + \Delta t F_j \quad (52)$$

This method is implemented in some quantum espresso packages, and can be used for faster, if perhaps less stable optimisations.

2.5.2 – MOLECULAR DYNAMICS

Molecular Dynamics (MD) is the simulation of atomic movements, calculated by integration of Newton's Equations of Motion (EOM) with respect to time for each of N interacting particles within a system.⁵

2.5.2.1 – FORCES

A cornerstone of *classical* Molecular Dynamics is to treat an atomic system as a classical mechanical problem, calculating forces instantaneously from the atomic positions, ignoring the quantum nature of light species. This simplification is critical to modelling large systems, but additional parameters to account for effects such as spin-spin interactions and Van der Waals forces can be added later. In *ab initio* molecular dynamics, by consideration of the Born-Oppenheimer approximation, the many-body electronic wavefunction can be described by the time-independent Schrödinger equation. The energy is thus a function of the positions of the nuclei, and this wavefunction may be used as a potential to calculate the forces acting on the nuclei, again according to Newton's Equations of Motion. Thus, according to Newton's second law of motion:

$$F_i = m_i a_i \quad (53)$$

Here, the resultant force on a particle is the product of its mass and acceleration, and its acceleration is the second derivative of its displacement with respect to time:

$$|F_i\rangle = m_i \frac{d^2|r_i\rangle}{dt^2}, \quad i = 1, 2, 3 \dots N \quad (54)$$

Using the Lagrangian function:

$$L = T - V \quad (55)$$

which describes the difference between kinetic and potential energy, we can define the Lagrangian equation of motion as

$$\frac{d}{dt} \left(\frac{\partial L}{\partial \frac{\partial q_k}{\partial t}} \right) - \left(\frac{\partial L}{\partial q_k} \right) = \emptyset \quad (56)$$

where q_k are the generalised atomic coordinates. According to equation 54, we may describe the force acting on an atom as the product of its mass, and the second derivative of its motion with respect to

time. With equations 55 and 56, we may also determine the force upon an atom from its kinetic or potential energy:

$$|F_i\rangle = \nabla_{r_i} L = -\nabla_{r_i} V \quad (57)$$

To calculate the trajectories of N particles within a system, a numerical solution to $3N$ second-order differential equations would be required. This would be impractical, and so in many MD simulations this is tackled by the *finite differences approach*. By which, the velocities and positions of each particle within a system for a given t are used to compute the same information for $t + \Delta t$. For meaningful results, Δt must be much smaller than the time for the fastest atomic movement within a system, i.e. the molecular or lattice vibration of the lightest nuclei.

2.5.2.2 – VELOCITY VERLET ALGORITHM

One common method of solving this problem is known as the *Velocity Verlet* algorithm, which is in fact the method of choice for the majority of the codes used in this work.³⁸ The Velocity Verlet algorithm is used to directly solve equation 54, utilising the positions $|r_t\rangle$, $|r_{t-\Delta t}\rangle$ and accelerations $|a_t\rangle$ calculated in each previous step. The positions are calculated both forward and backward in time by a third-order Taylor series expansion:

$$|r(t + \delta t)\rangle = |r(t)\rangle + \delta t|v(t)\rangle + \frac{1}{2}\delta t^2|a(t)\rangle + \dots \quad (58 a)$$

$$|r(t - \delta t)\rangle = |r(t)\rangle - \delta t|v(t)\rangle + \frac{1}{2}\delta t^2|a(t)\rangle - \dots \quad (58 b)$$

giving

$$|r(t + \delta t)\rangle = 2|r(t)\rangle - |r(t - \delta t)\rangle + \delta t^2|a(t)\rangle \quad (59)$$

Which is the basic form of the Velocity Verlet algorithm. As we are integrating Newton's equation of motion, $a(t)$ is simply F/m , and using equation 57, we know that the force is just a function of the atomic positions, giving

$$a(t) = -\left(\frac{1}{m}\right)\nabla V \cdot r(t) \quad (60)$$

We notice that the velocities are not required in equation 59, as they have been neutralised by the Taylor expansion about $|r_t\rangle$. However, whilst they may not be needed to calculate the trajectory, the

calculation of several important systemic properties requires these velocities, and as such they are calculated as

$$|v(t)\rangle = \frac{|r(t + \delta t)\rangle - |r(t - \delta t)\rangle}{2\delta t}. \quad (61)$$

2.5.2.3 – THE CANONICAL ENSEMBLE

These algorithms enforce a condition upon the functions describing the interactions between atoms: they must be differentiable. Additionally, to realistically model the reactions or phenomena of experimental chemistry, we need to impose a set of conditions upon the system. Typically, during an experiment a chemical reaction will take place within a reaction vessel which is of fixed volume, under constant pressure and containing a finite number of atoms. To simulate reactions or processes, we must also impose conditions upon the system of study, although computation allows for flexibility in how these conditions are imposed. Statistical methods address *ensembles* of molecules in dynamic equilibrium, and the definitions of three common ensembles are as follows:

- i) *NVE* – the system contains a constant number of atoms, under constant volume and constant energy. This is known as the *microcanonical ensemble*.
- ii) *NVT* – the system contains a constant number of atoms, under constant volume and constant temperature. This is the *canonical ensemble*.
- iii) μVT – the system is under constant chemical potential, constant volume and constant temperature. This is the *grand canonical ensemble*.

The microcanonical ensemble represents a system that is in complete isolation, enforcing conservation of the total energy and number of atoms. The canonical ensemble represents a system that is kept at constant temperature by coupling with a heat bath, in other words, the total kinetic energy of the system is conserved. The grand canonical ensemble is used to describe a system which is in thermodynamic equilibrium with an external reservoir, such that it is the total kinetic energy of the system and the coupled “bath” that is conserved, thus the temperature of both the bath and atomic system may fluctuate. The canonical ensemble is most commonly used for chemical simulation.⁵

2.5.2.4 – KINETIC ENERGY, TEMPERATURE AND PRESSURE

Upon starting an MD simulation, sufficient time and steps should be dedicated to equilibration, especially if starting from optimised geometries, as the system is starting from its lowest energy configuration. For each MD step, every particle is moved simultaneously, and within each MD step according to the canonical ensemble, the temperature will usually need to be maintained.

Statistical thermodynamics defines temperature as a function of the velocities of the particles within a system, and so allows us to control the temperature of a system by scaling the velocities of all particles, in a manner that keeps temperature constant. The analogy is that of an external heat bath maintaining the isothermal conditions. At each time step, the scaling is applied, a process known as the *Berendsen* algorithm, initiation of which requires evaluating the kinetic energy:

$$E_{kin} = \sum_i^N \frac{m_i v_i^2}{2} = \frac{3}{2} N K_B T \quad (62)$$

Which yields the real temperature of the system, T . we then apply a scaling factor which is defined as

$$\lambda = \sqrt{1 + \frac{\Delta t}{\tau} \left(\frac{T}{T_0} - 1 \right)} \quad (63)$$

Where τ is relaxation time and T_0 is the target temperature.^{4,5}

2.5.2.5 – NOSÉ HOOVER THERMOSTAT

Within computational theory, the algorithm or protocol controlling the temperature is often referred to as a *thermostat*. Another example is the *Nosé-Hoover* thermostat.³⁹⁻⁴³

Originally conceived by S. Nosé in 1984 and refined by W. G. Hoover in 1985, the Nosé-Hoover thermostat introduces a Hamiltonian which possesses an additional degree of freedom:

$$H^* = \sum_i \frac{p_i^2}{2m_i} + \Phi(q) + \frac{Q}{2} \zeta^2 + g K_B T \ln s \quad (64)$$

Here p_i and q_i are the virtual momenta and coordinates of an atom, m_i is the mass of the atom, $\Phi(q)$ is the potential energy of an atom, g is the number of degrees of freedom in a system where i.e. $g = 3N$. K_B is the Boltzmann constant, T is the temperature and s is a velocity scaling factor. The novel

introduction is ζ , the Nosé coefficient, which is essentially a friction parameter introduced to alter the velocity of an atom based on its current velocity. It should be noted that ζ is a dynamic variable, of varying sign and differing value for each atom, derived from:

$$m_i \frac{d^2 r_i}{dt^2} = F_i - \zeta m_i v_i \quad (65)$$

allowing the temperature to be rescaled to the desired value. Finally from equation 64, Q is a variable that determines the relaxation time by coupling of the system to the “bath”; a small Q and thus weak coupling will result in a slow equilibration.

2.5.2.6 – SOLID STATE SYSTEMS

So far, this chapter has largely been ambiguous with the state of simulated systems. The work of this thesis concerns exclusively solid state systems, and this creates some interesting points to consider when modelling them. To model extended systems there are three major points to consider:

- i) Periodicity
- ii) Molecular orbitals
- iii) Symmetry

Periodicity and Symmetry are interrelated, and these two concepts can be used to reduce the calculation complexity, while Molecular orbitals in crystals and amorphous extended solids require slightly different approaches to those of molecules in free space.

2.5.2.7 - PERIODICITY

Much of solid state modelling starts with flawlessly crystalline materials, that is, a material that can be considered to possess semi-infinite long-range order. Modelling a single crystal of just a few millimetres, possessing several trillion atoms is impractical, however if this crystal is larger than a few cubic nanometres, one may model the bulk properties of the material by performing the calculation on a minimal, repeatable image; a crystalline system may be described fully by its unit cell. For many calculable properties, such as band structures, phonon structures, bulk moduli and equations of state, the unit cell, or smallest possible descriptor of a crystal, may contain just a few atoms, but is able to describe the entire system.⁴⁴

For molecular dynamics, or other advanced techniques, to study phase transitions, lattice defects, chemical impurities, transport properties and long wavelength phonons, it may be necessary to use a larger image containing several unit cells.

For the repeat image describing a bulk system, the use of *Periodic Boundary Conditions* (PBC) allows us to model the interactions with the rest of the lattice. Under PBC conditions, the velocities, energies and forces experienced by each atom are calculated for every atom within range of a certain cutoff, including those of the repeat images. In molecular dynamics, it is possible for an atom to leave through a face of the cell, provided another enters from the opposing face with the exact same velocity and energy, maintaining the conditions applied by the canonical ensemble.

The cell may not necessarily be cubic or even orthorhombic, and can in fact take the form of any parallelepiped. Moreover, under variable-cell conditions, for example in molecular dynamics or geometry optimisation, the angles and lengths that define the cell may change to reflect atomic movement, under the condition that periodicity is maintained.

2.5.2.8 - MOLECULAR ORBITALS

Whilst atomic or molecular orbitals are perceived as being little larger than the molecule of interest, in an infinite molecule the molecular orbitals are both infinite in number and infinitely large. The practical connotation is that the molecular orbitals within a system are also periodic, meaning that the wavefunctions describing them need not necessarily possess zero (or infinitesimal) value at the model boxes boundaries. This was addressed by F. Bloch and computational methods were devised by G. Wannier.^{45,46}

2.6 - REFERENCES

- 1 J. C. Slater, *The Calculation of Molecular Orbitals*, John Wiley & Sons, New Jersey, 1979.
- 2 D. A. McQuarrie, *Quantum Chemistry*, University Science Books, 1983.
- 3 L. F. Phillips, *Basic Quantum Chemistry*, John Wiley & Sons, 1965.
- 4 B. M. Rode, T. S. Hofer and M. D. Kugler, *The Basics of Theoretical and Computational Chemistry*, Wiley-VCH, 2007.
- 5 G. D. Billing and K. V. Mikkelsen, *Introduction To Molecular Dynamics and Chemical Kinetics*, John Wiley & Sons, 1996.
- 6 V. Kumar, *Introduction to Parallel Computing*, Addison-Wesley Longman Publishing Co., Inc., Boston, MA, USA, 2nd edn. 2002.
- 7 J. M. Soler, E. Artacho, J. D. Gale, A. García, J. Junquera, P. Ordejón, D. Sánchez-Portal, *Journal of Physics: Condensed Matter*, 2002, **14**, 2745.
- 8 P. Giannozzi, S. Baroni, N. Bonini, M. Calandra, R. Car, C. Cavazzoni and D. Ceresoli, *Journal of Physics: Condensed Matter*, 2009, **21**, 395502.
- 9 B. Aradi, B. Hourahine and T. Frauenheim, *J. Phys. Chem. A*, 2007, **111**, 5678–5684.
- 10 E. Schrodinger, *Collected papers on wave mechanics*, Blackie & Sons Ltd, 1928.
- 11 F. Rohrlich, *Foundations of Physics*, 1987, **17**, 1205–1220.
- 12 S. M. Blinder, *American Journal of Physics*, 1965, **33**, 431–443.
- 13 J. E. Jones, *Proceedings of the Royal Society A: Mathematical, Physical and Engineering Sciences*, 1924, **106**, 463–477.
- 14 H. C. Urey, *Chem. Rev.*, 1930, **6**, 546–547.
- 15 L. H. Thomas, *Mathematical Proceedings of the Cambridge Philosophical Society*, 1927, **23**, 542–548.
- 16 E. Fermi, *Zeitschrift für Physik*, 1924, **29**, 315–327.
- 17 P. Hohenberg and W. Kohn, *Phys. Rev.*, 1964, **136**, B864–B871.

2.6 - REFERENCES (CONTINUED)

- 18 W. Kohn and L. J. Sham, *Phys. Rev.*, 1965, **140**, A1133–A1138.
- 19 J. Harris, *Phys. Rev. B*, 1985, **31**, 1770–1779.
- 20 P. L. Jones, K. E. Khor, A. P. Roberts, P. V. Smith, *Journal of Physics C: Solid State Physics*, 1970, **3**, 1211.
- 21 D. G. Blair, *Proc. Phys. Soc.*, 1967, **91**, 736.
- 22 J. P. Perdew and W. Yue, *Phys. Rev. B*, 1986, **33**, 8800–8802.
- 23 A. D. Becke, *Phys. Rev. A*, 1988, **38**, 3098–3100.
- 24 A. D. Becke, *J. Chem. Phys.*, 1993, **98**, 5648–5652.
- 25 C. Lee, W. Yang and R. G. Parr, *Phys. Rev. B*, 1988, **37**, 785–789.
- 26 J. Bardeen and J. H. Van Vleck, *Proceedings of the National Academy of Sciences*, 1939, **25**, 82–86.
- 27 J. C. Slater and G. F. Koster, *Phys. Rev.*, 1954, **94**, 1498–1524.
- 28 T. Frauenheim, F. Weich, T. Köhler, S. Uhlmann, D. Porezag and G. Seifert, *Phys. Rev. B*, 1995, **52**, 11492–11501.
- 29 C. M. Gorings, D. R. Bowler, E. Hernández, *Reports on Progress in Physics*, 1997, **60**, 1447.
- 30 M. Ghorbani-Asl, *Electronic transport through two-dimensional transition-metal chalcogenides*, PhD Thesis, Dresden, 2014.
- 31 M. Paulsson, *Non Equilibrium Green's Functions for Dummies: Introduction to the One Particle NEGF equations*, arXiv:cond-mat/0210519, 2006.
- 32 J. R. Reimers, G. C. Solomon, A. Gagliardi, A. Bilić, N. S. Hush, T. Frauenheim, A. Di Carlo and A. Pecchia, *J. Phys. Chem. A*, 2007, **111**, 5692–5702.
- 33 P. Giannozzi, O. Andreussi, T. Brumme and O. Bunau, *Journal of Physics: Condensed Matter*, 2017, **29**, 465901.
- 34 B. Hourahine, S. Sanna, B. Aradi, C. Köhler, T. Niehaus and T. Frauenheim, *J. Phys. Chem. A*, 2007, **111**, 5671–5677.

2.6 - REFERENCES (CONTINUED)

- 35 J. M. Bofill, *Molecular modeling annual*, 1995, **1**, 11–17.
- 36 M. R. Hestenes and E. Stiefel, *J Res Natl Bur Stand*, 1952, **49**, 409–436.
- 37 D. P. Sheppard, R. Terrell and G. A. Henkelman, *J. Chem. Phys.*, 2008, **128 13**, 134106.
- 38 M. G. Paterlini and D. M. Ferguson, *Chemical Physics*, 1998, **236**, 243–252.
- 39 S. Nosé, *J. Phys. Soc. Jpn.*, 2001, **70**, 75–77.
- 40 S. Nosé, *Molecular Physics*, 2006, **52**, 255–268.
- 41 S. Nosé, *J. Chem. Phys.*, 1984, **81**, 511–519.
- 42 N. Shuichi, *Prog. Theor. Phys. Suppl.*, 1991, **103**, 1–46.
- 43 W. G. Hoover, *Phys. Rev. A*, 1985, **31**, 1695–1697.
- 44 V. A. Kuzkin, *Z. Angew. Math. Mech.*, 2014, **95**, 1290–1295.
- 45 A. A. Mostofi, J. R. Yates, G. Pizzi, Y.-S. Lee, I. Souza, D. Vanderbilt and N. Marzari, *Computer Physics Communications*, 2014, **185**, 2309–2310.
- 46 G. H. Wannier, *Phys. Rev.*, 1937, **52**, 191–197.

CHAPTER 3 – THERMOELECTRIC MATERIALS REVIEW

This chapter introduces the concepts and applications of thermoelectric materials, offering an overview of the fundamental phenomena that lead to observable thermoelectricity and a review of the literature on the design and synthesis of current, state-of-the-art thermoelectric devices.

“Thermoelectric Materials And Devices” by Cadoff and Miller, and *“Charge Density and Structural Characterisation of Thermoelectric Materials”* by Saravanan were used extensively to build the background of this chapter.^{1,2}

3.1 – INTRODUCTION TO THERMOELECTRIC MATERIALS

Thermoelectric Materials (TEs) exhibit a difference in potential across the material when subjected to a temperature gradient.³ The resultant potential across the material is a direct consequence of charge-carrier migration. With doping, control over the amount and type of charge carriers can be demonstrated, and solid-state ThermoElectric Devices (TEDs) may be constructed from combinations of p- and n-type materials, allowing for the direct conversion of thermal energy to electrical energy.⁴

Originally discovered and utilised in the 1960’s, due to their unique properties, thermoelectrics have been used in a variety of applications during the last several decades. Needless to say, modern demands for sustainable energy have resulted in a renaissance in thermoelectric research, with renewed interest in the development of efficient, solid-state, waste-heat-harvesting technologies as the driving force.⁵

3.1.1 – THE THERMOELECTRIC EFFECT

The thermoelectric effect is better described as the amalgamation of 3 distinct phenomenological observations: the Peltier Effect, the Seebeck Effect, and the Thompson Effect. These combined with several other notable effects in the fields of thermal conduction, magnetism and electronic fields laid the foundations for the modern principles of thermoelectricity.²

3.1.2 – THE SEEBECK EFFECT

In the early 1820's, T. Seebeck discovered that a circuit consisting of two different metals could deflect a compass needle upon the selective heating of one end of the circuit. Initially believing the induced magnetic field to be a direct consequence of the temperature difference, it was later understood that the field was induced by the induced electrical currents according to *Ampere's Law*, as defined by Maxwell.¹

3.1.3 – THE PELTIER EFFECT

In 1834, J. Peltier discovered that in the simple circuit of a bismuth wire connected to a battery at both ends by two copper wires, a difference in temperature is established at each of the junctions. The temperature increased at the junction where current passed from copper to bismuth, and decreased where the current passed from bismuth to copper. The extent of this effect is directly proportional to the magnitude of the current.

$$Q = I \cdot (\Pi_a - \Pi_b) \quad (2.1)$$

The *Peltier Effect*, Q , generated per unit time is equal to the respective *Peltier Coefficients*, Π , of material a and b multiplied by the current.

3.1.4 – THE THOMSON EFFECT

In 1854, W. Thomson (soon to be Lord Kelvin) discovered that a circuit consisting of a single material may evolve or absorb heat if there is a temperature difference across its length. This is in addition to the energy lost as a thermal product of electrical resistance. Thomson also distinguished the interrelationship of the *Seebeck* and *Peltier effects* through thermodynamics. He noted that the Peltier coefficient is the product of the Seebeck coefficient and the absolute temperature.

3.1.5 – THE HALL EFFECT

In 1879, E. Hall observed the manifestation of a potential difference in a material, orthogonal to applied, orthogonal electric and magnetic fields.⁶ Also known as the *Ordinary Hall Effect*, due to the multiple extensions of the observation, this was the point of interest that led to the discoveries of W. Nernst and A. Ettingshausen. The effect is measured by the *Hall Coefficient*:

$$R = \frac{E_y}{J_x \cdot B_z} \quad (2.2)$$

In which, E_y is the electric field induced in y by the effect of the orthogonal magnetic field, B_z , on x-component of the electric current density, J_x .

3.1.6 – THE NERNST EFFECT

W. Nernst discovered that if a material, that is either conducting or semiconducting, is subjected to an orthogonal temperature gradient and magnetic field, an electric field will be induced orthogonal to both.^{1,6} This is also known as the *1st Nernst-Ettingshausen Effect*. The effect is quantized by the *Nernst Coefficient*:

$$|N| = \frac{E_y / B_z}{\delta T / \delta x} \quad (2.3)$$

Where E_y is the y-component of the electric field induced by the z-component of the magnetic field, B_z , and the temperature gradient, $\delta T / \delta x$.

3.1.7 – THE ETTINGSHAUSEN EFFECT

Whilst studying the Hall Effect with his student, W. Nernst, A. Ettingshausen noticed that a temperature gradient may be induced across a material that is subjected to orthogonal electric and magnetic fields. Also known as the 2nd *Nernst-Ettingshausen Effect*, the inclusion of these two effects allow for the complete categorisation of the relationship between electronic, magnetic and thermal fields.⁶ The *Ettingshausen Coefficient*:

$$P = \frac{\delta T / \delta x \cdot \delta z}{|B_z| \cdot I_y} \quad (2.4)$$

Where $\delta T / \delta x$ is the resultant temperature gradient of the effect of y-component of the electric current, I_y , and the z-component of the magnetic field, B_z . The term δz incorporates the thickness of the material into the expression, as the total heat flow is dependent on the cross section of the material.

3.1.8 – THE RIGHI-LEDUC EFFECT

In 1887, it was discovered separately by A. Righi and S. Leduc that for a material subjected to temperature gradient, upon the application of a perpendicular magnetic field, an additional temperature gradient was established orthogonal to both.⁶ The extent of the effect is measured by the *Righi-Leduc Coefficient*:

$$A_{RL} = \left(\frac{\frac{\delta T}{\delta y}}{B_z \frac{\delta T}{\delta x}} \right) \quad (2.5)$$

Whereby, $\frac{\delta T}{\delta y}$ is the difference in temperature induced by the magnetic field, B_z , applied across the existing temperature gradient, $\frac{\delta T}{\delta x}$. As we can see, the *Righi-Leduc Effect* is essentially the thermal analogue to the *Hall effect*.

3.2 – MODERN THEORY OF THERMOELECTRICITY

With the determination of these effects, the original thermoelectric devices were created in the 19th century, but the quest for more efficient materials was first impacted by E Altenkirch, who utilised the constant property model to derive the maximum efficiency of a thermoelectric generator. This equated to about 0.5%, due to the metals in use. The proposal of semiconductors as thermoelectric materials in the early 19th century allowed for theoretical efficiencies of the order of 4%. In 1949, A. F. Ioffe developed the modern theory of thermoelectricity, by defining a thermoelectric *Figure of Merit*:

$$Z = S^2 \cdot \frac{\sigma}{\lambda} \quad (2.6)$$

Where S is the *Seebeck Coefficient*, σ is the electrical conductivity and λ is the thermal conductivity.^{7,8} Later attempts to better quantify thermoelectric materials saw the inclusion of an operating temperature, and the specification of a material-specific figure of merit, zT :

$$zT = \frac{S^2 T}{\rho \kappa} \quad (2.7)$$

Where S is the Seebeck Coefficient, T the operating temperature, ρ the electrical resistivity and κ the thermal conductivity.⁹ Since

$$\rho = \frac{1}{\sigma} \quad (2.8)$$

i.e. the electrical resistivity is simply the inverse of the electrical conductivity, it is common to see the figure of merit defines as

$$zT = \frac{S^2 \sigma T}{\kappa} \quad (2.9)$$

Such that each of the coefficients in the numerator should clearly be increased to maximise zT , whereas the converse is true of the denominator. This led to the development of the criteria for an *ideal thermoelectric material*, i.e. the *Phonon-Glass, Electron-Crystal* (PGEC) model suggested by G. Slack.^{5,10} The rationalisation of these criteria can be observed from the figure of merit; to achieve a higher figure of merit, a higher Seebeck coefficient is desirable, as is a higher electrical conductivity and a lower thermal conductivity.

The term *Electron-Crystal* is obvious, a high electrical conductivity is needed to exploit the difference in potential, by allowing for the maximal mobility of charge carriers. The *Phonon-Glass* term suggests that the obvious way to retard thermal transport is to curb the crystal lattice vibrational modes, or *phonons*,

that are responsible for the majority of thermal transport in semiconductors at low temperatures, and metals at high temperatures.¹

The reason for this differentiation is that there is another mechanism of thermal transport that comes in to play at high temperatures in semiconductors and low temperatures in metals, although most notably in semiconductors. Electrons also have kinetic energy, and though their masses and therefore kinetic energies are relatively low compared to ions, their high mobility in high temperature semiconducting systems results in electronic contributions to thermal energy that are comparable, if not greater, than the ionic contribution. This established the need to further break down the equation for the figure of merit to:

$$zT = \frac{S^2 \cdot \sigma \cdot T}{\kappa_L + \kappa_e} \quad (2.10)$$

Where κ_L and κ_e are the lattice thermal conductivity and electronic thermal conductivity respectively. With a suitable figure of merit defined, work could begin on the optimisation of each thermoelectric coefficient. However, these properties are closely interrelated, and to improve one often comes at the cost of another.¹¹ For example, the electronic term κ_e is directly related to the electrical conductivity, σ , by the *Wiedemann-Franz Law*:¹²

$$\kappa = \kappa_L + \kappa_e \quad (2.11)$$

and

$$\kappa_e = \sigma L T \quad (2.12)$$

where

$$\sigma = n_{cc} q \mu \quad (2.13)$$

giving

$$\kappa_e = n_{cc} q \mu L T \quad (2.14)$$

Here, n_{cc} is the number of charge carriers, μ is the mobility and q is the charge of the carrier, usually the charge of an electron. L is the Lorentz factor which, for free electrons, equates to $2.4 \times 10^{-8} \text{ J}^2 \text{ K}^{-2} \text{ C}^{-2}$.¹³ Substituting Equation 2.13 into Equation 2.9 allows us to rewrite the figure of merit as a product of two sets of unilaterally detrimental properties:

$$zT = (S^2 n_{cc}) \left(\frac{\mu}{\kappa} \right) q T \quad (2.15)$$

The coefficients in (μ/κ) are written as one term because defects and impurities that affect one property usually affect the other.¹⁴ It is generally accepted that increasing the carrier concentration will usually decrease the Seebeck coefficient, such that for an ideal Seebeck coefficient, a low carrier concentration is desired. However, this will negatively impact the electrical conductivity and, in fact, equation 2.9 may also be written as:

$$zT = (S^2\sigma) \left(\frac{\kappa}{T}\right) \quad (2.16)$$

Highlighting the interdependence of the Seebeck coefficient and electrical conductivity. The effect of carrier concentration on the Seebeck coefficient may be appreciated from simple models of electron transport, such as:

$$S = \frac{8\pi^2 k_B^2}{3eh^2} m^* T \left(\frac{\pi}{3n}\right)^{\frac{2}{3}} \quad (2.17)$$

Where m^* is the carriers effective mass.³ This applies to semiconductors and metals, and represents a parabolic band model, with an energy-independent scattering approximation. Clearly an approach to improve the figure of merit in thermoelectric materials must seek to optimise several parameters at once, while preventing the degradation of the others.

3.3 – METHODS OF IMPROVING THERMOELECTRIC MATERIALS

This section reviews the methods devised to optimise the thermoelectric coefficients, both historic and modern. Thermoelectric materials have been known for over a century, and while the classic materials are relatively well categorised, advanced methods of materials design have been developed over the last decade, thanks to renewed interest in sustainable energy generation.^{1,3,5}

3.3.1 – DEFECT MECHANISMS

Defects in a crystal structure can be thought of as reductions in translational or rotational lattice symmetry. Ideally, the use of defects should aim to tackle multiple adversely interdependent properties within the material.^{5,15} An example is the use of doping to affect charge carrier concentrations, while providing point defects to scatter phonons which should ideally increase the Seebeck coefficient, S , while retarding lattice thermal conductivity, κ_L .⁴

3.3.1.1 – POINT DEFECTS

A point defect is a defect in a crystal lattice that perturbs the crystal pattern at a specific site. Point defects can be *intrinsic* or *extrinsic*. Intrinsic point defects occur in pure materials, of which there are two: *atomic vacancies* and *atoms occupying interstitial sites* that would usually be vacant. For compounds, there is a third possibility, whereby two atoms of differing species may swap positions, otherwise known as *anti-site defects*. Extrinsic defects are foreign atoms present intentionally, *solutes*, or otherwise *impurities*. There are also two possible types: Substitutional solutes/impurities, which occupy what would be atomic positions, and interstitial solutes/impurities.⁴

The use of dopants in TEMs is commonplace, initially added to address resistivity, modern doping paradigms intentionally alter the electronic structure of the TEM to achieve several objectives (See 3.6.1.2 & 3.6.1.3). Doping, or the introduction of *extrinsic point defects*, facilitate the formation of *intrinsic point defects*, which in turn alter the carrier concentration, n_{cc} . This is an example of intrinsic point defect manipulation; it is also possible to manipulate intrinsic point defects mechanically and thermally.¹⁶

3.3.1.2 – RESONANT LEVELS

Impurity levels that lie within the conduction and valence bands of the material, *Resonant Levels*, affect two TE properties:

- i) RLs induce a peak within the density of states centred at the *resonant energy*, E_D , which affects S in a positive, almost temperature-independent manner.
- ii) RLs also conduct and scatter charge carriers, with the resonant scattering creating a strong electron energy filtering effect, which increases S at cryogenic temperatures where electron-phonon scattering is weaker.

The effectiveness of RLs is dependent on the position of the DOS peak at resonant energy with respect to the fermi energy, ϵ_f .^{5,14,17}

3.3.1.3 – BAND CONVERGENCE

The aim of the *Band Convergence* method is to increase *band degeneracy*, with the aim of increasing Seebeck Coefficient, without drastically altering resistivity. Two factors contribute to band degeneracy:

- i) The energy extrema of several bands occurring within a few $k_B T$ of ϵ_f , or *Orbital Degeneracy*.
- ii) The presence of multiple symmetry-induced carrier pockets within the fermi surface, or *Valley Degeneracy*. The Valley degeneracy, N_v , affects the DOS effective mass by $N_v^{2/3}$.

The efficaciousness of the Band Convergence method is confined by the temperature-dependent band shift, interband scattering and dopant solubilities.^{13,17}

3.3.1.4 – TOPOLOGICAL DEFECTS

Defects that cannot be rectified by any local rearrangement are known as *topological defects*. One such class of topological defects are 1-dimensional dislocations, which can be formed through plastic deformation processes, such as extrusions or hot forging. It has been shown that these dislocation sites contribute to phonon scattering over a wide range of wavelengths, yielding low κ_L values and state-of-the-art zT values.^{3,18}

3.3.1.5 – INTERFACIAL PREFERENTIAL SCATTERING

2D planar defects such as interfaces and grain boundaries have been used in a three-tier approach to affect zT:

- i) Phonons may be scattered more effectively than charge carriers, leading to lower κ_L , while maintaining S .
- ii) Low energy charge carriers are scattered more effectively than high energy carriers, increasing S , maintaining σ .
- iii) Minority carriers are scattered more effectively than majority charge carriers, Increasing S , maintaining σ .

Provided grain boundaries are at least semi-coherent, and sufficient intergrain band alignment is present, the mobility, μ , should be retained while κ_L is suppressed. Approaches ii and iii seek to increase S by implementing the Carrier Energy Filtering scheme (CEF) which exploits energetic barriers

to filter out low-energy charge carriers such that S is improved.^{19,20} This allows for improvement of zT by increasing S in a manner that maintains μ and reduces κ_L .

3.3.1.6 – MODULATION DOPING

For 2D materials exhibiting ionised impurity scattering at high temperatures, it is possible to separate charge carriers from zonal dopants by implementing “spacer layers” between specialised layers, a practice termed *Modular Doping*. Charge carriers are irreversibly donated by the dopant layers to the active TE layer, which has high mobility, maintaining mobilities and negating the effects of ionised impurity scattering.^{21,22}

3.3.2 – SIZE EFFECTS

The concepts of TE Nano-materials, 2D and 1D thermoelectrics are underpinned by the effects of reduced dimensionality. There are two regions of scale when discussing size effects, *Classical Size Effects* and *Quantum Size Effects*.⁵

3.3.2.1 – CLASSICAL SIZE EFFECTS

The size effects dominating κ_L are known as *Classical Size Effects*. By restricting the phonon mean free path, the contribution to zT can be minimised, up to the *amorphous limit* whereby the mean free path approaches the scale of atomic bonds. Thus, the amorphous material, where random-walking Einstein modes dictate thermal transport, is the natural limit to phonon facilitated thermal transport. This minimal lattice thermal conductivity is defined as:

$$\kappa_{min} = \left(\frac{\pi}{6}\right)^{1/3} \kappa_B n_a^{2/3} \sum_i v_i \left(\frac{T}{\theta_i}\right)^2 \int_0^{\theta_i/T} \frac{x^3 e^x}{(e^x - 1)^2} dx \quad (2.18)$$

Where the cutoff frequency

$$\theta_i = v_i \left(\frac{\hbar}{\kappa_B}\right) (6\pi^2 n_a)^{1/3} \quad (2.19)$$

n_a is the number density of atoms, \hbar is the reduced Planck’s constant and v_i is the sound velocity for each polarisation mode.

3.3.2.2 – QUANTUM SIZE EFFECTS

Sharp DOS features, exploitable for increased S if ε_f is favourably positioned, can be achieved utilising the *Quantum Size Effect*. When the charge carriers de Broglie wavelength approaches the dimensions of the material, they become strongly confined in the relevant directions, reducing mobility.²³

Both effects are likely present to some extent at the small scales required to observe either of the effects, though it is believed that the Classical Quantum Effect contributes most to zT , as the majority of advances in nanocomposite TEs have come from reduced thermal transport.

3.3.3 – CRITICAL PHENOMENA

C. B. Vining states that $1 + zT$ in a TE process is the equivalent of:

$$\lambda_{Ei} = \frac{C_p}{C_v} \quad (2.20)$$

in a gas cycle engine, where C_p is the heat capacity at constant volume.²⁴ It is observed that λ_{Ei} diverges at a gas-liquid phase transition, and hypothesised that zT may be enhanced near an *electronic phase transition*.²⁵ This forms part of the basis for the study of the thermoelectric properties of the black phosphorus to grey phosphorus phase transition in Chapter 4.

Evidence of this principle is observed in the zT peak at the phase-transition of I-doped Cu_2Se which has been suggested to be the result critical scattering of charge and heat carriers.²⁵ In other work by D. R. Brown *et al.*, the exploitation of phase transitions in copper chalcogenides allowed for Larger S by allowing charge carriers to access more microstates.²⁶

Naturally, materials that readily undergo phase transitions are not expected to be useful in thermoelectric devices, but the work allows for the exploration of novel phenomena near phase transitions. The consensus is that the exploitable phenomena in *subcritical* materials, which exhibit electronic instability in the absence of structural phase transitions, may yield useful insights.

3.3.4 – ANHARMONICITY

Another approach to reduce κ_L is the concept of *Anharmonicity*. Where scattering processes seek to reduce the mean free path i.e. space domain of phonons, the Anharmonicity approach aims to reduce the lifetime of phonons, i.e. the time domain. By manipulation of phonon-phonon interactions, low κ_L may be achieved by means of a “rattler atom” which vibrates in an anharmonic manner, resulting in interactions between low-lying optical phonons and acoustic phonons.⁴ Materials that exhibit strong anharmonicity tend to have large, complex unit cells, heavy elements and weak or asymmetric bonding. Examples include skutterudites and clathrates, with incorporated guest atoms within the cage-like structure.²⁷⁻²⁹

The Umklapp process dominates κ_L at high temperatures, allowing for the formulation of the simple equation:

$$\kappa_L = \frac{MV^{1/3}\theta_D^3}{\gamma^2 T} \quad (2.21)$$

where M is the average atomic mass, V is the average atomic volume, θ_D is the Debye temperature, and γ is the volume *Grüneisen parameter*. Typical materials have a Grüneisen parameter between 1 and 2, although a mode-specific γ can be much larger.

3.3.5 – SPIN EFFECTS

Due to the dependence of the Seebeck coefficient, or *thermopower*, on the charge carriers within a material, it is often neglected that spin effects are important in the modelling of thermoelectric materials. There are 3 main effects of spin on thermoelectric properties.

The *Rashba Effect* manifests as the splitting of bands in the electronic structure, due to the effect of Spin-Orbit Coupling (SOC) in crystals with no inversion symmetry.³⁰⁻³² This splitting is present as a sharp feature in the Density of States (DOS), which has implications for the Seebeck coefficient.³³ The *Spin Seebeck Effect* (SSE) is the spin analogue of the Charge-based Seebeck Effect (CSB), the major difference being that in the SSE, the spin voltage is maintained orthogonal to the temperature gradient. The spin Seebeck effect is notably weaker than the CSE, however it has gained traction in the emergent field of spin caloritronics.³⁴

The Final noteworthy spin effect in thermoelectrics is that of *Topological Insulators* (TI's).³⁵ In topological insulators, the bulk material displays a band gap which is strongly dependent on the spin-orbit coupling of such systems, whereas at the surface topologically protected conducting states are observed. Materials such as Bi₂Se₃ and Bi₂Te₃, which are well known thermoelectrics, happen to also make good TI's.³⁶ This is a consequence of the heavier elements large SOC, and tendency to form compounds with a bulk band gap. As such, some investigation has taken place into the relationship between thermoelectric and topological insulator properties.³⁷

3.3.6 – HIERARCHICAL ARCHITECTURES IN THERMOELECTRICS

A common method of affecting the thermal conductivity in thermoelectric materials, is to selectively scatter lattice vibrations, or *phonons*, at specific length scales, by the inclusion of structural defects. Such examples include the application of grain boundaries in polycrystalline systems, the use of Superlattices as 1 dimensional scatterers to achieve anisotropic properties, and the presence of secondary phases in bulk materials.^{15,18,22,38} Many thermoelectrics are polycrystalline, and formed from the sintering of nano-powders under pressure. In the grain boundary regime, this approach is taken to the extreme by creating materials that are 100% dense, and created either from the sudden cooling of melts, or mechanical shock. At the atomic scale, the materials are crystalline and thus possess the Seebeck coefficients and electronic conductivities associated with single crystals. However, the mean free path of large wavelength phonons has been reduced, and the scattering at interfaces has been shown to be an effective method of perturbing thermal transport.

Superlattices have been shown to create a disparity in the directional transport properties of otherwise isotropic bulk-thermoelectrics.^{39,40} As a result, these materials have been suggested for niche applications. Materials with an excess of certain species have a tendency to form nanocrystals of secondary phases within the bulk structure. In Cu₂SnSe₃, it has been demonstrated that the presence of the secondary phase SnSe₂ may result in a significant increase in the Seebeck coefficient and power factor.^{41,42}

3.4 – MATERIALS OF INTEREST

As we have seen, the thermoelectric effect has been known for over a century, whilst *thermoelectric materials* as we know them today have been around since the 1960's. However, in recent years the renaissance in thermoelectric research has led to the discovery of several more families of materials with desirable and, more importantly, tuneable thermoelectric properties. This section covers the common materials in the field of thermoelectrics, alongside some more recent discoveries.

3.4.1 – POST-TRANSITION METAL CHALCOGENIDES

Binary Tellurides, such as Bismuth Telluride and Lead Telluride were the original state-of-the-art thermoelectric materials in the 1950's.^{1,4,43} It was apparent that by alloying Bi_2Te_3 with Bi_2Se_3 and Sb_2Te_3 , control over carrier concentration and lattice thermal conductivity was possible, and complex materials such as p-type $(\text{Sb}_{0.8}\text{Bi}_{0.2})_2\text{Te}_3$ and n-type $\text{Bi}_2(\text{Te}_{0.8}\text{Se}_{0.2})_3$ were studied and further developed.^{3,5,18} These materials have reported zT values of 0.8 to 1.1 for temperatures up to 500 K, with p-type materials having the highest values. Optimal temperature ranges can be tuned by altering carrier concentration, allowing for application specific compositions.

Materials with peak zT 's in mid-range temperatures (500-900 K) are typically group IV Tellurides, such as PbTe, SnTe and GeTe, included here for completeness.³ Similar principles are used to tune carrier concentration, the best-known being $(\text{GeTe})_{0.85}(\text{AgSbTe}_2)_{0.15}$ or 'TAGS' as it is often called. At these temperatures, this family of compounds has reported zT 's of slightly larger than 1.^{3,5}

3.4.2 – OXYSELENIDES

In 2010 it was reported by Zhao et al. that BiCuSeO Oxyselenides demonstrated thermoelectric properties.^{27,44-46} BiCuSeO is a mid-temperature range material, with a zT that surpasses 1.0 around 650 K. The materials are typically stacked layers of Bi_2O_2 and Cu_2Se_2 , and it is this layered structure that is suggested to be responsible for their thermoelectric properties, largely due to their remarkably low κ_L . This is thought to be due to the difference in bond lengths between Bi-O (~ 2.33 Å) and Bi-Se (~ 3.2 Å), which leads to anharmonic effects and a large Grüneisen parameter. In single crystals, there are large anisotropic effects, as the thermal conductivity within the plane of the sheets is almost twice that of the out of plane thermal conductivity.

Another aspect of the structure that may play a strong role in the thermal conductivity is the presence of lone pairs on Bi, albeit indirectly.^{29,44,47} The presence of these lone pairs results in a large valence shell, yielding a large Grüneisen parameter, which suggests strong interactions between optical phonons and acoustic phonons. The phonon-phonon Umklapp processes scatter the heat-carrying acoustic phonons, thus reducing thermal conductivity.

3.4.3 – SILICON-GERMANIUM COMPOUNDS

For high-range temperatures (> 900 K), the most commonly used materials are alloys of silicon and germanium. A typical alloy consists of silicon as a major component, stoichiometric germanium and a fractional dopant, such as $\text{Si}_{0.795}\text{Ge}_{0.2}\text{X}_{0.005}$, where X is P for the n-type component and B for the p-type component. The material adopts the diamond crystal structure which is normal for ground state silicon.⁴⁸⁻⁵¹

These alloys have relatively low zT 's compared to other state-of-the-art materials, but operate over a wider range of temperatures, specifically high temperatures (~900 K). reported zT 's for the n-type material are around 1.0, whereas the p-type material has zT 's of around 0.6. The lower zT values are, in part, due to the higher κ_L values for SiGe compounds. They are low with respect to most materials, though are still at least an order of magnitude higher than those of the recently discovered complex materials, such as TAGS.³

3.4.4 – COPPER CHALCOGENIDES

Since the 1960's (possibly even as early as 1827), copper chalcogenides have been known to exhibit thermoelectric properties. An example is Cu_2Se , which has an ordered structure of selenium atoms, with a disordered arrangement of Cu ions permeating the structure.²⁶ Cu_2Se undergoes a phase transition at ~400 K, where α - Cu_2Se transforms into β - Cu_2Se in a reversible manner. At high temperatures, the copper ions behave as an ionic liquid, which allows for the evolution of the phonon-glass electron-crystal (PGE) concept to that of a phonon-liquid electron crystal (PLEC).

This behaviour leads to interesting properties, such as ultralow thermal conductivities at high temperatures, which is primarily responsible for the high zT values reported for Cu_2Se , such as 1.5 – 1.7 at 1000 K, for the base material, with ultrahigh values of 2.62 reported for doped materials such as

$\text{Cu}_{1.94}\text{Al}_{0.02}\text{Se}$ at 1030 K. Note that this value is anisotropic, and that a value of 1.4 was reported for the perpendicular direction in a single crystal, much closer to the values obtained for polycrystalline bulk material.⁵²

Unfortunately, it is widely believed that the phenomena responsible for these high zT values make these materials unsuitable for device construction, as the eventual migration of Cu ions will lead to localised structural rearrangements across a device, rendering the device efficiency vastly reduced.

3.4.5 – HALF HEUSLER COMPOUNDS

Half Heusler compounds are intermetallic compounds with an ABX formula, where A is transition metal, noble metal or rare earth element, B is a transition metal or noble metal and X is a main group element. They are known for their high-temperature efficiencies and thermal stability. For some time, it has been noted that the zT of the n-type materials, is commonly far higher than the equivalent p-type half Heusler. For example, typical n-type zT values of 0.8 – 1 have been reported, while p-type zT values of <0.5 are common. Recent advances in half Heusler's however, have seen zT values of ~1.5, which is far greater than the industry standard of 0.8 for SiGe compounds.

3.4.6 – FILLED SKUTTERUDITES

Skutterudite, CoAs_3 , is a crystalline mineral with a cubic structure. The structure can be described by considering a $2 \times 2 \times 2$ superlattice of simple cobalt cubes. 6 of these 8 cobalt cubes are filled with square planar rings of 4 arsenic atoms, which are arranged such that the arsenic planes between neighbouring cubes are orthogonal. Isostructural compounds were found to exist, and to possess reasonable thermoelectric figures of merit, such as CoSb_3 , doped samples of which have are reported to achieve zTs of up to 1. The vacancies in the structure, i.e. the two cobalt cubes which remain unfilled, may be filled with guest species. These "filler" atoms serve both to dope the electronic structure, as well as "rattlers" (see 3.3.4), thus also affecting phonon transport. Filled Skutterudites, such as $\text{La}_{0.8}\text{Ti}_{0.1}\text{Ga}_{0.1}\text{Fe}_3\text{CoSb}_{12}$, have achieved zTs of up to 1.2.

3.5 – DERIVATION OF THERMOELECTRIC COEFFICIENTS FROM ELECTRONIC TRANSMISSION

Much of the work in this thesis involves the derivation of the electronic coefficients required by the figure of merit, in order to derive theoretical zT 's for novel materials. As such, the derivation of these coefficients is provided here, and referenced in subsequent chapters.

According to the Landauer-Buttiker Formalism, the resistivity of a system can be expressed as a scattering problem.^{53,54} In the coherent transport limit, where inelastic scattering and electron-phonon coupling is absent, the formalism is exact.⁵⁵ The electric current may be derived from the electronic transmission function, $T(E)$, using the linear response:

$$I = -\frac{2q}{h} \int_0^\infty d\varepsilon_k [f_0(\varepsilon_k - \mu_1) - f_0(\varepsilon_k - \mu_2)] = -\frac{2q}{h} T(E)[\mu_1 - \mu_2] \quad (2.22)$$

The electronic transmission function, $T(E)$, defines the rate at which electrons of energy (E), are propagated from the source contact to the drain contact, via the device region. This is output by the dftb-negf code, as a text file containing data for a 2 dimensional plot, or curve. It is the calculation of the transmission curve, $T(E)$, for multiple materials, that forms the basis of the work of this PhD thesis.

Subsequently, thermoelectric coefficients may be derived from the integrals of the product of the transmission, second derivative of the fermi function and the normalisation with respect to the fermi energy:

$$K_n = \frac{2}{h} \int dE T(E) \left(-\frac{\delta f}{\delta E} \right) (E - \mu)^n \quad (2.22)$$

Where n is varied to derive the coefficients, such as conductivity, $n = 0$:

$$\sigma = q^2 K_0 \quad (2.23)$$

Seebeck coefficient, $n = 1$:

$$S = \frac{K_1}{qTK_0} \quad (2.24)$$

And electronic thermal conductivity, $n = 2$:

$$\kappa_e = \frac{K_2 - \frac{K_1^2}{K_0}}{T} \quad (2.25)$$

Using this formalism and these derivations, a program was prepared to calculate the temperature and potential dependent thermoelectric coefficients from the electronic transport calculations output electronic transmission spectra.^{56,57} This script further included an estimate zT in the absence of the lattice thermal conductivity:

$$zT_e = \frac{\sigma S^2 T}{\kappa_e} \quad (2.26)$$

3.6 – REFERENCES

- 1 I. B. Cadoff and E. Miller, *Thermoelectric Materials And Devices*, Reinhold Publishing Corporation, 1959.
- 2 R. Saravanan, *Charge Density and Structural Characterization of Thermoelectric Materials*, Materials Research Forum LLC, 2016.
- 3 G. J. Snyder and E. S. Toberer, *Nature Mater*, 2008, **7**, 105–114.
- 4 G. Tan, L.-D. Zhao and M. G. Kanatzidis, *Chem. Rev.*, 2016, **116**, 12123–12149.
- 5 J. He and T. M. Tritt, *Science*, 2017, **357**, eaak9997.
- 6 O. Lindberg, *Proceedings of the IRE*, **40**, 1414–1419.
- 7 N. S. Rasor, *Journal of Applied Physics*, 1960, **31**, 163–167.
- 8 A. Polozine, S. Sirotinskaya and L. Schaeffer, *Mat. Res.*, 2014, **17**, 1260–1267.
- 9 R. P. Chasmar, R. J. Stratton, *J. Electron. Control*, 1959, **7**, 52.
- 10 G. A Slack, *Phys. Revs. B: Solid State*, 1979, **34**, 1-71.
- 11 T. Zhu, Y. Liu, C. Fu, J. P. Heremans, J. G. Snyder and X. Zhao, *Adv. Mater.*, 2017, **29**, 1605884.
- 12 N. Wakeham, A. F. Bangura, X. Xu, J.-F. Mercure, M. Greenblatt and N. E. Hussey, *Nature Communications*, 2011, **2**, 396.
- 13 Y. Pei, A. D. LaLonde, H. Wang and G. J. Snyder, *Energy Environ. Sci.*, 2012, **5**, 7963–7969.
- 14 J. P. Heremans, B. Wiendlocha and A. M. Chamoire, *Energy Environ. Sci.*, 2012, **5**, 5510–5530.
- 15 D. Selli, S. E. Boulfelfel, P. Schapotschnikow, D. Donadio and S. Leoni, *Nanoscale*, 2016, **8**, 3729–3738.
- 16 X. Shi, L. Chen and C. Uher, *International Materials Reviews*, 2016, **61**, 379–415.
- 17 Y. Pei, H. Wang and G. J. Snyder, *Adv. Mater.*, 2012, **24**, 6125–6135.

3.6 – REFERENCES (CONTINUED)

- 18 B. Poudel, Q. Hao, Y. Ma, Y. Lan, A. Minnich, B. Yu, X. Yan, D. Wang, A. Muto, D. Vashaee, X. Chen, J. Liu, M. S. Dresselhaus, G. Chen and Z. Ren, *Science*, 2008, **320**, 634–638.
- 19 C. Ou, J. Hou, T.-R. Wei, B. Jiang, S. Jiao, J.-F. Li and H. Zhu, *NPG Asia Mater*, 2015, **7**, e182–e182.
- 20 A. Shakouri and J. E. Bowers, *Appl. Phys. Lett.*, 1997, **71**, 1234–1236.
- 21 M. Zebarjadi, G. Joshi, G. Zhu, B. Yu, A. Minnich, Y. Lan, X. Wang, M. Dresselhaus, Z. Ren and G. Chen, *Nano Lett.*, 2011, **11**, 2225–2230.
- 22 M. Ibáñez, Z. Luo, A. Genç, L. Piveteau, S. Ortega, D. Cadavid, O. Dobrozhan, Y. Liu, M. Nachtegaal, M. Zebarjadi, J. Arbiol, M. V. Kovalenko and A. Cabot, *Nature Communications*, 2016, **7**, 10766.
- 23 L. D. Hicks and M. S. Dresselhaus, *Phys. Rev. B*, 1993, **47**, 12727–12731.
- 24 C. B. Vining, *MRS Proceedings*, 1997, **478**, 3.
- 25 H. Liu, X. Yuan, P. Lu, X. Shi, F. Xu, Y. He, Y. Tang, S. Bai, W. Zhang, L. Chen, Y. Lin, L. Shi, H. Lin, X. Gao, X. Zhang, H. Chi and C. Uher, *Adv. Mater.*, 2013, **25**, 6607–6612.
- 26 D. R. Brown, T. Day, K. A. Borup, S. Christensen, B. B. Iversen and G. J. Snyder, *APL Materials*, 2013, **1**, 052107.
- 27 C. Chang and L.-D. Zhao, *Materials Today Physics*, 2018, **4**, 50–57.
- 28 T. Matsunaga, N. Yamada, R. Kojima, S. Shamoto, M. Sato, H. Tanida, T. Uruga, S. Kohara, M. Takata, P. Zalden, G. Bruns, I. Sergueev, H. C. Wille, R. P. Hermann and M. Wuttig, *Adv. Funct. Mater.*, 2011, **21**, 2232–2239.
- 29 M. D. Nielsen, V. Ozolins and J. P. Heremans, *Energy Environ. Sci.*, 2013, **6**, 570–578.
- 30 L. Wu, J. Yang, T. Zhang, S. Wang, P. Wei, W. Zhang, L. Chen and J. Yang, *Journal of Physics: Condensed Matter*, 2016, **28**, 085801.
- 31 G. Bihlmayer, O. Rader and R. Winkler, *New J. Phys.*, 2015, **17**, 050202.
- 32 A. Manchon, H. C. Koo, J. Nitta, S. M. Frolov and R. A. Duine, *Nature Mater*, 2015, **14**, 871–882.
- 33 L. Wu, J. Yang, S. Wang, P. Wei, J. Yang, W. Zhang and L. Chen, *Phys. Rev. B*, 2014, **90**, 195210.

3.6 – REFERENCES (CONTINUED)

- 34 Y. Wang, N. S. Rogado, R. J. Cava and N. P. Ong, *Nature*, 2003, **423**, 425–428.
- 35 M.-S. Nam, B. H. Williams, Y. Chen, S. Contera, S. Yao, M. Lu, Y.-F. Chen, G. A. Timco, C. A. Muryn, R. E. P. Winpenny and A. Ardavan, *Nature Communications*, 2018, **9**, 56.
- 36 H. Shi, D. Parker, M.-H. Du and D. J. Singh, *Phys. Rev. Applied*, 2015, **3**, 014004.
- 37 J. P. Heremans, R. J. Cava and N. Samarth, *Nat. Rev. Mater.*, 2017, **2**, 17049.
- 38 A. Shakouri, *Annu. Rev. Mater. Res.*, 2011, **41**, 399–431.
- 39 Sreeparvathy, P.C. and V. Kanchana, *Journal of Physics and Chemistry of Solids*, 2017, **111**, 54–62.
- 40 J. O. Sofo and G. D. Mahan, *Appl. Phys. Lett.*, 1994, **65**, 2690–2692.
- 41 R. Ma, G. Liu, J. Li, Y. Li, K. Chen, Y. Han, M. Zhou and L. Li, *Ceramics International*, 2017, **43**, 7002–7010.
- 42 Y. Li, G. Liu, T. Cao, L. Liu, J. Li, K. Chen, L. Li, Y. Han and M. Zhou, *Adv. Funct. Mater.*, 2016, **26**, 6025–6032.
- 43 T. Caillat, J. P. Fleurial, G. J. Snyder and A. Borshchevsky, *International Conference on Thermoelectrics, ICT, Proceedings*, 2001, pp. 282–285.
- 44 P. Vaquero, R. A. R. Al Orabi, S. D. N. Luu, G. Guelou, A. V. Powell, R. I. Smith, J. P. Song, D. Wee and M. Fornari, *Phys. Chem. Chem. Phys.*, 2015, **17**, 31735–31740.
- 45 S. Das and Anbalagan Ramakrishnan and Kuei-Hsien Chen and Dinesh Kumar Misra and Ramesh Chandra Mallik, *Journal of Physics D: Applied Physics*, 2018, **51**, 035501.
- 46 S. D. N. Luu and P. Vaquero, *Special Issue on Advances in Thermoelectric Research*, 2016, **2**, 131–140.
- 47 E. J. Skoug and D. T. Morelli, *Phys. Rev. Lett.*, 2011, **107**, 235901.
- 48 A. Nozariasbmarz, Z. Zamanipour, P. Norouzzadeh, J. S. Krasinski and D. Vashaee, *RSC Adv.*, 2016, **6**, 49643–49650.
- 49 T. H. Geballe and G. W. Hull, *Phys. Rev.*, 1955, **98**, 940–947.

3.6 – REFERENCES (CONTINUED)

- 50 C. M. Bhandari and D. M. Rowe, *Contemporary Physics*, 2006, **21**, 219–242.
- 51 G. Bernard-Granger, K. Favier, M. Soulier, C. Navone, M. Boidot, B. Deniau, P. Grondin, J. Leforestier and J. Simon, *Scripta Materialia*, 2014, **93**, 40–43.
- 52 D. Chen, Y. Zhao, Y. Chen, T. Lu, Y. Wang, J. Zhou and Z. Liang, *Adv. Electron. Mater.*, 2016, **2**, 1500473.
- 53 R. Landauer, *Philosophical Magazine*, 2006, **21**, 863–867.
- 54 R. Landauer, *IBM Journal of Research and Development*, 1957, **1**, 223–231.
- 55 H. D. Cornean, A. Jensen and V. Moldoveanu, *Journal of Mathematical Physics*, 2005, **46**, 042106.
- 56 S. Datta, *Electronic Transport In Mesoscopic Systems*, Cambridge University Press, 1995.
- 57 M. P. Anantram, M. S. Lundstrom and D. E. Nikonov, *Proceedings of the IEEE*, **96**, 1511–1550.

CHAPTER 4 – EFFECT OF PRESSURE-INDUCED PHASE-TRANSITIONS ON THE THERMOELECTRIC PROPERTIES OF BLACK PHOSPHORUS

The focus of this chapter is the calculation of electronic transport properties and the derived thermoelectric properties of phosphorus materials. More specifically, the properties are calculated for nanowires of Black Phosphorus (BP), in the form of Mono-, Bi- and Tri-Layers. Subsequently, these properties are calculated for bulk black phosphorus. The methods are then applied to the case of the black phosphorus to Grey Phosphorus (GP) phase transition, by studying both black and grey phosphorus, along with a series of metastable intermediates from the transition pathway.

4.1 – INTRODUCTION

Thin films and 2D materials are a hot topic in the field of materials research.¹⁻³ The anisotropic effects of 2D layered materials are extreme in some cases, and so it was hypothesised that the thermoelectric properties of these materials would otherwise be affected in an interesting manner, potentially allowing for the separation of the intertwined thermoelectric properties.² By perturbing thermal transport along one direction, and maintaining or even improving the electronic transport in the orthogonal plane, it was hoped that one may construct an improved thermoelectric device. A material with weakly bound layers, where “weak” means as an inter-layer bonding scheme relative to the covalently bonded intra-layer scheme, presents interesting opportunities for methods such as intercalation, and at the theoretical level, the opportunity to create novel “stacks” of planar materials.⁴

Thus, it was determined that phosphorus would be an interesting model system for the transition metal chalcogenides, which have recently gained traction as thermoelectric materials with high efficiencies.

5-7

This chapter was inspired by previous work on thermoelectrics (Selli et al.) combined with the work on phosphorus phase transitions by Boulfelfel et al.^{8,9} The concept was that a metastable intermediate, from the black phosphorus to grey phosphorus phase transition pathway, could have reduced thermal conductivity due to long-range disorder, while maintaining the electrical properties of black phosphorus. In order to model these large, asymmetric systems, a method had to be conceived in which the electronic properties of large systems of atoms could be calculated with near DFT accuracy. Assuming that the phases of phosphorus were stable, and that the intermediate phases were metastable, one could ignore the kinetics of the system and calculate the electronic properties for the static phonon state. This naturally meant that the DFTB method became the method of choice.^{10,11} Using the Landauer-Büttiker formalism, one may map the conduction of electrons across a system as a transmission problem, in which the conductivity of a material may be calculated from a system in which a “wire” of the relevant material is held between two contacts.^{12,13}

4.1.1 – ALLOTROPY IN PHOSPHORUS

Phosphorus is a pnictogen that is known to have 6 allotropes under various conditions. It is highly reactive, and thus elemental phosphorus does not occur naturally, though it is also essential to life, as a vital component of both DNA and ATP.¹⁴

The ground state allotrope of phosphorus is *White Phosphorus*, WP, which has two forms, α -WP and β -WP. α -WP has a cubic structure and is the more energetically favourable under atmospheric conditions, whereas the β -WP phase is hexagonal and forms at 195.3 K. Both phases consist of Van der Waals bound P₄ tetrahedra, as seen in figure 4.1. The phase transition induces a change in the orientation of these tetrahedra with respect to each other, and no immediately apparent alteration to the covalent bonding scheme within each P₄ molecule. WP is highly reactive, not observed in nature, and thus obtained by synthetic methods. WP naturally degrades with time to Red Phosphorus, RP.¹⁵

Red phosphorus is obtained from white phosphorus under standard conditions, though heating and exposure to light accelerate the process. It is often described as the polymeric form of WP, with each tetrahedron forming two bonds with its neighbours, weakening and even breaking one of the tetrahedral bonds, usually between the two atoms involved in the polymeric bonding scheme. Several different structural polymorphs of RP are believed to exist, and the exact crystal structure is under some debate.

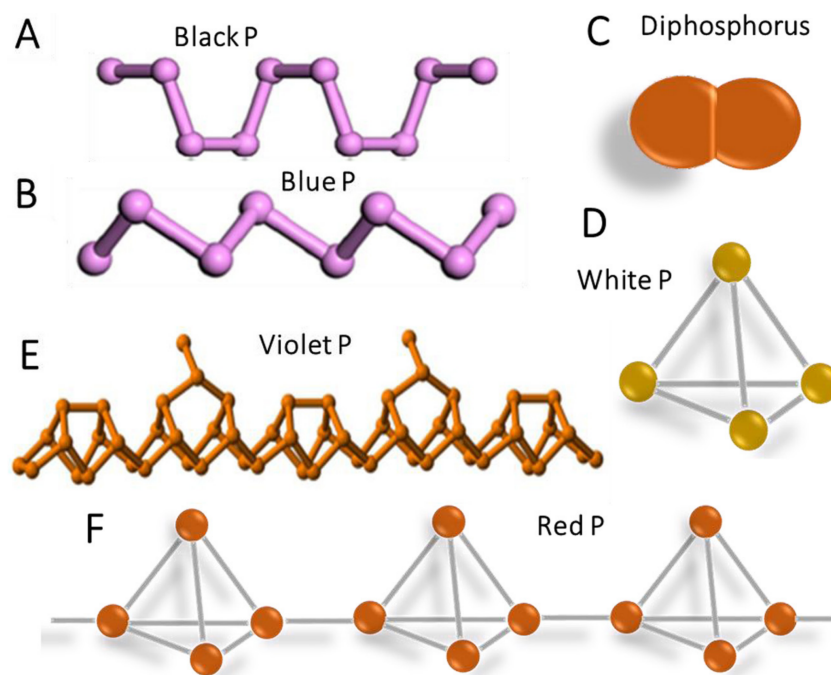


Figure 4.1 – Representation of the known allotropes of phosphorus. Each allotrope features a large degree of Van der Waals bonding between covalently bound molecules. Adapted from “Liquid-phase exfoliation of black phosphorus and its applications” by Lin et al.¹⁶

Black Phosphorus, BP, is also obtained from white phosphorus, though under high pressures and temperatures. It has a likeness to graphite, and is often described as having a “puckered” or “corrugated” graphene structure.¹⁵ The structure consists of graphene-like layers of corrugated phosphorus rings of 6 atoms, which are bound by Van der Waals forces, as in graphite. These layers however, are stacked directly upon one another, in an A-B’ stacking scheme, as opposed to the A-B stacking scheme of graphite, where in B, each layer is offset by half the length of the unit cell axes in direction *a* and *b*, whereas in B’ the offset is only along *a*. This is due to the optimum orbital overlap between the lone pairs of each phosphorus atom. Black phosphorus is sometimes known as β -metallic phosphorus, however BP is actually a semiconductor, with a small yet distinct band gap of 0.3 eV.^{6,7}

Grey Phosphorus, GP is obtained from black Phosphorus under high pressures, around 5 GPa, and is the only truly metallic allotrope of phosphorus, having no band gap.⁹ GP is, however, an example of a “poor” or “bad-metal”, in that it has a very low density of states about the Fermi level, and thus a small number of charge carriers involved in conduction. Grey phosphorus is isostructural with the α -phase crystal structure of arsenic, and consists of Van der Waals bound layers of distorted graphene-like sheets, as in black phosphorus, though with a different topology.¹⁷

Violet Phosphorus, VP, the final exotic phase of phosphorus, sometimes referred to as *Hittorf's Phosphorus* after its discoverer, is obtained from red phosphorus at elevated temperatures. Also known as α -metallic phosphorus, again due to its small band gap. It has gained interest in recent years as a potential 2D material with novel properties.¹⁸

4.1.2 – OBJECTIVES

Black phosphorus is known to undergo a phase transition at around 5 GPa, resulting in the GP structure.^{9,16} Previous work by Boulfefel et al. proved that this phase transition could be modelled, and highlighted the effect of lone pairs on the bonding of the structural intermediates. A structural map of this phase transition presented a unique opportunity to probe several questions:

- i) What is the effect of pressure on the thermoelectric properties of a 2D layered material, such as Black Phosphorus?

- ii) What is the effect of critical phenomena on the thermoelectric properties of phosphorus intermediates?

- iii) Does the structural phase transition occur simultaneously with an electronic phase transition?

The third point is an interesting topic, the structural phase transition is known to occur at 5 GPa, and this transition is visually obvious to the computational chemist. Moreover, since black phosphorus is a semiconductor and grey phosphorus is a metal, of interest to the theoretical physicist is the coinciding electronic phase transition. The hypothesis for this third point, was that the electronic phase transition occurred at a lower pressure than the structural phase transition, i.e. the two were not simultaneous.

These three questions form the basis for the work of this chapter.

4.2 – BLACK PHOSPHORUS

Black phosphorus is a small band gap semiconductor, with a band gap of 0.3 eV reported in the literature.^{7,6} As an initial step, the geometry was obtained, and optimised using DFT Plane Wave methods, using a PBE functional, norm-conserving pseudopotential, k-grid of 4 x 4 x 4, energy cut off of 30 Ry, and the BFGS method of optimisation.¹⁹⁻²² The electronic structure was then calculated using the same methods, with a finer k-grid of 12 x 12 x 12, and a K-path chosen to be compatible with the space group according to the work of Curtarolo et al.²³ Figure 4.2 contains the calculated electronic structure, which has a direct band gap of approximately 0.3 eV, which nicely fits with the literature value.

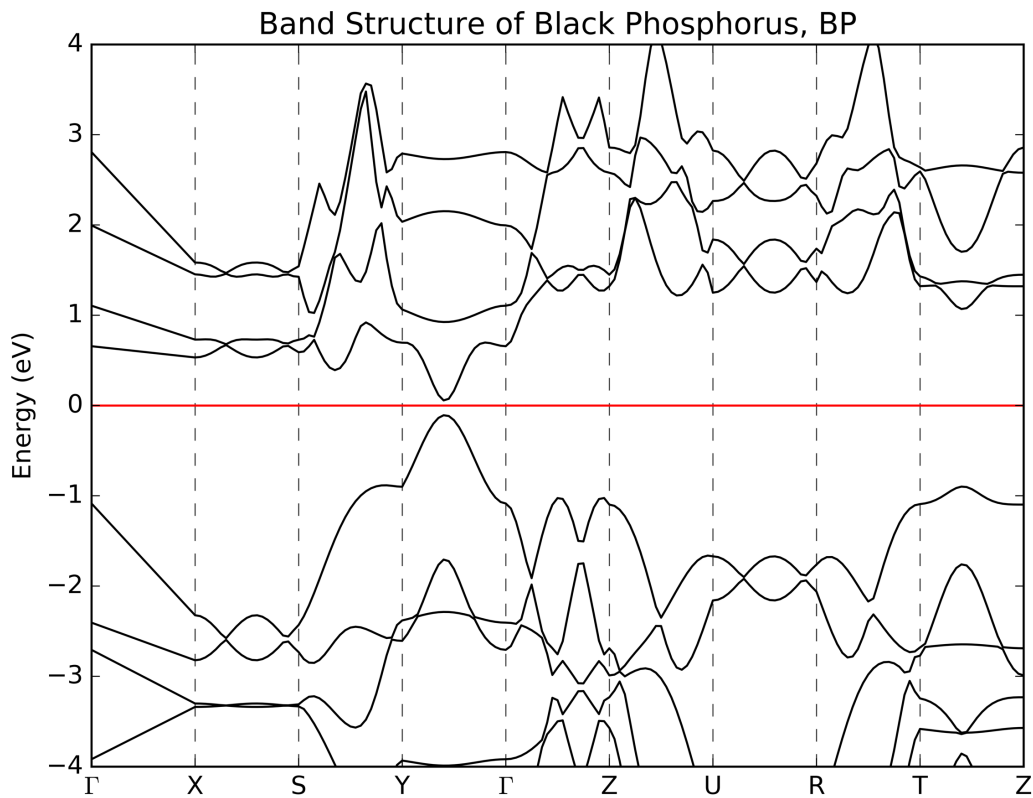


Figure 4.2 – The band structure of black phosphorus, calculated using quantum espresso plane wave code, a 12x12x12 k-grid and wavefunction cutoff of 30 Ry.

4.3 – ELECTRONIC TRANSPORT IN BLACK PHOSPHORUS THIN FILMS

Before working with bulk black phosphorus, a series of thin-film nanowires were created and used to model transport in single layered phosphorene. Each nanowire was built from a principle layer, PL, which consists of a supercell of 5 x 5 unit cells. These principle layers are large enough such that there are no interactions with identical atoms at distances larger than 2 principle layers. This section formed the initial work of the PhD, and was an opportunity to gain experience with the DFTB_NEGF software, as well as transport calculations, before building up to the bulk and then self-consistent calculations that would form the final stage of the project, which would be computationally expensive.

To build the wire, a script is used to replicate the principle layer in the specified direction, structuring the coordinate file such that the first portion of the file contains the data of the device region of the wire, while the second and third portions contain the atoms located within the source and drain respectively.

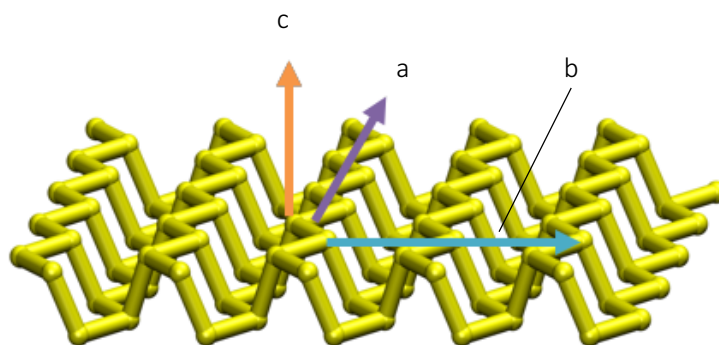


Figure 4.3 – Principle layer of mono-layer black phosphorus. The coloured arrows indicate each of three directions within the materials, along the corrugation within the plane (**a**), across the corrugations within the plane (**b**) and across the layers within the bulk materials (**c**).

Calculations were then performed for two BP nanowires constructed by replication of the original PL in each of direction *a* and *b*. Calculations were performed for a device consisting of 600 atoms, and within an energy range of -20 to +10 eV, with an energy step of 0.01 eV. Slater-koster files describing phosphorus-phosphorus interactions were obtained, and used to perform the dftb-negf calculation.^{31,32} The resulting transmissions were plotted as a function of energy as in Figure 4.5. The nanowires were considered to be clusters, that is, nanocrystals of finite size in free space, with no applied periodic boundary conditions.

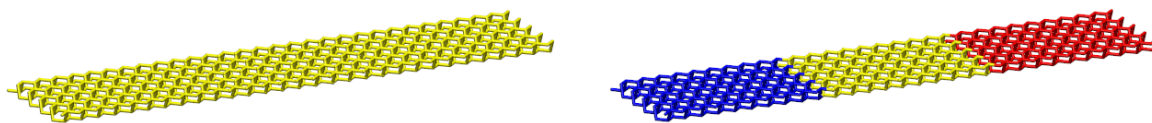


Figure 4.4 – Left: A nanowire of monolayer black phosphorus, replicated along the a direction. Right: Construction of the *device* as required by the DFTB_NEGF code, where the blue and red sections are the source and drain of electrons respectively, whilst the yellow middle section represents the device regions, which may be several times larger for later calculations.

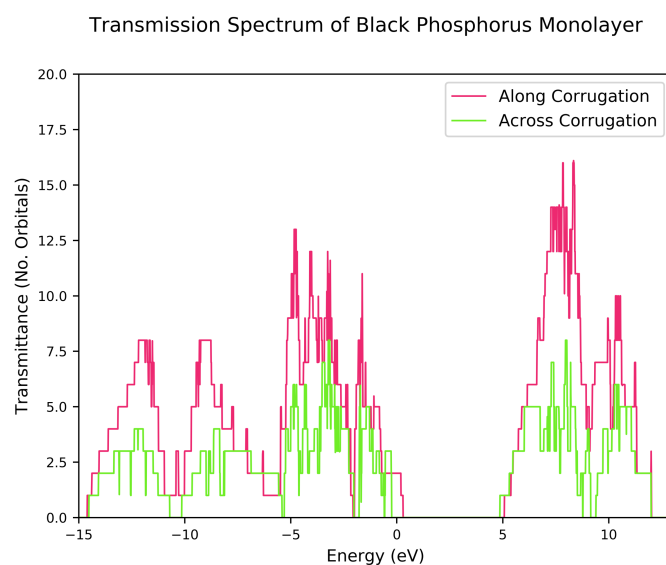


Figure 4.5 – Electronic transmission of a black phosphorus monolayer nanowire. The effect of anisotropy can clearly be seen as a difference in transmission and band gap. Calculated using dftb-negf, with a k-grid of $4 \times 4 \times 4$.

The most apparent difference in the transmission of each direction is that for direction a , the transmission is consistently almost twice that of b . This is an effect of the *anisotropy* within the crystal structure, or more specifically the lack of rotational symmetry describing the two directions within an extended lattice. This can be rationalised by considering the bonding within the layer, as there is clearly more directional overlap between atomic orbitals in a , whereas in b , the corrugation introduces a nonlinear bonding scheme, which may perturb the transport of electrons across the structure. It is interesting to note however, that for a given energy value, the transmission in a is not always exactly twice that of b . Moreover, the band gap of the material is actually direction dependent, and here we notice that the band gap for the projection along the corrugation is actually slightly narrower than that

of the perpendicular case, by approximately 0.5 eV. Another important observation for this material, is that the band gap of ~ 5 eV is significantly larger than the experimentally determined bulk black phosphorus band gap of 0.3 eV. The reason for this is two-fold: the band gap of black phosphorus is directly affected by the interlayer spacing as will be demonstrated in 4.6, whilst DFTB methods are known to over-estimate band gaps.¹¹

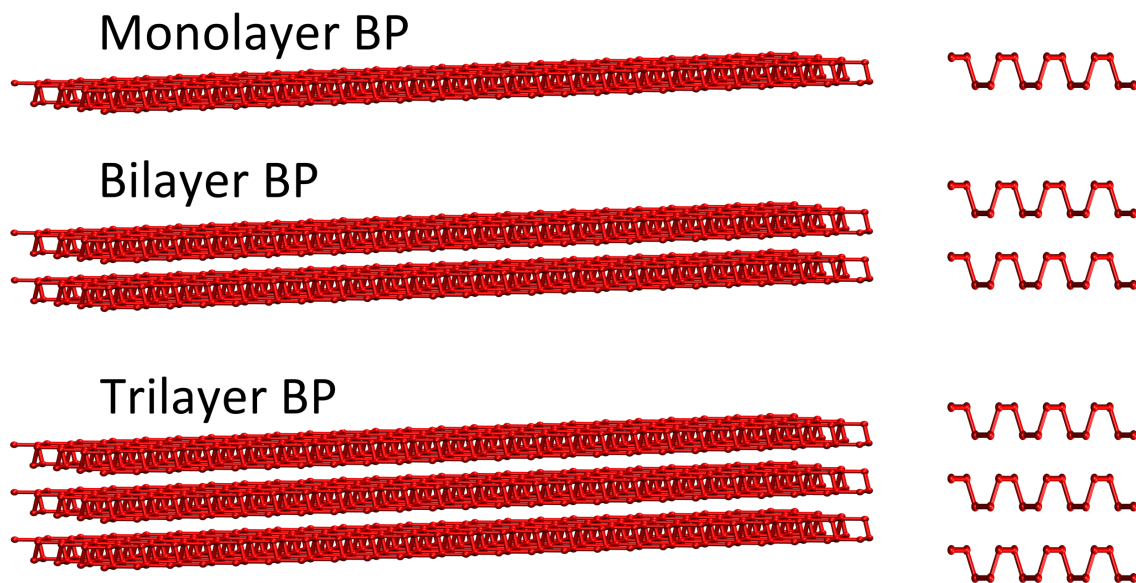


Figure 4.6– Representations of the Mono-, Bi- and Tri-layer nanowires of black phosphorus, shown here replicated along the **a** direction. The images to the left show each respective nanowire in its entirety, the images to the right show the profile along which the transmission was calculated. 6 such wires were created, to model transport along the **a** and **b** directions.

Progressively larger systems incorporating additional layers of black phosphorus were created to model the effect of increasing device thickness, or more specifically, the effect of the contribution of inter-layer orbitals to the electronic transport of black phosphorus thin films.

It should be noted, that for all calculations of electronic transport in this chapter, dispersion correction was not included. This is in part due to the calculations being extrapolated from those defined in the tutorial for the dftb-negf code, which did not include a dispersion correction. Additionally, DFTB does not include Van der Waals interactions, and so any attempted correction is purely empirical, requiring an additional set of parameters which had not been acquired for this work.

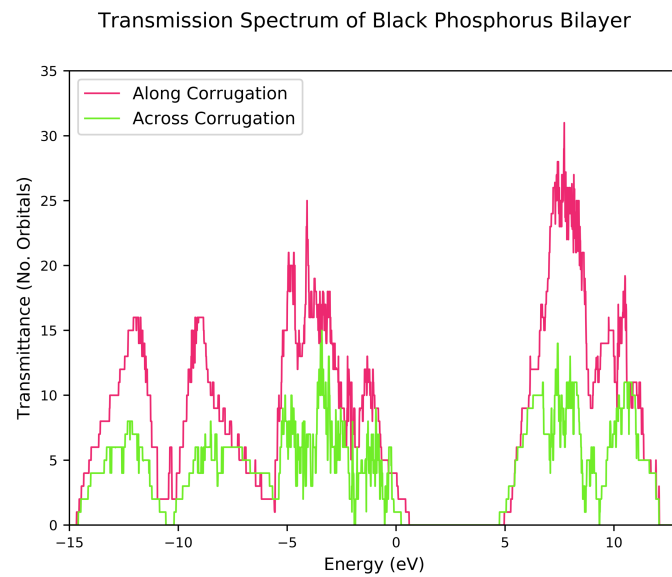
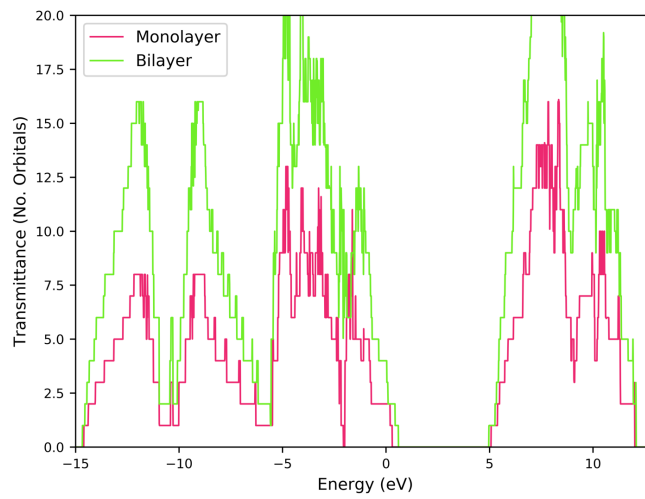


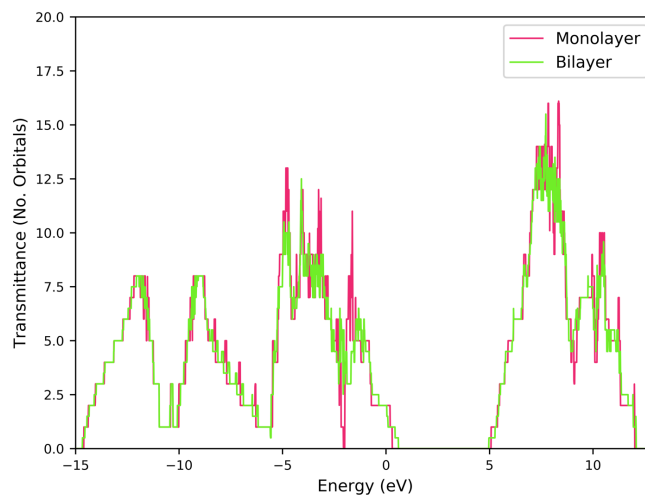
Figure 4.7 – Calculated transmission across directions **a** and **b** for the black phosphorus bilayer. Calculated using dftb-negf, with a k-grid of 4x4x4.

Transmission was calculated in each direction for a nanowire of bilayer black phosphorus containing 1200 atoms. As for the monolayer, transmission was largely greater in **a** than for **b**. The band gap was again slightly larger in **b**. Figure 4.8a shows the calculated transport along **a** for both the monolayer and bilayer. As expected, with twice the number of available orbitals, the transmission of the bilayer is almost twice that of the monolayer. However, the difference is not exactly a factor of two, and we can see from Figure 4.8b and 4.8c that by plotting the transmission of the monolayer versus the transmission of the bilayer over 2, that the difference (grey line in Figure 4.68c) is non-zero. This is due to the contribution of inter-layer orbitals towards the intra-layer conductivities, and as can be observed at the top of the valence band in Figure 4.8c, the contribution of these states close to the Fermi level is significant.

a) Transmission Spectrum of Black Phosphorus Thin Films



b) Transmission Spectrum of Black Phosphorus Thin Films



c) Transmission Spectrum of Black Phosphorus Thin Films

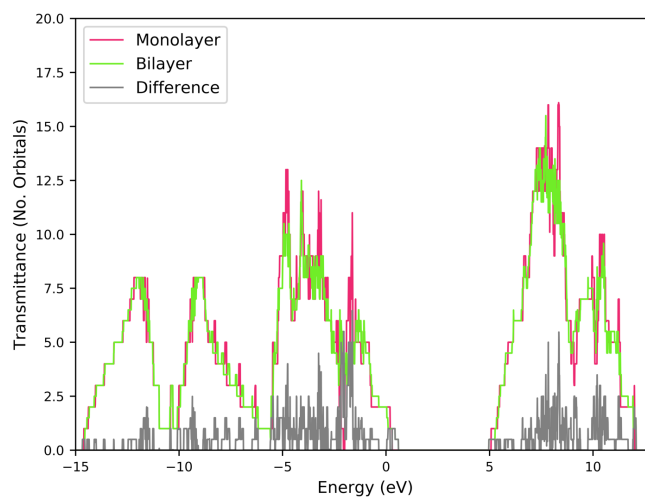


Figure 4.8 –Calculated transmissions across α for a) both the monolayer and bilayer, b) the monolayer and the transmission of the bilayer divided by 2, c) as in b, with the plotted difference. Calculated using dftb-negf, with a k-grid of 4x4x4.

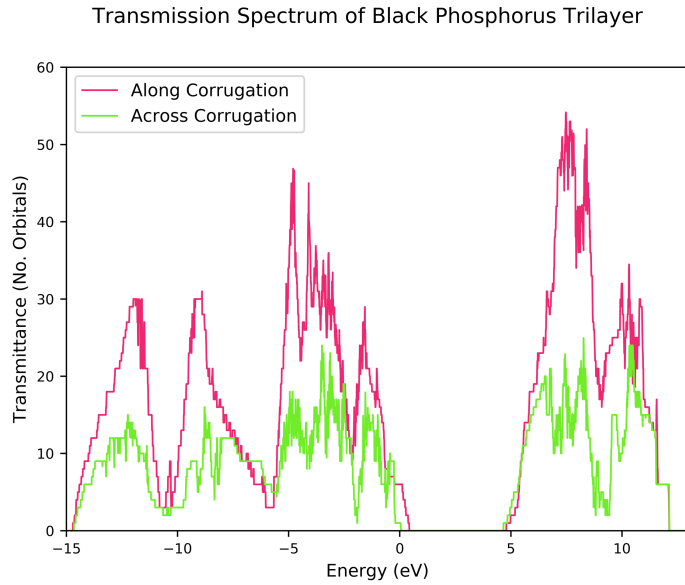


Figure 4.9 – Calculated transmissions across direction a and b for a nanowire of trilayer black phosphorus. Calculated using dftb-negf, with a k-grid of 4x4x4.

As we approach the bulk, we notice a softening of the step-function-like features of the transmission curves, notably in the case of figure 4.9, wherein the same trends with regards to anisotropy hold true. The band gap is smaller still, though still an order of magnitude larger than the experimentally determined value of 0.3 eV for bulk black phosphorus.

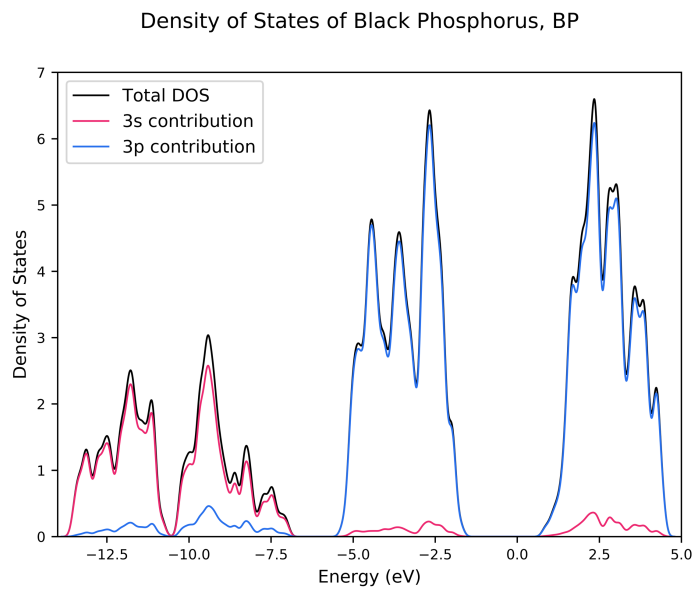


Figure 4.10 – Partial density of states of Black Phosphorus. Calculated using dftb+, code, with a k-grid of 8x8x8.

The structure of the transmission curves can be understood by comparison to the Partial Density Of States (PDOS) of bulk black phosphorus. As seen in Figure 4.10, the lower energy orbitals are mostly of s orbital character, whereas the higher energy portion of the graph consists of p orbital character, with the p orbitals below the Fermi level, and the p* orbitals above. From this comparison, it is clear that the states about the Fermi level of the transition curves correspond to the contribution of p-orbitals to the transmittance, and we shall see that it is the p-orbitals that dominate the description of the thermoelectric properties of black phosphorus and its intermediates.

The main difference between the transmission function and the density of states, is that the transmission function, $T(E)$, corresponds to the rate at which electrons travel across the device region. $T(E)$ is simply a coefficient from which an electric current, I , may be derived, from knowledge of the dimensions of the nanowire. The density of states represents the number of electronic states, per energy interval, which may be occupied. The higher the density of states at each energy interval, the higher the electronic transmission function for the same energy interval. The Fermi level is in the same position, or should be, for each of $T(E)$ and DOS, as it represents the interface between the occupied and unoccupied electronic states, i.e. it is the energy at which the relevant states have a 50% probability of being occupied at any time. This position therefore, is a function of the electronic structure of a material, and independent of the transmission or density of states.

4.4 – ELECTRONIC TRANSPORT IN BULK BLACK PHOSPHORUS

Using similar methods, the electronic transport of bulk black phosphorus was then calculated, using a nanowire consisting of 4 atomic layers, and 3840 atoms with applied periodic boundary conditions in the x and y directions, such that the transmission can be considered to be across a semi-infinite slab.

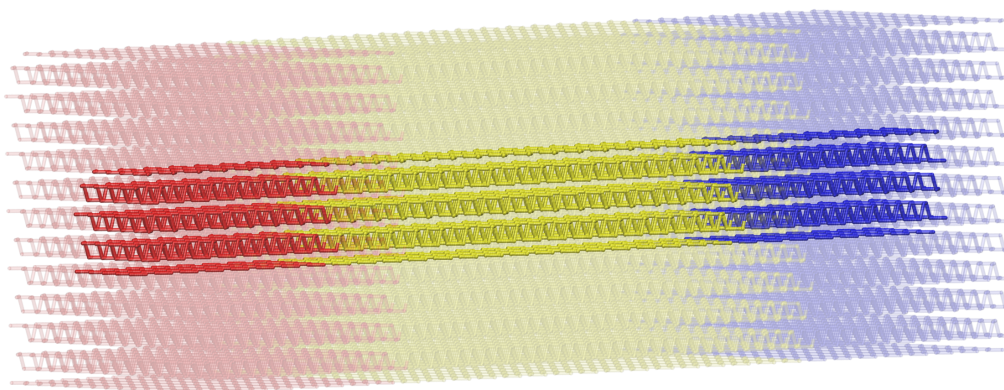


Figure 4.11 – An example of a bulk device, the boldly coloured region is the constructed device, the transparent surrounding region represents the periodic boundary conditions applied within the calculation for bulk systems. The periodicity is applied in the x and y directions, whereas transport is calculated along z (the length). The red, yellow and blue regions illustrate the source, device and drain respectively.

As can be seen in Figure 4.12, the trends such as band gap reducing, and anisotropic transmission continue, with the latter resulting in a third and final directionality to the bulk calculations, as the transmission *across the layers* (out of plane transport) is now possible. Transmission along this direction was considered to be meaningless for nanowires systems, as the weak intermolecular forces, such as Van der Waals effects, allow for exfoliation of the “phosphorene” sheets that make up the structure. This is a proven method of preparing thin layers of graphene and phosphorene, and would allow for the synthesis of such nanowires with “in plane” transport properties. However, this also has consequences for the practical synthesis of nanowires with long range order in the *c* or *across layers* direction, as any attempt to create these nanowires would likely cleave the weakly bound layers. As such, study of electronic transport along this direction has previously been neglected.

As predicted, the out of plane transport is significantly weaker than the in-plane, and this is again rationalised by the weaker orbital overlap between layers. As we have seen previously, the lone pair orbitals responsible for the inter-layer bonding also contribute to the intra-layer transmission, and so it is in the bulk that these contributions are at their maximum.

Transmission Spectrum of Black Phosphorus (Literature Values), BP-LV

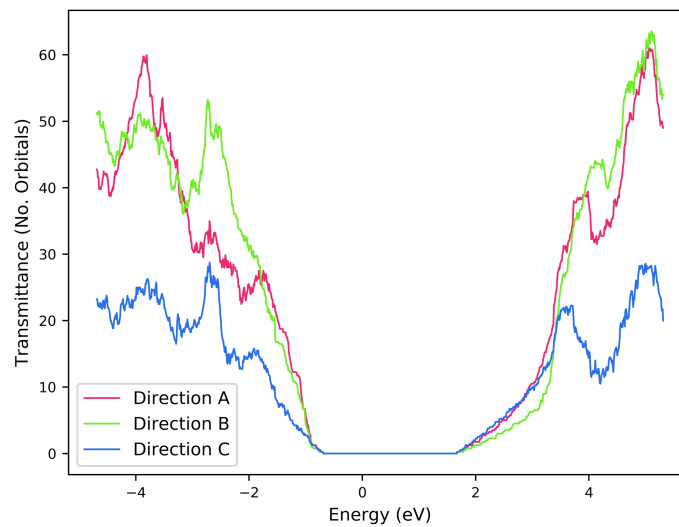


Figure 4.12 – Calculated transmission of bulk black phosphorus. Direction *C* is the previously uncalculated *across layer* transmission, and is notable weaker than the in-plane transmission. Calculated using *dftb-negf*, with a *k*-grid of 4x4x4.

One important observation from figure 4.12, is that whilst the transmission along *c* is clearly weakest in general across the whole energy range, the contribution at the bottom of the conducting band is the largest, which would lead to interesting effects, as we shall see in 4.6.2.1. Here however, the Fermi energy is clearly closer to the edge of the valence band, and so one would expect the transmission of the intra-layer directions to dominate the electronic properties of this model of black phosphorus.

With the calculated anisotropic electronic transmission of black phosphorus, the thermoelectric properties may now be derived, according to the Landauer-Büttiker formalism, wherein the electronic conductivity is obtained directly from the transmission and volume of the device region. The Seebeck coefficient is obtained from the transmission and conductivity, and is independent of the volume, while the electronic contribution to the thermal conductivity is dependent on each of the prior coefficients and is again derived from the conductance and the volume of the device region. Figure 4.13 shows the calculated temperature dependent thermoelectric properties of black phosphorus.

Immediately apparent, is that both the electronic conductivity, σ , and the electronic contribution to thermal conductivity, k_e , are rather small compared to the values often reported in the literature for the state-of-the-art in thermoelectric materials.²⁴ This is to be expected, as black phosphorus is a semiconductor, thus the conductivity can be defined as a function of the band gap and the width of the first derivative of the Fermi function, which is temperature dependent. As such, one would expect the conductivity to scale exponentially with temperature, at least in the absence of scattering mechanisms such as electron-phonon coupling, which was not accounted for in this study and so would be a prime candidate for further study. As DFTB methods are widely known to overestimate band gaps, the band gap of black phosphorus in this model is notably larger than that expected from both theoretical calculations and experimental evidence. Therefore, the conductivity and electronic thermal conductivity are lower than expected.

Conversely, due to the inversely proportional relationship between conductivity and Seebeck coefficient, the Seebeck coefficient is an order of magnitude larger than that commonly reported in the literature for high-performance systems. This is attributed to the reduced carrier mobility in the large band gap model of black phosphorus. As the Seebeck coefficient is large, the power factor, which is proportional to the square of the Seebeck coefficient, would be expected to be rather large also. However, since the electronic conductivity is approximately 3 to 4 orders of magnitude lower than for reported thermoelectric systems, the power factor is clearly dominated by the poor electronic conductivity in this system, as can be seen from the positive exponential nature of the power factor in figure 4.13.

The electronic contribution to the thermal conductivity is also significantly smaller than would be expected, as the thermal transport phenomena of this contribution necessitate the flow of electrons as carriers of kinetic energy; the magnitude of which is clearly weak in this system. Consequently, the zT_e reported in figure 4.13 is unexpectedly large for black phosphorus.

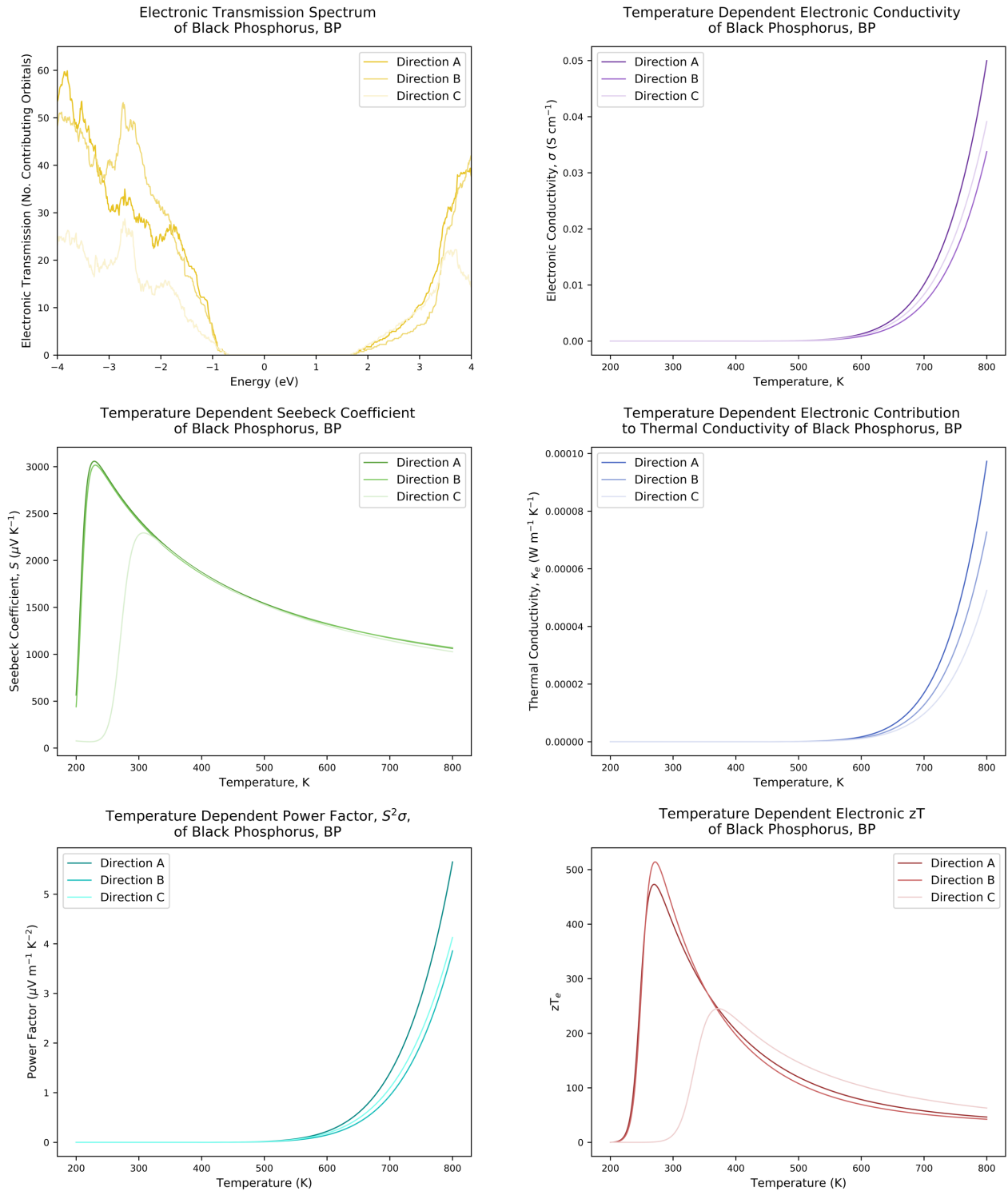


Figure 4.13 – The thermoelectric properties of black phosphorus. Top left: electronic transmission spectrum of black phosphorus. Each of the following thermoelectric coefficients is derived exclusively from this transmission, in accordance with the Landauer-Büttiker Formalism. Top right: electronic conductivity, middle left: Seebeck coefficient, middle right electronic contribution to thermal conductivity, bottom left: power factor, bottom right calculated zT_e . Transmission calculated using dftb-negf, with a k-grid of 4x4x4. Thermoelectric coefficients derived using program (see section 3.5), each series contains 6000 points.

To explain this high zT_e , we must once again appreciate that in this model, electronic structure describes black phosphorus as a large band gap semiconductor. Thus, the thermoelectric properties would be expected to reach their respective optima at higher temperatures. zT_e is the *electronic figure of merit*, and is therefore highly band gap sensitive; it does not consider the contribution of the lattice phonons, k_l , to the total thermal conductivity of the system, k or k_{tot} . For a large band gap semiconductor, the thermal conductivity of the electrons is significantly lower than the average reported in the literature, by several orders of magnitude, while the reported values of k_l are rather large, of the order of $10^2 \text{ W m}^{-1} \text{ K}^{-1}$. The predicted zT would therefore be expected to be 5 orders of magnitude lower than the zT_e for pure, undoped bulk black phosphorus, i.e. of the order of 10^{-3} for this system. This is now lower than expected, and the rationale is that the large band gap yields such a poor power factor, of the order of 10^{-6} rather than $10^{-4} \text{ W m}^{-1} \text{ K}^{-2}$. This would therefore give a zT of the order of 10^{-1} , which seems reasonable for black phosphorus.

Interesting to note is the effect of anisotropy in the transmission spectrum on the thermoelectric properties. We have seen that the transmission along c is lower on average than that of the intra-layer transmissions, however, the electronic conductivity of direction c is higher than that of b . This can be explained by noting that the transmission across c is marginally higher than that across b in the immediate area of the valence band edge.

Interestingly, the anisotropy manifests within the Seebeck coefficient at lower temperatures, as being distinctly lower for c than both a and b . This is an effect of the *gradient* of the transmission about the Fermi level. Importantly, while the shape of the conductivity defines the shape of the power factor, it is the Seebeck coefficient which impacts the shape of the zT_e curve, and this is due to the nature of the σ / k_e term in the figure of merit. Effectively, the exponents cancel negate one another, and the contribution of this term is then the linear relationship between the ratio of $\sigma : k_e$.

4.5 – EFFECT OF PRESSURE ON THE BAND STRUCTURE OF BLACK PHOSPHORUS

As seen in the previous section, the band gap of ~ 2.5 eV attained for the bulk black phosphorus was up to an order of magnitude larger than the expected band gap of 0.3 eV – 1.5 eV from experimental work and previous calculations in the literature.^{6,7} It was determined that the parameter set used by the DFTB code may not properly describe the effect of Van der Waals bonding between phosphorene layers, thus overestimating the band gap. This is justified by the published band gap of 1.5 – 2.5 eV for atomically thin films of phosphorene by both theory and experiment, suggesting that the layers in our black phosphorus system were not close enough to be strongly interacting.

To investigate whether this band gap could be reduced as a function of the inter-layer spacing, the following study was performed on frozen structures based on DFT optimised black phosphorus, with progressively smaller inter-layer gaps. As the DFTB parameters obtained evidently describe the inter-layer interactions somewhat poorly, it was decided that since the geometry had been optimised, the covalent bonding within the layers was likely described well, since the band gap and band structure are comparable to those for thin films of black phosphorus. As such, an investigation into the effects of reducing the inter layer spacing was undertaken, to study the effect of anisotropic pressure on the electronic structure of the system.

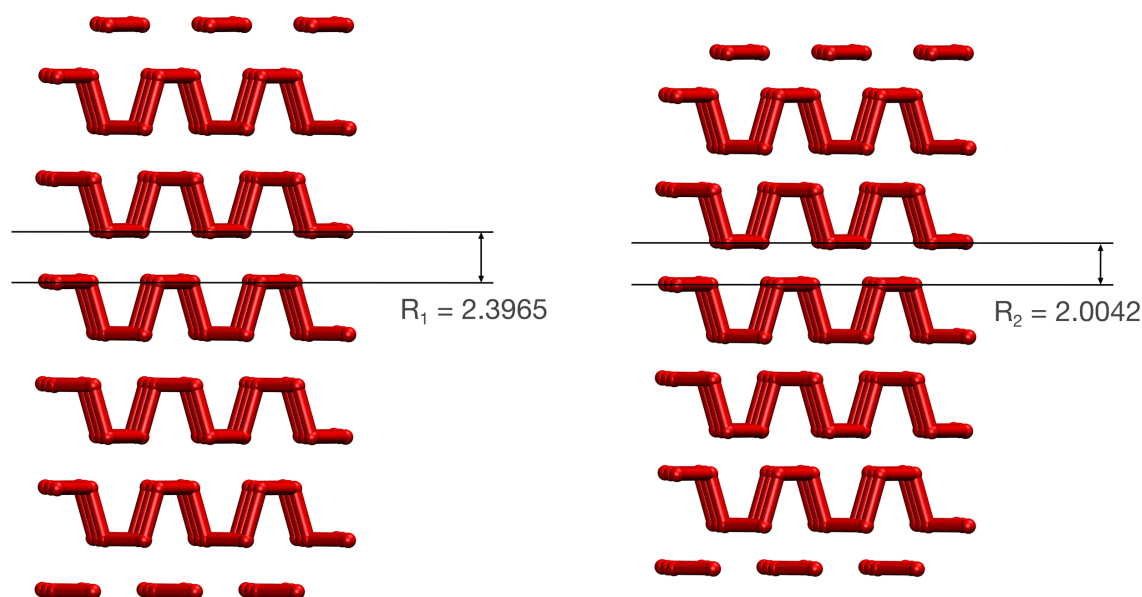


Figure 4.14 – The effect of compression in the *c*-axis on the DFT optimised black phosphorus structure. The “phosphorene layers” are treated as static sheets, and the inter-layer spacing is reduced in a coarse attempt to account for the poorly described molecular forces in the DFTB parameters for phosphorus.

As shown in Figure 4.15 the band gap decreases with the inter layer spacing, until the gap approaches that of the experimental literature, at a spacing of 2.00 Å. The first reduction of the band gap results in little change in the magnitude of the band gap, the main feature of this step is the lifted degeneracy of the conductance band at Γ , where the valence band has become partially degenerate. For each additional decrease, the degeneracy decreases for all bands within the vicinity of the Fermi level, and eventually the bands “kiss” at a spacing of 1.994 Å resulting in a metallic system.

Taking the band spectra and structure of figure 4.15c, we see that the band gap is a more acceptable 0.5 eV, whilst the electronic structure is arguably comparable to that of black phosphorus obtained by a DFT level of theory. This structure was then termed *Compressed Black Phosphorus*, CBP, and used in the next stage of study. The transmission spectrum of compressed black phosphorus is plotted in figure 4.16, and we see that the band gap of the electronic structure is observed in the transmission in its strictest sense, though the gradient at the band edges is rather shallow, which is likely due to the diffuse nature of the bands in the compressed band structure.

The energy range for the calculation was kept deliberately small, so that only the window about the Fermi level is considered. As in section 3.8, the temperature dependent equations for the thermoelectric coefficients are heavily restricted by the first derivative of the Fermi function, meaning that a full calculation of the transmission for all valence orbitals is not necessary to attain a meaningful zT_e for the material, which is the goal of this section.

One immediate observation is that the compression in the c-axis has perturbed the effect of anisotropy on the transmission spectrum. While in Figure 4.12 the largest transmission in bulk black phosphorus is obtained along the corrugation of the material, henceforth known as *direction a*, for the compressed black phosphorus the distinction is not so apparent. In fact, here the transmission in each direction is almost equivalent for the unoccupied conductance band to the right of the band gap, whereas for the valence band to the left of the band gap, direction *a* and *b* offer similar transmittance. Direction *c*, formerly *across the layers*, has overtaken direction *a* as the highest transmitting. This obviously introduces a small flaw into the compressed model of black phosphorus, and steps would need to be taken to ensure that any spurious result as a consequence of this would be accounted for.

The Effect of Uniaxial Compression on the Band Spectrum of Black Phosphorus

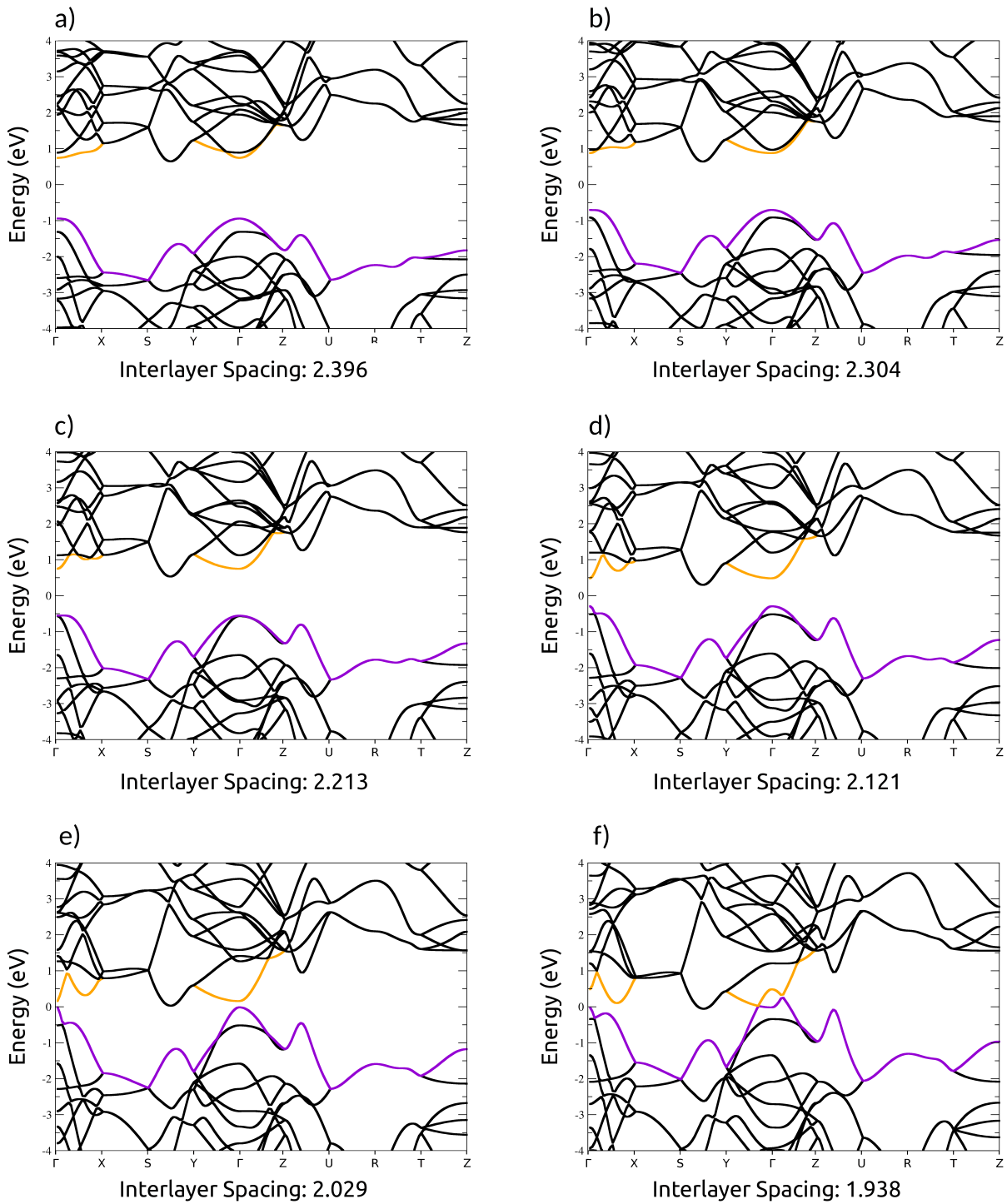


Figure 4.15 – The effect of reduced inter-layer distance on the band gap of black phosphorus. The band gap is demonstrably tuneable by the interlayer distance, and this methodology was used to achieve the *Compressed* Black Phosphorus, CBP. Interlayer spacing is in Angstroms, Å. Calculated using dftb+, with a 12x12x12 k-grid.

This simple study allowed for the investigation of the effects of anisotropic pressure on black phosphorus, and whilst it may be considered a rather coarse approach, the literature appears to support the notion that the band gap of black phosphorus is tuneable by the inter-layer spacing, and that under isotropic pressure, it is the c axis that experiences the most dramatic alteration at low pressures. This can be conceptualised by considering the inter-layer bonding to be “soft” compared to the “hard” covalent intra-layer bonding scheme, though it should be noted that the large compression in c observed in this investigation is not representative of the forces involved in the DFT derived structure. This is due to the DFTB parameters obtained for phosphorus apparently describing the covalent interactions well, and the Van der Waals forces poorly.

Transmission Spectrum of Black Phosphorus (Compressed), BP

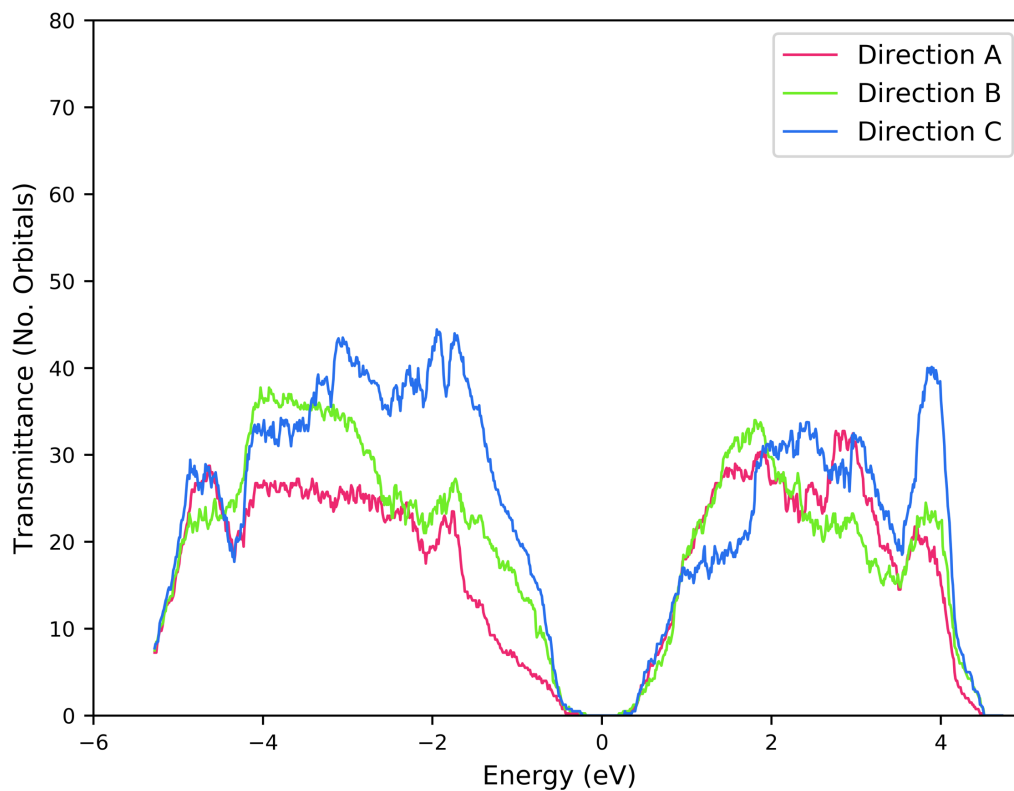


Figure 4.16 – Transmission Spectrum of the new “Compressed” Black Phosphorus, CBP. Calculated using dftb-negf, with a k-grid of 4x4x4.

4.6 – HIGH PRESSURE PHASE TRANSITIONS – THE EFFECT OF PRESSURE ON THERMOELECTRICITY

So far, we have seen the use of DFTB methods and the Landauer-Büttiker formalism to derive the thermoelectric properties of black phosphorus, along with a simple investigation into the effect of pressure on its electronic structure. This simple study indicated that in an isolated system, with anisotropic pressure and ignorance of the structural rearrangements and possible structural phase transitions, one may observe an electronic phase transition at high pressures. We have seen, that this methodology is computationally demanding and expensive. The work until now had been carried out with the express intention of utilising the key feature of this methodology, the ability to efficiently calculate transport properties for a system of thousands of atoms, so as to model the asymmetric systems which occur along the transition pathway of the structural phase transition. This subchapter introduces the novel concepts used to model these properties, and investigates the impact of coinciding structural and electronic phase transitions on the thermoelectric properties of phosphorus materials.

4.6.1 – PHASE TRANSITIONS IN BLACK PHOSPHORUS

As we have seen, black phosphorus is known to undergo a phase transition at 5 GPa, adopting the geometry of α -Arsenic, and this phase is referred to as Grey Phosphorus, GP.^{9,16,25} It has been demonstrated that pressure can significantly affect the electronic structure of black phosphorus. Topological defects, such as grain boundaries or dislocations are known to be beneficial in many thermoelectric materials, as a means of controlling thermal transport properties by scattering phonons. During the phase transition, the start and end points, i.e. black phosphorus and grey phosphorus, are highly symmetric crystalline structures. However, the phase transition is known to process along a pathway that forces the system to adopt several metastable, asymmetric intermediates.⁹

The key concept for the next subchapter, was the hypothesis that a large, asymmetric system may act as a phonon glass, yet if the electronic structure could remain semiconducting, it could be considered to obey the phonon-glass electron-crystal concept of Slack.^{1,26,27}

The concept of critical phenomena, where the electron-phonon coupling results in significant increases in thermoelectric properties, is a legitimate means of affecting the thermoelectric figure of merit, zT .^{28,29} additionally, the effect of a structural phase change has been shown to be beneficial to the zT of SnSe.³⁰ With this in mind, the rich phase space of the BP to GP phase transition began to unfold, as

both an electronic and structural phase change were known to occur simultaneously. If the electronic and structural phase transitions could be uncoupled, is there scope for an asymmetric phosphorus material, with perturbed thermal transport and a larger power factor to be realised? The middle image of figure 4.17 illustrates the sought material.

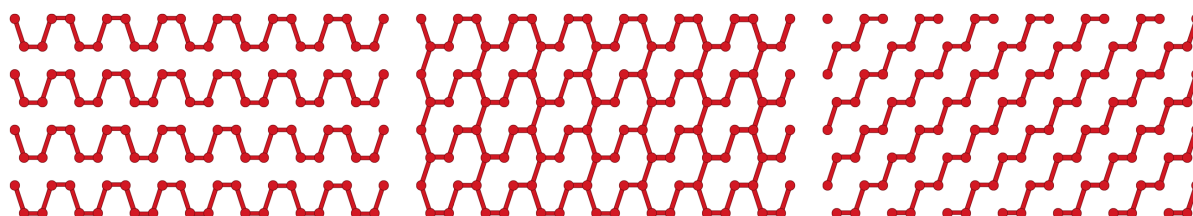


Figure 4.17– Graphic representation of the high-pressure phase transition of black phosphorus. Left: black phosphorus, middle: highly symmetric intermediate, right: grey phosphorus. N.B. this image is a purely illustrative, and is not to scale.

Initially, to test the method, a frame from an arbitrary point in the BP – GP phase transition was taken, in the form of Cartesian coordinates. This geometry was then orthogonalised, as variable cell conditions had been allowed (and necessary) for the Transition Path Sampling (TPS) simulation in which it was generated. The Non Equilibrium Green’s Functions formalism as implemented in the DFTB methodology calculates transport explicitly in whichever arbitrary direction is set to z , and so one of the requirements of a “wire” built for the code is that it must be orthonormal. With this cell symmetry enforced, the structure was then optimised by performing a CG relaxation, and enforcing symmetry. This resulted in the highly symmetric Intermediate Phosphorus 1, IP1, which is shown in figure 4.18 top middle, and which is clearly similar to the theorised intermediate represented by Figure 4.17, in that it has mostly BP geometry, with several channels of bonds formed across the BP layers.

Due to the variable cell conditions of the previous work that these structures had been generated from, it was necessary to “enforce” orthogonality on the phosphorus intermediates of this chapter. For IP1, this was achieved by the aforementioned “aggressive optimisation”, wherein each of the 6 minor ($<10\%$ of $alat$) values in the cell matrix specifying the cell vectors were set to zero, leaving 3 orthogonal cell vectors. This geometry was then re-optimised, using variable-volume but fixed-angle cell conditions, yielding IP1. This resulted in a geometry that had been forcibly achieved, which is believed to be the reason for the semi-metallic nature of the transmission of IP1.

To determine the electronic structure of the materials of interest so far, we had used band spectra and density of states. Both, calculations are routine and somewhat trivial for the case of unit cells with less than 10 atoms, however, the unit cell describing the IP1 structure contained 144 atoms, and despite being somewhat symmetric, it was deemed too large to calculate a full band spectrum for this material. This was due to the computational expense of calculating a band structure with a fine k-point sampling (at least an 8x8x8 grid), and 576 orbitals (144 atoms x one 2s and three 2p orbitals). Therefore, for the large systems in the rest of this chapter, it was deemed acceptable to derive the band gap from the calculated density of states.

Upon calculating the density of states, intermediate phosphorus 1 was found to be metallic, with no band gap, (see Figure 4.19 top right DOS of IP1). This was not unexpected, as it was hypothesised that the electronic phase transition would occur during the structural phase transition, however, it was hoped that there would be an intermediate which could be metastable, with a small yet distinct band gap. This is due to the belief by the thermoelectric community that a metal makes a poor thermoelectric material, as the electronic conductivity is high, though the Seebeck coefficient suffers as a direct consequence, and the thermal conductivity would be expected to be detrimentally high.

As such, 3 more frames were taken from the transition pathway, at evenly spaced points along the structural phase transition trajectory obtained in previous work by Leoni et al., and were also optimised and orthogonalised.⁶ This was achieved in a “gentle” fashion, by allowing the atomic positions to relax between subsequent, minor alterations to the angles of the unit cell, resulting in 3 orthorhombic cells with increasing grey phosphorus character.

For IP2, IP3, and IP4, this issue caused by the “aggressive optimisation” was addressed via the aforementioned “gentler optimisation”. This entailed a series of consecutive optimisations, wherein each of the minor values of the cell matrix were reduced, in turn, by 20% and re-optimised under variable-volume, fix-angle conditions before further reduction, until the cell was orthorhombic. This is believed to be the cause of the dissimilarity between the transition spectra of IP1, and the set of IP2-4.

Intermediate 2 (See figure 4.18, top right) is unique in that it has 3 dimensional disorder. As can be seen from the other structures, all others have domains of black and grey phosphorus within them, along one direction (left to right in this image). The domains are planar, and the material is periodic in the x and y directions (here, up and down, and through the plan of the page). For IP2, there is bond formation and breakage in each direction, although each atom has the same coordination and hybridisation as each atom in pure black or grey phosphorus. In fact, this geometry strongly resembles that predicted by Wang et al., otherwise known as Phosphorus K4.³³

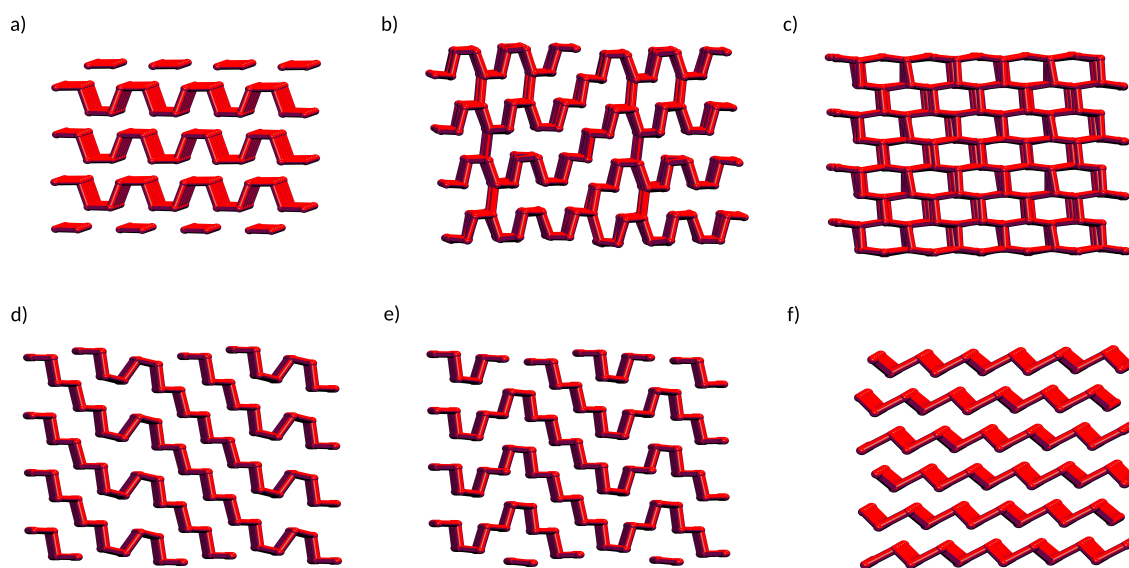


Figure 4.18 – Optimised and orthogonalised structures from the pressure induced phase transition of black phosphorus. Top left: Black Phosphorus, top middle: IP1, top right: IP2, bottom left: IP3, bottom middle: IP4, bottom right: Grey Phosphorus.⁶

Intermediate Phosphorus 3 and 4 both have clear domains of BP and GP, with IP3 possessing larger BP domains. Both structures have a truly unique disrupted quasi-planar geometry of stacked phosphorene derived sheets, with IP4 having a largely folded geometry, which looks to reduce a degree of freedom in the dislocation of the phosphorene sheets.

Density of states calculations were performed for each of the six structures using DFTB methods, the results of which are presented in Figure 4.19. Each DOS has been scaled by the number of atoms present in the unit cell of the calculation to yield comparable densities. This was to account for the number of atoms required to model the unit cell of each phosphorus intermediate (576 atoms each for IP2, 3 & 4), which was largely due to the lack of symmetry.

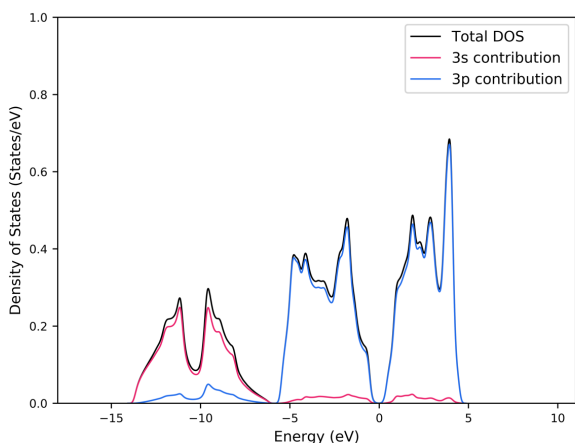
As can be seen, the Compressed black phosphorus has the most “black phosphorus-like” shape, which is clearly comparable to the DOS of bulk black phosphorus with no compression (see figure 4.10). Intermediate phosphorus 1 has the most striking shape, in that it appears “noisy”, and that it is metallic, with a minimum DOS off-centre from the Fermi level. For IP2, IP3 and IP4, the zero density, or minimal density occurs at the Fermi level, as with grey phosphorus. As the structure becomes more GP-like, the DOS flattens and widens, with less sharp features. Also of interest, for IP2, IP3 and IP4, the right-hand lobe of the 3s orbitals has two distinct maxima, whereas BP and GP have only one.

IP1 is clearly a unique case, and this is rationalised as being an artefact of the methods used to optimise the structure. Ignoring IP1, as the trajectory moves from BP to IP2 through IP4 and then to GP, the band gap visibly reduces, up to a point in IP4 where it is at its minimum: there is a node in the density at the Fermi energy, and the gap is of the order of 1×10^{-2} eV.

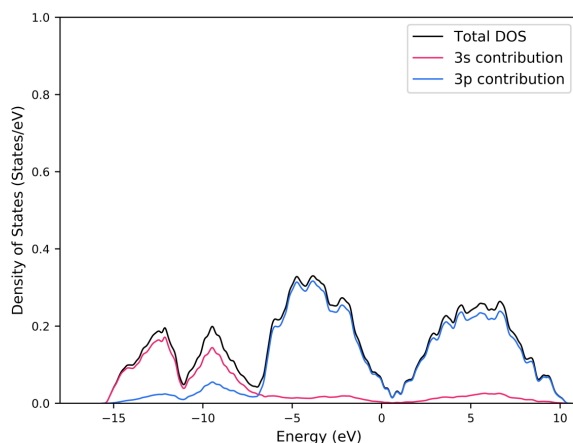
Structure	Pressure		Volume		Number of Atoms	Fermi Energy eV
	au	pa	au	per atom		
CBP	7.07E-04	2.08E+10	4.53E+04	1.41E+02	320	-3.71E+00
IP1	1.27E-03	3.72E+10	1.76E+04	1.22E+02	144	-3.34E+00
IP2	1.42E-03	4.17E+10	6.97E+04	1.21E+02	576	-2.65E+00
IP3	8.36E-04	2.46E+10	6.97E+04	1.21E+02	576	-2.34E+00
IP4	1.41E-03	4.15E+10	6.97E+04	1.21E+02	576	-2.07E+00
GP	3.10E-03	9.11E+10	3.72E+04	1.03E+02	360	-1.57E+00

Table 4.1 – the trend data from the BP to GP phase transition. Note the increasing Fermi energy and decreasing volume per atom.

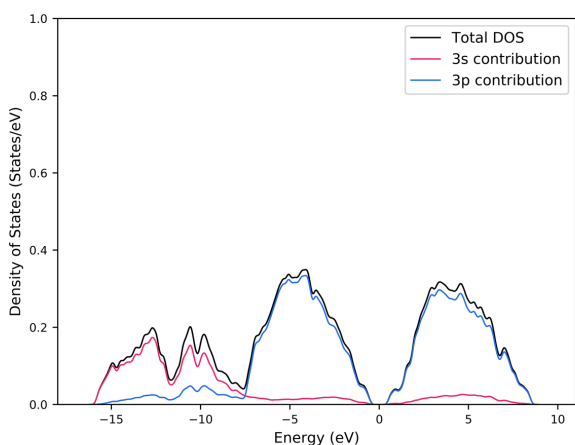
Density of States (States/eV) of Compressed Black Phosphorus, CBP



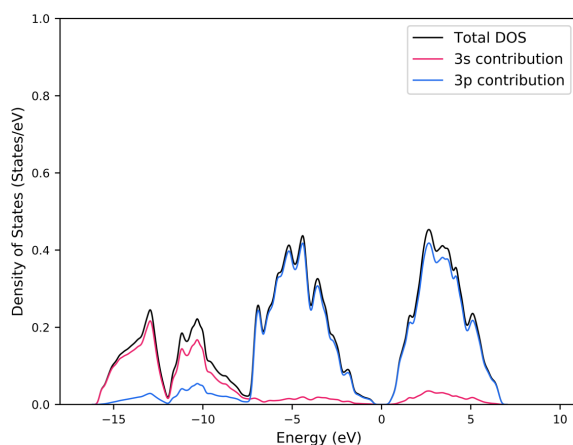
Density of States (States/eV) of Phosphorus Intermediate - 1, IP1



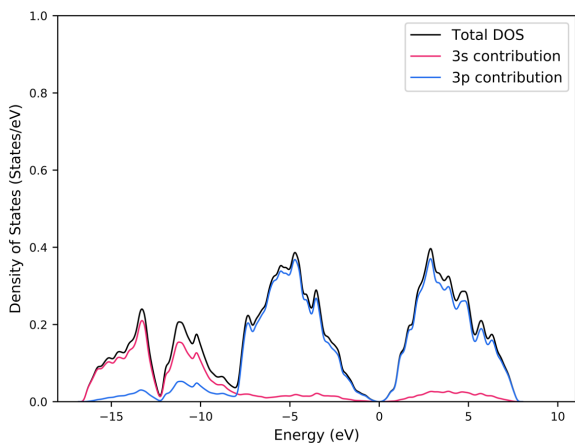
Density of States (States/eV) of Phosphorus Intermediate - 2, IP2



Density of States (States/eV) of Phosphorus Intermediate - 3, IP3



Density of States (States/eV) of Phosphorus Intermediate - 4, IP4



Density of States (States/eV) of Grey Phosphorus, GP

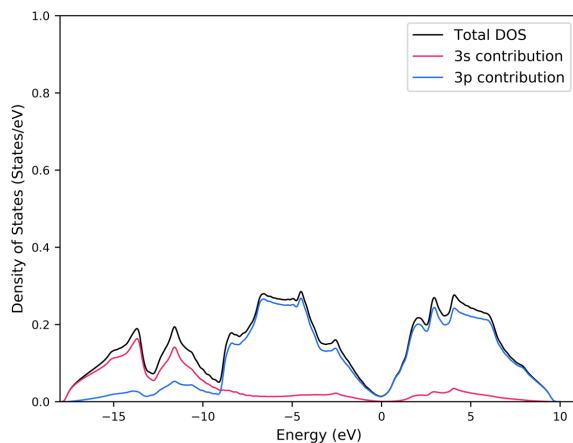


Figure 4.19 – Density of states for black phosphorus, grey phosphorus, and each structural intermediate along the transition pathway. Each DOS has been normalised to account for the differing number of atoms in each calculation. As such, the DOS presented is the effective DOS for a single atom. Calculated using dftb+ code, with a 12x12x12 k-grid for CBP & GP, and an 8x8x8 kgrid for IP1, IP2, IP3 & IP4 due to size constraints.

Table 4.1 shows the data from each structure within the phase transition, and some interesting trends are observed. First, the volume per atom of GP with respect to the BP geometry is significantly less, reduced by almost a third. The volume per atom for each of the intermediates falls roughly halfway between the two, which is unsurprising considering each contains approximately half BP domains, half GP domains. This reduction in volume is likely part of the driving force for the atomic rearrangement at high temperatures, and is largely due to the reduced spacing between layers in the GP structure. In fact, both BP and GP geometries may be thought of as “distorted rock salt” structures, in the sense that both can be modelled from cleaving the rock salt structure in either the 100 or 110 plane. As a matter of fact, cubic phosphorus is predicted to exist at pressures greater than 10 GPa.

Another interesting trend is the increase in Fermi energy as the transition trajectory moves from BP to GP. This is likely due to the “spreading” of the density of states, and the rise in energy of the valence orbitals associated with reduced atomic spacing. The pressure has a similar trend in that it increases along the trajectory, although that of IP3 appears somewhat anomalous. This pressure was calculated during the optimisation of each geometry by DFT methods.

Figure 4.20 contains the electronic transmission spectra for compressed black phosphorus, grey phosphorus, and each of the 4 intermediates. As for the density of states, we see a clear reduction in the band gap as the transition progresses, and a softening of the gradient of the transmission at the band edges, which are steep in the transmission of black phosphorus and progressively shallower in the intermediates (again excluding IP1). As noted in sections 4.1.1 and 4.2, the band gap of bulk black phosphorus is experimentally determined to be 0.3 eV.^{7,6} we have overestimated the band gap, as addressed in section 4.5, which has been compensated for by alteration of the structure of Black phosphorus, yielding compressed black phosphorus, used in Figure 4.20. We note that at the Fermi level, the transmission along each direction is largely similar, and that of direction *c* is in fact the largest for CBP, IP3 and IP4. This is thought to be due to the compression greatly affecting axis *c* and introducing bonding channels along this axis, as observed in the paper by Leoni et al.⁶ For GP, the transmission in direction *c* is again the weakest, and this is likely due to the lack of bonding between layers in the *c* direction. The transmission of IP1 is the odd one out, and exception to each of the trends previously described. This is thought to be a result of the aggressive optimisation used for this test structure, which may have resulted in frustrated atomic coordination's as a result of the enforced symmetry.

The concept of phase transitions and metastable intermediates has been introduced, and the anisotropic electronic transmission spectra have been calculated for each of our model systems. The next subchapter details the derivation of the thermoelectric properties.

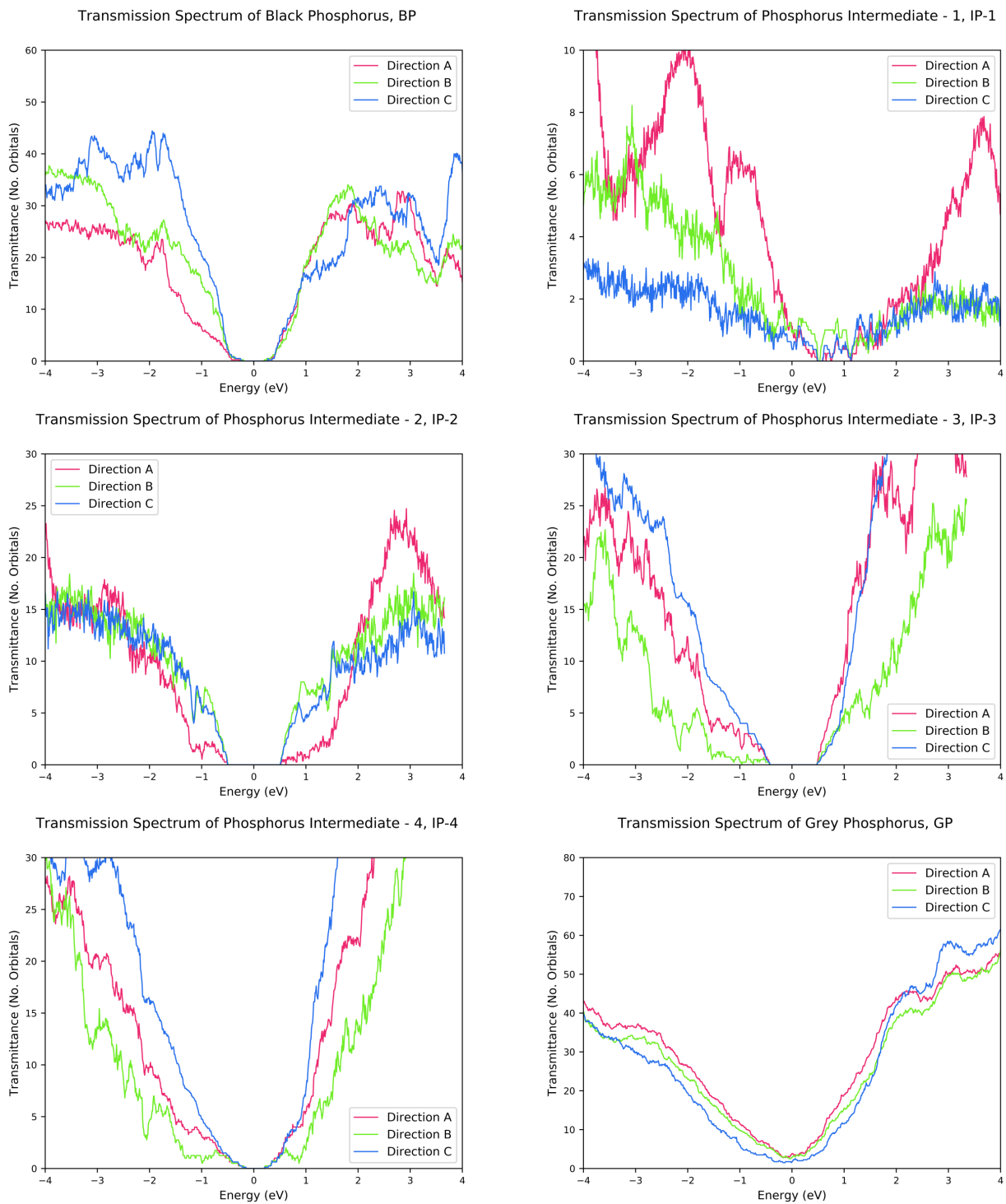


Figure 4.20 – Direction dependent transmission spectra for black phosphorus, grey phosphorus, and each structural intermediate from the transition pathway. Calculated using dftb-negf, with a k-grid of 4x4x4.

4.6.2 – PHASE TRANSITIONS AND THERMOELECTRIC TRANSPORT PROPERTIES

We have seen that black phosphorus undergoes a phase transition at around 5 GPa, and that previous work by the group has modelled the transition pathway using transition path sampling, an advanced modelling method. The electronic transmission across each of 3 directions has been calculated, from which the temperature dependent electronic thermoelectric coefficients have been derived using the methods and code defined in chapter 3. These properties are presented here, for each geometry of phosphorus previously described in this chapter.

4.6.2.1 – COMPUTATIONAL DETAILS

For each material in this section, a device was constructed in the same manner as for the original black phosphorus transmission, that is, a large, cubic principle layer was constructed, from which a device was built possessing two contact regions of two principle layers each, and a device region of 4 principle layers. The transmission was calculated along each of 3 directions in the orthorhombic principle layers, and for each calculation it was necessary to split the energy range under consideration into two to four regions, depending on the number of atoms. For compressed black phosphorus, grey phosphorus, and the symmetrical intermediate, between three and 8 thousand cpu hours were necessary to calculate these properties.

For the asymmetric systems, which required larger principle layers to fully describe the geometry, approximately thirty thousand cpu hours were required to calculate the transmission in each of three directions, explicitly within the region of the Fermi level +/- 4 eV, and at a suitable resolution (0.01 eV) to result in smooth derivations of the thermoelectric properties. The calculations were, however, primarily memory intensive, and for the larger calculations, the requested cpu's were mostly necessary to meet the memory allocation, which was restricted to 4GB per thread on HPCW. In total, for the final calculations, approximately 329'000 cpu hours were necessary to fully calculate the electronic transport in these systems. This is clearly an expensive methodology, though the unique feature is the ability to model large, asymmetric systems such as metastable intermediates, and potentially the effect of non-stoichiometric doping.

The full details of the calculations and respective parameters for the non-self-consistent calculations are summarised in table 4.2.

Transmission Calculation Parameters

Material	Parameters	Direction		
		<i>a</i>	<i>b</i>	<i>c</i>
BP	K-grid	4-4-4	4-4-4	4-4-4
	Energy Step	0.01	0.01	0.01
	Processors	256	256	256
	Time (hours)	31.5	30	29.8
	Cost (CPU hours)	8064	7680	7628.8
	No. Atoms	3840	3840	3840
CBP	K-grid	4-4-4	4-4-4	4-4-4
	Energy Step	0.01	0.01	0.01
	Processors	512	512	512
	Time (hours)	5.98	4.13	4.1
	Cost (CPU hours)	3061.76	2114.56	2099.2
	No. Atoms	2560	2560	2560
GP	K-grid	4-4-4	4-4-4	4-4-4
	Energy Step	0.01	0.01	0.01
	Processors	512	512	512
	Time (hours)	10.64	10.36	10.15
	Cost (CPU hours)	5447.68	5304.32	5196.8
	No. Atoms	2880	2880	2880
IP1	K-grid	4-4-4	4-4-4	4-4-4
	Energy Step	0.01	0.01	0.01
	Processors	256	256	256
	Time (hours)	13.99	13.24	12.16
	Cost (CPU hours)	3581.44	3389.44	3112.96
	No. Atoms	1728	1728	1728
IP2	K-grid	4-4-4	4-4-4	4-4-4
	Energy Step	0.01	0.01	0.01
	Processors	512	512	512
	Time (hours)	56.18	57.98	59.144
	Cost (CPU hours)	28764.16	29685.76	30281.728
	No. Atoms	4608	4608	4608
IP3	K-grid	4-4-4	4-4-4	4-4-4
	Energy Step	0.01	0.01	0.01
	Processors	512	512	512
	Time (hours)	59.28	58.76	58.47
	Cost (CPU hours)	30351.36	30085.12	29936.64
	No. Atoms	4608	4608	4608
IP4	K-grid	4-4-4	4-4-4	4-4-4
	Energy Step	0.01	0.01	0.01
	Processors	512	512	512
	Time (hours)	61.63	60.31	61.64
	Cost (CPU hours)	31554.56	30878.72	31559.68
	No. Atoms	4608	4608	4608

Table 4.2 – Parameters used in the calculation of the transmission spectra. Total computational time:

329779 hours.

In 4.5 we saw the compression along axis c in black phosphorus, which was performed with the intention of reducing the band gap in pure black phosphorus, so that an accurate picture of the thermoelectric properties could be attained. The issue faced with the black phosphorus optimised from literature values using DFT methods, was that the band gap predicted by DFTB methods for the same geometry was up to an order of magnitude larger than both the reported theoretical and experimental values.

Using this geometry, and the consequent transmission calculated in 4.6.1, the temperature dependent thermoelectric properties were calculated, as shown in figure 4.21. The transmission as a function of potential has been included once again for ease of comparison (top left). The first thing we observe, is the curvature of the electronic conductivity, and by extension the electronic thermal conductivity, which again has the positive exponential curvature expected of a semiconductor, yet with a gentler gradient than that of the uncompressed black phosphorus seen in 4.4, which will henceforth be referred to a Literature Value Black Phosphorus (BPLV). This is a consequence of the reduced band gap, which allows for increased overlap between the transmission and the smearing of the Fermi function at lower temperatures. This yields an average conductivity of 5×10^3 that of the literature value black phosphorus, a substantial increase, which is in much better agreement with the conductivity reported in the literature.

For the Seebeck coefficient, the effect of anisotropy is stark. It appears that the sign and magnitude of the Seebeck coefficient varies drastically with directionality. An explanation was sought, and it is the opinion of the author that the negative sign of the Seebeck coefficient for direction a is a product of the difference in the gradient of the edge of the valence band, compared to that of the edge of the conduction band. For compressed black phosphorus, we saw earlier that transmission along direction a is reduced compared to that of the literature value black phosphorus. This would result in a reduced mobility of the positive *holes* in the valence band, with respect to the electrons in the conduction band, which are created by the thermal excitation and subsequent promotion of electrons into the conduction band. The reduced mobility of the holes would result in a higher Seebeck coefficient, due to the inherent inverse proportionality between the two. Thus, a negative potential would be established in this direction, enforcing n-type behaviour. This is reaffirmed by the fact that at higher temperatures, the Seebeck coefficient for direction b is negative, with a change of sign at approximately 400 K. as can be seen in the transmission of direction b , the gradient at -1 eV plateaus, whilst the gradient at +1 eV is steep and positive. This would again result in increased mobility of electrons in the conduction band with respect to the holes in the valence band.

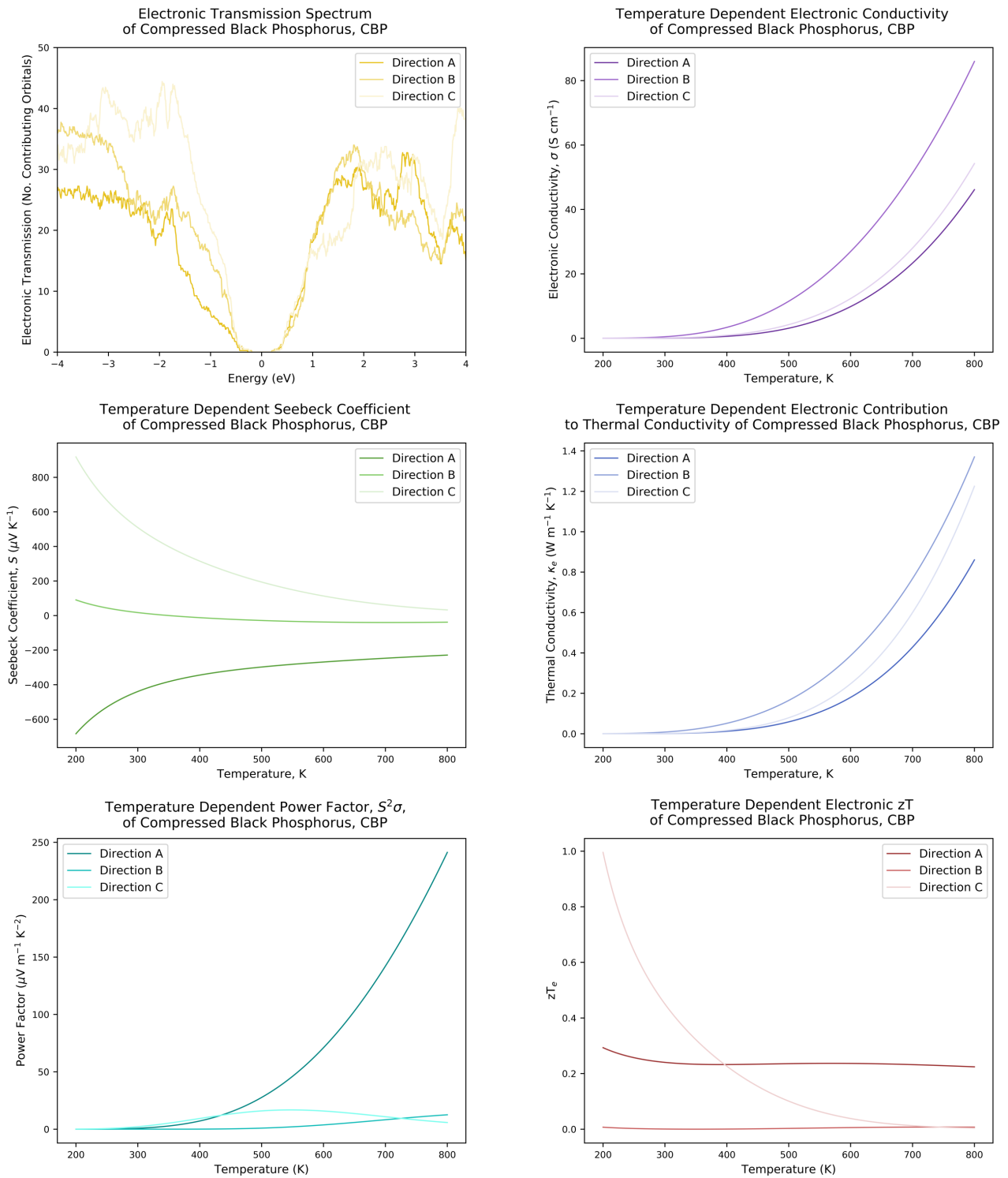


Figure 4.21 – The calculated thermoelectric properties of Compressed Black Phosphorus, CBP.

Transmission calculated using dftb-negf, with a k-grid of 4 x 4 x 4. Thermoelectric coefficients derived using program (see section 3.5), each series contains 6000 points.

As for BPLV, the electronic contribution to the thermal conductivity maps onto the electronic conductivity, as it is the electrons acting as thermal carriers. The only marginal difference is that the thermal conductivity along direction **c** is somewhat closer to that of direction **b**, which is due to the slight dependence of the thermal conductivity on the Seebeck coefficient (see chapter 3).

The Power Factor (PF) of CBP demonstrates the marked effects of anisotropy in the material, as the values of direction **a** begin to drastically differ from the other directions, by several orders of magnitude at higher temperatures. This is a consequence of the square dependence of the power factor on the Seebeck coefficient, and the semiconducting nature of CBP. At low temperatures, the conductivity is exceedingly small, as few electrons possess the energy to undergo thermal excitation to the conduction band. This results in a relatively “flat” conductivity curve at lower temperatures, although in actuality the curve is a positive exponential, but the magnitude is infinitesimal. As the power factor is the square of the Seebeck multiplied by the conductivity, the infinitesimal conductivity dominates this at lower temperatures. At higher temperatures, the conductivity is larger and the power factor of direction **a** reflects this. However, whilst the Seebeck coefficient direction **c** is the largest at low temperatures, the magnitude at high temperatures is significantly reduced, i.e. approximately 30 at 800 K. However, at 800 K, the Seebeck coefficient of direction **a** is much larger, approximately 230 $\mu\text{V K}^{-1}$, and due to the square relationship of the Seebeck coefficient and power factor, the latter is markedly larger for direction **a**.

The electronic figure of merit, zT_e , is the final stage in the derivation of the electronic thermoelectric properties, and as a consequence of the consecutive nature of the derivations of each property, the amplification of the effects of anisotropy is exceedingly evident. We note that the zT_e along **c** is large at low temperatures, purely due to the large Seebeck coefficient at the corresponding temperatures, whilst the zT_e along **a** is larger than that of direction **b**, again due to its larger Seebeck coefficient. The sign of the Seebeck coefficient is negated here, as zT_e is dependent on the square. At elevated temperatures, the zT_e of direction **c** rapidly decreases, whilst that of the other directions remains fairly consistent. At high temperatures, zT_e is dominated by the magnitude of the conductivities. The flat nature of zT_e then is therefore explained (as in chapter 4.4) by the cancelling of the exponents of the electronic and thermal conductivity. Compressed black phosphorus thus has an average zT_e of approximately 0.1. with the contribution of the lattice thermal conductivity, the zT of this material would be exceedingly small.

Grey Phosphorus, GP, occasionally referred to as blue phosphorus or the α -Arsenic phase of phosphorus, is a metallic, high pressure polymorph of phosphorus, which is well documented in the literature. As seen in the previously calculated DOS (4.6.1), the grey phosphorus phase is a “poor-metal”, in that it has no band gap at the Fermi energy, yet the density of states is low in this region, and thus the available states for charge carriers to occupy is lower than for a transition metal such as Nickel where the Fermi energy cuts the density of states at the maxima of the d-orbitals contribution. As we shall see, this results in metallic behaviour (first order conductivity), and a poor thermoelectric material.

Figure 4.22 illustrates the thermoelectric properties derived from the transmission of 4.6.1. The transmission maps the DOS in the sense that there is no band gap and a minimum at the Fermi level. At this point we reiterate the demand for orthorhombic systems in the implementation of the Landauer-Büttiker method in DFTB methods. To the observant crystallographer, there should be 2 discrete crystallographic directions in grey phosphorus, as the unit cell is hexagonal (with 2 atoms), or trigonal-rhombohedral (with 6 atoms) depending on the setting. To implement orthogonality, a larger, primitive orthorhombic cell was constructed from the hexagonal setting, with 12 atoms and twice the volume. Thus, the transmission along direction \mathbf{a} equates to the transmission along one of the 3 degenerate, crystallographic directions in the plane of the grey phosphorus “sheet”, whereas the transmission along direction \mathbf{b} is again in plane, but does not correspond to a crystallographic vector. The transmission along direction \mathbf{b} has therefore been included for completeness, as it is meaningful in the bulk paradigm. The key feature then, is that the transmission along direction \mathbf{b} is far more similar in intensity to that of direction \mathbf{a} , as both are “in plane”.

The electronic conductivity of grey phosphorus is highly anisotropic, significantly larger than that of both the aforementioned black phosphorus structures (BPLV, CBP), and shows first order conductivity, i.e. the shape of the curve is almost linear compared to the cubic exponential nature of both black phosphorus structures. The transmission along the \mathbf{a} and \mathbf{b} directions is almost twice that of direction \mathbf{c} , although direction \mathbf{c} is by no means a poor conductor.

The anisotropy of the material is exemplified by the Seebeck coefficients, which determine the shape of the resultant power factor and zT_e . The Seebeck coefficient of direction \mathbf{c} is the largest in magnitude, and it should be noted that the respective Seebeck coefficients of grey phosphorus are the only values to be negative in the rest of the materials of interest in this chapter. This n-type behaviour is thought to be a direct consequence of the steeper DOS and transmission of the region formally referred to as the “conduction band”, with respect to that of the “valence band”. This would be expected to result in a higher mobility of electrons and thus n-type character.

The high mobilities of the electrons in directions **a** and **b** are believed to cause the large conductivities and lower Seebeck coefficients in these directions. The electronic contribution to the thermal conductivity has a large, positive gradient, and is near-linear in shape, as would be expected for a poor metal. The magnitude of **c**'s contribution is smaller as a direct consequence of the lower electronic conductivity.

The shape of the power factor is governed by the shape of the Seebeck coefficient, as the conductivity is almost linear with respect to temperature. The “swapping” of the order with direction **c** being largest is due to the fact that the power factor is dependent on the square of the magnitude of the Seebeck coefficient, which is largest for direction **c**.

The zT_e is largely reminiscent of the power factor, though the contribution of the large disparity between the thermal contribution of **c** versus **a** and **b** amplifies the magnitude of zT_e for **c**. Here we note that the average zT_e of grey phosphorus is unquestionably lower than for both previously mentioned forms of black phosphorus. Whilst the electronic conductivity of grey phosphorus is larger than that of black phosphorus, the Seebeck coefficient suffers as a direct consequence, and is in fact several orders of magnitude smaller than the respective values for BPLV and CBP. Since the zT_e is dependent on the square of the Seebeck coefficient, there are catastrophic consequences for the thermoelectric properties of grey phosphorus. The final nail in the coffin as it were, is that the electronic contribution to the thermal conductivity of grey phosphorus is orders of magnitude larger than in both black phosphorus schemes, due to its metallic behaviour.

It is for this reason, that thermoelectric properties of metals are rarely calculated in the modern literature, as the Seebeck coefficient – otherwise known as the thermopower, is always likely to be tiny as a consequence of the high charge carrier mobility.

So far, we have calculated the thermoelectric properties of both phases of phosphorus from the high temperature phase transition. The results are as expected, both black and grey phosphorus are poor thermoelectric materials, though black phosphorus is marginally better on account of its small band gap.

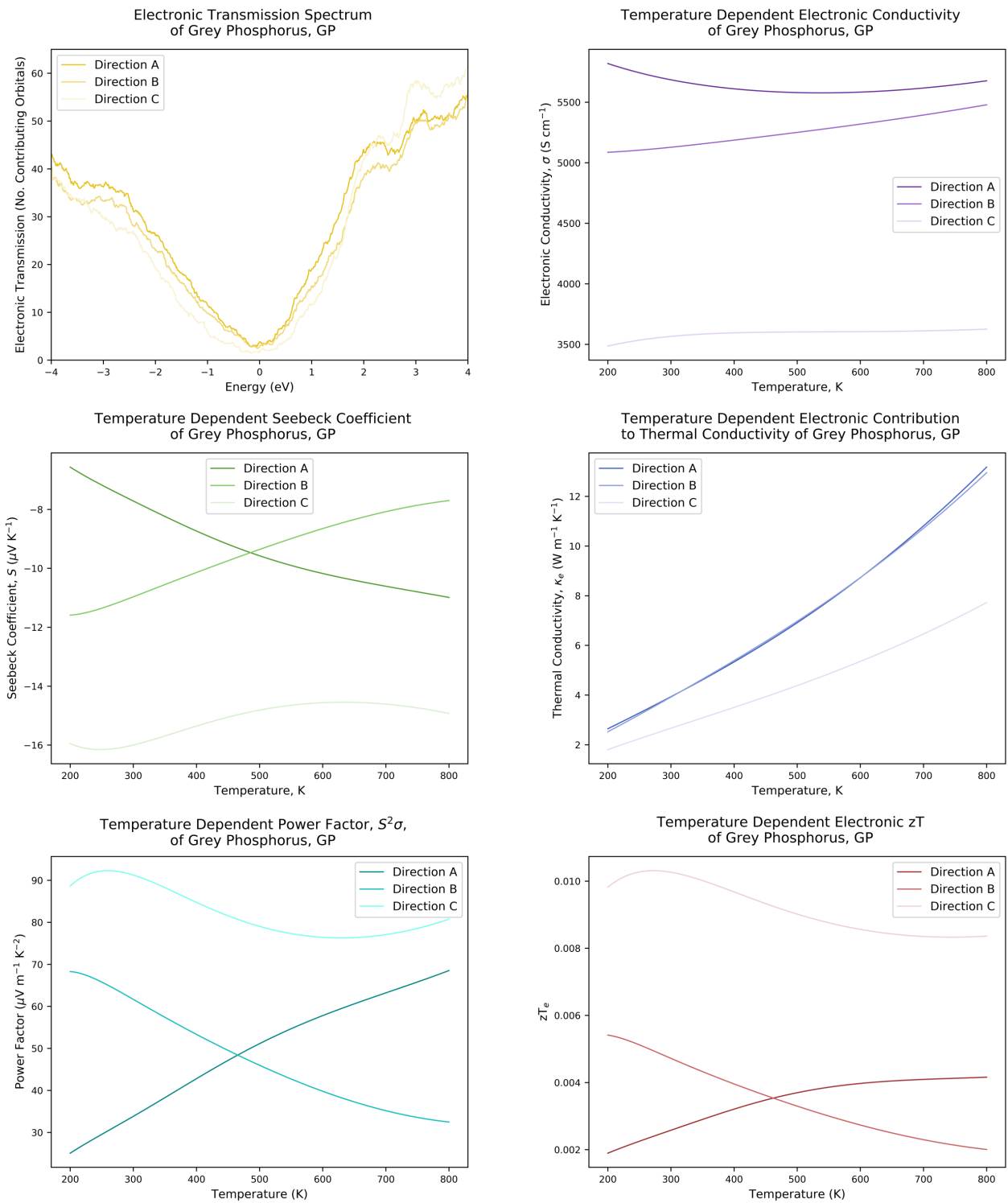


Figure 4.22 – The calculated thermoelectric properties of Grey Phosphorus, GP. Transmission calculated using dftb-negf, with a k-grid of 4 x 4 x 4. Thermoelectric coefficients derived using program (see section 3.5), each series contains 6000 points.

The optimisation of highly symmetric intermediate 1 was detailed in section 4.6.1. Using this frozen snapshot from the BP to GP phase transition, it was hoped to glean some insight into the effect of the phase transition on the electronic thermoelectric properties of phosphorus.

The transmission is reminiscent of grey phosphorus, a poor metal, yet the minimum of the “well” in the density of states and transmission is offset with respect to the Fermi energy. The conductivity is linear as expected of a poor metal, though rather high, and comparable to that of grey phosphorus. Interestingly, the conductivity along direction c is the largest, and this is thought to be due to the opening of “conduction channels” formed by the associated bonding between the layers of black phosphorus. This scheme is due to increased overlap between lone pairs, a topic further detailed in the work of Leoni et. al.

Once more, we see the effect of the gradient of the transmission about the Fermi energy on the Seebeck coefficient. Here, direction a has the largest disparity between the region to the left and right of the Fermi level, and thus the largest, positive Seebeck coefficient. The curvature is slight, and this is likely due to the lack of band gap, and relatively consistent DOS about the Fermi energy.

The electronic contribution to the thermal conductivity reflects the trends of the electronic conductivity, as expected. In a similar fashion, the power factor is clearly dominated by the expression of the Seebeck coefficient, and so by extension is zT_e . The take home from this, is that the magnitude of zT_e for this phosphorus intermediate lies somewhere between that of black and grey phosphorus, leaning towards grey phosphorus, probably due to its metallicity.

As previously mentioned, it had been hoped that the lack of short range symmetry in the phosphorus intermediate would allow for a greater zT . This was based on two assumptions, first, the assumption that the thermal transport of the lattice would be perturbed, an issue not dealt with here but based on the work of Selli et. al. on the scattering of phonons at grain boundaries within lead selenides. Secondly, the scattering of phonons would likely coincide with the scattering, albeit to a lesser extent, of charge carriers, which may see a decrease in the conductivity, and increase in the Seebeck coefficient. For this reason, the second set of phosphorus intermediates were obtained from the trajectory of the transition pathway, as discussed in 4.6.1.

The investigation hinged on the belief that the pressure range of the electronic phase transition would be smaller than the range at which the structural phase transition occurred. If this were the case, the intermediate phosphorus at lower pressures may be semiconducting. The results obtained in this investigation form the remainder of this chapter.

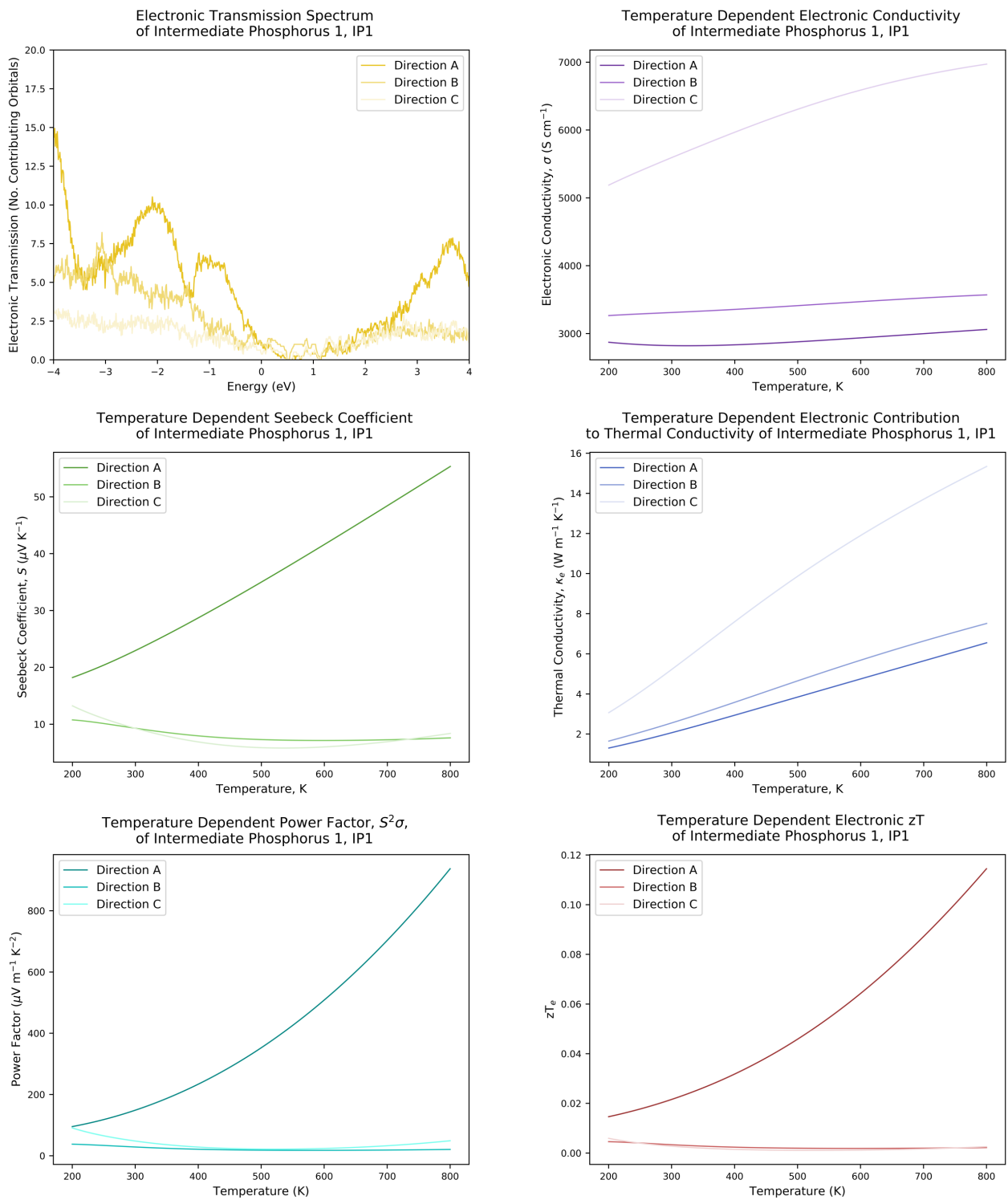


Figure 4.23 – The calculated thermoelectric properties of Intermediate Phosphorus 1, IP1. Transmission calculated using dftb-negf, with a k-grid of 4 x 4 x 4. Thermoelectric coefficients derived using program (see section 3.5), each series contains 6000 points.

The density of states and transmission obtained for phosphorus intermediate 2 showed that it is a semiconductor, with a clear band gap, and a transmission spectrum that indicated the transmission along direction **a** suffered as a consequence of the increased pressure, or better yet, that the transmission along direction **b** and **c** improved as a consequence of the applied pressure.

The electronic conductivity displayed the expected cubic exponent of a semiconductor, with the size of the band gap determining the temperature range at which the material becomes conducting. The direct relationship between transmission and conductivity resulted in a far lower conductivity for direction **a**. The magnitude of the average conductivity was approximately three orders of magnitude smaller than that of GP and IP1, and an order of magnitude smaller than that of CBP.

The Seebeck coefficient however, was up to 2 orders of magnitude larger than for each of the preceding structures, and as in IP1, far larger along direction **a**. The thermal conductivity mirrored the trends of the electronic conductivity, which also defined the shape of the power factor, however, the magnitude of the power factor at high temperatures was determined by the magnitude of the Seebeck coefficient, and was thus largest for direction **a**.

The large Seebeck coefficients defined the shape of zT_e , yet the reduction in conductivity resulted in a magnitude similar to that of IP1, somewhere between that of CBP and GP.

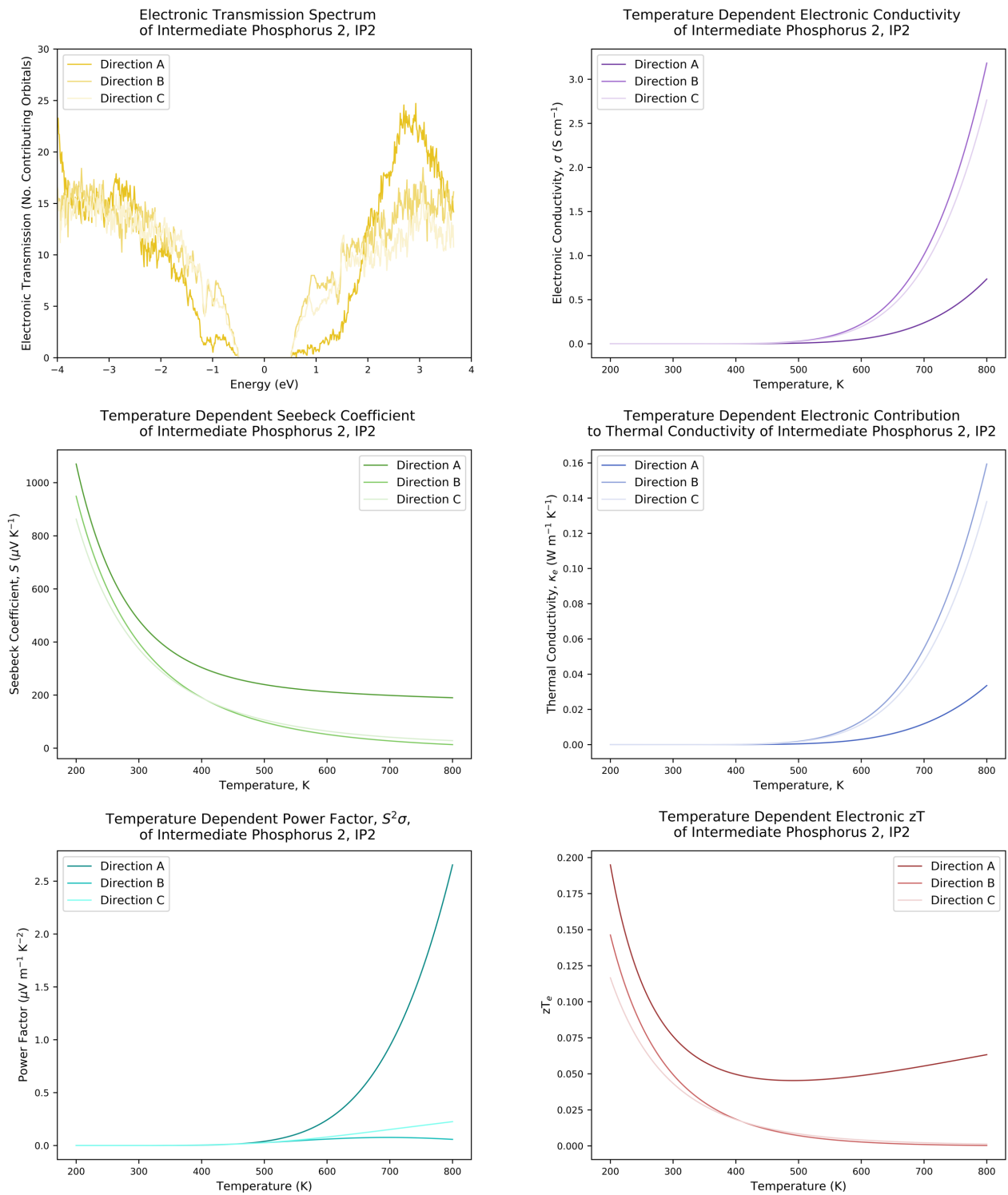


Figure 4.24 – The calculated thermoelectric properties of Intermediate Phosphorus 2, IP2. Transmission calculated using dftb-negf, with a k-grid of 4 x 4 x 4. Thermoelectric coefficients derived using program (see section 3.5), each series contains 6000 points.

As for IP2, intermediate phosphorus 3 is a small band gap semiconductor. The major difference between the transmission spectra of the two is the disparity between the gradient of the valence and conductance bands in IP3. The electronic conductivity reflects the anticipated curvature of a semiconductor, and is similar in both shape and magnitude to that of IP2.

The Seebeck coefficient, whilst similar in shape and gradient, is twice the magnitude of that of IP2 on average across the temperature range. Interestingly, the Seebeck coefficient of direction *c* is the largest across the temperature range, whereas it does not possess the lowest values of conductivity. Whilst the gradient of the valence band edge is shallower than that of the conductance band, we note that the valence band edge is between 0.1 – 0.2 eV closer to the Fermi energy than the conductance band, and so at the low temperatures, the shape of the valence band governs the Seebeck coefficient.

The electronic contribution to the thermal conductivity maps the electronic conductivity, and it is the large magnitude of the Seebeck coefficient for direction *c* that dominates the power factor at high temperatures. Whilst the magnitudes of the electronic and thermal conductivities are similar to those of IP2, the magnitude of the Seebeck coefficient is almost twice that of its counterpart, resulting in a power factor an order of magnitude larger. This has a strong impact on the zT_e of IP3, which is also an order of magnitude larger than that of IP2, and indeed the largest zT_e of all the materials in this subsection. A zT_e of greater than 1 at 300 K for in direction *c* is striking result, not least because the zT_e 's seen so far in this work have been around 0.1 or less at 300 K.

The large zT_e is thought to have be a consequence of two factors, that the material has a band gap and thus high Seebeck coefficient, and that the gradients of the transmission and density of states at the band edges are asymmetric with respect to the Fermi energy.

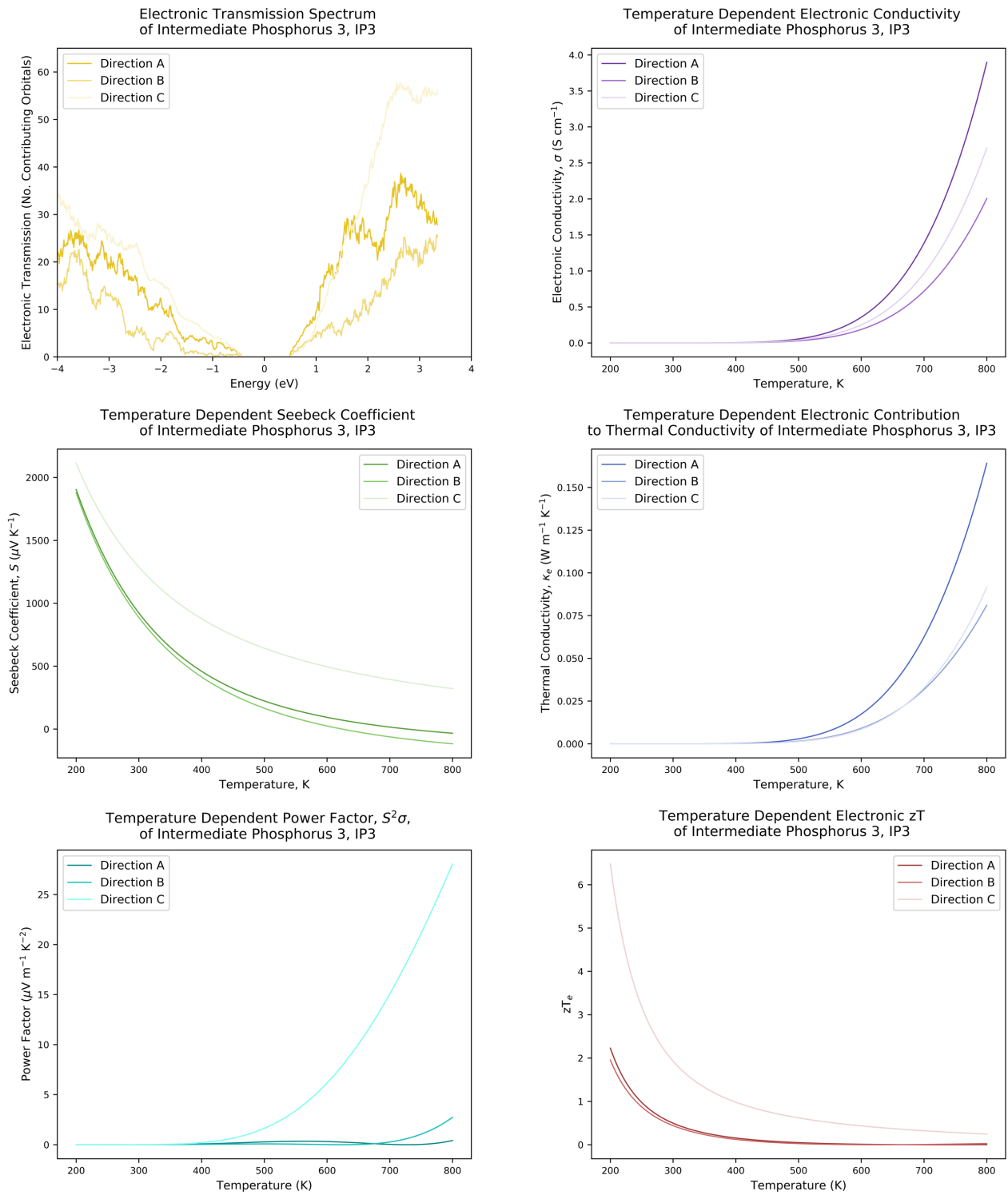


Figure 4.25 – The calculated thermoelectric properties of Intermediate Phosphorus 3, IP3. Transmission calculated using dftb-negf, with a k-grid of $4 \times 4 \times 4$. Thermoelectric coefficients derived using program (see section 3.5), each series contains 6000 points.

4.6.2.7 – INTERMEDIATE PHOSPHORUS 4

The transmission of Intermediate Phosphorus 4, IP4, is similar to that of IP3, in that it is asymmetric about the Fermi level, shallower as in GP in character, but with a distinct if smaller band gap, as in CBP. Perhaps due to this smaller band gap, the electronic conductivity is ten times greater than that of IP3, with a gentler gradient, although still clearly somewhat exponential. The disparity between directions is small, though it is interesting to note that at lower temperatures the two *in plane* directions are closer in range, while at larger temperatures the conductivity of direction **b** crosses that of direction **c**.

The Seebeck coefficients are fairly large despite this, though smaller than those of IP3. The electronic thermal conductivity is much larger than that of IP2 and IP3, as expected from the larger electronic conductivity. The power factor is actually larger in each direction than for IP3, especially in the region of 400 – 700 K, where the maximum value for each direction is found. The curves of the maxima are present here, as for the first time in the semiconducting case, the exponents of both the Seebeck coefficient and electronic conductivity are similar but opposing.

The zT_e of IP4 is again large, especially below 300K, however it is not as large as that of IP3. This is mostly attributed to the larger conductivity, and associated thermal conductivity, which negates the large power factor, however, a zT_e of approximately 1 in direction **c** is another impressive feature.

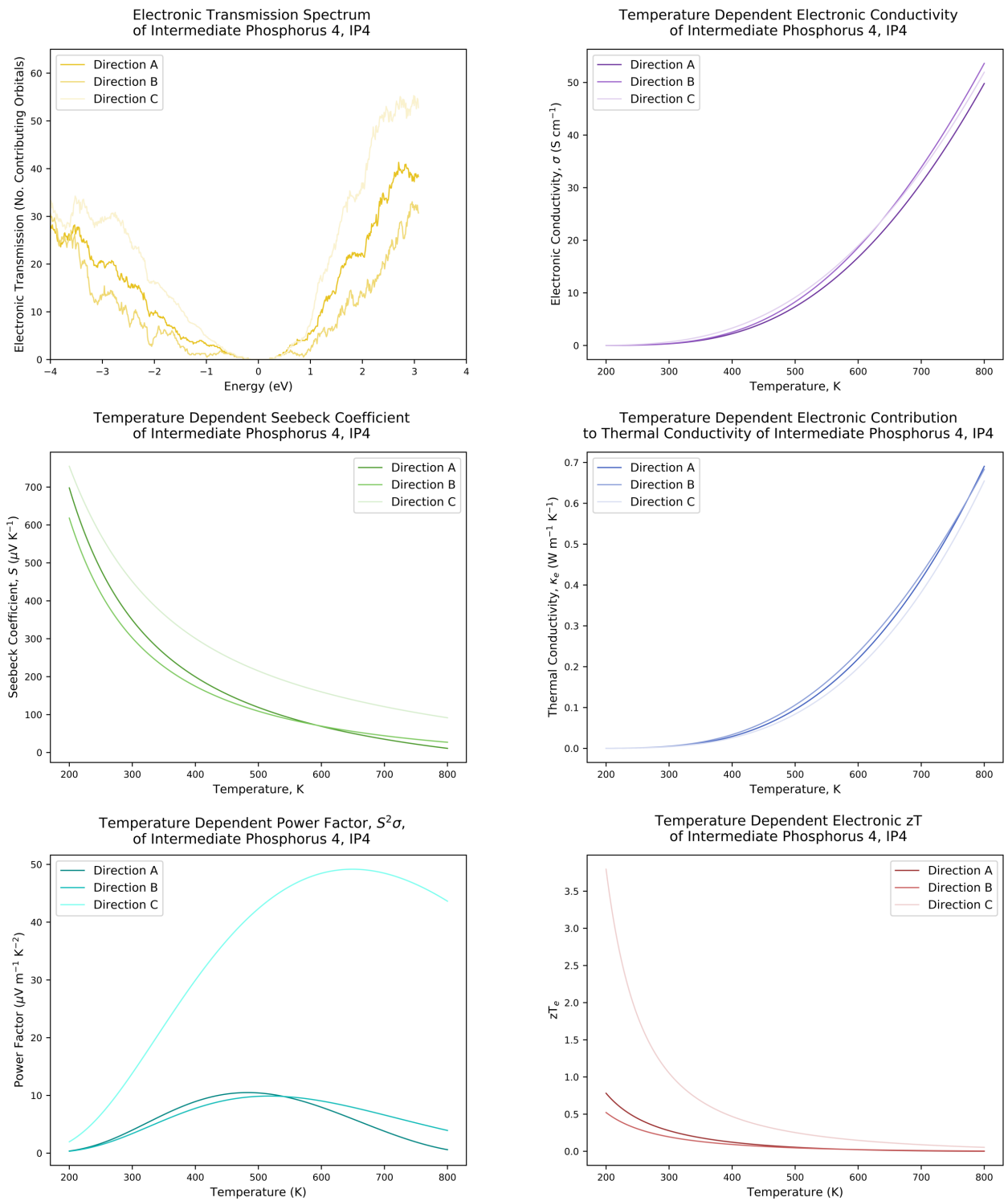


Figure 4.26 – The calculated thermoelectric properties of Intermediate Phosphorus 4, IP4. Transmission calculated using dftb-negf, with a k-grid of 4 x 4 x 4. Thermoelectric coefficients derived using program (see section 3.5), each series contains 6000 points.

4.6.2.8 – DISCUSSION: THE IMPACT OF PHASE TRANSITIONS ON THERMOELECTRIC PHENOMENA

In this section, we have seen the effect of the pressure induced phase transition on the thermoelectric properties of black phosphorus and its analogues. This unique insight was achieved using several metastable intermediates from the previously modelled black phosphorus – grey phosphorus phase transition, by mapping the thermoelectric properties for each. There are several important messages in the results, and these are interpreted here.

From this work, the primary conclusion is that the largely asymmetric geometries achieved by the metastable intermediates of phase transitions allow for far higher electronic figures of merit than exhibited by either the initial or final crystallographic polymorph in the phase transition. This is due to a combination of factors, such as the drastic increase of the Seebeck coefficient in these asymmetric systems, the reduction in electronic and thus thermal conductivity, and the reduced band gap, which allows for the simultaneous presence of both large Seebeck coefficients and electronic conductivities with respect to large band gap insulators.

Whilst the highest observed electronic figure of merit was in fact that of the literature value based black phosphorus geometry with an overestimated band gap, the ignorance of the phononic contribution to thermal transport is largely anticipated to negate this. In fact, the consideration of the phononic contribution will result in a significantly lessened figure of merit for each material studied. However, the intention of this work is not to suggest black phosphorus as a high-efficiency thermoelectric material, but to imply that this methodology, when applied to an inherently efficient thermoelectric material, may result in a noticeable increase in zT . The critical assumption, is that the magnitude of the phononic contribution to the thermal conductivity will be of the same order of magnitude for each material, such that the holistic zT for each may display the same trends as zT_e . That is, except for BPLV, which has an infinitesimal k_e , and thus its zT will likely be many orders of magnitude smaller than its zT_e .

This is rationalised by the standard practice of predicting k_l from the Wiedemann-Franz law and Lorenz factor, the resultant values of which will not widely vary for differing geometries of elemental phosphorus with similar densities and covalent bonding schemes. Indeed, it is believed that the asymmetric intermediates would likely possess lower lattice conductivities, as a result of the distorted bonding leading to increased scattering of phonons. This rationale is based on the work of Leoni et. al. wherein the inclusion of grain boundaries and asymmetric interfaces resulted in the perturbed propagation of phonons through PbSe. If this were true, the implementation of a transition intermediate scheme would be doubly beneficial to the zT of the system.

The highest zT_e achieved (excluding that of BPLV) was in the Intermediate Phosphorus 3, although the Intermediate Phosphorus 4 was a close second. In both of these materials, coexisting black phosphorus and grey phosphorus domains are observed to coexist, as seen in Figure 4.18. This further affirms the likeness of the work to the “grain boundary” scheme implemented in PbSe, as the scattering of charge carriers and phonons is believed to occur at the boundaries between the black and grey phosphorus domains. Whilst these systems may at first appear frustrated, it should be noted that each atom in the intermediate phosphorus 1 - 3 geometries exhibits the expected sp^3 hybridised phosphorus coordination, with 3 covalent bonds between neighbouring phosphorus atoms and a lone pair projected into “ionic voids” within the structure. This implies that upon the subsequent quenching of a pressure induced phase transition between black and grey phosphorus, metastable semi-glasses of black-grey hybridised phosphorus may be attainable. The term “metastable” should not concern the reader, indeed diamond is metastable with respect to the lifetime of the earth; it may be that as a low temperature thermoelectric material, these systems may be long lived.

Due to the large electronic and thermal conductivities, along with the small Seebeck coefficients associated with metallic systems, the electronic figures of merit will always be small for such materials. As such, care should be taken in the exploitation of any structural phase transition that coincides with an electronic phase transition, as the further the system proceeds along the transition pathway, the more likely the material will adopt the undesirable metallic nature. This pressure induced phase transition is somewhat unique, in that a structural and electronic phase transition occur simultaneously. Although it would be expected that most *electronic* phase transitions would occur alongside a large structural rearrangement, it is not necessarily true that all *structural* phase transitions coincide with an electronic transition.

This is the case in the oxides for example, as for Fe_2O_3 there are at least 3 distinct, well-documented phases: α , β and γ , yet each phase is a small band gap semiconductor. A study of such a system would further determine if it is the asymmetry of the geometry, or the reduction in the band gap that has the greatest impact on thermoelectric phenomena, or if it is indeed necessary to possess coexisting metallic and semiconducting domains. The results of which may also apply to state-of-the-art composite paradigms, where the local material properties differ across the material, reflecting the chemistry at each site.

This methodology is implemented in the pure black phosphorus scheme, without the standard doping commonly implemented in thermoelectric materials to achieve higher Seebeck coefficients, improved conductivities and reduced thermal transport. As such, it would be interesting to see the impact of the approach in a synergistic optimisation scheme, where the material is engineered at the chemical, nano- and meso-scale to achieve high state-of-the-art zT 's.

Whilst it is clear that this method is computationally expensive, the unique insight into the thermoelectric phenomena of a material undergoing coinciding structural and electronic phase transitions is believed to have been worth the computational cost. This means may also be applicable to computationally study the effect of non-stoichiometric doping in such a system, were such a parameter set developed.

4.7 – SUMMARY

In this chapter, we have seen the calculation of the electronic transmission spectra of nanowires of black phosphorus, as a natural progression from the introductory calculations performed for graphene in the evaluation of the DFTB code. We then built up to the calculation of stable, bulk black phosphorus, and used the Landauer-Büttiker formalism to derive the electronic thermoelectric properties of black phosphorus. Due to the overestimation of the band gap of black phosphorus by the DFTB method, a simple study of the effect of anisotropic pressure was performed to “tune” the band gap of bulk black phosphorus, as it was inferred that the DFTB parameters for phosphorus did not adequately describe the inter-layer interactions between phosphorene layers. The resultant “compressed” black phosphorus (CBP) was then used in the study of the effect of the pressure-dependent phase transition of black phosphorus on the materials thermoelectric properties. The introduction of the grey phosphorus material, along with several metastable intermediates followed. The intermediates were obtained from a previously performed transition path sampling simulation of the same phase transition at DFT level theory. The compressed black phosphorus and grey phosphorus were then used to determine the suitability of the Landauer-Büttiker method implemented in the DFTB formalism to predict the thermoelectric properties of these materials. Once this stipulation was satisfied, the methodology was applied to the constructed metastable intermediates, and it was ascertained that the methodology developed in this work may have meaningful contributions to the development of improved thermoelectric materials, when applied synergistically with existing methods of thermoelectric materials optimisation.

4.8 – REFERENCES

- 1 J. He and T. M. Tritt, *Science*, 2017, **357**, 2017.
- 2 M. R. Burton, T. Liu, J. McGettrick, S. Mehraban, J. Baker, A. Pockett, T. Watson, O. Fenwick and M. J. Carnie, *Adv. Mater.*, 2018, **321**, 1801357.
- 3 S. D. N. Luu and P. Vaquero, *Special Issue on Advances in Thermoelectric Research*, 2016, **2**, 131–140.
- 4 G. Seifert, T. Lorenz and J. O. Joswig, *Semiconductor Science and Technology*, 2014, **29**, 064006.
- 5 H. Y Lv, W. Lu, D.-F. Shao and Y. Sun, *Large thermoelectric power factors in black phosphorus and phosphorene*, arXiv:1404.5171 [cond-mat.mtrl-sci].
- 6 L. Craco, T. A. D. S. Pereira and S. Leoni, *Phys. Rev. B*, 2017, **96**, 075118.
- 7 A. Castellanos-Gomez, *J. Phys. Chem. Lett.*, 2015, **6**, 4280–4291.
- 8 D. Selli, S. E. Boulfefel, P. Schapotschnikow, D. Donadio and S. Leoni, *Nanoscale*, 2016, **8**, 3729–3738.
- 9 S. E. Boulfefel, G. Seifert, Y. Grin and S. Leoni, *Phys. Rev. B*, 2012, **85**, 014110.
- 10 B. Aradi, B. Hourahine and T. Frauenheim, *J. Phys. Chem. A*, 2007, **111**, 5678–5684.
- 11 B. Hourahine, S. Sanna, B. Aradi, C. Köhler, T. Niehaus and T. Frauenheim, *J. Phys. Chem. A*, 2007, **111**, 5671–5677.
- 12 M. P. Anantram, M. S. Lundstrom and D. E. Nikonov, *Proceedings of the IEEE*, **96**, 1511–1550.
- 13 J. R. Reimers, G. C. Solomon, A. Gagliardi, A. Bilić, N. S. Hush, T. Frauenheim, A. Di Carlo and A. Pecchia, *J. Phys. Chem. A*, 2007, **111**, 5692–5702.
- 14 C. Fernández-García, A. J. Coggins and M. W. Powner, *Life*, 2017, **7**, 31.
- 15 U. Müller, *Inorganic Structural Chemistry*, John Wiley & Sons, 1993.
- 16 S. Lin, Y. Chui, Y. Li and S. P. Lau, *FlatChem*, 2017, **2**, 15–37.
- 17 F. Shojaei and H. S. Kang, *J. Phys. Chem. C*, 2015, **119**, 20210–20216.
- 18 Z. Zhang, D.-H. Xing, J. Li and Q. Yan, *CrystEngComm*, 2017, **19**, 905–909.

4.8 – REFERENCES (CONTINUED)

- 19 R. T. Downs, M. Hall-Wallace, *American Mineralogist*, 2003, **88**, 247-250.
- 20 P. Giannozzi, S. Baroni, N. Bonini, M. Calandra, R. Car, C. Cavazzoni and D. Ceresoli, *Journal of Physics: Condensed Matter*, 2009, **21**, 395502.
- 21 J. P. Perdew and W. Yue, *Phys. Rev. B*, 1986, **33**, 8800–8802.
- 22 D. P. Sheppard, R. Terrell and G. A. Henkelman, *J. Chem. Phys.*, 2008, **128 13**, 134106.
- 23 W. Setyawan and S. Curtarolo, *Computational Materials Science*, 2010, **49**, 299–312.
- 24 H. Liu, Y. Du, Y. Deng and P. D. Ye, *Chem. Soc. Rev.*, 2015, **44**, 2732–2743.
- 25 F. Bachhuber, von Appen Jörg, R. Dronskowski, P. Schmidt, T. Nilges, A. Pfitzner and R. Wehrich, *Angew. Chem. Int. Ed.*, 2014, **53**, 11629–11633.
- 26 G. J. Snyder and E. S. Toberer, *Nature Mater*, 2008, **7**, 105–114.
- 27 G. A Slack, *J. Phys. Chem. Solids*, 1979, **34**, 321-335.
- 28 H. Liu, X. Yuan, P. Lu, X. Shi, F. Xu, Y. He, Y. Tang, S. Bai, W. Zhang, L. Chen, Y. Lin, L. Shi, H. Lin, X. Gao, X. Zhang, H. Chi and C. Uher, *Adv. Mater.*, 2013, **25**, 6607–6612.
- 29 T. Matsunaga, N. Yamada, R. Kojima, S. Shamoto, M. Sato, H. Tanida, T. Uruga, S. Kohara, M. Takata, P. Zalden, G. Bruns, I. Sergueev, H. C. Wille, R. P. Hermann and M. Wuttig, *Adv. Funct. Mater.*, 2011, **21**, 2232–2239.
- 30 H. Yu, S. Dai and Y. Chen, *Nature Publishing Group*, 2016, **6**, 386.
- 31 R. Luschtinetz, A. F. Oliveira, J. Frenzel, J. Joswig, G. Seifert, H. A. Duarte, *science*, 2008, **602**, 1347-1359.
- 32 J. Frenzel, A. F. Oliveira, N. Jardillier, T. Heine, G. Seifert, Semi-relativistic, self-consistent charge Slater-Koster tables for density-functional based tight-binding (DFTB) for materials science simulations, TU-Dresden, Dresden, 2004-2009.
- 33 J. Liu, S. Zhang, Y. Guo, Q. Wang, *Scientific Reports*, 2016, **6**, 37528.

CHAPTER 5 – TIN SULFIDES AS THERMOELECTRIC MATERIALS

This chapter concentrates on the thermoelectric properties of tin sulfide compounds, and the high temperature phases of tin mono-sulfide. These properties are derived from the transmission as in the previous chapter, though the inclusion of multiple species dictates the need to account for charge transfer. The chapter begins with a crystallographic study of the ground-state of naturally occurring tin sulfides, before an investigation into the thermoelectric properties of these materials. The novel high-temperature phases of tin mono-sulfide are then introduced, and subjected to the same investigative procedure.

5.1 – INTRODUCTION

The transition metal chalcogenides have become the subject of intensive research in recent years, owing to the discovery of tin selenide as a thermoelectric material, with one of the highest recorded zT 's of any material observed to date.¹⁻⁴ This high zT is largely due to the ultralow thermal conductivity of the material, one of the lowest observed, at $0.23 \text{ W m}^{-1} \text{ K}^{-1}$.¹ The ultralow thermal conductivity is a consequence of the layered structure of SnSe, which consists of stacks of corrugated SnSe sheets bound weakly by intermolecular forces, as in graphite. In fact, the material is very nearly a binary analogue of the black phosphorus structure observed in the preceding chapter, the main dissimilarity being the differing bonding angles exhibited by each species.

As such, tin selenide has become a recent candidate for thin films, and similar materials from the transition metal chalcogenides have become candidates for thermoelectrics.⁵ Tin sulfide is one such material, possessing an identical structure and similar chemistry to the heavier tin selenide, it is ideally placed as a material constituting earth-abundant, low-toxicity elements.⁶ These criteria are a preference of the thermoelectric community to search for cheap, safe materials, that may be readily available to develop into thermoelectric generators to aid in the generation of sustainable energy.

5.2 – LITERATURE

As previously mentioned, one of the most impressive discoveries in the field of thermoelectrics in recent years was the revelation that tin selenide, SnSe, possessed a zT of 2.6 ± 0.3 at 923 K along **b**, 2.3 ± 0.3 along **a** and 0.8 ± 0.2 along **c**.¹ This was found to be due to one of the lowest observed thermal conductivities in a thermoelectric material, of $0.23 \pm 0.03 \text{ W m}^{-1} \text{ K}^{-1}$. The root of this ultralow thermal conductivity was determined to be the large degree of anharmonicity found within the material, along with the anisotropic nature of the compound. Due to its structural and chemical similarity, tin sulfide has also been investigated as a thermoelectric material.⁶ It has been shown that Tin sulfide has thermoelectric figure of merit of around 0.8, which is definitively in the realms of thermoelectric promise, if not as high as tin selenide's.⁷

Tin Sulfide has a rich phase space, with 3 distinct phases of differing stoichiometry occurring under ambient conditions: SnS, SnS₂ and Sn₂S₃.⁸ Additionally, the mono-sulfide (SnS) has been shown to possess at least 3 separate phases under the influence of pressure and temperature. Tin Selenide is subject to a similar phase transition, from the α -phase to the β -phase at 825 K. This phase transition has been shown to positively affect the power factor of SnSe, and the temperature at which it occurs has been proven to be reducible as a function of increased hydrostatic pressure.⁹ Tin sulfide is isostructural with the α -phase of tin selenide, whilst also undergoing an identical phase transition to the β -phase at 905 K, via a λ -transition pathway.¹⁰

There have been reports in the literature of cubic phases of both SnS and SnSe, though the structure has not been unanimously agreed until recently, as the proposed crystal structures did not match the X-ray Diffraction Data (XRD) of experiment, while theoretical predictions were unable to reliably suggest that these phases would be stable under atmospheric conditions.¹¹ Interestingly, the signature of this mystery cubic phase had been found only in thin films synthesised for use in the photovoltaic industry, and observed under atmospheric conditions. Thus, the theoretical predictions that the proposed Wurtzite (W) and Rock Salt (RS) phases would not be stable at low pressures, combined with the difficulty in assigning a crystal structure to the XRD data, meant that the exact structure of this material remained under dispute for several years. Recently, a novel structure was proposed by Rabkin et al. and later refined by Abutbul et al., which allowed for the fitting of Precession Electron Diffraction (PED) spectra to crystallographic planes.^{11,12} These findings were reinforced by the fitting of XRD data to the geometry. This unique non-centrosymmetric crystal structure has an exciting potential as a piezoelectric, while its large, cubic unit cell suggested it may hold promise for thermoelectric applications.^{2,3,13,14}

5.3 – CRYSTALLOGRAPHIC STUDY OF GROUND STATE AND PREDICTED STRUCTURES

To begin the investigation into the thermoelectric properties of tin sulfides, a crystallographic study was performed for several known tin sulfides, as a preliminary investigation into their electronic properties. To achieve this, the structural data was acquired from the American Mineralogist Database, and each geometry was optimised using quantum espresso.¹⁵⁻¹⁷ Subsequently, Density of States (DOS) and band structure calculations were performed using the optimised geometries. This data is presented here, along with insights into the vectors along which the transport properties will be calculated.

Material	Space Group	<i>a</i>	<i>b</i>	<i>c</i>	α	β	γ	No. Atoms in Unit Cell
Herzenbergite (α -SnS)	P n m a	11.18	3.98	4.33	90	90	90	8
Berndtite (SnS ₂)	P -3 m 1	3.638	3.638	5.88	90	90	120	3
Ottemannite (Sn ₂ S ₃)	P n m a	8.878	3.751	14.02	90	90	90	20
β -SnS	C m c m	4.31	11.705	4.318	90	90	90	8
π -SnS	P 2 ₁ 3	11.7	11.7	11.7	90	90	90	64

Table 5.1 – Crystallographic information for the crystal structures of the tin sulfides investigated in this study.

Herzenbergite, SnS is the classic tin sulfide compound in the thermoelectric literature. It is isostructural with SnSe, consisting of folded or “corrugated” sheets of hexagonal Sn(II)S, which are stacked in an A - B pattern. The structure is reminiscent of black phosphorus, as seen in the previous chapter, also possessing of a large degree of anisotropy. Figure 5.1 demonstrates the anisotropy present in this material, with projected views along the three crystallographic vectors, which in this case happen to align with the transport directions later in the chapter. From the projection along *b*, the alternating A – B stacking pattern is not obvious, but from the projection along *a* one observes “handedness” of the layers, that is the tin (silver) atoms are present on only one side of the corrugations at the surface of each layer. The off-centre nature of the stacking is highlighted by the projection along *c*.

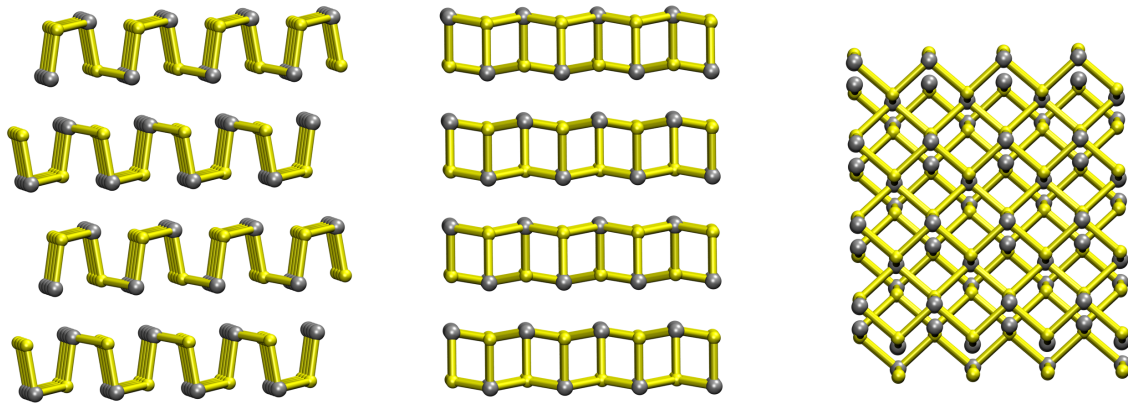


Figure 5.1 – The Herzbergite, α -SnS, crystal structure. Left to right: looking down the a , b and c axis. The geometry is very similar to that of black phosphorus.

Herzbergite is the ground-state phase of SnS, and it has recently been determined that this phase is subject to two subsequent phase transitions at elevated temperatures. This fact allows for a unique opportunity to investigate the effect of temperature induced phase transitions in thermoelectrics, a key consideration when the operating temperatures of an application are close to the critical temperature of the phase transition.

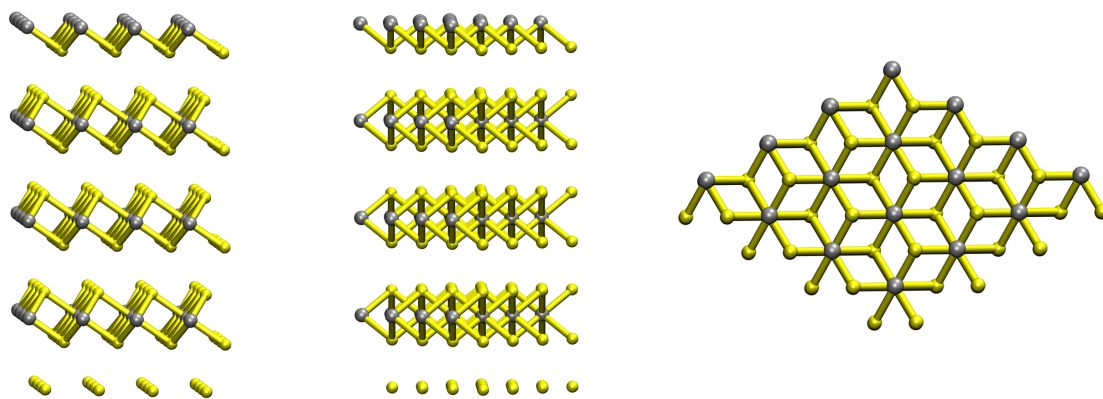


Figure 5.2 – The Berndtite, SnS_2 , crystal structure. Left to right: looking down the a , b , and c direction. The crystallographic vectors, a and b are at 60° to one another, but to model transport, an orthogonal Principle Layer (PL) was constructed.

Berndtite is the crystal structure of the Disulfide of tin (SnS_2). Another 2D, layered material, Berndtite is believed to be a poor thermoelectric, owing to its large band gap. Despite this, it has received attention within other fields of thin film applications. The chemistry of the surface of each layer is explicitly governed by the sulphur atoms which sandwich the layer of tin atoms. Berndtite has a hexagonal unit cell, as observed in figure 5.2, however, for transport calculations a primitive

orthorhombic cell was constructed, the orthogonal vectors of which are demonstrated by the projections in figure 5.2.

The final, somewhat rarer compound of tin and sulphur is Ottemannite, Sn_2S_3 . The scarcity of the mineral is often attributed to its propensity to phase separate as SnS and SnS_2 . The material consists of stacks of one dimensional “ribbons” which are bound by weak intermolecular forces. The ribbons are actually layers identical to those of Berndtite, cleaved either side of the tin atoms, leaving a material that possess two charge states on tin, formally Sn(II) and Sn(IV) . This ribbon-structure was hoped to yield some interesting thermoelectric properties due to its 1-dimensional nature.

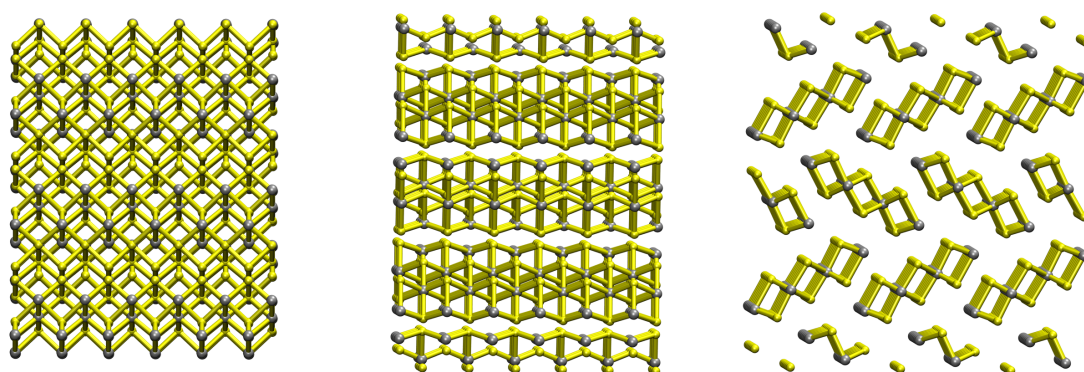


Figure 5.3 – The crystal structure of Ottemannite, Sn_2S_3 , along transport vectors a , b and c . This unique crystal structure consists of stacks of “1-dimensional” nanoribbons.

It had been known for some time, that at elevated temperatures, the ground state phase of tin selenide transformed into a nearly tetragonal phase, $\beta\text{-SnSe}$ at 825 K. It has recently been shown that due to its similar chemistry tin sulfide, $\alpha\text{-SnS}$, also transforms into the $\beta\text{-SnS}$ phase at 905 K. Upon investigation, it was determined that $\beta\text{-SnS}$ is not a metastable phase of SnS at all, but a superposition of the two degenerate structures of Herzenbergite, i.e. a result of the simultaneous breaking and formation of bonds in the SnS layers. Despite this, $\beta\text{-SnS}$ is widely recognised as a distinct phase, as its symmetry reflects the properties of the material above these temperatures.

In Figure 5.4, it can clearly be seen that a compression or “averaging” along b in Herzenbergite (figure 5.1) would result in a higher symmetry SnS layer. Whilst each layer is actually degenerate along a and b , the stacking configuration necessary to minimise atoms overlap between layers results in an $A - A'$ scheme, where the layers are displaced along a by 0.5 of a unit cell length. This is the cause of the Orthorhombic space group, Cmca .

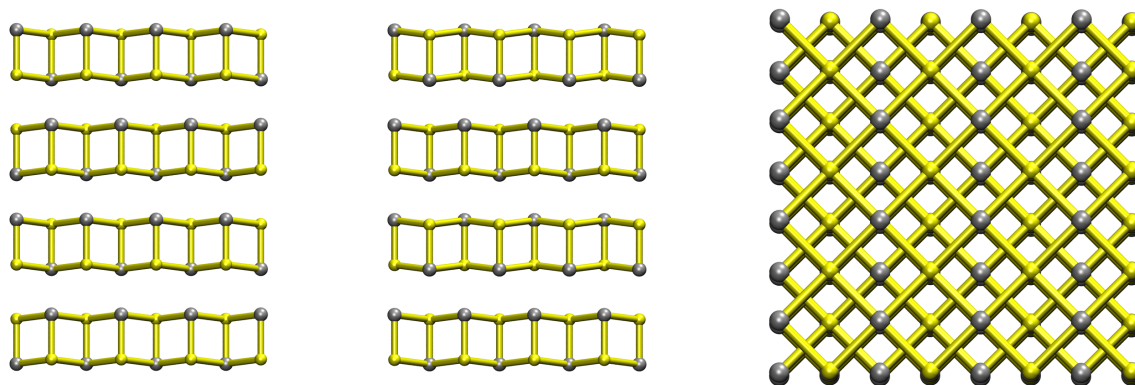


Figure 5.4 – The crystal structure of the high temperature phase of tin mono-sulfide, β -SnS. Left to right: looking along transport vector a , b , and c .

The most recent addition to the tin sulfide family is the cubic π -phase of SnS, the structure of which had only been recently determined, despite the knowledge that a cubic phase was present in the deposition of thin films of SnS for use in the photovoltaic industry. The reason for the delay in identifying the structure was the misattribution of both the rock salt and wurtzite crystal structures to the X-ray Diffraction (XRD) patterns of the cubic phase, neither of which was deemed to be a perfect explanation for the data obtained. This material has been detected under ambient conditions, though only in thin films and as nanoparticles. The structural rearrangement required to form α -SnS is slight, and it is believed that in the bulk, this material would readily undergo a phase transition to Herzenbergite. Figure 5.5 shows the cubic geometry of this material, the unit cell of which is large at 64 atoms, potentially ideal for thermoelectric applications.

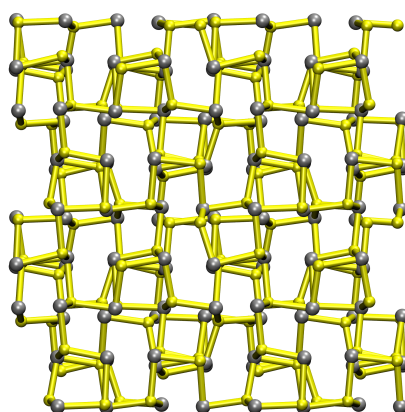


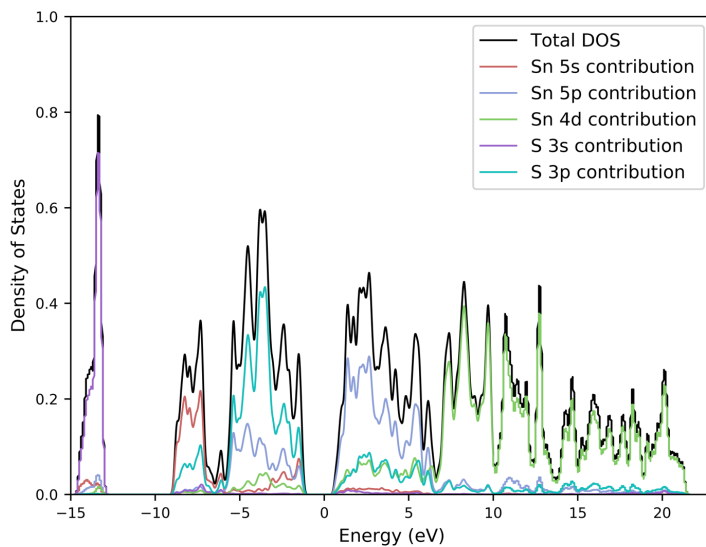
Figure 5.5 – The recently discovered high temperature phase of tin mono-sulfide, π -SnS. This material has cubic symmetry (α , β & $\gamma = 90^\circ$, $a = b = c$), and so there is only one possible representation. π -SnS therefore, is the only tin sulfide phase to possess isotropic properties.

Figure 5.6 contains the calculated density of states of each of the ambient tin sulfides. The band gap of Herzenbergite is acceptably close to that of the literature, at 1.6 eV, while that of Berndtite is somewhat larger at around 4.5 eV. The band gap of Ottemannite is somewhere between the others, as may be expected from the mixing of stoichiometries and coordination spheres, at approximately 2.5 eV. This is rationalised as follows. In crystal field theory, the splitting of the d-orbitals is known to increase with increasing oxidation state. For the case of Herzenbergite, tin(II) sulfide, the tin ions are in their lowest (formal) oxidation state of +2, and therefore the gap is relatively small (though still present). In Berndtite, tin(IV) sulfide, the tin atoms are formally in oxidation state +4. Here the splitting between the bands corresponding to the d-orbitals will likely be much greater than for tin(II) sulfide, and thus the material possesses a larger band gap. In Ottemannite, there are two crystallographically distinct tin species, and due to their coordination, one is formally in the oxidation state +4, whilst the other is in +2, i.e. tin(II)(IV) sulfide. Whilst the splitting of the d orbitals at each site would likely be very similar to that of each of the respective aforementioned species, the overlap between these d-orbitals in the solid state would result in bands with a gap between these two extremes in size.

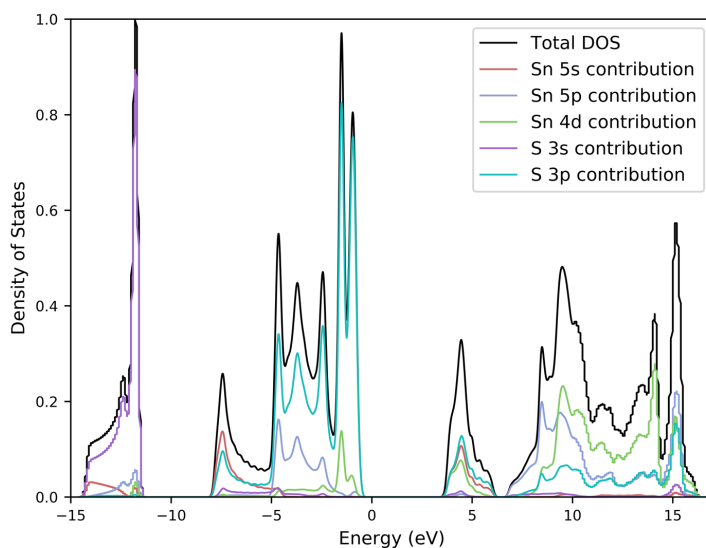
The majority of the work in this chapter focusses on the region within +/- 4 eV of the Fermi level for each material. As such, we can see from the corresponding density of states that this region of the “Fermi window” for Herzenbergite is predominantly defined by the p orbitals of both tin and sulphur, with noticeable contributions from the tin 5s and 4d. For Berndtite, the DOS is dominated by the sulphur 3p orbitals in the valence band, whilst the conduction band is almost equally defined by the tin 5s, 5p and sulphur 3p. For Ottemannite, the scenario is a similar story, the tin and sulphur p orbitals are the main contributors, though the tin 5p and 4d orbitals are present. The DOS therefore allow for a consideration of the orbitals that are likely contributing to the transmission spectra significantly, and thus defining the thermoelectric properties of the tin sulfides.

The DOS calculations were performed using the DFTB formalism and self-consistency as implemented by the dftb+ code. Using a k-grid of 15-15-15, the partial contributions from each shell were calculated, along with the total.

Density of States of Herzenbergite, α -SnS



Density of States of Berndtite, SnS₂



Density of States of Ottemannite, Sn₂S₃

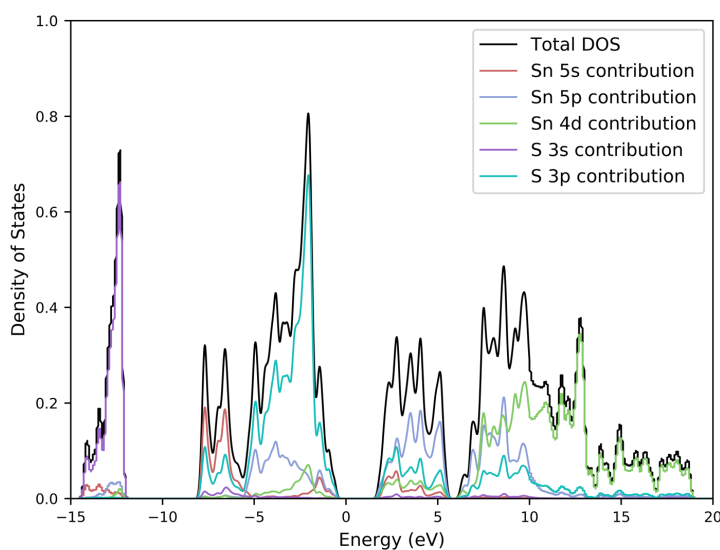


Figure 5.6 – Density of States for each of the ground-state tin sulfides. Calculated using the dftb+ code, with k-grids of 5x5x5 for Herzenbergite and Berndtite, and 4x4x4 for Ottemannite.

5.3.2 – BANDS

Using the optimised ground-state structures, the geometries were re-optimised and symmetrised using DFT level theory, as implemented in the quantum espresso plane wave package. The pseudopotentials were norm conserving, and implemented the PBE functional. K-grids of 4-4-4 were used for the optimisation, 6-6-6 for the self-consistent step and 12-12-12 for the consequent non-self-consistent step. The K-point path was explicitly specified for the final bands calculation, according to the convention specified by Cortarolo.

We see a different convention with band gaps compared to those of the DOS, where the bandgap of Berndtite is more than that of Ottemannite, which is less than that of Herzenbergite. The band gap of Herzenbergite is less than that of Berndtite. DFT methods are often known to underestimate the band gap, and so it was taken as a good sign that the magnitudes were comparable using this methodology to those obtained by the DOS using the DFTB approach. Specifically, the band gap of Herzenbergite is direct, and approximately 1.2 eV, for Berndtite it is indirect and approximately 1.5 eV, and for Ottemannite it is approximately 0.9 eV. The band gap of Herzenbergite is close to that of experiment, which is reportedly 1.1 eV. The band gap of Berndtite is a little smaller than that of experiment at 2.3 eV.¹⁸ However, in this report, the band gap of bulk Herzenbergite is expected to be 0.87 eV using DFT level theory, or 0.89 eV using DFTB theory. This was seen as reasonable agreement for the methods used, and encouraging in that the reported DFT and DFTB values did not vary greatly.

We note for all structures, that the effective mass of the valence band is visually fairly small, with bands that span several electronvolts. For Ottemannite, we also note the higher band degeneracy of the valence band, which is a criteria for higher Seebeck coefficients that do not necessarily come at the cost of lower conductivities.

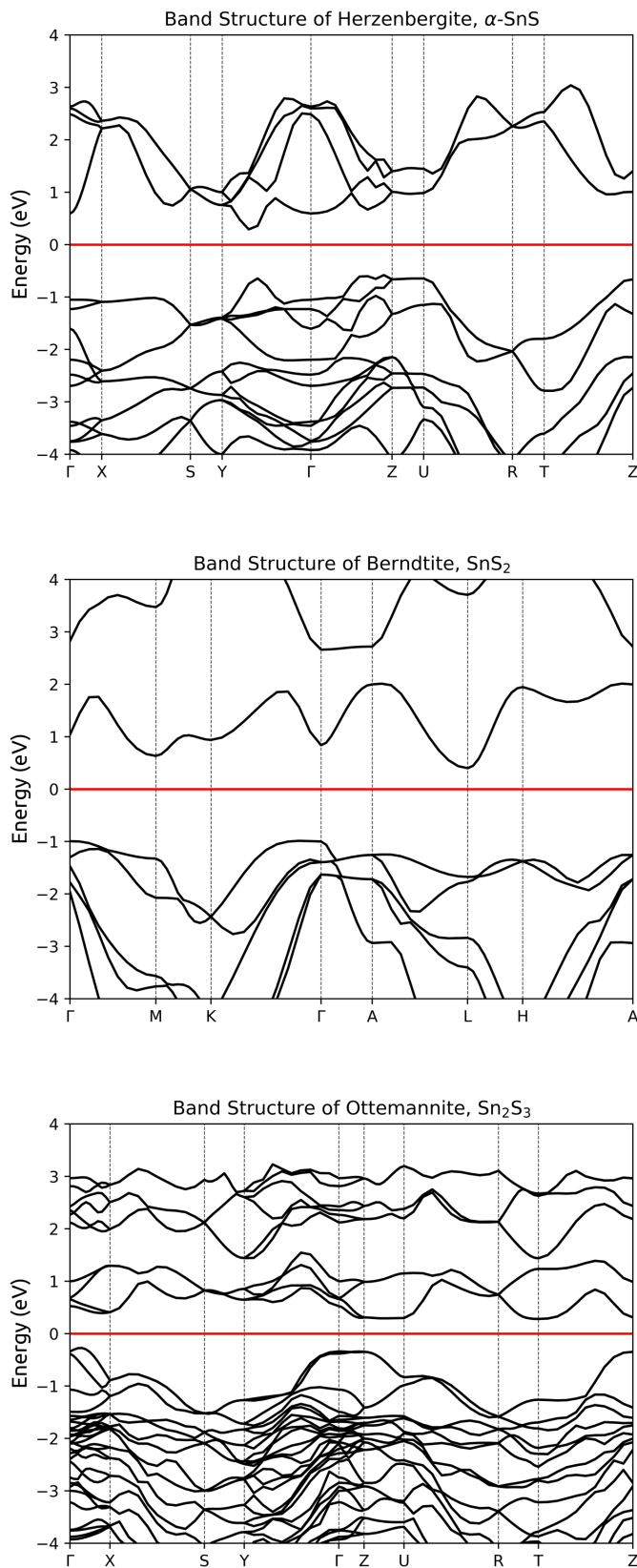


Figure 5.7 – The band structures of the ground-state tin sulfide compounds. The red line indicates the Fermi level. Calculated with the quantum espresso plane wave code, using wavefunction cutoff of 50 Ry, DFT-D Van der Waals correction, and a 12x12x12 k-grid.

5.3.3 – EQUATIONS OF STATE

The equations of state for several existing and predicted tin mono-sulfide compounds were calculated. Figure 5.8 demonstrates the findings. The mono-sulfides were chosen due to the known rich phase-space, the Herzbergite and β -SnS were chosen as they were known to exist. The Rock Salt (RS) Wurtzite, Zinc Blende and Cesium Chloride geometries were chosen as candidate structures for the cubic phase, which had not been published at the time of this initial investigation. The equations of state are essentially a plot of total energy versus volume, and this data was calculated using DFT Plane Wave (PW) methods, using PBE functionals and norm-conserving pseudopotentials. The approach was as follows.

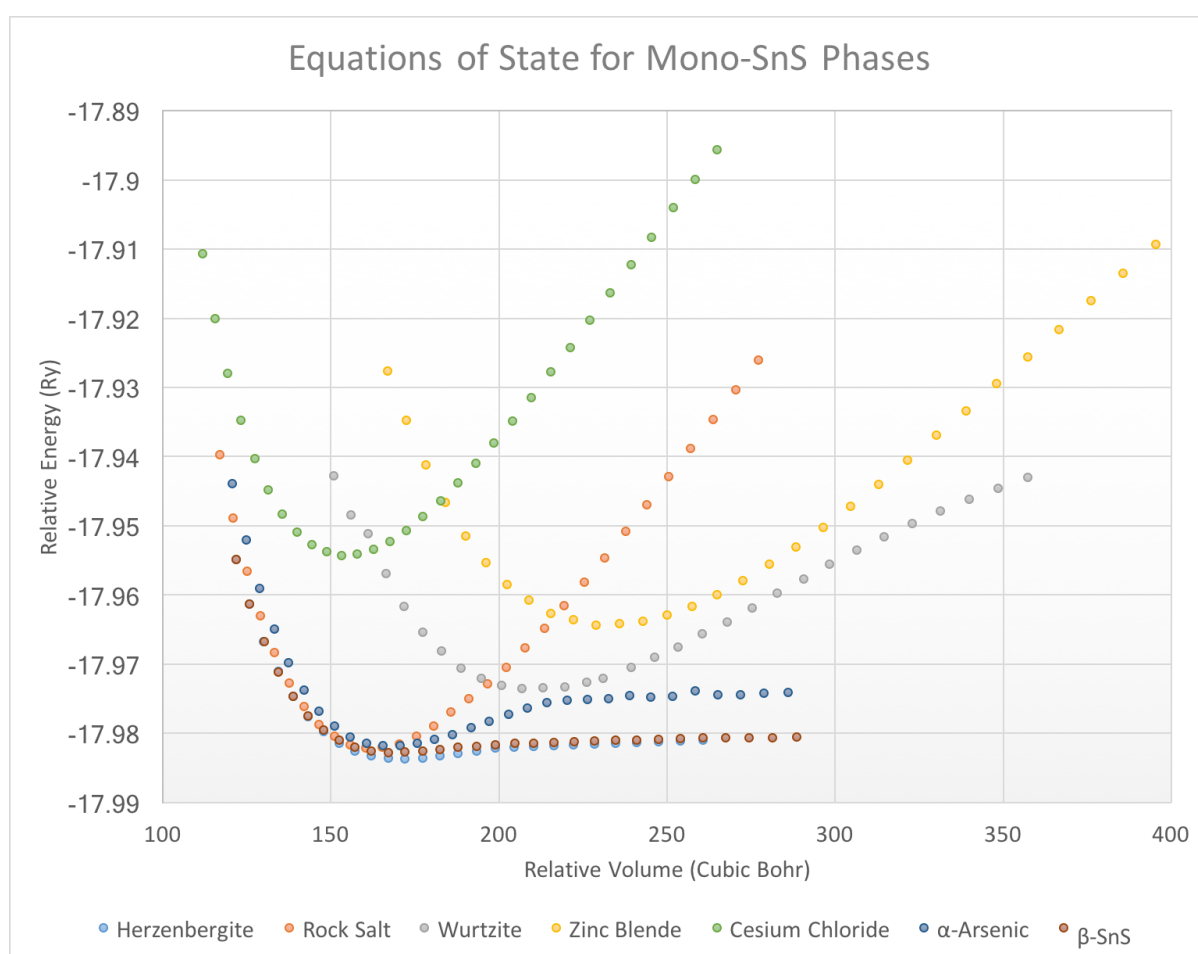


Figure 5.8 – The equations of state the known and possible phases of tin mono-sulfide. Calculated using the quantum espresso plane wave code, wavefunction cutoff of 50 Ry, k-grid of 4x4x4.

The crystal structures were prepared for Herzenbergite and β -SnS from published crystal structure data. The “theoretical phases” were prepared by obtaining the relevant crystallographic information for the compounds in which these materials are known to occur, before rescaling to fit the volume of the unit cell to:

$$V_u = N \cdot V_a$$

Where V_u is the volume of the generated unit cell, N is the number of atoms in the theoretical unit cell, and V_a is the average volume per atom in the Herzenbergite unit cell. These generated geometries were then relaxed according to the BFGS formalism, under variable volume – fixed cell angle conditions. These relaxed structures were then scaled incrementally to both smaller and larger volumes by varying cell length a by 1%, while maintaining the ratios b/a , c/a . These frustrated cells were then relaxed under variable cell – fixed volume conditions. The total energy from the final relaxations were then divided by the total number of atoms in the unit cell, as shown in figure 5.8.

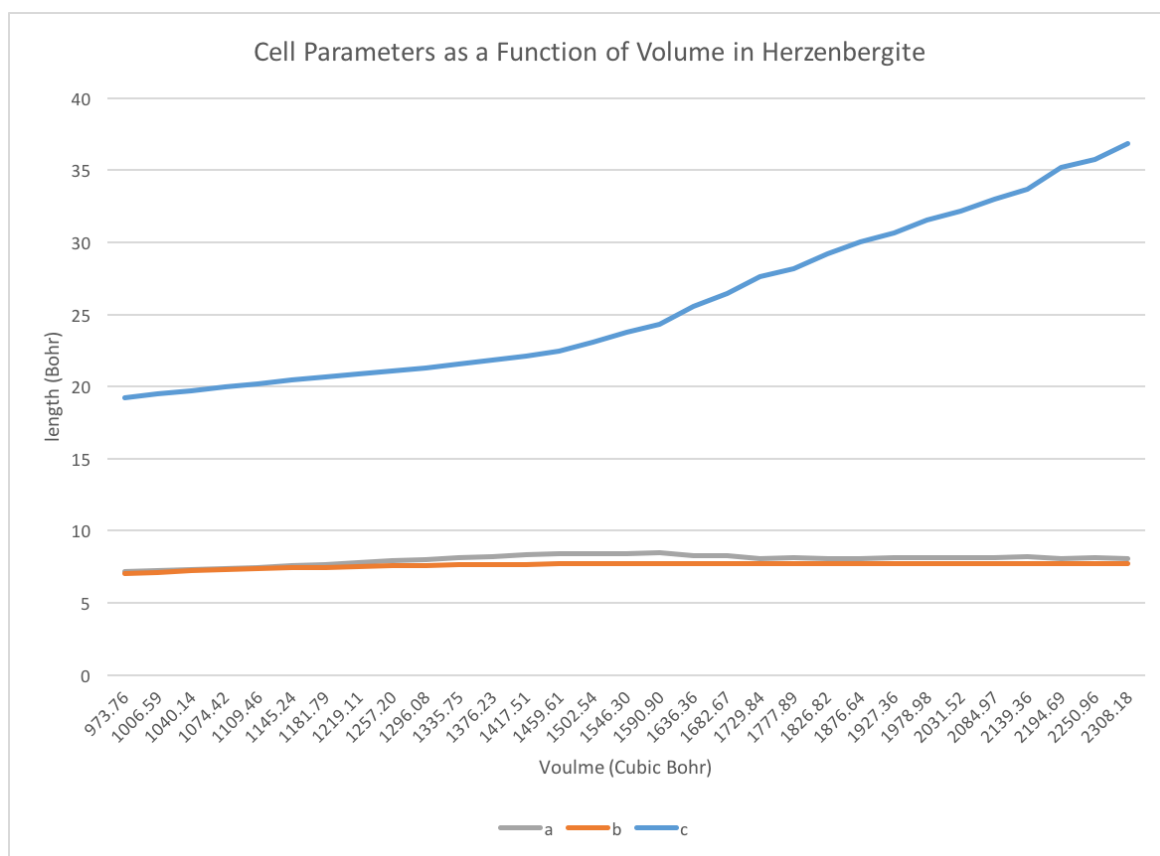


Figure 5.9 – The effect of increasing volume in the cell parameters of Herzenbergite. Calculated using quantum espresso, with a wavefunction cutoff of 50 Ry, and a 4x4x4 k-grid.

The observation that the Herzenbergite structure is the lowest in energy across the range is reassuring, as this is known to be the ground state structure under ambient conditions. Clearly, the zinc blende and cesium chloride crystal structures are rather high in energy compared to the rest of the structures, and it seems unlikely that a phase transition would occur towards these geometries, as at no point are they the most favourable in energy. The Wurtzite geometry is a little lower in energy than the zinc blend, but it is still far higher than the curves for Herzenbergite and β -SnS.

An interesting observation, is that the materials which would possess 3-dimensional covalent bonding schemes exhibit a similar “well-like” curve, whereas the layered structures possess a shallow curvature at greater volumes. This behaviour was reasoned to be due to the ability of these materials to expand in their respective interlayer directions, in which they are bound by weaker intermolecular forces, whilst maintaining their covalent bonding scheme in the lateral directions, reducing the strain on the higher energy covalent bonds. This was confirmed by a study of the effect of volume on the lattice parameters of Herzenbergite and Wurtzite, where it was found that in Herzenbergite, the cell length c diverged from a and b at higher volumes, while a and b remained fairly constant, as in figure 5.9. For Wurtzite, the cell remained cubic.

Figure 5.10 shows an inflated view of the point where the equations of state of Herzenbergite, β -SnS, α -Arsenic and Rock Salt are close in energy. Herzenbergite remains the lowest in energy, but at lower volumes, it can be seen that the curves for Herzenbergite and β -SnS become isoenergetic. The Rock Salt phase is very close in energy to Herzenbergite at this volume, however, it is still greater in energy than the β -SnS phase, thus it seems unlikely that this phase may be adopted over the lower energy pair.

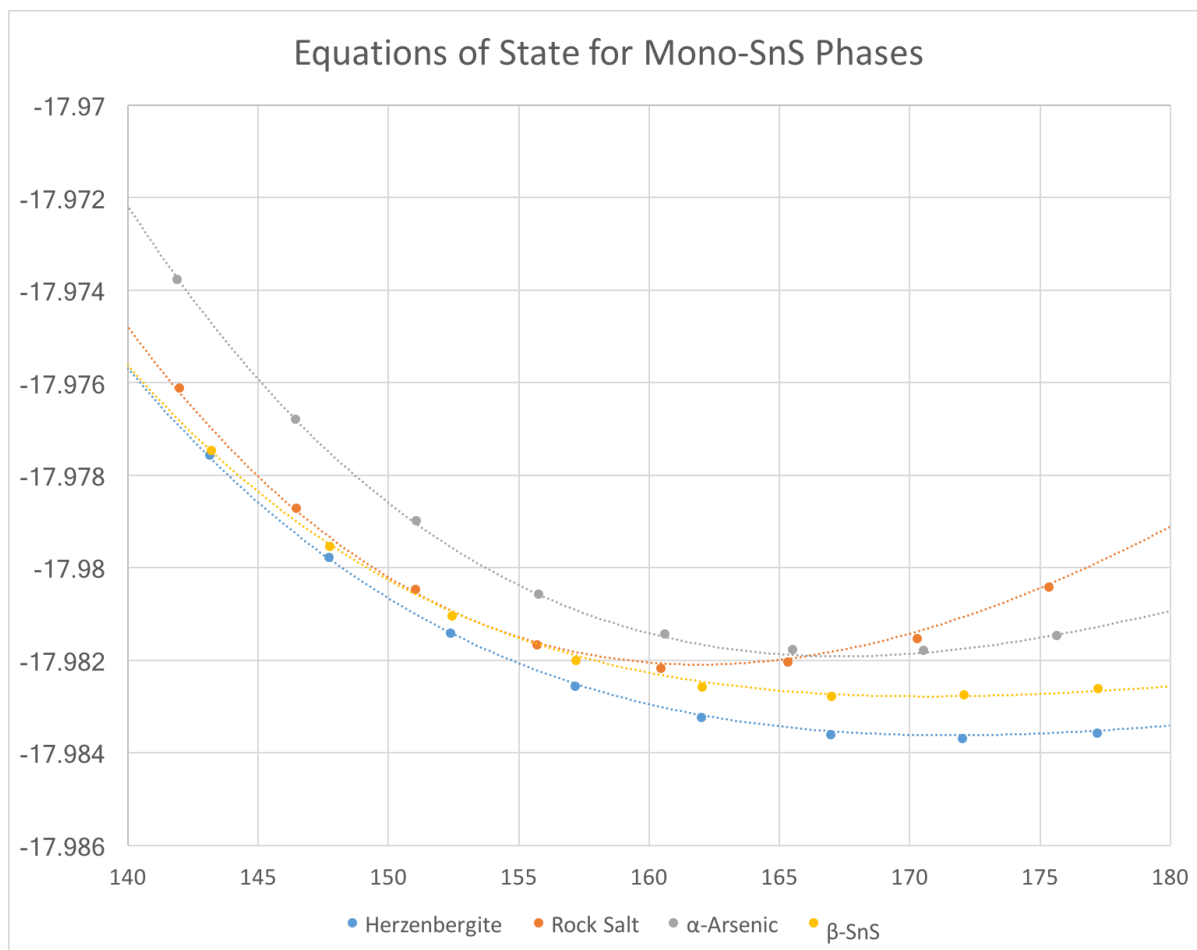


Figure 5.10 – Inflated view of equations of state crossing. Calculated using the quantum espresso plane wave code, wavefunction cutoff of 50 Ry, k-grid of 4x4x4.

5.4 – TRANSPORT IN TIN SULFIDES

In this section, the calculation of transmission spectra, and subsequent derivation of thermoelectric properties is presented for the naturally occurring ground-state tin sulfide compounds. The transmission was originally calculated in the non-self-consistent (NSCC) manner as in the previous chapter, though an appreciation of the requirement of self-consistency (SCC) is then demonstrated.

5.4.1 – TRANSMISSION OF TIN SULFIDES

Nanowires of Herzenbergite were prepared for each of the 3 crystallographic replications, in order to fully characterise the effects of anisotropy in this material. The wires consisted of 6 Principle Layers (PLs) of 400 atoms, for a total of 2400 atoms. Two PLs were required for each of the contact regions, the remaining two formed the device region. The inclusion of the d-orbitals and additional electrons (compared to phosphorus) dramatically increased the calculation times for the density of states, and so it was anticipated to detrimentally effect the time necessary to calculate the electronic transport. As such, the initial transport calculation was performed with a small K-grid sampling of 2-2-2 and a large energy range sampling of 0.1 eV.

All tin sulfide dftb-negf calculations in this chapter were performed utilising the Slater-Koster (slako) files provided by J. Joswig and T. Lorenz.^{18,19,20}

Figure 5.11 shows the original transport calculation for a in Herzenbergite. This calculation was performed to gain some insight into the structure of the wider electronic transmission spectrum before work could focus on the window within ± 4 eV of the Fermi level. Calculation of transport was only necessary in one direction to appreciate the structure. The shape of the transmission spectra is clearly reminiscent of the DOS of Herzenbergite (fig. 5.6) with a large peak corresponding to the sulphur 3s orbital around -15 eV, the distinctive triplet of the sulphur 3p orbitals between -1 and -8 eV, the 5p orbitals of tin at 1 to 6 eV and part of the tin 4d orbitals above 5 eV. The tin 5s orbitals are suspected to be hidden by the magnitude of the lowest energy 3p orbitals at around -7 eV.

As for chapter 4, for all calculations of electronic transport in this chapter, dispersion correction was not included. This is in part due to the calculations being extrapolated from those defined in the tutorial for the dftb-negf code, which did not include a dispersion correction. Additionally, DFTB does not include Van der Waals interactions, and so any attempted correction is purely empirical, requiring an additional set of parameters which had not been acquired for this work.

Electronic Transmission Spectrum of Herzenbergite, SnS

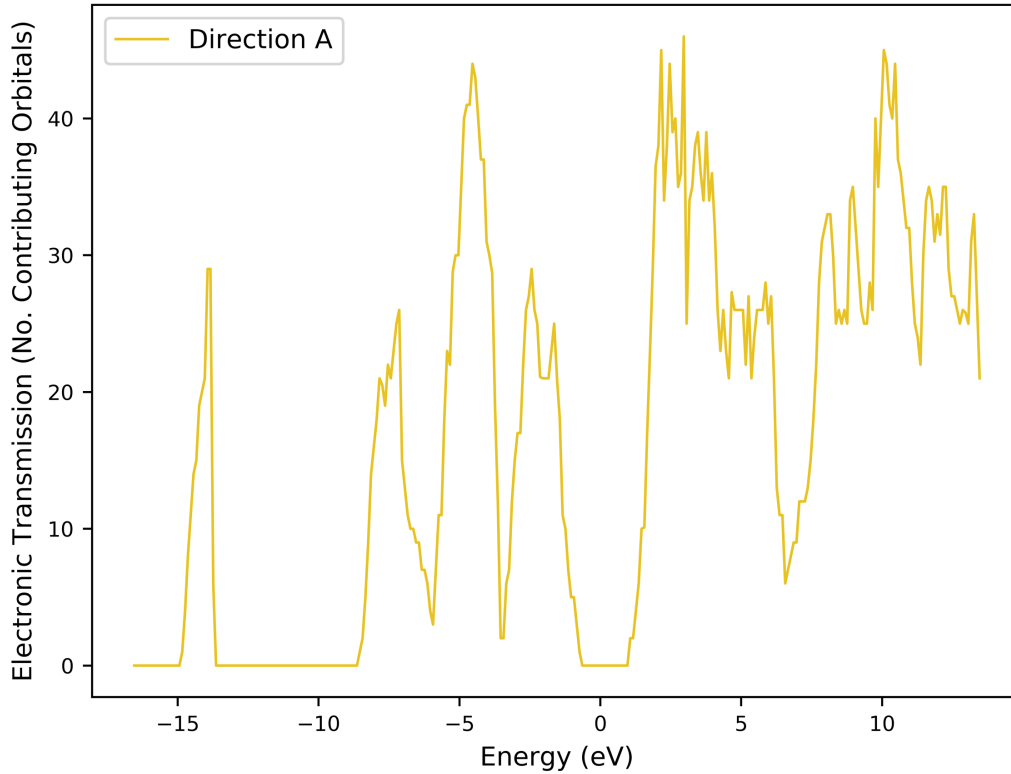


Figure 5.11 – The initial transmission calculation of Herzenbergite along a . This calculation was performed with `dftb-negf`, using a reduced K-grid of $2 \times 2 \times 2$ and a large energy step of 0.2 eV, in order to visualize the wider transmission spectrum. Subsequent calculations would be performed utilising a larger K-grid and energy sampling, within a smaller energy range.

Figure 5.12 details the transmission in the 8 eV region about the Fermi level for Herzenbergite, at a far higher resolution, and for each of the three transport directions. The effects of anisotropy are clear for the valence band, though the gradient of the conduction band is similar for each direction. As would be expected from the model of weak inter-layer bonding proposed in the previous chapter for the isostructural black phosphorus, the transport along c is less than that along a and b for the whole energy range. The high orbital overlap along a is the likely root of the high transmission along this vector.

Electronic Transmission Spectrum of Herzenbergite, SnS

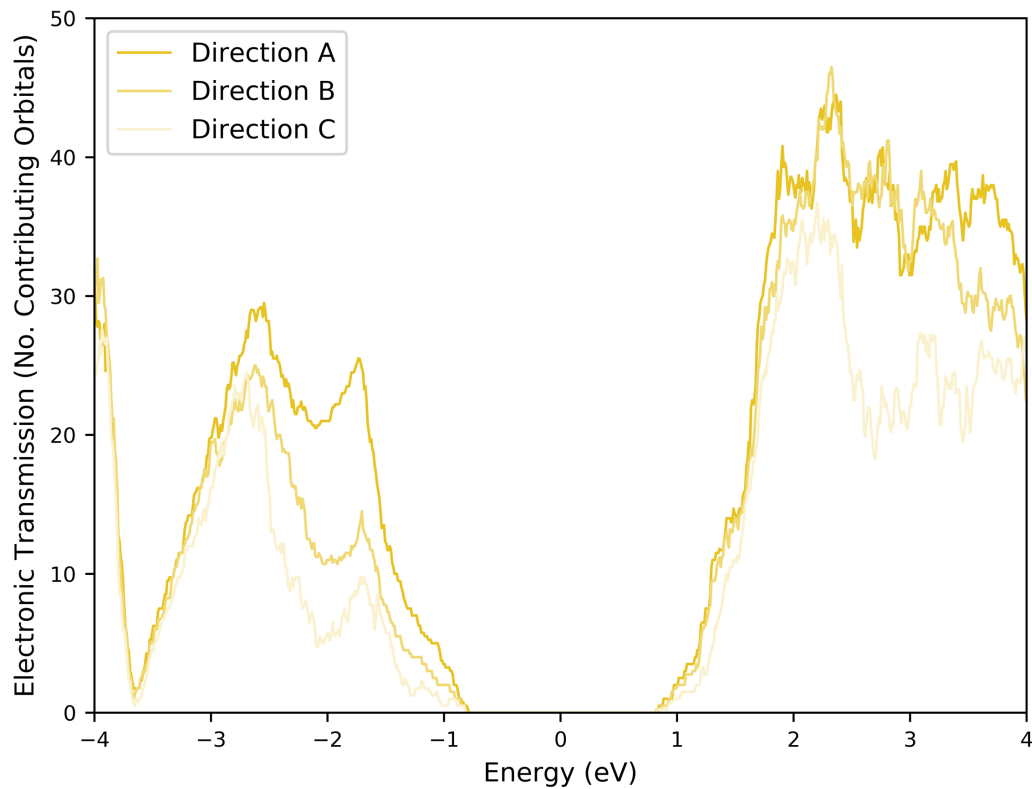


Figure 5.12 – The high-resolution transmission spectrum of Herzenbergite. The energy range of +/- 4 eV from the Fermi level was determined to be suitable for the temperatures considered. Calculated using dftb-negf with an energy step of 0.01 eV and k-grid of 4x4x4.

Another distinction between the transmission of Herzenbergite and black phosphorus is the shape of the transmission, i.e. the gradient and magnitude of the contribution of the valence versus the gradient and magnitude of the conduction band. In black phosphorus, the gradient and magnitude was observed to be distinctly similar for both conduction and valence bands, and the bands themselves were formed of just the 3p orbitals of phosphorus. Here, the differing contributions of chemical species and their respective orbitals is likely to govern the thermoelectric properties.

Electronic Transmission Spectrum of Berndtite, SnS₂

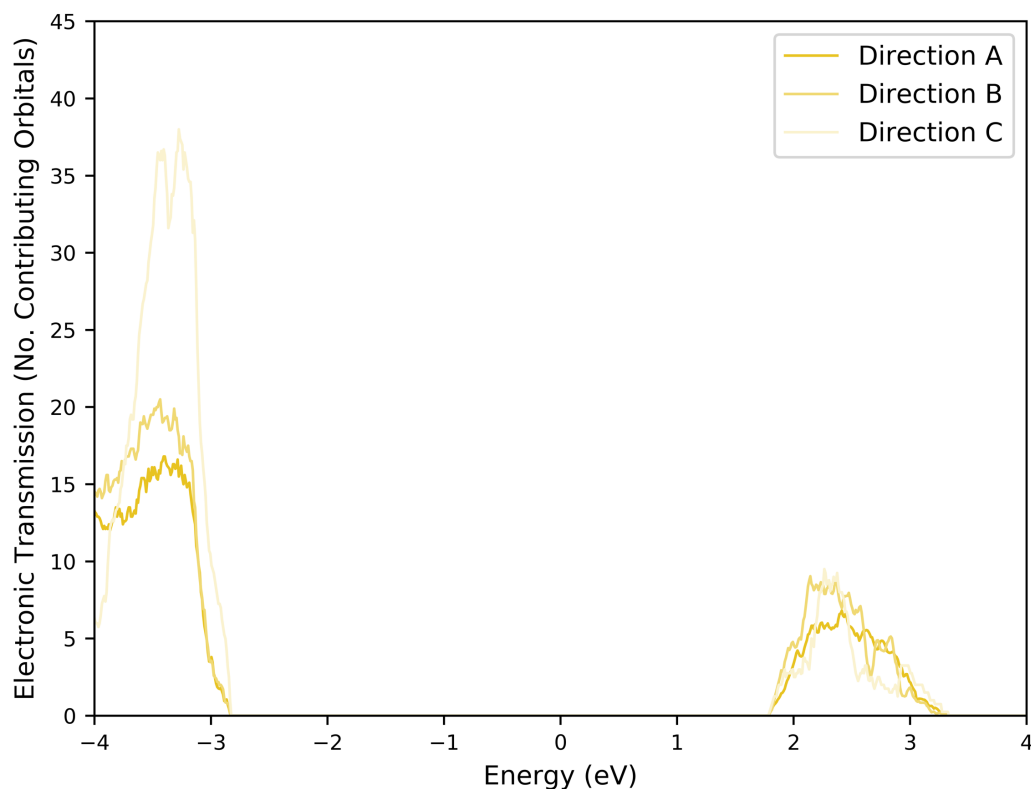


Figure 5.13 – Transmission spectrum of Berndtite. The system appeared to have a particularly large band gap, as well as a small number of orbitals forming the conduction band above the Fermi level. Calculated using dftb-negf with an energy step of 0.01 eV and k-grid of 4x4x4.

The transmission of Berndtite is detailed in the figure 5.13. We note the unique shape, with the large band gap separating the valence band, formed of mostly sulphur 3p orbitals, from the small conduction band which consists of the sulphur 3p, and the tin 5s and 4d. This unique feature will likely lead to some interesting results for the electronic thermoelectric properties. The Fermi level is noticeably closer to the conduction band, and so it is likely the conduction band that will govern these properties, however, of note is the large transmission along c in the valence band, which suggests a strong overlap between orbitals in the neighbouring sheets of SnS₂. The band gap is somewhat large, at approximately 4.5 eV, meaning the thermal conductivity of the electrons is likely to be far smaller than that of the phonons.

Electronic Transmission Spectrum of Ottemannite, Sn_2S_3

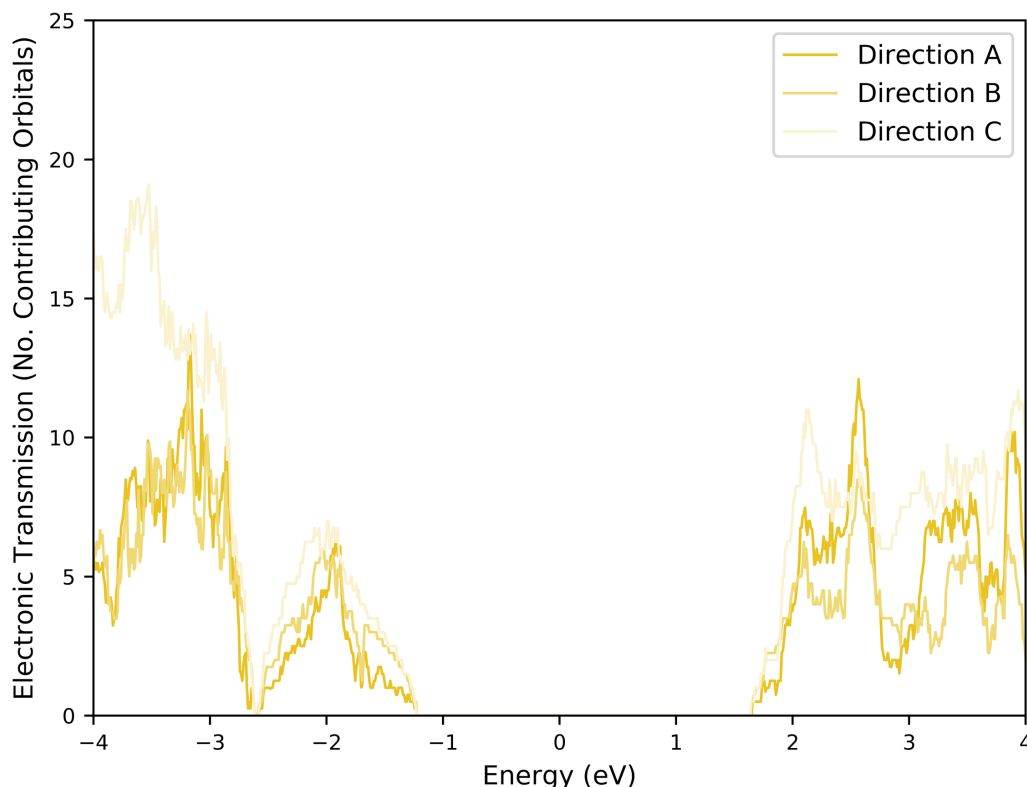


Figure 5.14 – Transmission spectrum of Ottemannite. The band gap is between that of Herzenbergite and Berndtite in size, which is likely due, in part, to the stoichiometry. Calculated using dftb-negf with an energy step of 0.01 eV and k-grid of 4x4x4.

The transmission spectrum of Ottemannite, as shown in figure 5.14 has a large degree of anisotropy in both the conduction and valence bands. The transmission along *c* is noticeably higher, which corresponds to the *c* axis. It should be noted that the bonding along *c* is exclusively covalent, and so it would be expected that transport along this direction would differ greatly from *a* and *b*. The thermoelectric properties are likely to be governed by the valence band, as the fermi energy is noticeably closer to this side of the band gap. As such, one could argue it is the 3p orbitals that govern the thermoelectric properties of this material, opening these crystallographic positions to the possibility of doping with guest species to tune the shape of the DOS and transmission in this region.

5.4.2 – THERMOELECTRIC PROPERTIES OF HERZENBERGITE, SNS

Using the transmission calculated in the previous section, the thermoelectric properties of Herzenbergite were derived using the same methods as detailed in the preceding chapter, namely, the Landauer-Büttiker formalism within the Non-Equilibrium Green's-Functions (NEGF) approach.

5.4.2.1 – TEMPERATURE DEPENDENT THERMOELECTRIC PROPERTIES

Figure 5.15 displays the temperature dependent thermoelectric properties of Herzenbergite, derived from the transmission spectrum calculated in the previous section, which is included in the top left of this figure for convenience. The striking feature is the magnitude of the zT_e in the region of 300K to 400K, the ideal operating range for room temperature thermoelectrics. This is predominantly due to the magnitude of the Seebeck coefficient in the region.

The electronic conductivity demonstrates the exponential curve typical of semiconductors at high temperatures. The ranking of magnitudes for each direction closely follows the overall average ranking of the transmission, with c being the weakest and a the largest. The electronic contribution to the thermal conductivity follows the same trend, albeit with less distinction between a and b .

The Seebeck coefficient is large and positive for each direction above 300 K, though is rather large and negative for b under 280K. The cause of this is not immediately apparent, though is further explored in 5.4.2.2. It is this negative Seebeck coefficient that is responsible for the large upturn in the zT_e below 280K for b . This highlights an important feature in the zT_e and zT that may go unnoticed until such an example is apparent: zT does not account for the “type” of charge carriers dominating the materials output at a given temperature, i.e. whether it is p- or n-type. This makes the zT_e of 5.13 particularly unique, as it demonstrates that the presence of more than one type of peak in the zT of a material may mean that the charge carriers operating at different temperatures possess differing sign. For example, at approximately 250K, this material is likely an n-type thermoelectric, however, at approximately 320K, whilst the average zT_e may be almost identical in magnitude, the material is now a p-type thermoelectric. An important consideration, were such a material to be incorporated into a device!

The power factor is clearly dominated by the shape of the conductivity, although a 's is significantly larger than b and c , due to the difference in the magnitude of the Seebeck coefficient at elevated temperatures. Thus, the ordering of the zT_e 's mimics that of the Seebeck coefficients, as the electronic and thermal conductivities effectively cancel one another in magnitude.

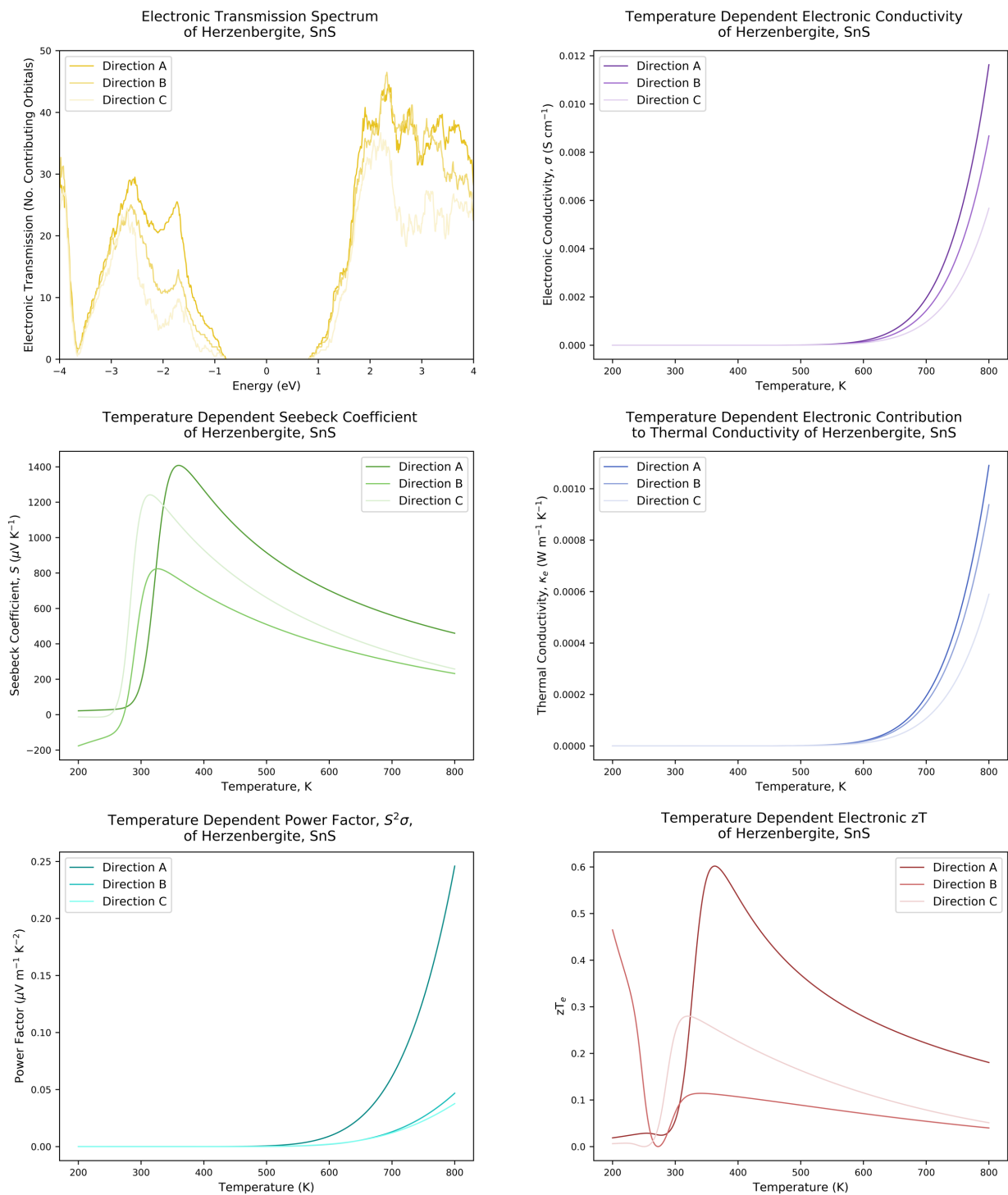


Figure 5.15 – Temperature dependent thermoelectric properties of Herzenbergite. Transmission calculated using dftb-negf with an energy step of 0.01 eV and k-grid of 4x4x4. Thermoelectric coefficients derived using program (see section 3.5), each series contains 6000 points.

5.4.2.2 – POTENTIAL DEPENDENT THERMOELECTRIC PROPERTIES

To investigate the cause of the change of sign in the Seebeck coefficient, as well as to gain a better understanding of the effects on the thermoelectric properties due to temperature, the potential dependent thermoelectric properties of Herzenbergite were calculated at 100, 300 and 500 K. The methodology implemented in the work presented so far has required the iterative derivation of the potential dependent thermoelectric properties of a range of materials, such that the value of each at $\mu = 0$, i.e. the value at the Fermi energy, could be taken and compiled across a range of temperatures, usually 200 K to 800 K.

Figure 5.16 presents the potential dependent electronic conductivity of Herzenbergite at 100, 300 and 500 K. The curvature of this property as a function of potential, clearly maps that of the transmission spectrum, as in figure 5.15. The obvious effect of increasing temperature is the smoothing of the curvature of the transmission. As the values at each μ are dependent on the first derivative of the fermi function, they are non-zero. Whilst it may appear that the conductivity is 0 at 0 eV, one must notice that the order of magnitude of the units of the y axis is huge compared to that reported in the temperature dependent case. The increasing temperature does not drastically alter the maximum values present in the spectra, though the smoothing of the curvature raises the minimum values slightly, and this is responsible for the increase of the conductivity at $\mu = 0$ that is apparent in figure 5.15.

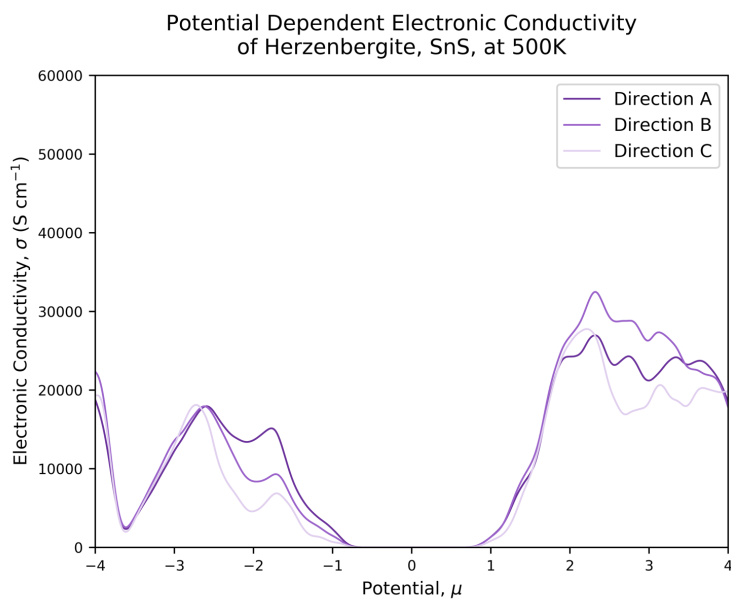
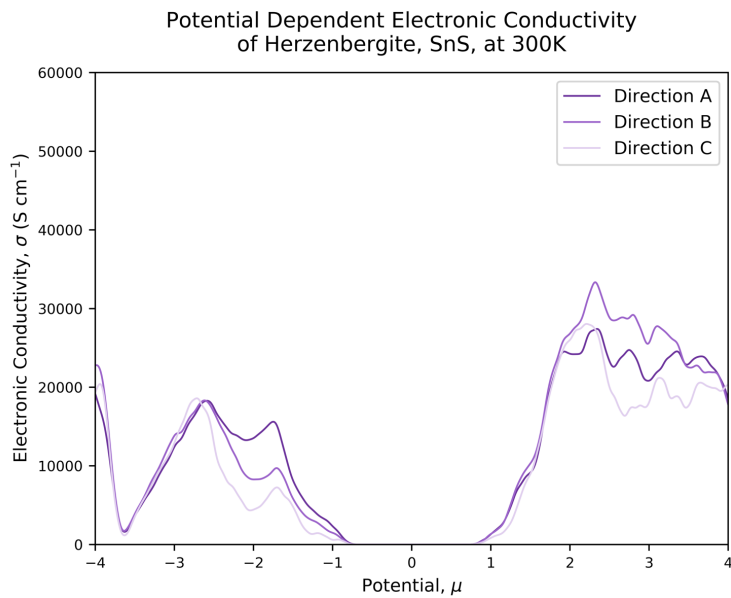
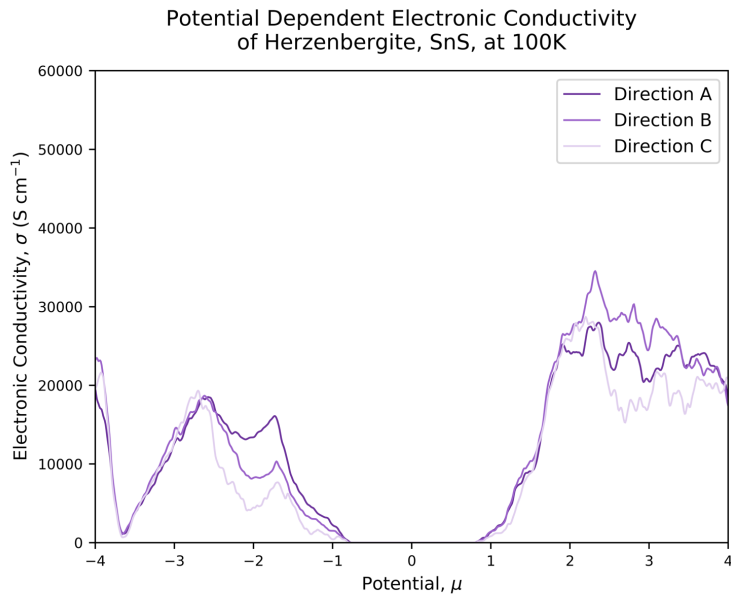


Figure 5.16 – Potential dependent Conductivity of Herzenbergite, at differing temperatures. Transmission calculated using dftb-negf with an energy step of 0.01 eV and k-grid of 4x4x4. Thermoelectric coefficients derived using program (see section 3.5), each series contains 8000 points.

Figure 5.17 demonstrates the effect of increasing temperature on the Seebeck coefficient of Herzenbergite. The Seebeck curve at 500 K is typical of the data reported in the literature, and we note that the effects of anisotropy are almost non-apparent. At low temperatures however, the extrema of the curves are split, as a function of the size of the band gap. The positions of the extrema are similar for each transport vector, indeed the main dissimilarity between the data sets is the magnitude of each direction at a given temperature. The unique feature in the Seebeck curve of b at 100 K is the presence of several additional extrema about the Fermi level. It was determined that these peaks are a consequence of tiny atomic orbital contributions to the transmission in the band gap, which are amplified significantly by the effect of multiplication by the first derivative of the Fermi level and their proximity to the Fermi level, where the magnitude of the first derivative of the Fermi function is largest. It is these states which are responsible for the large, negative value of the Seebeck coefficient along b at lower temperatures as observed in 5.4.2.1.

The “kink” in the Seebeck of a at 300 K is related to the large conductivity of a , which results in a higher charge carrier mobility and thus reduced Seebeck coefficient at $\mu = 0$. The interesting consequence of the abrupt change of sign about $\mu = 0$ is that a slight displacement in the position of the Fermi level may result in a drastically improved value of the Seebeck coefficient at higher temperatures. The maximum value of the Seebeck coefficient is apparent in the lower temperatures, however it is reduced at 500 K. There is a direct correlation between the size of the band gap and the maximal value of the Seebeck.

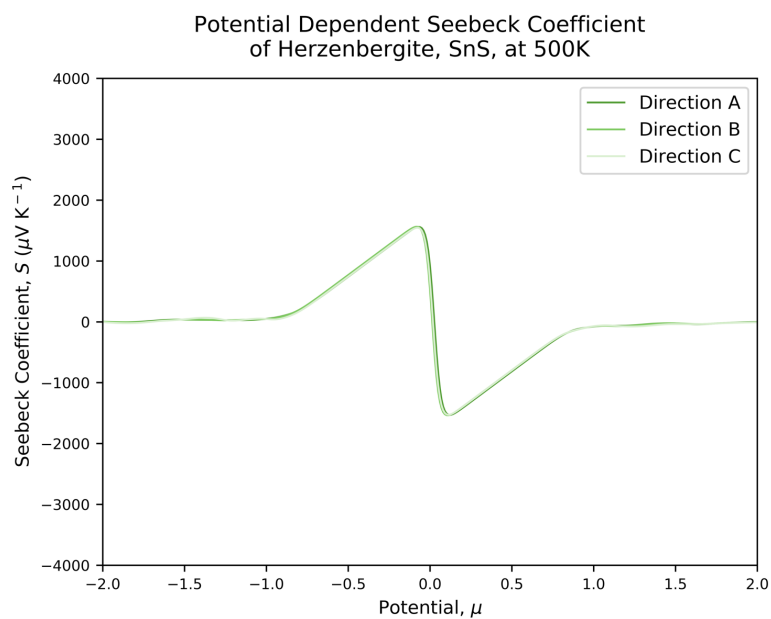
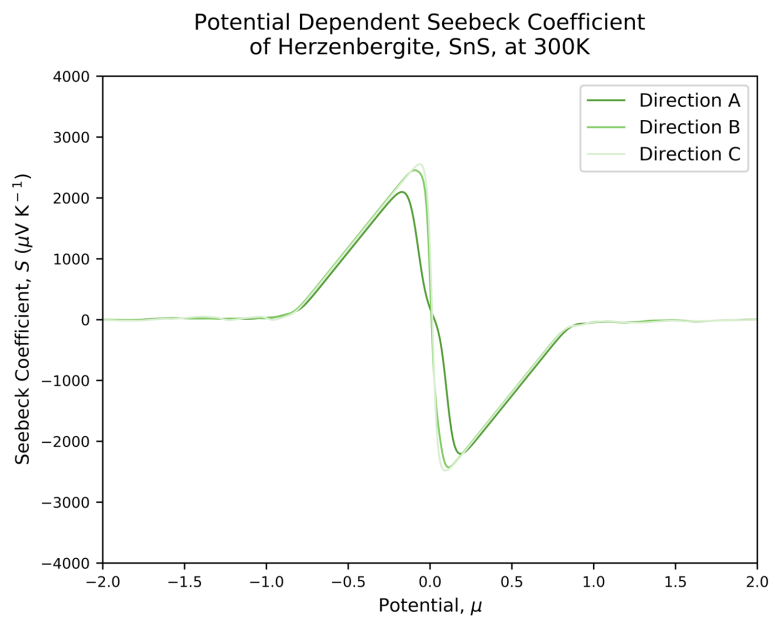
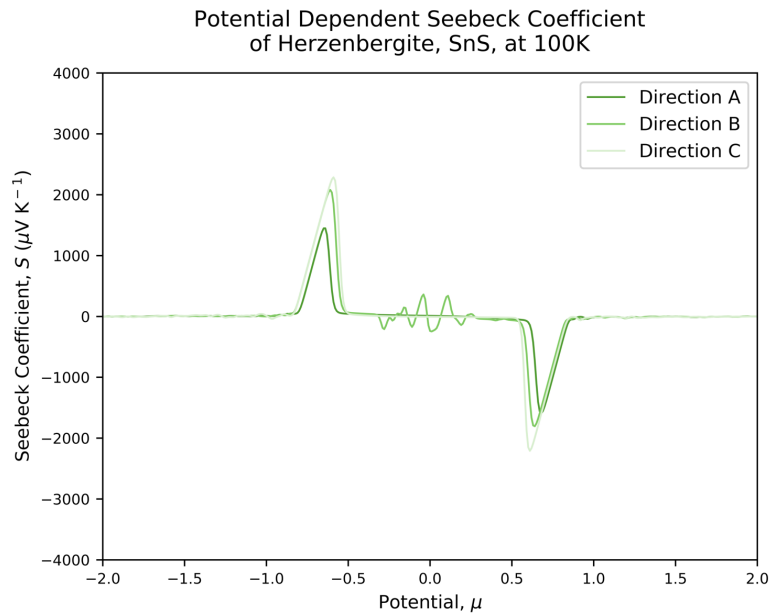
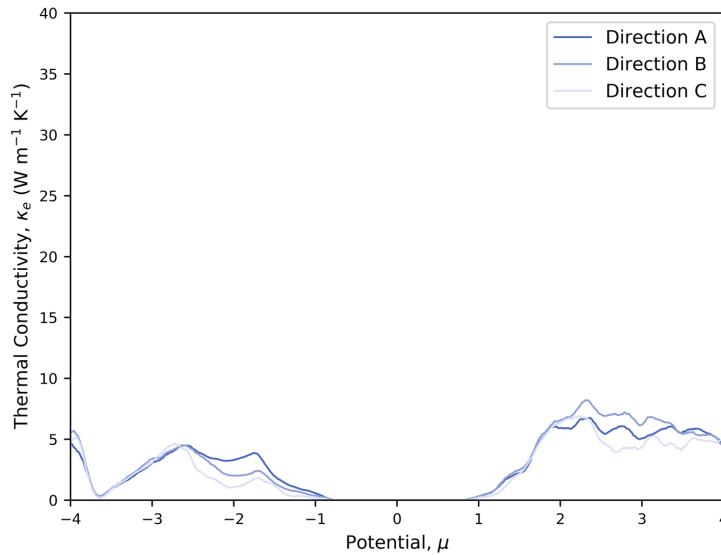


Figure 5.17 – Potential dependent Seebeck coefficients at increasing temperatures. The classic potential dependent Seebeck curve is apparent at high temperatures, but at lower temperatures there is a splitting of the minima and maxima that is governed by the band gap. Transmission calculated using dftb-negf with an energy step of 0.01 eV and k-grid of 4x4x4. Thermoelectric coefficients derived using program (see section 3.5), each series contains 8000 points.

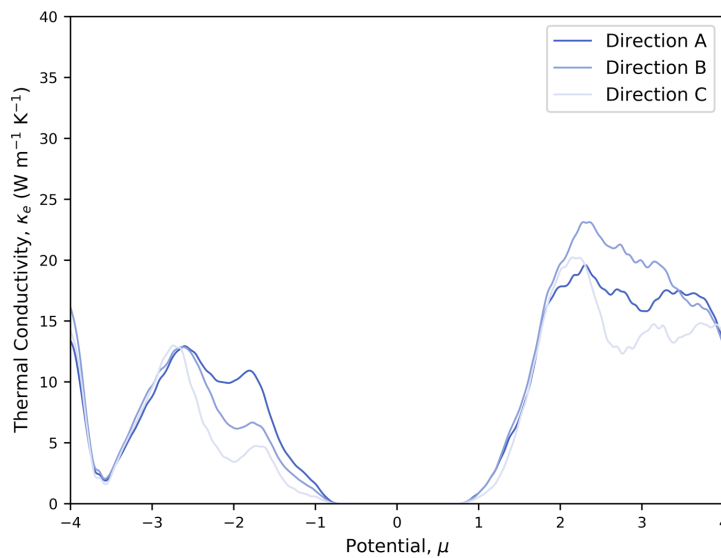
The potential dependent thermal conductivity, as shown in figure 5.18 again is representative of the shape of the transmission, however for this property, the magnitude increases across the potential range with temperature. The maximum value of approximately $10 \text{ W m}^{-1} \text{ K}^{-1}$ at 100 K is more than tripled at 500 K. There is again a smoothing of the curvature which may be attributed to the effect of the Fermi function.

Inspection of the potential dependent thermoelectric properties allows us to probe the causes of interesting features in the temperature dependent plots. Since the shape of both the electronic and thermal conductivities follows the typical exponent of temperature curvature, it is really the potential dependent Seebeck coefficient that holds most information about the thermoelectric properties of the system.

Potential Dependent Electronic Contribution to Thermal Conductivity of Herzenbergite, SnS, at 100K



Potential Dependent Electronic Contribution to Thermal Conductivity of Herzenbergite, SnS, at 300K



Potential Dependent Electronic Contribution to Thermal Conductivity of Herzenbergite, SnS, at 500K

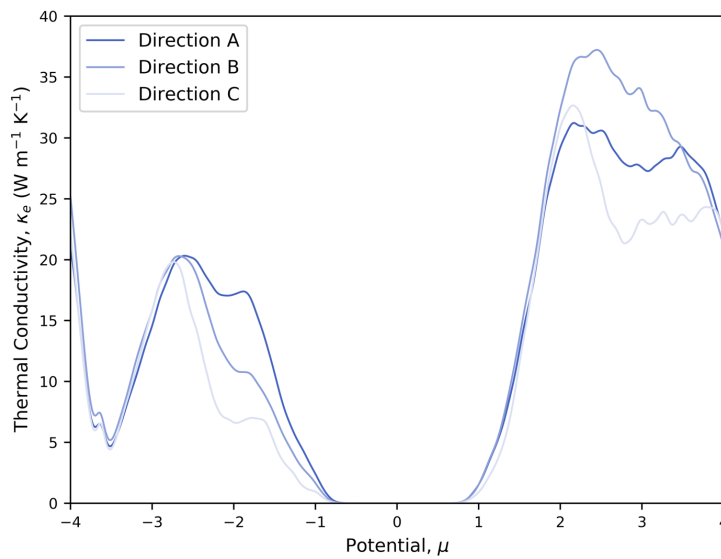


Figure 5.18 – Potential dependent thermal conductance of the electrons at increasing temperatures. The amplitude increases with temperature, though the shape of the original transmission spectrum is visible. Transmission calculated using dftb-negf with an energy step of 0.01 eV and k-grid of 4x4x4. Thermoelectric coefficients derived using program (see section 3.5), each series contains 8000 points.

5.4.3 – THERMOELECTRIC PROPERTIES OF BERNDTITE, SnS_2

The material Berndtite is a large band gap, layered material, with highly bound electrons involved in bonding with the tin(IV) and sulphur atoms. The large band gap is atypical of a good thermoelectric material, and so it would be unexpected for Berndtite to possess thermoelectric properties. Nevertheless, for a complete study of the ground state tin sulfides, Berndtite was included for comparison. Primarily due to its large band gap, the study revealed some interesting results.

5.4.3.1 – TEMPERATURE DEPENDENT THERMOELECTRIC PROPERTIES OF BERNDTITE, SnS_2

As may be seen in figure 5.19, the transmission spectrum of Berndtite is unusual in that there is an “island” of conduction band close to the Fermi level. The transmission along *c* is also far higher than expected, and this is believed to be due to strong overlap of the lone pairs between SnS_2 layers. The curvature of the electronic conductivity is the exponent function expected of a large band gap material. Formally an insulator, the actual values of the conductivity are infinitesimal in comparison to those predicted by the calculations of Herzbergite. The electronic contribution to the thermal conductivity mimics this effect, both in curvature and magnitude. The Seebeck coefficient however, is exceptionally large, as may be expected for an insulating material. Of particular interest, is that the maximal values of the Seebeck coefficient occur in the range of 400 to 600 K, although for *a* there is a significant value at lower temperatures, up to and including 300 K. The values are negative due to the proximity of the Fermi level to the conduction band.

Despite the large values of the Seebeck coefficient, the power factor reflects the curvature of the conductivity, primarily because the curvature of the conductivity is “flat” within the ranges of the large Seebeck values.

Due to the cancelling nature of the electronic and thermal conductivities, the zT_e values are astonishingly large. This is clearly due to the infinitesimal values obtained for the electronic thermal conductivities, which are of the order of $1 \times 10^{12} \text{ W m}^{-1} \text{ K}^{-1}$ at their maximal values. This results in a zT_e of nearly 1000 at 500 K for *c*, and a smaller value of nearly 500 at 700 K. Clearly, with the introduction of a lattice thermal conductivity of the order of $0.3 \text{ W m}^{-1} \text{ K}^{-1}$, if one were to use the record small value for SnSe as an indication of the minimal lattice thermal conductivity, the actually zT would be far less than 0.1. It is apparent, therefore, that when considering the electronic thermoelectric properties of large band gap insulators, one must be wary of the zT_e values, and evaluate the impact of the phononic contribution to thermal conductivity on zT .

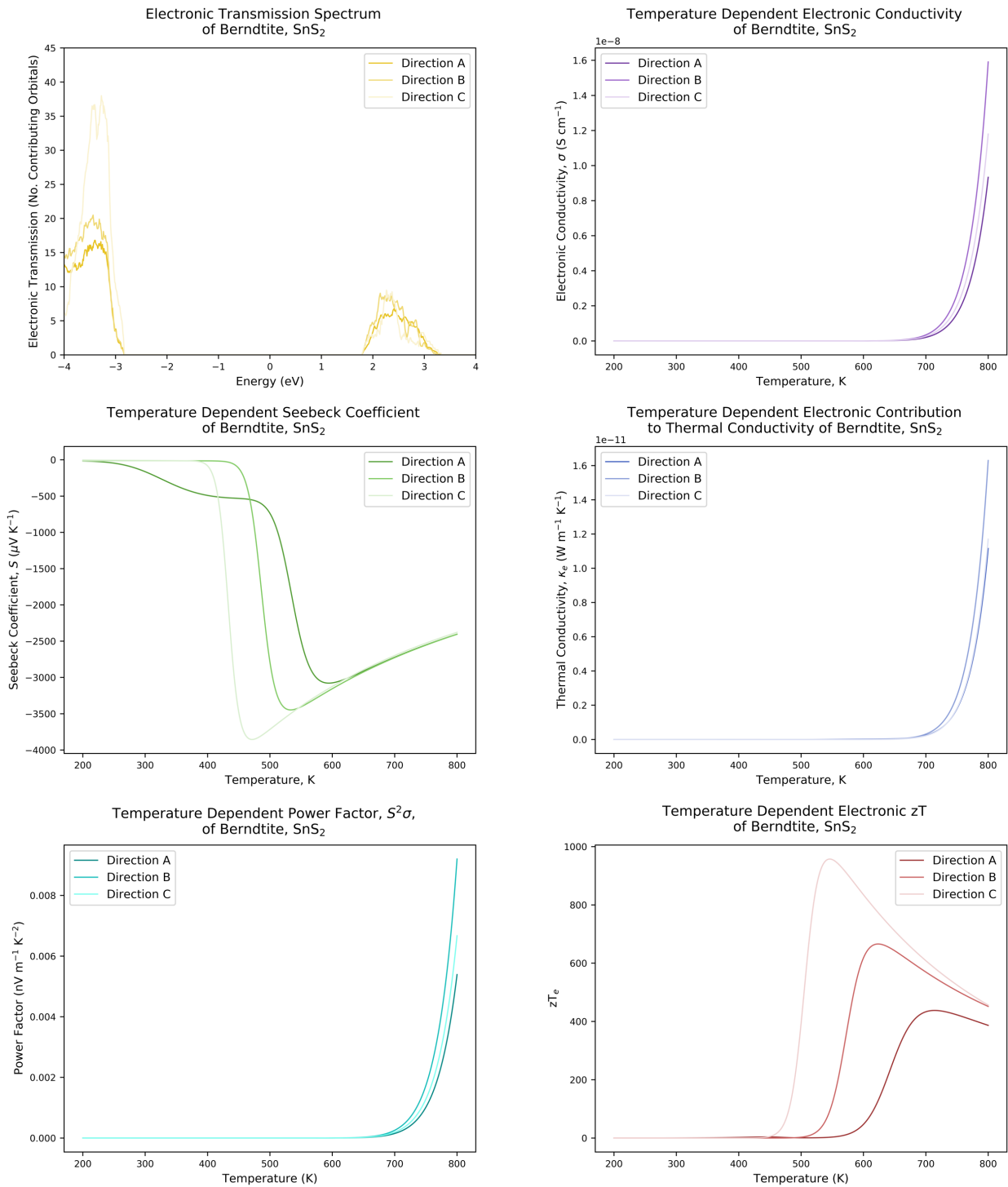


Figure 5.19 – Temperature dependent thermoelectric properties of Berndtite. The Seebeck coefficient is large and negative, and this is believed to be due to the proximity of the fermi level to the small conduction band. Transmission calculated using dftb-negf with an energy step of 0.01 eV and k-grid of 4x4x4. Thermoelectric coefficients derived using program (see section 3.5), each series contains 6000 points.

5.4.3.2 – POTENTIAL DEPENDENT THERMOELECTRIC PROPERTIES OF BERNDTITE, SbS_2

For Berndtite, the same trends are apparent in the potential dependent thermoelectric properties as for Herzenbergite. Namely, the smoothing of the features within the electronic conductivity curves, with no real enhancement of the maximal values, and the increasing magnitude of the electronic thermal conductivity, which increases significantly with temperature, as seen in figure 5.20 and 5.22.

The Seebeck curve (Figure 5.19) reveals the most interesting insights into Berndtite's thermoelectric properties. There are again additional extrema in the Seebeck curves of *a* and *b*, which contribute to the large Seebeck coefficients at low temperatures. The broadening of the peaks as a function of temperature applies to these additional extrema also, and this produces an interesting feature in the Seebeck curve of *a*, even at high temperatures. Whilst the Seebeck curves of *b* and *c* are almost the classic shape at 500 K, for *a* there is still a large additional extremum at $\mu = -0.5$ eV. It may be therefore, that the gradient of the centre of the curve is a function of both the band gap, and the magnitude of the transmission at the band edges. This suggests that the Seebeck coefficient is proportional to the area under the curve of the transmission within the range of the first derivative of the Fermi function at higher temperatures.

The final interesting feature in 5.21 is that the Seebeck curve is not centred on the Fermi energy as one may expect, but on the centre of the band gap, regardless of the position of the Fermi level. This means the temperature dependent Seebeck of Berndtite is able to access the large negative values of the minima about $\mu = 0$ eV. The clear consequence of this is that one must be very thorough in the calculation and specification of the Fermi level in the calculation of the transmission and subsequent derivation of the thermoelectric properties using the Non-Equilibrium Greens Functions Approach, as implemented in the DFTB formalism.

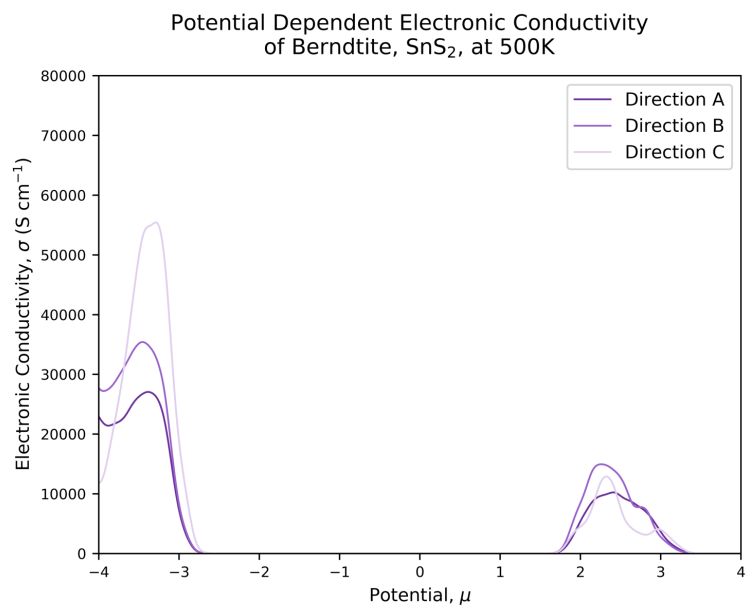
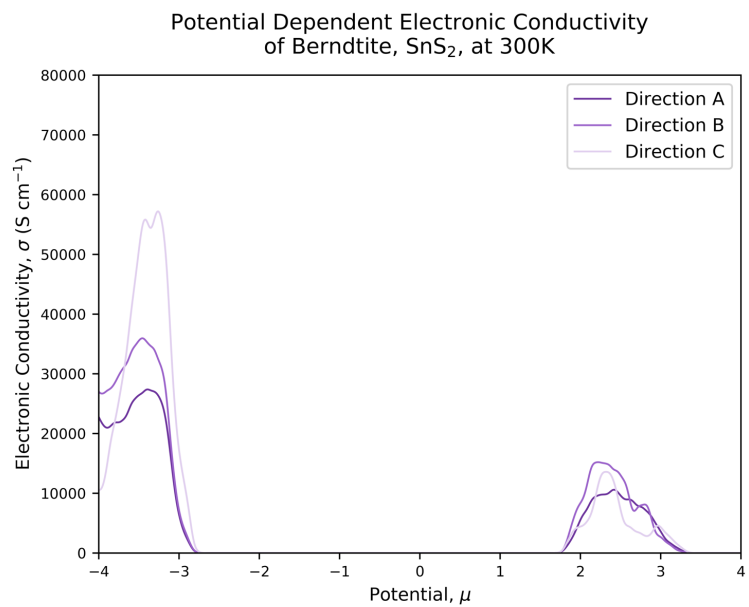
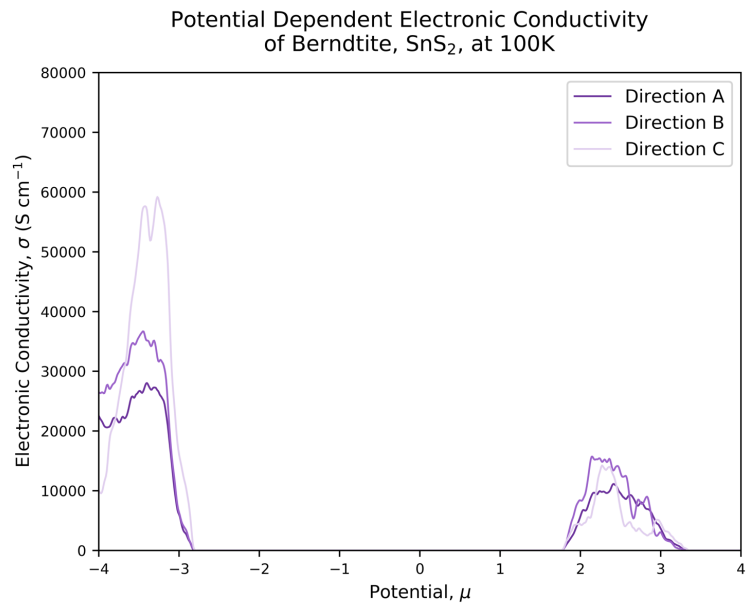


Figure 5.20 – Potential dependent conductivity of Berndtite. The same softening of features is observed. Transmission calculated using dftb-negf with an energy step of 0.01 eV and k-grid of 4x4x4. Thermoelectric coefficients derived using program (see section 3.5), each series contains 8000 points.

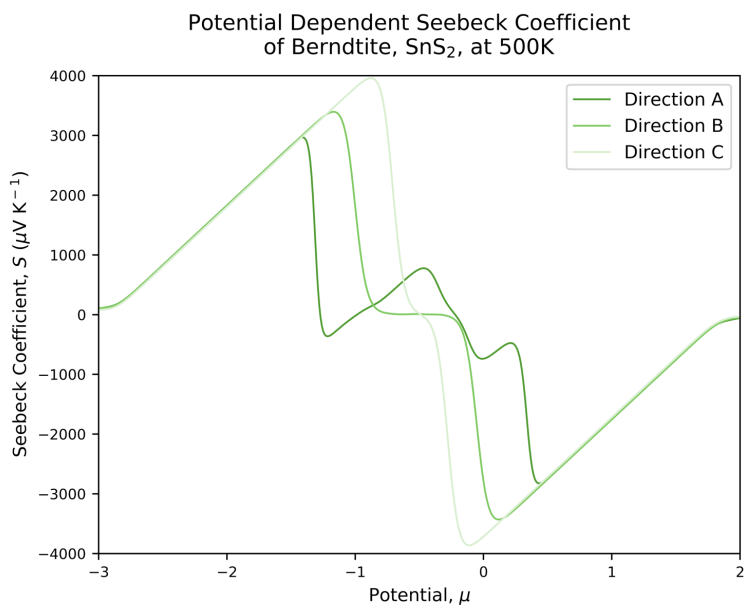
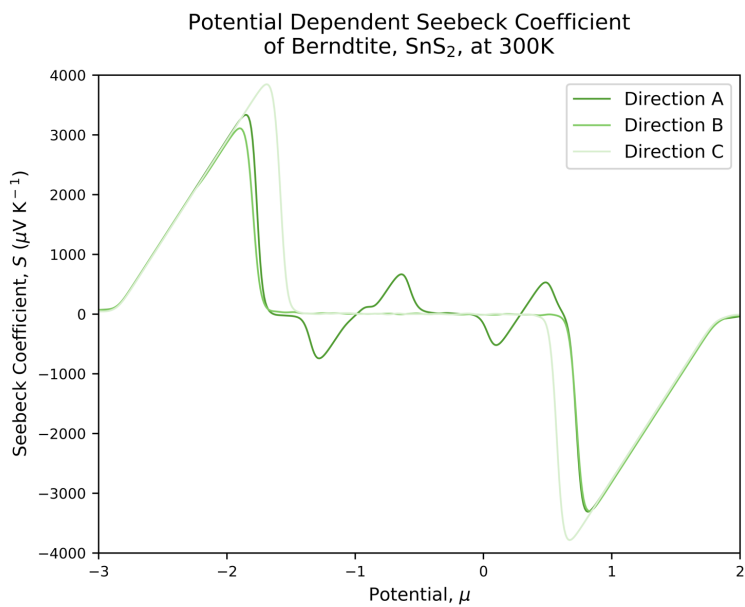
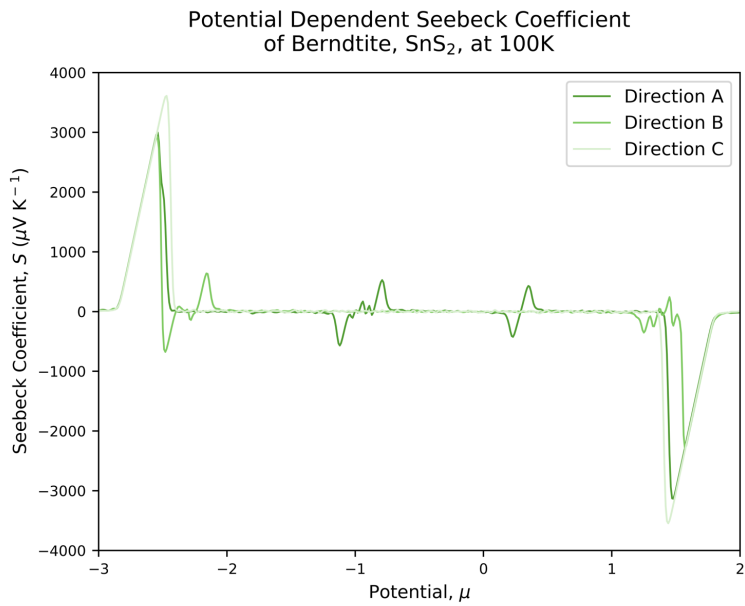
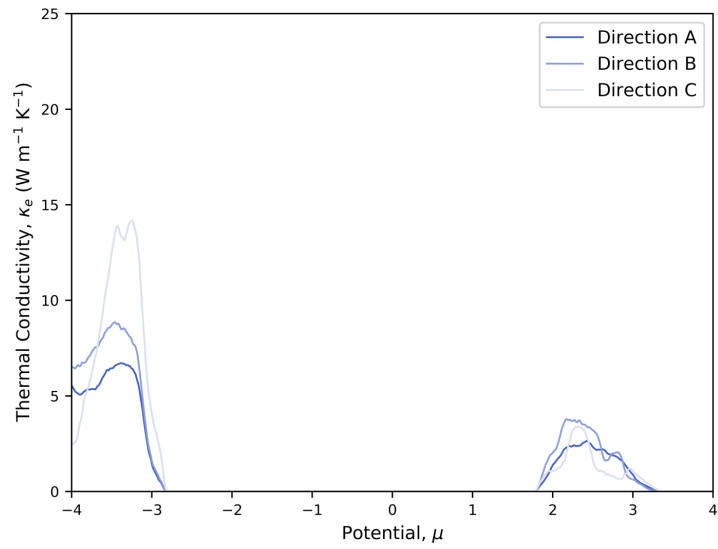
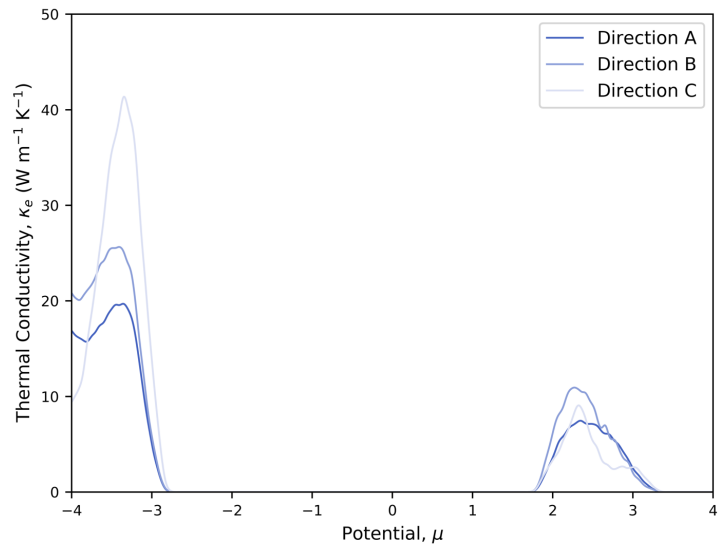


Figure 5.21 – The effect of increasing temperature on the potential dependent Seebeck coefficient of Berndtite. The unique features between the extrema are caused by the infinitesimal contributions of atomic orbitals within the band gap, amplified by the effect of the multiplication by the first derivative of the Fermi function. Transmission calculated using dftb-negf with an energy step of 0.01 eV and k-grid of 4x4x4. Thermoelectric coefficients derived using program (see section 3.5), each series contains 8000 points.

Potential Dependent Electronic Contribution to Thermal Conductivity of Berndtite, SnS_2 , at 100K



Potential Dependent Electronic Contribution to Thermal Conductivity of Berndtite, SnS_2 , at 300K



Potential Dependent Electronic Contribution to Thermal Conductivity of Berndtite, SnS_2 , at 500K

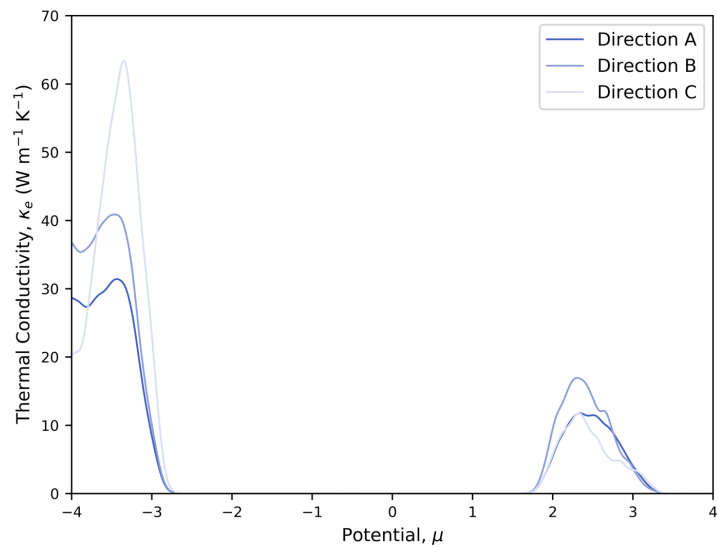


Figure 5.22 – Increasing magnitude of the thermal conductance of electrons with temperature. Transmission calculated using dftb-negf with an energy step of 0.01 eV and k-grid of 4x4x4. Thermoelectric coefficients derived using program (see section 3.5), each series contains 8000 points.

5.4.4 – THERMOELECTRIC PROPERTIES OF OTTEMANNITE, Sn_2S_3

The structure of the final naturally occurring tin sulfide compound is that of Ottemannite. This unique structure (fig 5.3), consists of “ribbons” of Berndtite geometry, held together by weak intermolecular forces. The term “ribbons” is applied, in that the molecules of Ottemannite are thin, flat and semi-infinite, essentially forming 1-dimensional nanowires, similar to those investigated in phosphorus. It was hoped that this novel structure may possess extremely anisotropic properties that may be beneficial for applications in thermoelectrics.

5.4.4.1 – TEMPERATURE DEPENDENT THERMOELECTRIC PROPERTIES OF OTTEMANNITE, Sn_2S_3

In figure 5.23 we see the derived thermoelectric properties of Ottemannite as a function of temperature. The transmission is presented again for convenience of comparison. Referring to figure 5.3 for an appreciation of the transport vectors, we note that c represents the transport *along* the ribbons of Sn_2S_3 , while a and b are orthogonal to this, spanning across the stacks of ribbons. We note therefore, that c has the highest average transmission, which would be predicted from the transmission observed thus far, in which there is a tendency for the directions which exhibit purely covalent bonding to demonstrate the highest transmission across the spectrum. It should be noted however, that this large transmission is not necessarily explicitly due to the electrons held in the covalent bonding scheme, but that the electrons occupying non-bonding lone-pairs contribute to the transmission along the surface of the wire, as seen in figure 4.11c.

The electronic and thermal conductivities of Ottemannite display the exponential behaviour typical of a semiconductor. Indeed, in this calculation Ottemannite is observed to have a band gap of around 3 eV, whilst an insulator would be defined as a material with a band gap larger than 3.5 eV, and so the band gap of this material is on the large side of a semiconductor. As such, the average value of the electronic conductivity is around $3 \times 10^{-5} \text{ S cm}^{-1}$ at 800 K, which is particularly small compared to that of most thermoelectrics. Whilst the transmission of c is significantly larger than that of a and b across the range of the spectrum, at the edges of the conduction and valence bands the values of b are very similar to those of c . As such, the electronic and thermal conductivities of b and c are far closer in value across the whole temperature range than either is to a .

The Seebeck coefficient is large and positive, in fact the Seebeck of b is appreciable at 300 K, whilst the values of all three are rather large (approximately $3000 \mu\text{V K}^{-1}$) between 350 K and 450 K. This is the ideal operating range for room temperature thermoelectrics, so it is interesting to observe this fact. Below 450 K, the effects of anisotropy are clear, however above this temperature the values along each direction are nearly degenerate. The cause of this is discussed in 5.4.4.2, and can be understood by consideration of figure 5.24.

Despite the large Seebeck coefficients observed in Ottemannite, the power factor is unfortunately small, due to the exceedingly small electronic conductivities. The shape is defined by that of the conductivity, whilst the anisotropy observed in the higher temperature range may also be attributed to the conductivity, as the values are apparently close to degenerate for the Seebeck coefficients at these temperatures.

Regardless of this fact, the zT_e of Ottemannite is large at an average of 530 at 450 K. This is significantly higher than the maximum observed in Herzenbergite (an average of approximately 0.3 at 400 K), but roughly half of that observed in Berndtite. Indeed, similar to Berndtite, one must take this value with some scepticism, as the large band gap of 3 eV has resulted in a very small electronic contribution to the thermal conductivity, which is 8 orders of magnitude lower than the remarkably low full thermal conductivity observed in SnSe, meaning the actual zT of Ottemannite would be expected to be exceedingly low. Interestingly, whilst there is clearly demonstrable anisotropy present in the zT_e of Ottemannite, the values of a and c are remarkably close in value despite their perceived crystallographic differences. It is assumed that the large zT_e value of a , which has the lowest electronic conductivity, is due to its large Seebeck coefficient, and the low electronic thermal conductivity.

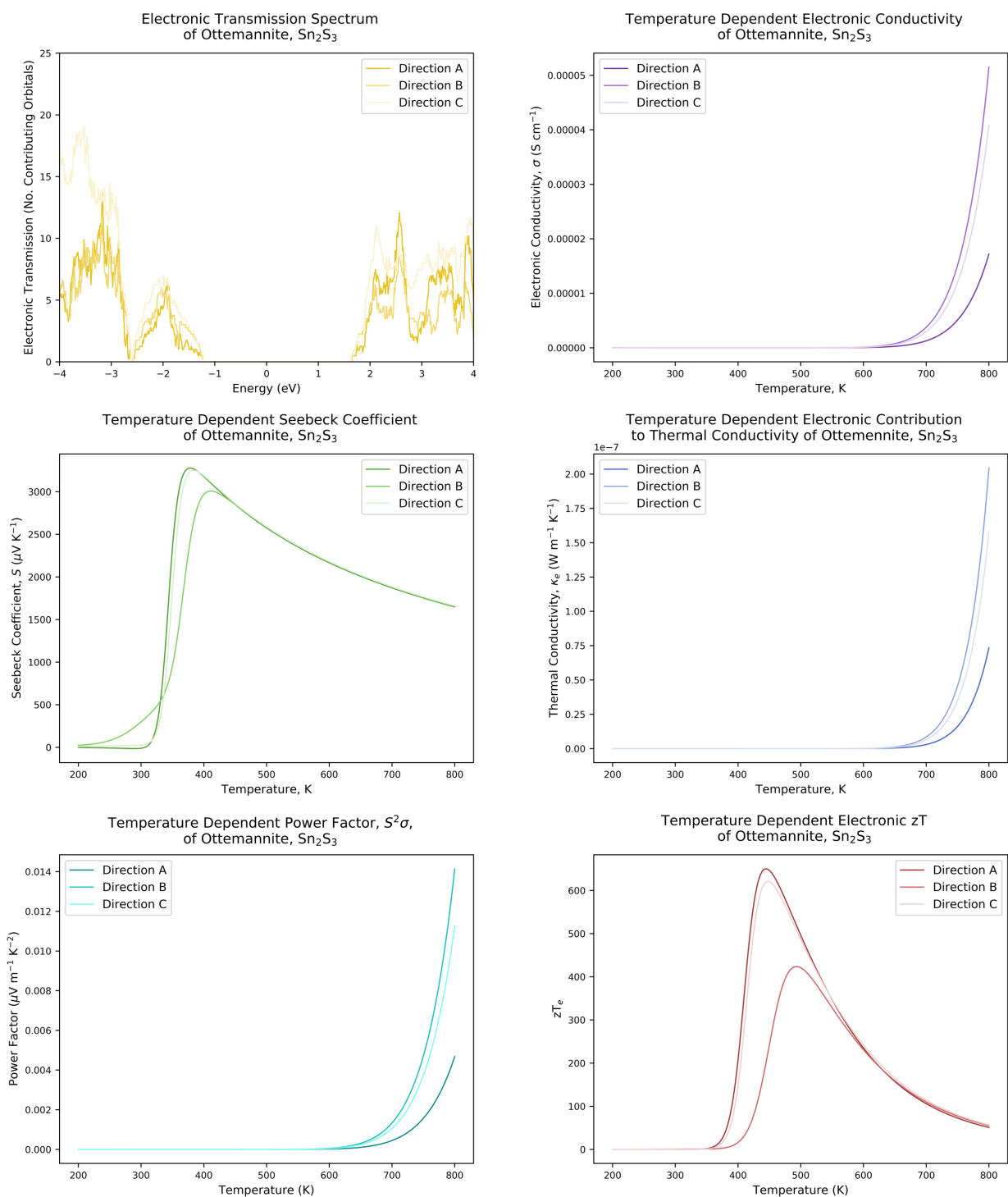


Figure 5.23 – The thermoelectric properties of Ottemannite as a function of temperature. The maximal zT_e around 450 K would make for a promising room temperature thermoelectric material. Transmission calculated using dftb-negf with an energy step of 0.01 eV and k-grid of 4x4x4. Thermoelectric coefficients derived using program (see section 3.5), each series contains 6000 points.

5.4.4.2 – POTENTIAL DEPENDENT THERMOELECTRIC PROPERTIES OF OTTEMANNITE, Sn_2S_3

Once again, plotting the thermoelectric properties as a function of potential allows for insight into the cause of the features observed above. Most notably the Seebeck coefficient, where it is now observed that it is the temperature which is responsible for the degeneracy of the Seebeck coefficient at high temperatures, which has been observed in almost all of the materials presented so far. We note that in the plot of the Seebeck coefficient at 500 K in figure 5.24, the values of the Seebeck coefficient are almost identical at each potential. It has been determined, that this shape is essentially the second derivative of the Fermi function, and therefore that at high temperatures, or cases where the band gap is small, the Seebeck coefficient as a function of potential is dominated by the contribution of the Fermi function. In these instances, the observation is a lack of degeneracy in the Seebeck coefficients at higher temperatures, and the potential for large values of S at $\mu=0$, provided the Fermi level is minimally offset from the centre of the gap in transmission. The effect of this is noted in Herzenbergite, where despite the small band gap, and appreciable values of S at 300 K in the potential dependent plots (figure 5.17), the Seebeck coefficient at elevated temperatures is smaller at $\mu=0$, as the Fermi level is closer to the point at which there is a change of sign in the Seebeck curve. At low temperatures, where the smearing of the Fermi function is narrow, the presence of low-density states in the band gap of the transmission is once again amplified yielding non-zero values at $\mu=0$.

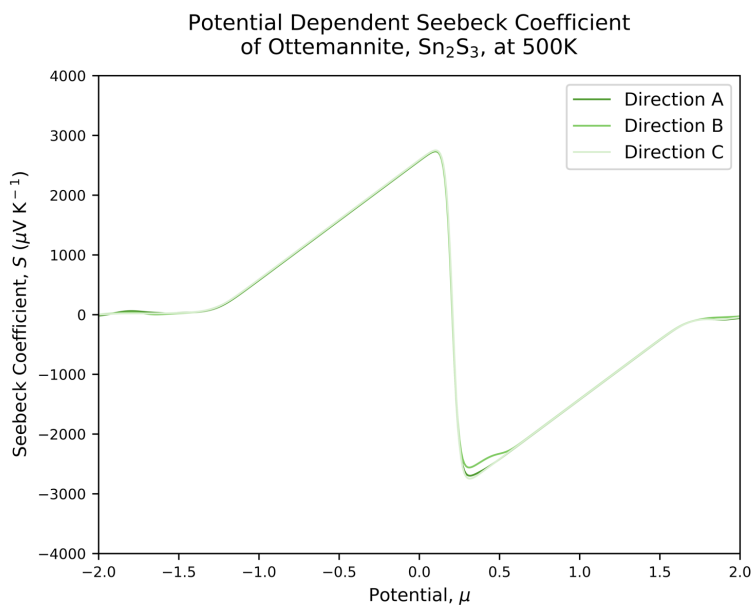
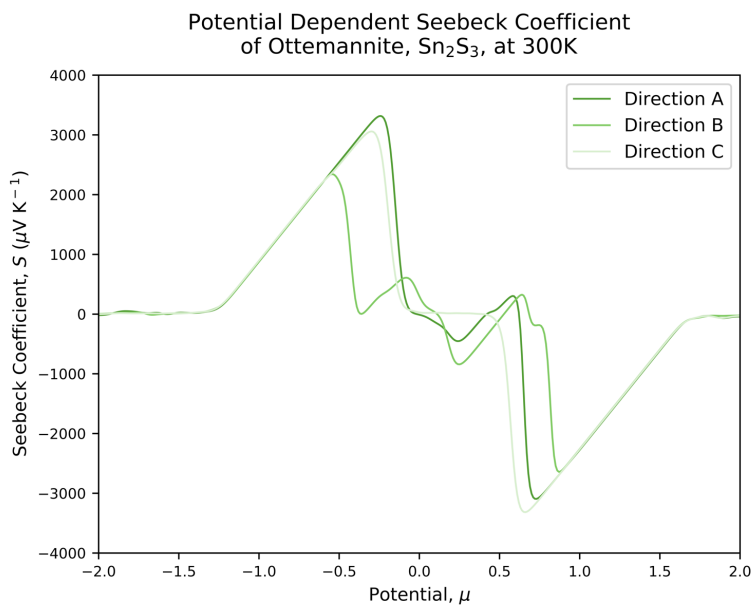
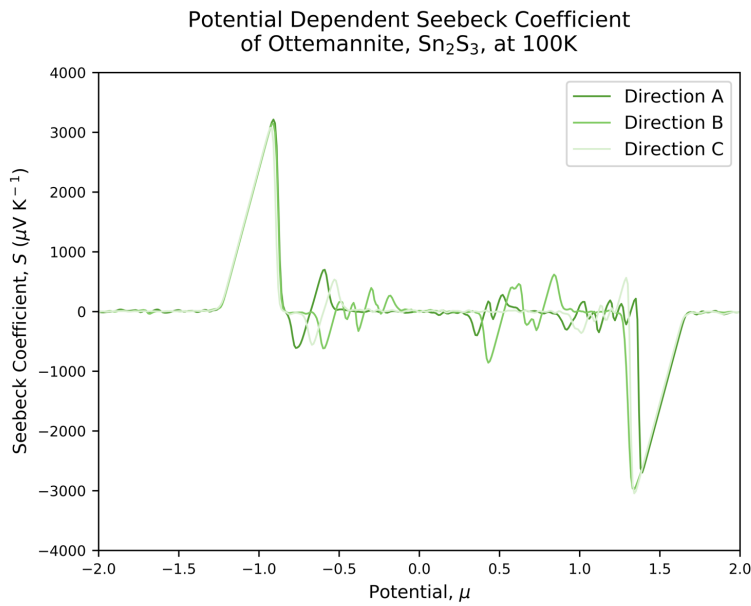


Figure 5.24 – The effect of temperature on the Seebeck coefficient of Ottemannite. Whilst the presence of anisotropy is clear at lower temperatures, at elevated temperatures the Seebeck coefficient along each direction is almost equivalent. Transmission calculated using dftb-negf with an energy step of 0.01 eV and k-grid of 4x4x4. Thermoelectric coefficients derived using program (see section 3.5), each series contains 8000 points.

We have seen the thermoelectric properties of the naturally occurring tin sulfides, as derived from the electronic transmission according to the Landauer-Büttiker method and its implementation in the Non-Equilibrium Green's-Functions (NEGF) approach of DFTB theory. One particular observation to make, is that in the previous chapter, we saw materials where the electronic structure about the Fermi level was almost exclusively determined by the 3p orbitals of phosphorus. In the tin selenides, the edges of the valence and conductance bands are defined by the presence of the 3p orbitals of sulphur, and the 5p and 5s orbitals of tin, with small contributions from the 4d and 5s of tin. The interesting feature, is that it is the 3p orbitals of sulphur which dominate the valence band edge, and so by substituting small amounts of sulphur for a dopant species, it may be possible to tune the shape of the valence band, for materials where the valence band dominates transport properties, like Ottemannite.

We have seen that the quirks found in the temperature dependent curves of the thermoelectric properties may be explained by inspection of the potential dependent curves at discrete temperatures. This is especially the case for the Seebeck coefficient, where the effect of temperature on the shape and magnitude of the temperature dependent curve is non-obvious.

We have also seen that whilst Berndtite and Ottemannite display large zT_e 's, the presence of large band gaps in the electronic structure result in a tendency for this method to yield large zT_e 's that may not reflect upon the true zT , as the *phononic* or *lattice* contribution to the thermal conductivity will likely be several order of magnitude larger than the electronic contribution. Indeed, it had not gone unnoticed that the band gaps observed in the transmission of Berndtite and Ottemannite as calculated in the non-self-consistent (NSCC) formalism, were significantly larger than those observed in the band structures as calculated by DFT level theory, incorporating self-consistency (SCC). The values of the band gap for Berndtite and Ottemannite from the NSCC-DFTB approach were 5 eV and 3 eV respectively, whereas in the bands calculated in the SCC-DFT formalism, the gaps were 1.5 and 0.8 eV for Berndtite and Ottemannite respectively. For Herzenbergite, the gap of 1.5 eV from the DFTB approach, and 1 eV from the DFT approach were considered acceptable, as they were comparable to those found in the literature. As a matter of fact, the expectation had been that DFTB would overestimate the band gap, whereas DFT would underestimate this value. The discrepancy of 0.5 eV was considered reasonable between these methods for Herzenbergite, though the large discrepancies of 3.5 eV and 1.2 eV for Berndtite and Ottemannite were deemed to negatively impact the prediction of the thermoelectric properties.

For phosphorus, omission of SCC methods was considered acceptable, as the resultant transmission spectra for a comparison study in grey phosphorus of the NSCC and SCC approach yielded little difference between datasets. This has been explained in the literature of the DFTB methodology, as a consequence of the lack of charge transfer in pure elemental systems. However, for a binary system with an appreciable difference in electronegativity's (1.96 for tin and 2.58 for sulphur), due diligence should be taken to account for the presence of charge transfer.

5.4.6 – SCC TRANSMISSION AND THERMOELECTRIC PROPERTIES OF HERZENBERGITE, SNS

As determined in 5.4.5, for binary systems with large differences in electronegativity's, a self-consistent approach should be taken to account for charge transfer. This is especially important for materials with unequal stoichiometries, such as Berndtite (SnS_2), as the band gap of such a material is liable to large overestimation. This is unfortunate for the method of obtaining thermoelectric properties of large systems under development here, as the inclusion of self-consistency results in a dramatic increase in computational cost. For the systems under study with between 2000 to 3000 atoms, this meant that calculations of the same level of accuracy became impractically expensive. As such, it was determined that to include self-consistent methods, a depreciation in the K-grid sampling mesh and an appreciation in the energy step for which the transmission was to be calculated would be necessary, and even provide acceptable resolution for such large systems.

Using a k-grid sampling of $2 \times 2 \times 2$ and an energy step of 0.02 eV, the electronic transmission spectra were calculated for the same materials, using the same nanowire devices constructed for 5.4.1 - 4. The results of which are presented in the next sections.

In the NSCC transmission calculation, we observed that Herzenbergite had a band gap of slightly larger than 1.5 eV. In the SCC methodology, we observe a band gap of approximately 1.25 eV, which is direction dependent. This has resulted in an increase of the electronic conductivity by 2 orders of magnitude and 800 K, whilst the Seebeck coefficient has increased by approximately 25% at 200 K. The electronic contribution to the thermal conductivity has increased accordingly, though not by 2 orders of magnitude as one may expect from looking at the electronic conductivity. The thermal conductivity has increased by a factor of 4, which is partly due to the dependence of this property on the Seebeck coefficient.

This yields a power factor of 3 orders of magnitude greater than that derived from the NSCC calculation, while the zT_e is also improved by a factor of 1×10^3 . It must be noted, that the magnitude of the transmission has not been particularly affected by the inclusion of self-consistency, the magnitude of the transmission is at about 30 for the valence band and 50 for the conduction band. This comparison is meaningful for these two calculations, as the devices used are identical. In fact, the defining factor for these thermoelectric properties appears to be the size of the band gap, which is now approximately 17% smaller.

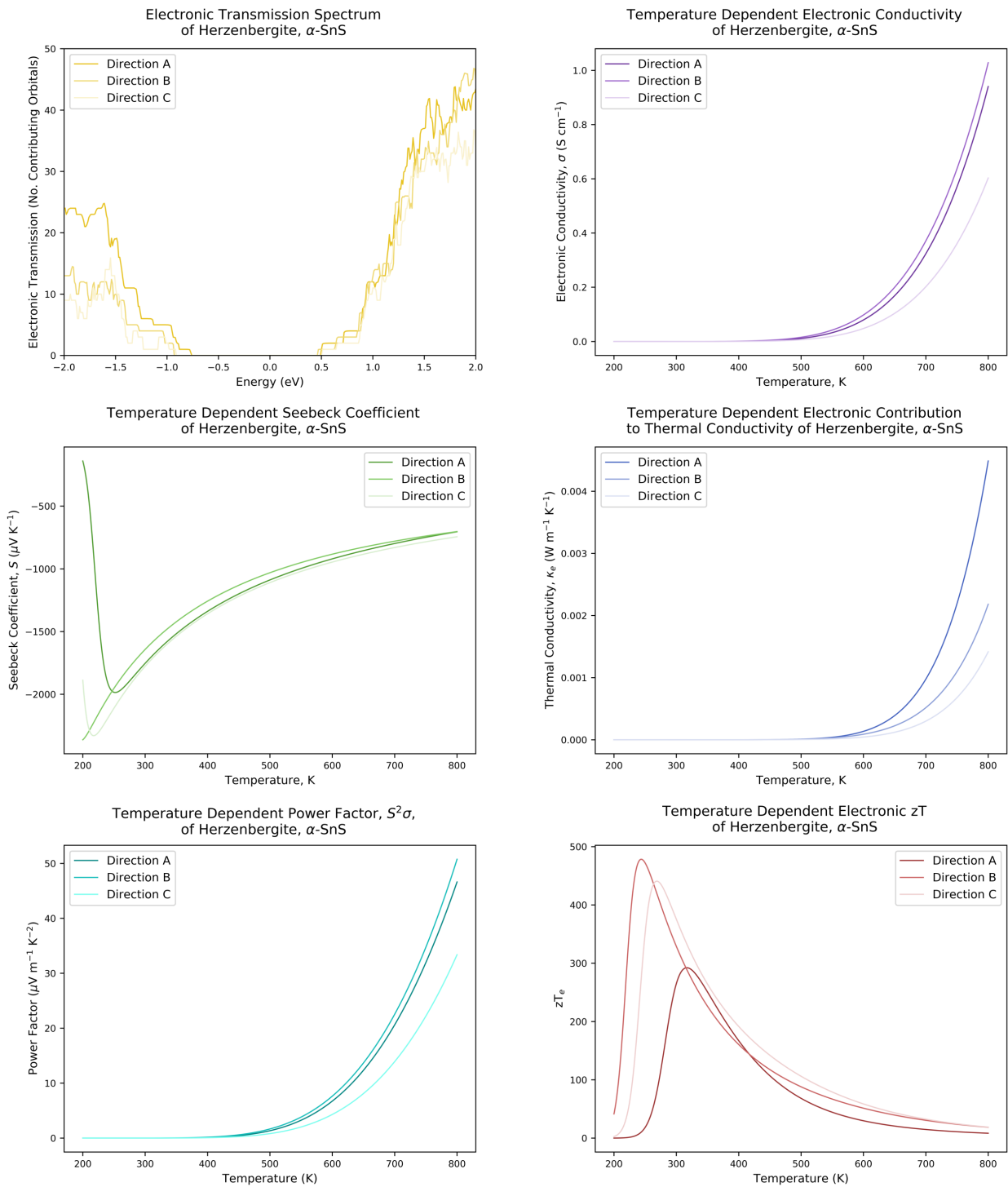


Figure 5.25 – The temperature dependent thermoelectric properties of Herzenbergite with the inclusion of self-consistency in the calculation of the transmission spectrum. Transmission calculated using dftb-negf with an energy step of 0.01 eV and k-grid of 4x4x4. Thermoelectric coefficients derived using program (see section 3.5), each series contains 6000 points.

The same trends are observed in the potential dependent thermoelectric properties as those calculated by NSCC methods, we see a smoothing of the features in the electronic conductivities, with no discernible alteration of the magnitude of each region. While we note an increase in the magnitude of the electronic contribution to the thermal conductivity, with a slight smoothing of the features, which is not as pronounced as for the electronic conductivities.

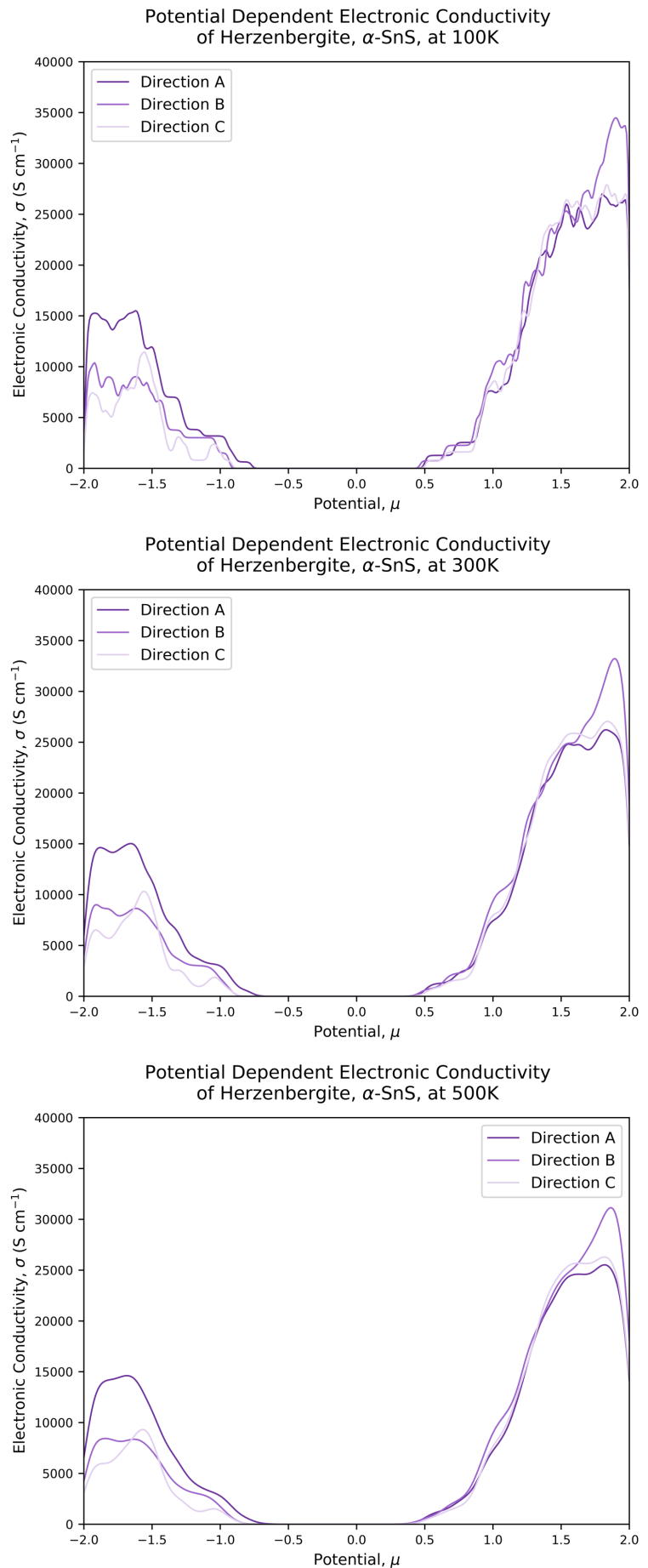
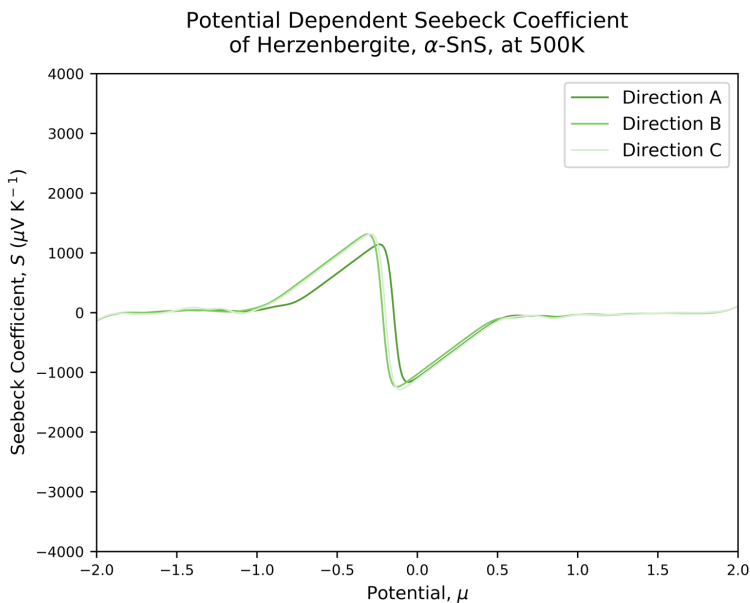
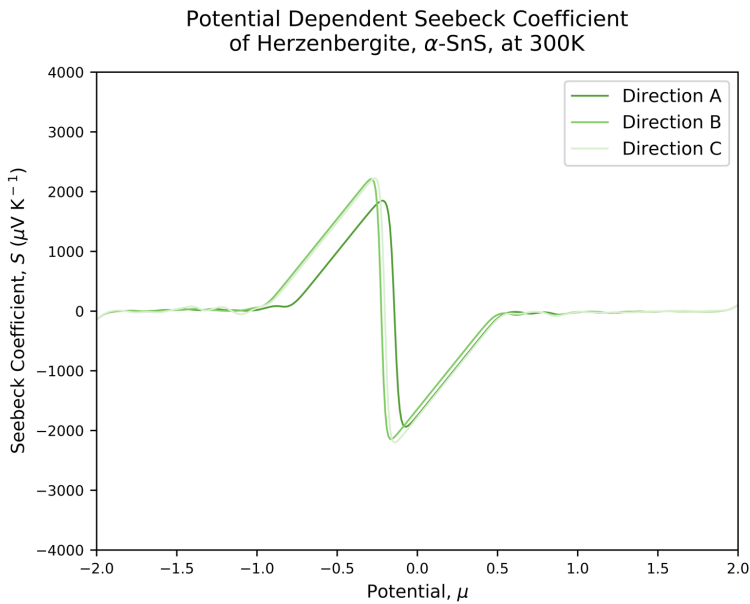
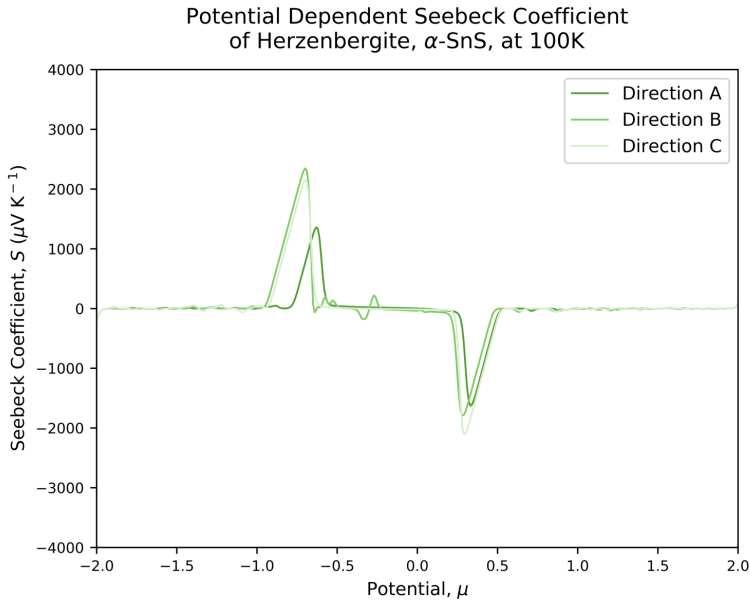


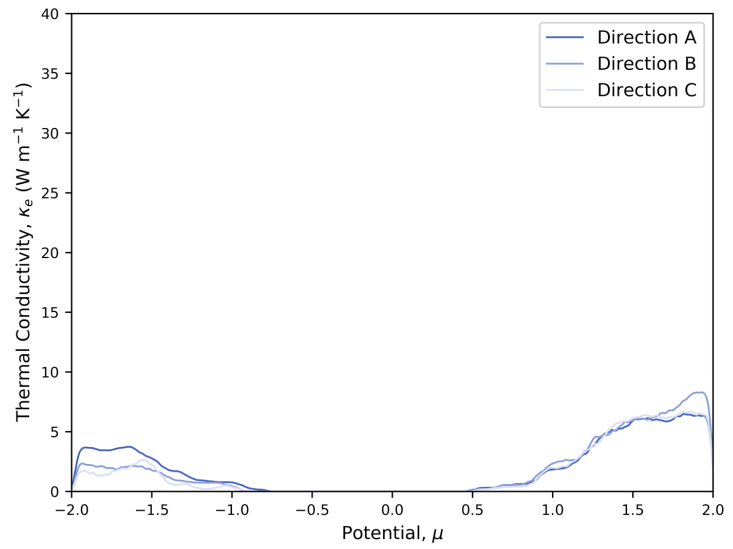
Figure 5.26 – The effect of the inclusion of self-consistency in the calculation of the transmission on the potential dependent conductivity of Herzenbergite. Transmission calculated using dftb-negf with an energy step of 0.01 eV and k-grid of 4x4x4. Thermoelectric coefficients derived using program (see section 3.5), each series contains 8000 points.



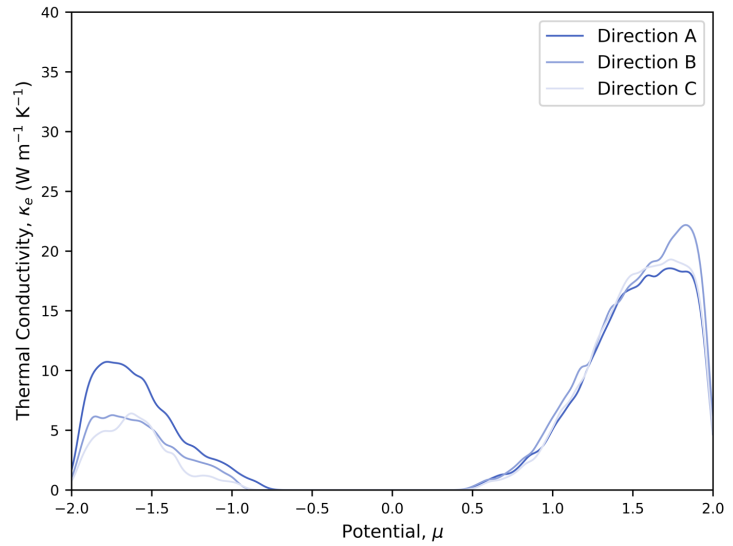
The potential dependent Seebeck coefficient again demonstrates the presence of diffuse states within the band gap, and a smoothing of these features at higher temperatures. Interestingly, curves of the Seebeck coefficients are not degenerate at 500 K, as that for *a* is slightly offset in energy from *b* and *c*, albeit of comparable magnitude. This is perhaps due to the size of the gap in the transmission of *a*, which is noticeable smaller than that of *b* and *c* in figure 5.26. This effect is amplified in 5.26 at 500 K, one may observe that the position of the valence band edge of *a* is nearly 0.2 eV closer to the Fermi level than those of *b* and *c*.

Figure 5.27 – The Seebeck coefficient of Herzenbergite with increasing temperature. Transmission calculated using dftb-negf with an energy step of 0.01 eV and k-grid of 4x4x4. Thermoelectric coefficients derived using program (see section 3.5), each series contains 8000 points.

Potential Dependent Electronic Contribution to Thermal Conductivity of Herzenbergite, α -SnS, at 100K



Potential Dependent Electronic Contribution to Thermal Conductivity of Herzenbergite, α -SnS, at 300K



Potential Dependent Electronic Contribution to Thermal Conductivity of Herzenbergite, α -SnS, at 500K

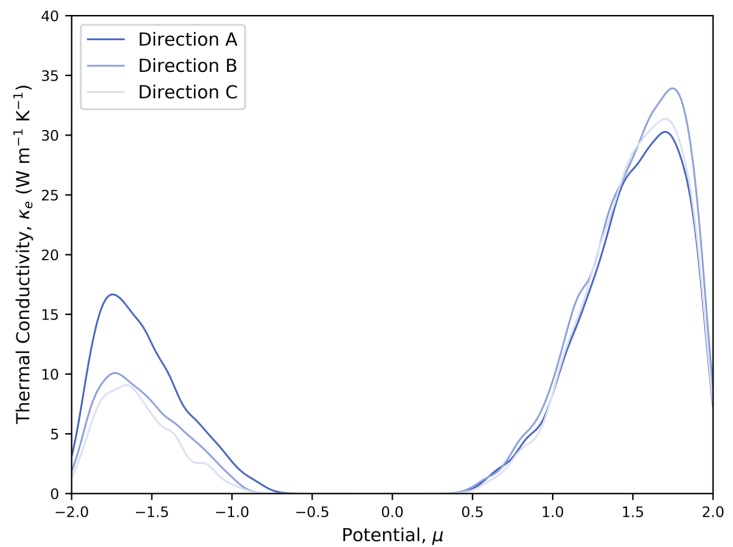


Figure 5.28 – The effect of increasing temperature on the magnitude of the electronic thermal conductance of Herzenbergite in the self-consistent methodology. Transmission calculated using dftb-negf with an energy step of 0.01 eV and k-grid of 4x4x4. Thermoelectric coefficients derived using program (see section 3.5), each series contains 8000 points.

For the transmission of Berndtite using the SCC approach, we notice a similar effect, with the band gap decreasing by nearly 1 eV, to about 3.8 eV. The gap is still rather large however, as the DFT calculated band gap is about 1.5 eV. That is not to say that the DFT calculated band gap is necessarily correct, as the PBE functional as applied by the DFT methodology is known to underestimate the gap, however it would be hoped that the disparity between the two was less than 1 eV. As a matter of fact, it seems that the tin sulfide parameters supplied were optimised for the Herzenbergite crystal structure and chemistry, and were not extensively optimised for the remaining tin sulfides. Despite this, the SCC calculations were performed, and insight into the effect of the size of the band gap on the electronic properties could be gathered.

The same “shape” was observed in the transmission, with a large valence band, and a smaller “island” of a conductance band, which is 1 eV closer to the Fermi level than the valence band edge. This has resulted in an increase of the electronic conductivity by nearly 4 orders of magnitude, while the thermal conductivity of the electrons has increased by 2 orders of magnitude. There was no apparent change in the magnitude of the Seebeck coefficient, however, the position of the optimal operating temperature has reduced, from about 500 K to about 380 K. In fact, the Seebeck curve is largely the same shape as that observed for the NSCC calculations of Berndtite, the notable difference being the positive values along a at lower temperatures. This artefact has little apparent effect on the power factor, but a large effect on the zT_e , where there is a large maximal value for a at 300 K, 7 times larger than that of b or c . Additionally, we observe a second, smaller peak in the value of zT_e for a above 600 K, another example of a material where the sign of the dominating charge carrier changes as a function of temperature. This was previously observed in the NSCC calculation of Herzenbergite, where the sign of the Seebeck for respective b was negative at lower temperatures, but large and positive at higher temperatures.

In Figure 5.30 we see a very similar situation for the Seebeck coefficient as in that of the NSCC derived Seebeck in figure 2.19. The presence of weak states within the perceived band gap of Berndtite makes for large fluctuations in the value of the Seebeck near the Fermi level. These states are even present at elevated temperatures along a , such as 500 K, similar to that observed in 2.21. The fact that the nature of the Seebeck coefficient is not dissimilar between the NSCC and SCC approaches, for both the temperature dependent and potential dependent plots, suggests that the Seebeck coefficient is more dependent upon the actual “shape” of the transmission, rather than the band gap of the material. This is distinct from the electronic and thermal conductivities, which appear to be directly correlated to the magnitude of the band gap.

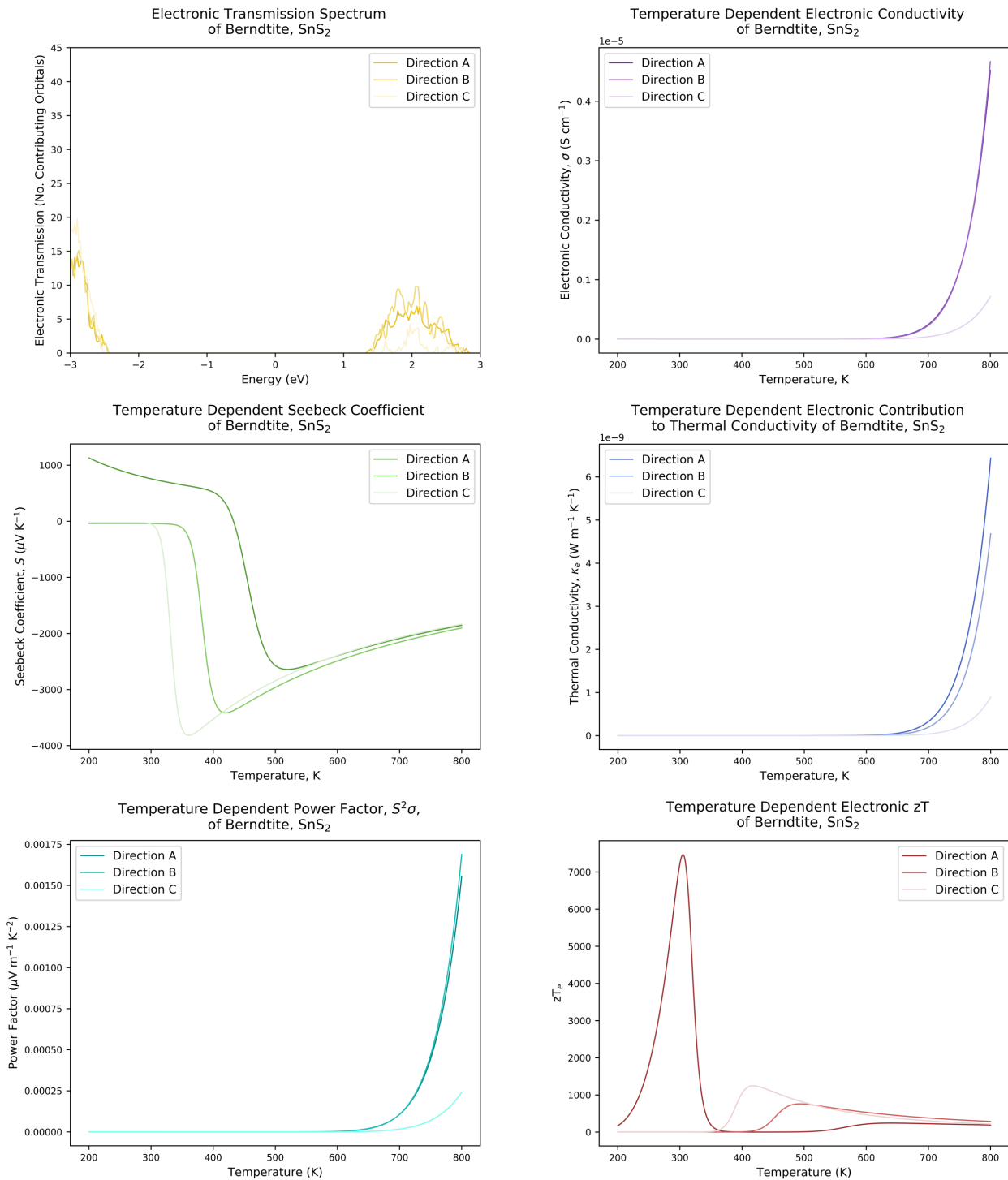
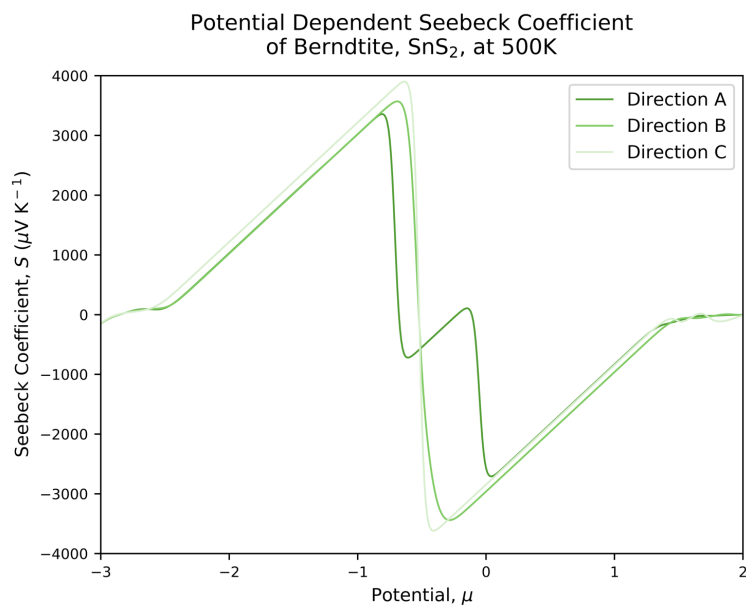
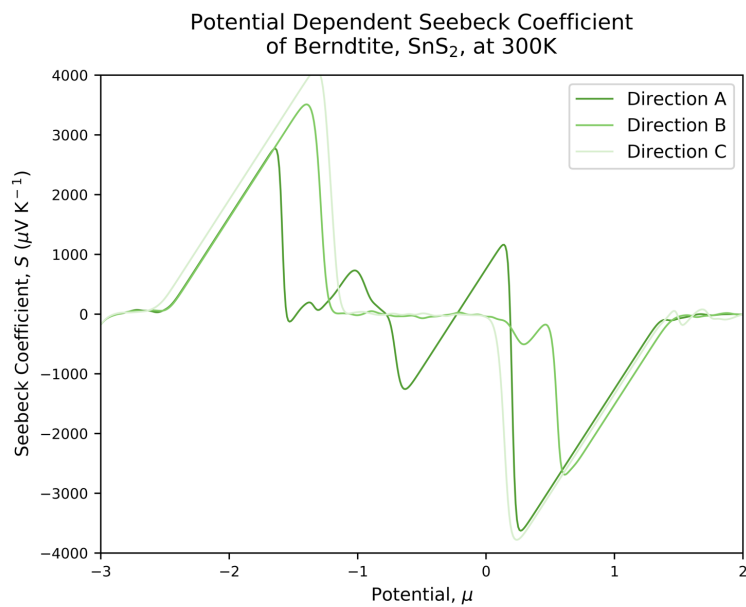
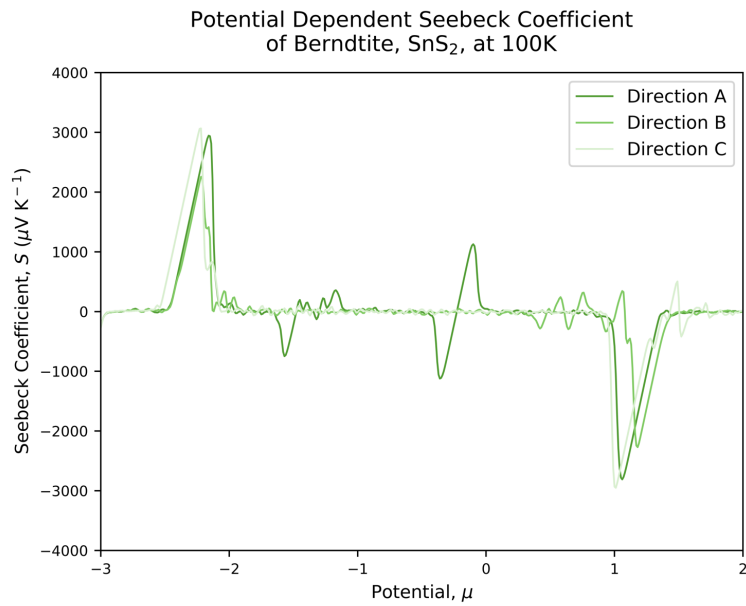


Figure 5.29 – The temperature depended thermoelectric properties of Berndtite, derived from the implementation of self-consistency in the calculation of the electronic transmission. Transmission calculated using dftb-negf with an energy step of 0.01 eV and k-grid of 4x4x4. Thermoelectric coefficients derived using program (see section 3.5), each series contains 6000 points.



Again, despite this marked improvement in zT_e , it cannot be overstated that the zT_e of large band gap materials will not be representative of the overall zT , due to the absence of the expectedly larger phonon contribution to thermal conductivity. Aside from this, it has been shown that the inclusion of self-consistent methods allows for the more accurate prediction of the electronic thermoelectric properties of non-elemental systems, where charge transfer effects need to be accounted for.

Figure 5.30 – The effect of temperature on the potential dependent Seebeck coefficient of Berndtite. Transmission calculated using dftb-negf with an energy step of 0.01 eV and k-grid of 4x4x4. Thermoelectric coefficients derived using program (see section 3.5), each series contains 8000 points.

5.5 – NOVEL MATERIALS

It has recently been proven that the tin mono-sulfide system has a rich chemistry with respect to temperature, by the discovery of two novel phases of SnS. The β -SnS phase is closely related to the α -SnS phase, and is obtained by heating α -SnS to 905 K. *Nota bene*, Herzenbergite will be referred to as α -SnS for the duration of this subsection to enable the distinction between these polymorphs. The presence of this β -phase may have interesting effects on the thermoelectric properties of tin sulfide thermoelectrics operating above this temperature. The π -phase SnS is a unique tin sulfide in that it has a 3-dimensional covalent bonding scheme, with internal lone pairs on sp³ hybridised tin and sulphur atoms. All other tin sulfides discovered to date have displayed highly anisotropic symmetry, with stacks of weakly bound 2D layers. The truly exciting feature about this π -SnS, is that it is apparently stable under atmospheric conditions, though it has only been observed in thin films and as nano-crystals, most notably in the photovoltaic industry. This fact allows for the consideration as a near room temperature thermoelectric, potentially for the field of thin film thermoelectric devices. Another exciting feature of π -SnS, is that it has a large, cubic unit cell, which is a criterion stipulated by Zhang et al. and Snyder et al.^{1,3} for ideal thermoelectrics, as the cubic symmetry implies the presence of degenerate valleys in the band structures of such materials, which is believed to allow for large electronic conductivities that are not present at the expense of a large Seebeck coefficient, which is maintained by the low effective mass of such bands.

For these reasons, the thermoelectric properties of these materials were investigated as a continuation of the wider-reaching consideration of the effect of phase transitions on the thermoelectricity.

5.5.1 – STRUCTURES, SYMMETRY

An introduction to these materials was given in 5.3, and so will not be covered in depth here, however the key points will be summarised. Both α -SnS and β -SnS are 2D layered materials, consisting of covalently bonded SnS layers, bound together by weak intermolecular (Van der Waals) forces. β -SnS is obtained via the compression along the b axis of α -SnS. The naming convention of the crystallographic vectors used for the transport calculations of α -SnS and β -SnS are explained by figures 5.1 and 5.4. For π -SnS, which has cubic symmetry, the crystallographic vectors are related by symmetry, and since $a = b = c$, only one transport direction was necessary to quantify the thermoelectric properties. More explicitly, π -SnS shows no anisotropy. Figure 5.29 shows the notable geometries of these 3 phases.

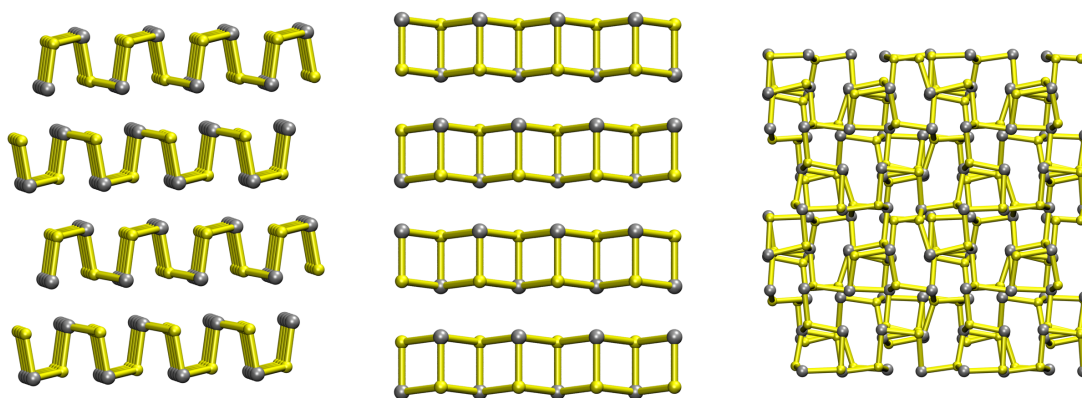


Figure 5.31 – The 3 known phases of tin mono-sulfide, SnS. Left to right: Herzbergite or α -SnS, β -SnS and π -SnS.

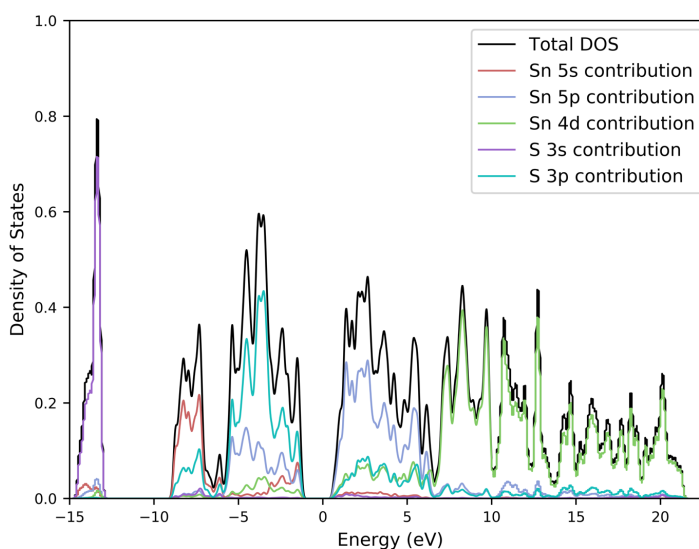
5.5.2 – DOS

In the same manner as for 5.2.1, the DOS of β -SnS and π -SnS were calculated using SCC methods implemented by DFTB theory, with the standard SnS parameter set, a 15 -15 -15 K-grid for β -SnS, and a 10 - 10 - 10 K-grid for π -SnS due to its size. The results are shown in figure 5.32, accompanied by the previously calculated DOS of α -SnS (formerly Herzbergite). The stoichiometry is identical for these 3 systems, as they are polymorphs, and therefore a meaningful comparison can be made between the DOS, as the differences between these plots are exclusively due to the geometry of the system, not the stoichiometry, indeed within each of the phases, tin is formally in the +2 oxidation state. The DOS calculations of α -, β - and π -SnS were performed on unit cells that contained 8, 8 and 64 atoms respectively. To allow for ease of comparison, the relative intensities were “normalised” by division across the energy range of the intensities by the number of atoms in the unit cell, such that the DOS’ presented are effectively for single atoms.

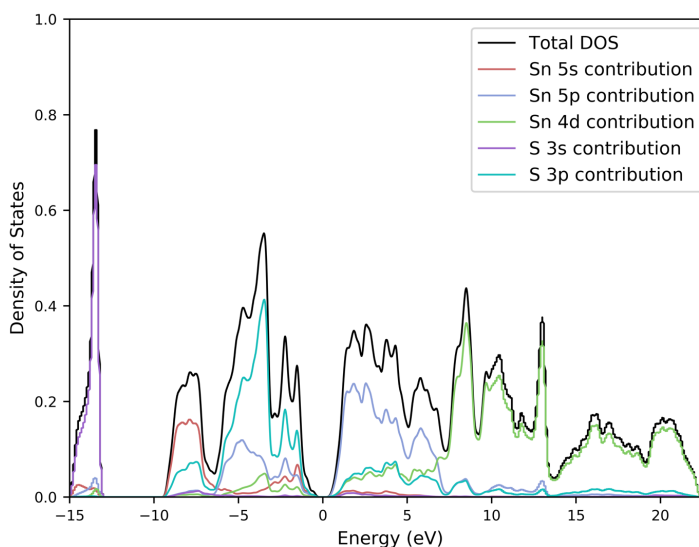
For β -SnS it is notable that there is less “fine structure” than for α -SnS. This is attributed to the coordination spheres of the atoms within each structure. While each tin atom in α -SnS is related by symmetry and thus chemically equivalent, the polyhedron formed by the bonds within the first coordination sphere is a highly distorted octahedron. This asymmetry results in distinct bonding between each atom in the coordination sphere. For β -SnS, each tin atom within the structure is again symmetrically and chemically equivalent, however in this case, the bonds formed with neighbouring atoms (within the first coordination sphere) are equivalent in the x- and y- (a and b) axes, resulting in a more symmetric, though still distorted octahedron. Hence, the DOS of β -SnS is “smoother” than that of α -SnS, as there are fewer “types of bond”.

For π -SnS, the peaks of the DOS are broader for the 5p and 4d orbitals, suggesting that there are a range of similar but distinct bonds in this geometry. However, the same trends hold true across the orbital contributions to each part of energy range for each phase of SnS.

Density of States of Herzenbergite, α -SnS



Density of States of β Tin Sulfide, β -SnS



Density of States of π Tin Sulfide, π -SnS

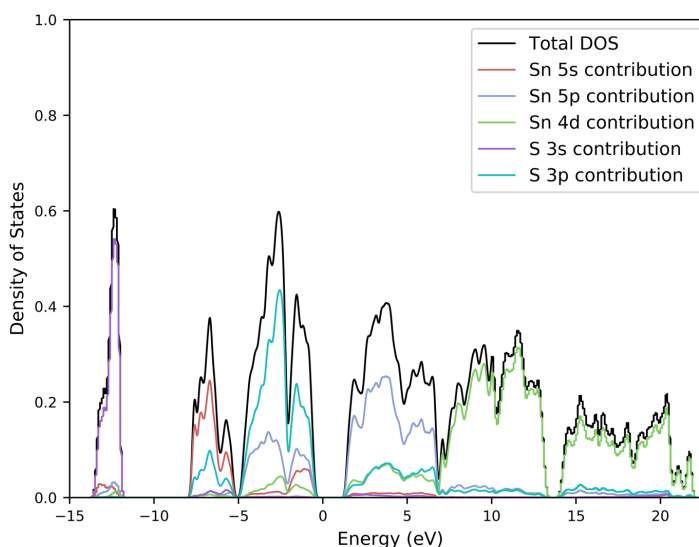


Figure 5.32 – the Density of States of each of the tin monosulfide polymorph's. Calculated using the dftb+ code, with k-grids of 5x5x5 for α -SnS and β -SnS and 4x4x4 for π -SnS.

5.5.3 – BANDS

The bands of the β and π phases were calculated, with the geometries optimised and symmetrised using DFT level theory, as implemented in the quantum espresso plane wave package. The pseudopotentials were norm conserving, and implemented the PBE functional. K-grids of 4-4-4 were used for the optimisation, 6-6-6 for the self-consistent step and 12-12-12 for the consequent non-self-consistent step. The K-point path was explicitly specified for the final bands calculation, according to the convention specified by Cortarolo. These are the same parameters used for the bands in 5.2.2, such that comparison could reasonably be made to the α phase, as demonstrated in figure 5.33.

Ignoring the effect of the large number of atoms in the unit cell of π -SnS, we can see that the effective band masses for π -SnS are far greater than those of α -SnS and β -SnS, whilst those of β -SnS appear the lightest. A curious observation, is that in the structural rearrangement of α - to β -SnS, we see a change from a direct to an indirect band gap, and a decrease in the size of the band gap, to 0.45 eV. The band gap in π -SnS is again indirect, at 1.2 eV.

The band spectra of π -SnS did not display the desired low effective mass, though they did display a large degeneracy (defined as several bands possessing the same energy, within a few $K_B T$).

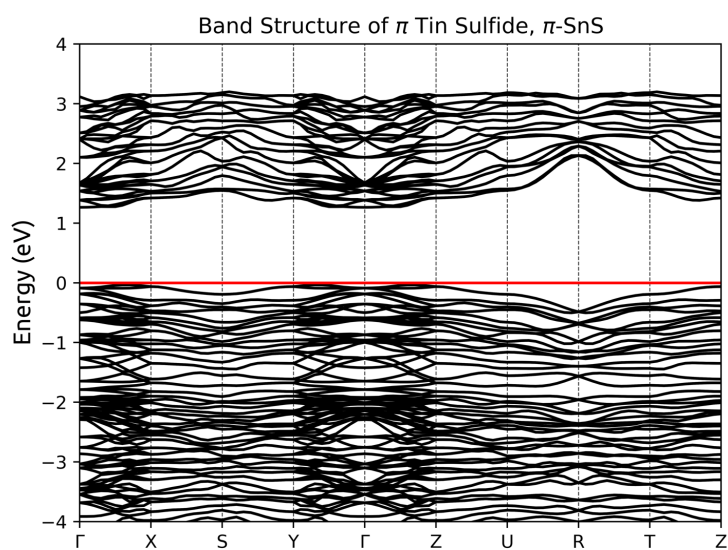
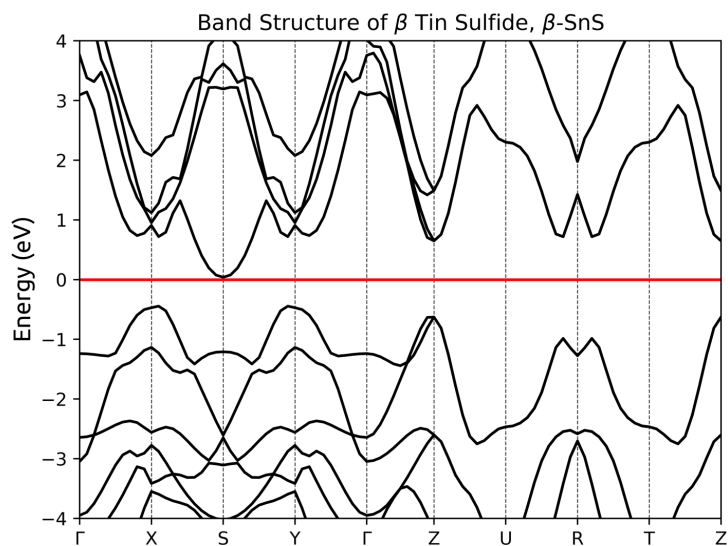
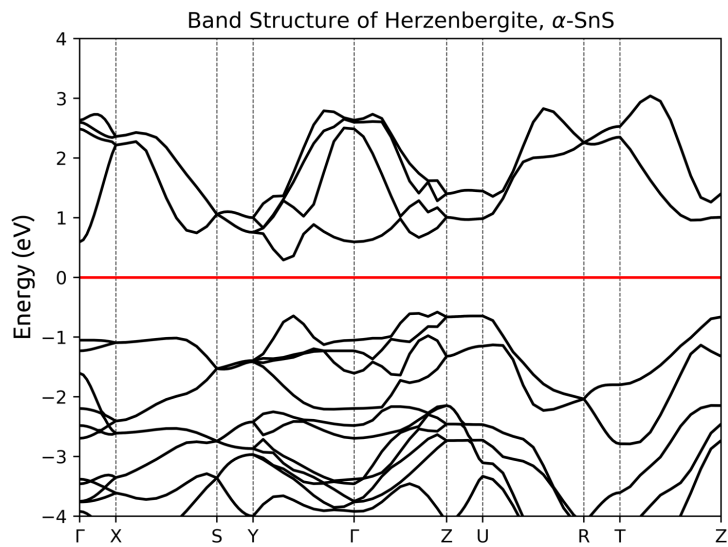


Figure 5.33 – The band spectra of the 3 phases of tin monosulfide, SnS. . Calculated with the quantum espresso plane wave code, using wavefunction cutoff of 50 Ry, DFT-D Van der Waals correction, and a 12x12x12 k-grid.

5.5.4 – TRANSPORT AND THERMOELECTRIC PROPERTIES OF β -SNS

The electronic transport of β -SnS was calculated as for 5.4.1 – 5.4.4 using NSCC methods as implemented within the NEGF-DFTB formalism. The thermoelectric transport coefficients were subsequently derived, as presented in figure 5.34. The transmission was comparable to that of α -SnS (fig. 5.12), in that it was asymmetric with respect to the transmission intensity about the Fermi level, and that the relative magnitudes were ordered: $a > b > c$. The electronic conductivity displayed the expected semiconducting shape, however, was 2 orders of magnitude greater than that of α -SnS – likely due to the reduction in band gap.

The shape and magnitude of the Seebeck coefficient was largely comparable to that of α -SnS, as obtained by NSCC methods, yet differing in sign to that of the NSCC α -SnS. This is somewhat remarkable, and believed to be entirely due to the proximity of the conduction band to the Fermi energy in the NSCC β -SnS. The electronic contribution to the thermal conductivity was a single order of magnitude greater than that obtained from NSCC α -SnS, largely due to the reduction in band gap. The power factor was found to be 2 orders of magnitude larger than that of the alpha phase, and the average maximal zT_e of 150 at around 300 K was found to be 3 order of magnitude larger than the alpha phase.

Considering that the contribution of the lattice thermal conductivity would likely be of the same order of magnitude for the α and β phases, it seems that the phase transition from the α to the β would likely result in an improved zT for SnS, as recently determined for SnSe. This appears to be primarily due to the band gap, which has seen a decrease of approximately 25% in the NSCC Transmission.

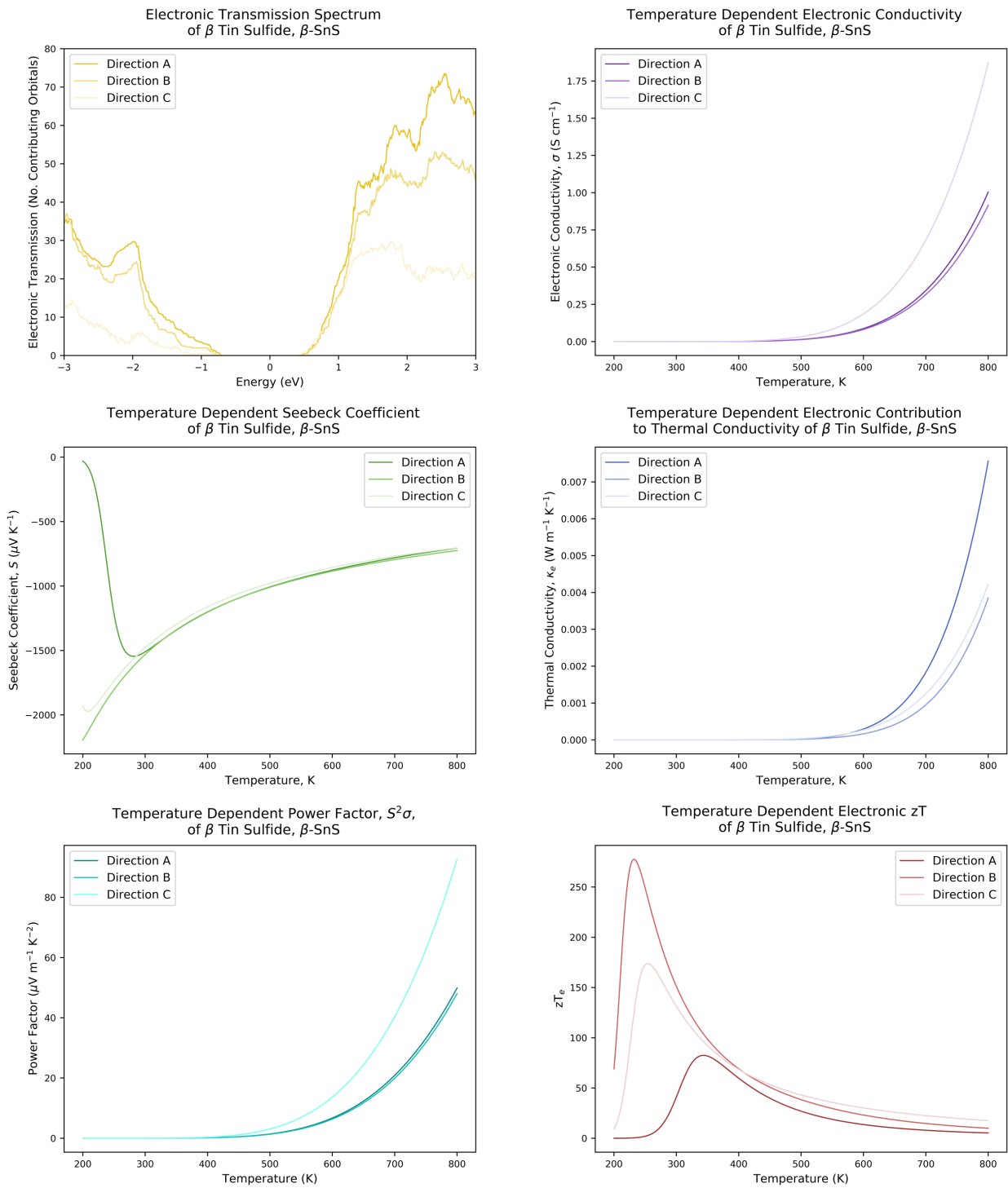


Figure 5.34 – The temperature dependent thermoelectric properties of β -SnS. Transmission calculated using dftb-negf with an energy step of 0.01 eV and k-grid of 4x4x4. Thermoelectric coefficients derived using program (see section 3.5), each series contains 6000 points.

The transport for π -SnS was calculated, also in the NSCC methodology and the NEGF-DFTB approach. The thermoelectric properties calculated as a function of temperature according to the Landauer-Büttiker formalism. Transport was calculated in a single direction, as the 3 crystallographic axes are symmetrically equivalent. This gave a transmission spectrum with a larger band gap than that predicted by the bands calculated by DFT means, as would be expected from the DFTB approach. Due to its large unit cell size, a single replication in each crystallographic vector to create a larger principle layer would result in a nanowire of minimum size with 4128 atoms, which resulted in a memory requirement slightly larger than available on the HPC Wales architecture. As such, it was necessary to calculate the transport with a nanowire consisting of 6 unit cells, 384 atoms. This resulted in a very low resolution transmission spectrum, as seen in figure 5.35.

The electronic conductivity was, remarkably, larger than that of α -SnS despite the larger band gap. A possible cause of this is the steepness of the transmission at the band edges, which may result in a larger overlap between transmission and the first derivative of the fermi function in the derivation of the thermoelectric coefficients in accordance with the Landauer-Büttiker formalism. This may be a fault of the poor resolution. Irrespective of this, the actual values of the conductivity are rather small, compared to those of most “good” thermoelectrics.

The Seebeck coefficient was found to be rather large, and positive, as may be expected from the proximity of the calculated Fermi level to the valence band. The thermal conductivity of the electrons was found to be an order of magnitude lower than that of β -SnS. This was anticipated as a result of the large (~ 3 eV) band gap.

The power factor is of the same order as that calculated for α -SnS under SCC conditions, though 3 orders of magnitude larger than that of α -SnS under NSCC conditions. These effects could be due to the covalent nature of the 3D structure, though it seems likely that the poor resolution is responsible. If this were not the case, the high zT_e of over 600 at 275 K could be considered promising.

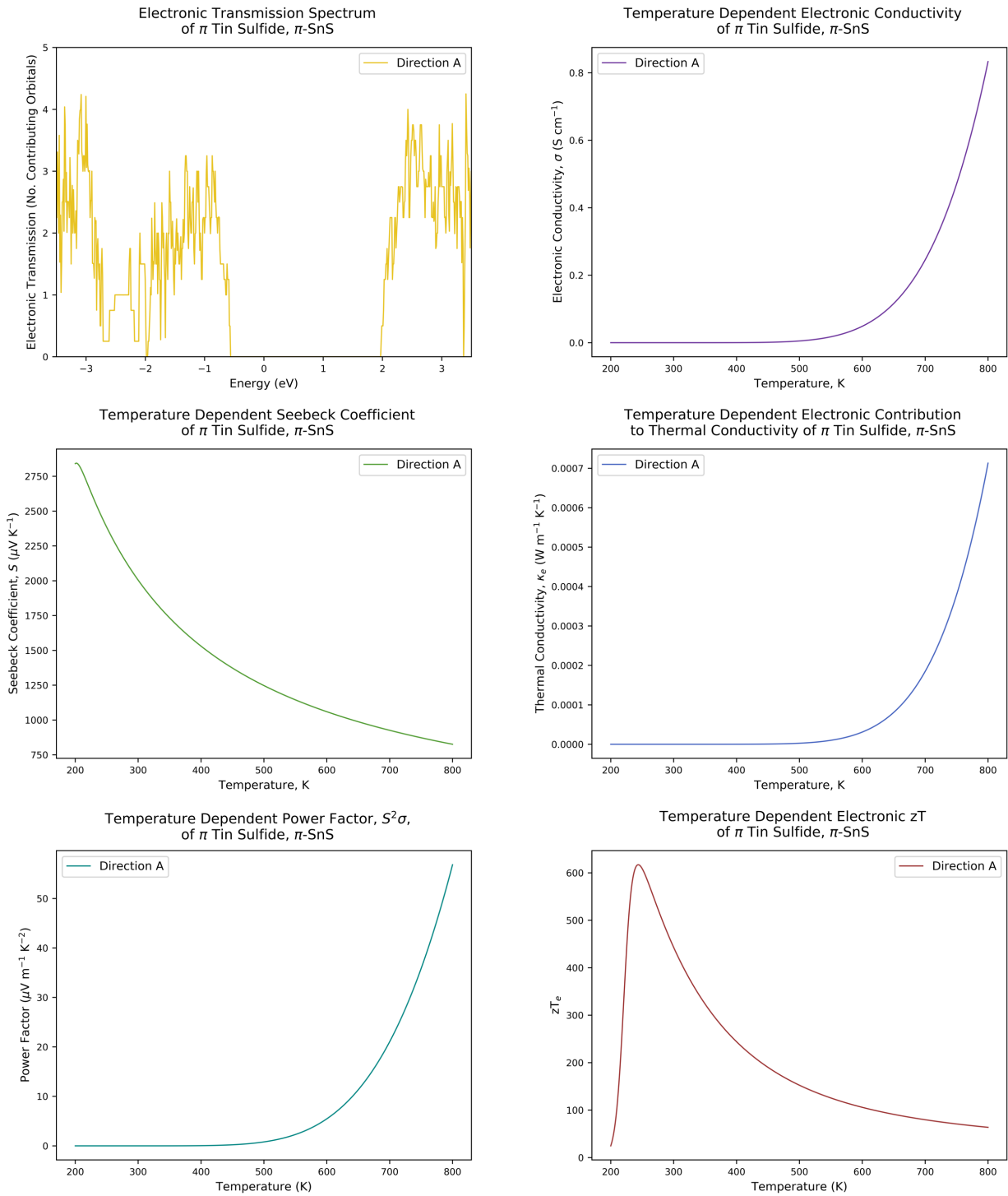


Figure 5.35 – The temperature dependent thermoelectric properties of cubic π -SnS. Due to the cubic symmetry, the transmission would be equivalent in each axis. Transmission calculated using dftb-negf with an energy step of 0.01 eV and k-grid of 4x4x4. Thermoelectric coefficients derived using program (see section 3.5), each series contains 6000 points.

It is clear that the occurrence of a phase transition within the operating temperatures of a thermoelectric material could have a large impact in the thermoelectric properties. For the pure phases of tin mono-sulfide, the α to β phase transition appears to offer a promising route to a higher efficiency material. This appears to be primarily due to the band gap, although additional study would be necessary to fully characterise the impact this has on bonding and lattice thermal conductivity. We have seen that the Seebeck coefficient appears to be dependent on the shape of transmission, i.e. the relative magnitudes and the position of the valence and conduction band edges in relation to the Fermi level. Alternatively, the electronic conductivity seems to bear stronger correlation to the band gap. The implications of this suggest that a small band gap is necessary for large conductivities, and that a disparity between proximity and magnitude of the transmission, at each band edge, with respect to the Fermi energy is an approach that may achieve a large Seebeck coefficient.

It appears that even a small change in the band gap of a material can drastically alter the magnitude of the electronic conductivity and Seebeck coefficient, along with the products of these properties, such as zT_e . The next stage would be the inclusion of self-consistent methods in the calculation of the electronic transmission, to try to tune the band gap of the π -phase to that observed in the band structure calculated using DFT methods.

5.6 – CONCLUSIONS

In this chapter, a crystallographic study of existing and theoretical tin sulfides was undertaken. This included calculation of the band spectra and DOS for each material, as well as calculation of the equations of state for each material. The effect of the volume on the total energy was seen as a way in which to determine the likely phases that may exist under higher pressures or temperatures.

The thermoelectric transport properties have been derived for the naturally occurring, ground state tin sulfide compounds, directly from the electronic transmission calculated by application of the Non-Equilibrium Green's Functions approach, as implemented in Density Functional based Tight Binding theory in accordance with the Landauer-Büttiker formalism of electronic transport. We have observed that the zT_e of the complex stoichiometry Ottemannite compound (Sn_2S_3) has promising characteristics, though concede that the large band gap may result in a significantly lower zT when accounting for the phononic contribution to thermal conductivity.

It has been demonstrated that for non-elemental systems, especially those which exhibit a large difference in electronegativity between chemical species, consideration of charge transfer effects is a necessary task, the application of which may be preferential over the high resolution and sampling of the transmission spectra.

It has also been suggested that whilst the use of this method is necessary for the modelling of large, asymmetric systems, conversely, it may be necessary that to use this method, large systems are necessary to obtain a smooth sampling and better resolved transmission spectrum.

At the higher level, the phase transitions observed in this section are examples of both temperature and size induced phase transitions. These phase transitions are purely structural, and do not occur alongside a simultaneous electronic phase transition. Along with the work on the pressure induced phase transitions in chapter 4, this presents a case for the study of phase transitions in thermoelectric materials. Many of the calculations within the literature offer thermoelectric properties calculated over a range of temperatures, without accounting for the structural rearrangements that occur with this increase in kinetic energy, even if an alteration of symmetry is not necessarily present. This is an important consideration, as it has been demonstrated that even the slightest change in the ionic and electronic structure can have vast implications for the thermoelectric properties.

5.7 – REFERENCES

- 1 L.-D. Zhao, S.-H. Lo, Y. Zhang, H. Sun, G. Tan, C. Uher, C. Wolverton, V. P. Dravid and M. G. Kanatzidis, *Nature*, 2014, **508**, 373–377.
- 2 J. He and T. M. Tritt, *Science*, 2017, **357**, 1369–1378.
- 3 G. J. Snyder and E. S. Toberer, *Nature Mater*, 2008, **7**, 105–114.
- 4 X. Shi, L. Chen and C. Uher, *International Materials Reviews*, 2016, **61**, 379–415.
- 5 M. R. Burton, T. Liu, J. McGettrick, S. Mehraban, J. Baker, A. Pockett, T. Watson, O. Fenwick and M. J. Carnie, *Adv. Mater.*, 2018, **321**, 1801357.
- 6 D. Parker and D. J. Singh, *Journal of Applied Physics*, 2010, **108**, 083712.
- 7 G. Ding, G. Gao and K. Yao, *Sci Rep*, 2015, **5**, 14.
- 8 J. M. Skelton, L. A. Burton, F. Oba and A. Walsh, *J. Phys. Chem. C*, 2017, **121**, 6446–6454.
- 9 H. Yu, S. Dai and Y. Chen, *Nature Publishing Group*, 2016, **6**, 386.
- 10 H. G. Schnering and H. Wiedemeier, *Zeitschrift für Kristallographie*, **156**, 143–150 (1981).
- 11 R. E. Abutbul, A. R. Garcia-Angelmo, Z. Burshtein, M. T. S. Nair, P. K. Nair and Y. Golan, *CrystEngComm*, 2016, **18**, 5188–5194.
- 12 A. Rabkin, S. Samuha, R. E. Abutbul, V. Ezersky, L. Meshi and Y. Golan, *Nano Lett.*, 2015, **15**, 2174–2179.
- 13 Y. Pei, H. Wang and G. J. Snyder, *Adv. Mater.*, 2012, **24**, 6125–6135.
- 14 G. Tan, L.-D. Zhao and M. G. Kanatzidis, *Chem. Rev.*, 2016, **116**, 12123–12149.
- 15 R. T. Downs, M. Hall-Wallace, *American Mineralogist*, 2003, **88**, 247–250.
- 16 P. Giannozzi, S. Baroni, N. Bonini, M. Calandra, R. Car, C. Cavazzoni and D. Ceresoli, *Journal of Physics: Condensed Matter*, 2009, **21**, 395502.
- 17 P. Giannozzi, O. andreussi, T. Brumme and O. Bunau, *Journal of Physics: Condensed Matter*, 2017, **29**, 465901.

5.7 – REFERENCES (CONTINUED)

- 18 T. Lorenz, J.-O. Joswig, G. Seifert, *Semiconductor Science and Technology*, 2014, **29**, 064006.
- 19 T. Lorenz, I. A. Baburin, J.-O. Joswig, *G. Seifert, Isr. J. Chem.*, 2017, **57(6)**, 553-559.
- 20 J. R. Brent, D. J. Lewis, T. Lorenz, E. A. Lewis, N. Savjani, S. J. Haigh, G. Seifert, B. Derby, P. O'brien, *J. Am. Chem. Soc.*, 2015, **137**, 12689-12696.

6 – FINAL NOTES

6.1 – COMPUTATIONAL METHODS

In this work, computational methods have been used to model a range of electronic and structural properties. It is clear that these methods allow some unique insights for the chemist, who so rarely witnesses the interactions of chemical species at the atomic level. The approaches used and developed here allow for the modelling of electronic properties of large systems, along with the derived influence on thermoelectric properties. As such, these approaches may be used to investigate the effect of macroscopic phenomena on the electronic properties of a material.

6.2 – THERMOELECTRIC MATERIALS

Thermoelectric materials have been known for a long time, and yet it is in recent years that a so called “revolution” has occurred, due to the renewed interest in sustainable energy generation, and an improved understanding of the fundamental properties of these materials. The goal of a zT greater than 3 is closer than ever, and it will be exciting to observe over the next decade, to see how these efficiencies are realised. It is widely the belief that a synergistic approach to the optimisation of thermoelectric materials is required to meet this target, however, we are still in an age of discovery, new or existing materials with astounding thermoelectric properties are constantly appearing. Therefore, an understanding of the fundamental phenomena of thermoelectric materials is vital to ensure that no known material is overlooked, and that any new material is thoroughly understood.

6.3 – ON PHOSPHORUS AS A MODEL THERMOELECTRIC MATERIAL

Phosphorus will unlikely be a commercial thermoelectric material. However, its rich phase space and the distinct structures it adopts allow for the consideration of the material as a model for the development of thermoelectric understanding. The expectation had always been that the principles developed using phosphorus would be applied to the more exotic layered compounds in an effort to drastically enhance the respective thermoelectric figures of merit. The effect of the coinciding structural and electronic phase transitions is striking, and it stands to reason that there is a level of exploitability to this approach.

It has been shown that the electronic thermoelectric figure of merit may be substantially improved by the selective introduction of asymmetry to the structure of black phosphorus, meanwhile ensuring that the electronic phase transition does not occur. This is an exciting result, that holds promise for the remaining layered materials in the thermoelectric family.

The presence of defect-rich phosphorene layers in the structures of the intermediate phosphorus' calls for an investigation into the effects of such defects on the electronic properties of thin films of phosphorene. Such boundaries between domains may allow for the tuning of scattering properties in the single layer.

6.4 – ON TIN SULFIDES AS THERMOELECTRIC MATERIALS

Tin Sulfide is a known thermoelectric, and there is a flurry of activity to understand and enhance the properties of this non-toxic, earth-abundant compound. The flexibility of this compound to adapt a wide set of phases encourages hope for new novel phases under potentially extreme conditions, which may have exciting properties. The impact of the high temperature phase transition is clear, the same improvement as observed in the isostructural tin selenides is present.

The next stage in this investigation would be to study the transition pathway between the α -phase and β -phase, such that the asymmetric, metastable intermediate approach may be taken, to selectively introduce both disorder and domain interfaces with the hopes of improving the power factor by the scattering of low energy charge carriers.

The π -phase shows promise as a thermoelectric, however the unfortunate dissimilarity between the electronic structure as calculated by Density Functional Theory and Density Functional based Tight Binding methods casts some suspicion over the result. The next step for this material would be to improve the parameters of the calculation to better model the electronic structure, before remodelling the effects of thermoelectricity.

6.5 – CLOSING REMARKS

There is significant evidence that the presence of phase transitions within the operating conditions of thermoelectric devices will have a critical effect on the thermoelectric properties of such materials. Should there be a semiconductor to metal electronic phase transition, the results may be disastrous. Should there be a structural transition that alters the symmetry of a system, there is significant scope for an improvement in the thermoelectric properties. Were it possible to “freeze” out a meta-stable intermediate structure from the transition pathway, either by the effect of temperature or pressure, there may be real benefit to the figure of merit of such a material, and this may be a legitimate way of enhancing room temperature thermoelectrics, where the low operating temperatures may preserve the frustrated geometry.

